

# **Processing of MgB<sub>2</sub> Bulk Superconductor by Infiltration and Growth**

A thesis submitted for the degree of

Doctor of Philosophy

By

**Ashutosh Bhagurkar**

BCAST

Brunel University London

Uxbridge, UB8 3PH

UK

January 2017

**Supervisor: Dr. N Hari Babu**

## Abstract

Superconductivity in magnesium diboride ( $\text{MgB}_2$ ) was discovered in 2001. The relatively high  $T_c$  (39 K), high critical current density, long coherence length ( $\sim 6$  nm), low raw material cost, lower density and relative ease of fabrication make this material an exciting choice for practical applications. Furthermore, lower anisotropy and strongly linked current flow in untextured polycrystalline samples, unlike its HTS counterparts, has enabled the development of different processing routes to fabricate  $\text{MgB}_2$  in the form of wires, tapes, thin films and bulks.

Conventionally,  $\text{MgB}_2$  is synthesized by *in situ* sintering, where elemental Mg and B powders are reacted to produce  $\text{MgB}_2$ . Although the superconducting phase can be obtained with relative ease, the resulting sample is generally only around 50% dense, due to formation of large pores inside sintered bulks arising from the volatility of magnesium and 25% volume contraction in  $\text{MgB}_2$  phase formation. Although the use of high pressure is effective to promote sintering and subsequent densification, the need to use large pressure vessels represents a significant practical limitation for the development of a practical process and of the achievable dimensions in the final  $\text{MgB}_2$  sample. As a result, the fabrication of high density, bulk  $\text{MgB}_2$  remains a challenging processing problem. This study explores the “Infiltration and Growth” (IG) technique, an established processing route for fabrication of dense ceramics/ceramic matrix composites, as a potential solution.

Boron powders of varying characteristics were infiltrated with Mg(l) to obtain bulk  $\text{MgB}_2$  samples. The samples were analysed using techniques such as XRD, SEM and hardness to analyse various phases formed during the process. These samples typically contained  $\text{MgB}_2$  with minor quantities of Mg. Physical properties of superconducting  $\text{MgB}_2$ , such as  $T_c$ ,  $J_c$  and  $H_{c2}$ , were established. Furthermore, the effective current carrying cross-section was estimated from resistivity measurements using Rowel’s analysis. Continuous Mg channels were major defects in IG processed samples and their presence was found to limit long range current flow. These channels are eliminated by incorporating Mg/AlB<sub>2</sub>/MgB<sub>2</sub> powders in the precursor to facilitate in-flux of Mg, leading to a more uniform infiltration process, thereby enabling fabrication of near-net shaped  $\text{MgB}_2$  bulk superconductors. Such samples showed an almost identical value of trapped magnetic flux at the top and bottom surfaces, suggesting a high degree of uniformity in  $\text{MgB}_2$ .

A careful microstructural analysis of a series of samples indicated that MgB<sub>2</sub> phase formation in IG process occurred in three distinct stages: (1) Intermediate boride formation (2) Bulk liquid Mg infiltration and (3) MgB<sub>2</sub> layer formation. Due to volume expansion involved in stage 1, cracks formed in the  $\beta$ -Boron particles and propagated radially inwards during stage 3. The growing MgB<sub>2</sub> particles sintered simultaneously with the formation of grain boundaries during the process.

Much enhanced performance of MgB<sub>2</sub> was achieved by virtue of C-doping. Increased  $J_c$  was attributed to generation of lattice strains and loss of crystallinity in MgB<sub>2</sub> as a result of C-doping. Finally, trapped field measurements were performed on homogeneous C-doped MgB<sub>2</sub> bulks. The trapped field obtained (4.13 T) in five stacked of bulks is the highest obtained in MgB<sub>2</sub> bulks synthesized under ambient pressure conditions.

## **Acknowledgements**

I sincerely thank Dr. Hari Babu and Prof. D. A. Cardwell for providing me such a wonderful opportunity to work on superconductivity. Hari was full of new ideas and his enthusiasm to try out new things was the key to much enjoyable journey I had during the past few years.

I am deeply indebted to Akiyasu Yamamoto (Tokyo University of Agriculture and Technology) not only for trapped field measurements, but also for his constant support and encouragement throughout the PhD.

I am thankful to Steve Cook, Graham Mitchell, Carmelo Nunez and Peter Lloyd who helped conduct experiments in BCAST laboratories. I am grateful to ETC staff: Dr. Ashley Hawkins, Dr. Nico Nelson, Nita Varma and Dr Lorna Anguilano for the assistance in using characterization facilities. I would like to express my gratitude to Tony Dennis and D K Namburi (University of Cambridge) for measurements with SQUID. The discussions we had on superconductivity helped me understand the subject to a greater depth.

Additionally, I thank my colleagues including but not limited to Utsavi Joshi, Nilam Barekar, Sanjeev das, Chandra Bhanu Basak.

Finally, I would like to acknowledge support of my loving family, especially my parents, my wife Vaibhavi and daughter Gauri, without which none of this work would be possible.

**Table of Contents**

Abstract.....	I
Acknowledgements.....	III
List of Symbols.....	VII
List of Abbreviations.....	IX
List of Publications.....	X
Chapter 1. Introduction.....	1
1.1 Superconductivity and MgB <sub>2</sub> .....	1
1.2 Basics of Superconductivity.....	1
1.3 Superconducting materials of practical importance.....	6
Chapter 2. Literature Review.....	8
2.1 MgB <sub>2</sub> : Structure and Basic Properties.....	8
2.2 Thermodynamics and reaction Kinetics.....	9
2.3 Anisotropy in Critical Field and Current Percolation.....	10
2.4 Flux pinning.....	13
2.4.1 Improving $H_{c2}$ .....	15
2.5 Connectivity.....	16
2.6 Factors determining $J_c$ .....	17
2.7 Alloying in MgB <sub>2</sub> .....	17
2.7.1 Aluminium Substitution.....	18
2.7.2 Carbon Substitution.....	18
2.7.3 Oxygen doping.....	19
2.8 MgB <sub>2</sub> Bulk Fabrication.....	19
2.8.1 <i>In situ</i> Technique.....	20
2.8.2 <i>Ex situ</i> Technique.....	21
2.8.3 A Novel Approach: Infiltration and Growth.....	22
2.9 Factors Affecting Growth of MgB <sub>2</sub> .....	22
2.9.1 Crystallinity and Purity.....	22
2.9.2 Particle size.....	23
2.9.3 Pressure.....	24
2.9.4 Reaction temperature.....	24
2.10 Advancements in Conventional Methods.....	25
2.10.1 Non-Stoichiometric Composition.....	26
2.10.2 Different Precursors: MgH <sub>2</sub> , MgB <sub>4</sub> .....	26

---

2.10.3 Sintering Aids .....	27
2.11 Aim of the Thesis.....	27
Chapter 3. Methodology .....	29
3.1 Inspiration and Adaptation of IG process .....	29
3.2 Sample Preparation .....	30
3.3 Modifications to the Infiltration and Growth Process.....	32
3.4 Sample Characterization .....	33
3.4.1 Optical Microscopy.....	33
3.4.2 X-Ray Diffraction .....	33
3.4.3 Electron Microscopy .....	34
3.4.4 Vickers Hardness Measurements .....	34
3.4.5 Physical Property Measurements .....	35
The $M-T$ and $J_c-B$ plots presented in this thesis for each representative bulks were measured at least twice to ensure reliability of the data.....	36
3.4.6 Resistivity Measurements .....	36
3.4.7 Trapped field Measurement .....	36
3.4.8 Thermal Conductivity Measurements .....	37
Chapter 4. 1 <sup>st</sup> Generation IG Processed MgB <sub>2</sub> .....	38
4.1 Introduction.....	38
4.2 Fabrication and characterization MgB <sub>2</sub> bulk obtained from various B powders .....	38
4.2.1 Reactivity of powders .....	38
4.2.2 Effect of Reaction Temperature .....	40
4.2.3 Phase Analysis .....	42
4.2.4 Microstructures .....	44
4.2.5 Defects in IG MgB <sub>2</sub> .....	48
4.2.6 Resistivity Measurements .....	49
4.2.7 Critical Current Density.....	53
4.2.8 Microhardness.....	54
4.3 Summary .....	55
Chapter 5. Fabrication of Homogeneous MgB <sub>2</sub> -IG Bulks .....	57
5.1 Introduction.....	57
5.2 Continuous Mg Channels: A Challenge.....	57
5.3 Mg addition.....	60
5.4 AlB <sub>2</sub> addition: Reactive wetting .....	63
5.4.1 Interactions between Mg and AlB <sub>2</sub> .....	63

5.4.2 B+AlB <sub>2</sub> Composite precursor .....	68
5.5 MgB <sub>2</sub> addition.....	69
5.5.1 Scanning Electron Microscopy .....	70
5.5.2 Spatial variation in MPIG samples .....	72
5.6 Fabrication of near-net complex shape .....	73
5.7 MgB <sub>2</sub> : Quasi-permanent Magnet .....	75
5.7.1 Trapped Field Measurement .....	75
5.7.2 Flux Creep.....	79
5.8 Summary .....	80
Chapter 6. Investigation of IG Process Mechanism.....	82
6.1 Introduction.....	82
6.2 Infiltration and Growth: A Three Stage process .....	83
6.2.1 Stage 1: Initiation of cracks in the Boron particle: Mg <sub>2</sub> B <sub>25</sub> phase formation process.....	83
6.2.2 Stage 2: Mg uptake in the porous precursor.....	85
6.2.3 Stage 3: Transformation of Mg <sub>2</sub> B <sub>25</sub> to MgB <sub>2</sub> : Rate determining step .....	86
6.3 Mg <sub>2</sub> B <sub>25</sub> Formation.....	90
6.3.1 EDX Analysis .....	92
6.4 Mg(l) Infiltration.....	94
6.5 MgB <sub>2</sub> formation on Mg <sub>2</sub> B <sub>25</sub> particle .....	94
6.6 Summary .....	98
Chapter 7. Carbon Doping in MgB <sub>2</sub> .....	100
7.1 Introduction.....	100
7.2 Effect on $T_c$ .....	101
7.3 Phase Analysis .....	102
7.4 EDS Analysis - C distribution.....	104
7.5 Strain Analysis .....	106
7.6 Effect on $J_c$ .....	107
7.7 Pinning Force .....	109
7.8 Fabrication of High Performance homogeneous C-doped samples .....	111
7.8.1 Trapped Field Measurements.....	112
7.8.2 Flux creep.....	115
7.9 Summary .....	117
Chapter 8. Conclusion.....	119
Chapter 9. Suggestions for Future Work .....	121
References.....	123



**List of Symbols**

<b>Symbol</b>	<b>Meaning</b>
$T_c$	Superconducting Transition Temperature
$E$	Induced electromotive force
$\Phi$	Magnetic flux
$\phi_0$	Magnetic flux associated with single fluxon
$\lambda_c$	Magnetic penetration depth
$H_c$	Critical field
$I_c$	Critical current
$J_c$	Critical current density
$P$	Momentum
$J_D$	Depairing current density
$S$	Momentum due to supercurrent
$\Xi$	Coherence length
$\xi_0$	Coherence length in a pure material without any defects
$\Delta$	Energy gap
$k_B$	Boltzmann constant ( $k_B=1.38 \times 10^{-23}$ J/K)
$L$	Mean free path of electrons
$k$	Ginzburg-Landau parameter
$\vec{F}_L$	Lorentz force
$\vec{B}$	Magnetic field
$\Delta G$	Condensation energy
$F_p$	Flux pinning force
$H$	Magnetic field strength
$f$	$f = f_p/f_p(max)$ is the normalized pinning force density
$f_p(max)$	Maximum pinning force
$a_i, b_i, c_i, d_i$	$a_i, b_i$ and $c_i$ are dimensions of pinning centre and $d_i$ is inter-flux line spacing
$a, b, c$	Lattice constants
$C_p$	Specific heat
$\gamma$	Anisotropy in critical field
$\theta_c$	Angle between external field and $c$ axis
$H_{\rho=0}/H_{irr}$	Irreversibility field
$A_{con}$	Current carrying cross-sectional area
$A_p$	Effective current carrying percolation, arising from anisotropy in $H_{c2}$
$p(J)$	Fraction of grains exceeding $J_c$
$d$	Average grain size
$h$	Normalised field $H/H_{irr}$
$\rho_0$	Residual Resistivity
$\lambda_{ep}$	Electron-phonon coupling constants
$D$	Diffusivity
$D_{\sigma,\pi}$	Charge carrier diffusivities for respective bands
$K_c$	Connectivity
$\rho$	Resistivity
$P_c$	Percolation threshold

$\gamma_v$	Electronic specific heat coefficient per volume
$\beta_B$	Ratio of mass of balls to mass of powder
$Wp$	Angular frequency
$r_p$	Radius of sun disk
$r_v$	Radius of vial
$t$	Time
$\theta$	Bragg angle
$C$	Dimensionless constant
$t_B$	Thickness of the cylindrical bulk sample
$k_G$	Geometrical factor (Biot-Savart law for cylinder)
$r$	Radius of the cylindrical bulk sample
$a$	Radius of unreacted B particle
$b_i$	Radius of spherical particle prior to reaction
$b$	Outer radius of spherical reacting particle
$\sigma_r$	Radial stresses at any distance R from centre of a spherical $\beta$ -B particle
$\sigma_\theta$	Tangential stresses at any distance R from centre of a spherical $\beta$ -B particle
$G$	Energy release rate
$Z$	Geometrical factor
$E$	Elastic modulus
$2b_c$	Crack length
$\sigma_y$	Yield strength
$\sigma_c$	Critical stress
$\chi_0$	Infiltration depth
$r_p$	Radius of cylindrical porous channels
$\gamma_s$	Surface tension
$\theta_w$	Wetting angle
$\eta$	Viscosity
$V_m$	Molar volume
$\varepsilon_V$	Volumetric strains
$\varepsilon_L$	Linear strains
$C_{Mg-MgB_2}$	Mg Concentration at Mg-MgB <sub>2</sub> interface
$C_{MgB_2-Mg_2B_{25}}$	Mg concentration at MgB <sub>2</sub> -Mg <sub>2</sub> B <sub>25</sub> interface
$J_{Mg}$	Flux of Mg atoms
$x$	Thickness of the MgB <sub>2</sub> layer
$t^*$	Time necessary to complete reaction II
$\beta_{Observed}$	Observed broadening in radian
$\beta_{Instrumental}$	Instrumental broadening in radian
$K_s$	Scherrer constant determined by crystallite size
$\lambda_{X-Ray}$	Wavelength of X-ray
$L$	Size of diffracting domain
$\varepsilon_N$	Non-uniform strain
$U_o$	Activation energy for de-pinning of flux line
$\alpha_c$	Material parameter (Flux creep)
$B$	Trapped field
$A$	$J_c$ extrapolated to 0 K
$K$	Reaction rate constant

## List of Abbreviations

<b>Abbreviations</b>	<b>Meaning</b>
BCS	Bardeen–Cooper–Schrieffer
LTS	Low Temperature Superconductors
HTS	High Temperature Superconductors
BCC	Body Centre Cubic
XRD	X-ray powder Diffraction
TEM	Transmission Electron Microscopy
GL	Ginzburg–Landau theory
PIT	Powder In Tube
IG	Infiltration Growth
RLI	Reactive Liquid Infiltration
RRR	Residual Resistivity Ratio
AIMI	Advanced Internal Mg Infiltration
CERMETS	Ceramics/Ceramic as well as Metal Matrix Composites
SEM	Scanning electron microscopy
EDS	Energy dispersive X-ray spectroscopy
FIB	Focus Ion Beam
HRTEM	High Resolution Transmission Electron Microscopy
MPMS-XL	Magnetic Property Measurement System
SQUID	Superconducting Quantum Interference Device
PPMS	Physical Property Measurement System
FCM	Field Cooled Magnetization
AA	Alpha Aesar
HCA	HC Starck Amorphous
NM	New Met
HCC	HC Starck Crystalline
IG	Infiltration and Growth
ZFC	Zero Field Cooled
MPIG	Modified Precursor Infiltration and Growth
BSE	Back Scattered Electron
MgB <sub>2</sub> -IG	MgB <sub>2</sub> fabricated by Infiltration-Growth
MgB <sub>2</sub> -(Source of B Powder)	MgB <sub>2</sub> fabricate using particular type of boron powder.
Stack-5	Stack of five cylindrical bulk MgB <sub>2</sub> samples

### List of Publications

- **A G Bhagurkar**, A Yamamoto, N Hari Babu, J H Durrell, A R Dennis and D A Cardwell “Synthesis of Dense Bulk MgB<sub>2</sub> by an Infiltration and Growth Process” 2015 *Supercond. Sci. Technol.* **28** 015012.
- **A G Bhagurkar**, N Hari Babu, A R Dennis, J H Durrell, D A Cardwell “Characterization of Bulk MgB<sub>2</sub> Synthesized by Infiltration and Growth” 2015 *IEEE Trans. Appl. Supercon.* **25** 6801504.
- J Zou, M D Ainslie, H Fujishiro, **A G Bhagurkar**, T Naito, N Hari Babu, J F Fagnard, P Vanderbemden and A Yamamoto “Numerical Modelling and Comparison of MgB<sub>2</sub> Bulks Fabricated by HIP and Infiltration Growth” 2015 *Supercond. Sci. Technol.* **28** 075009.
- **A G Bhagurkar**, A Yamamoto, L Anguilano, A R Dennis, J H Durrell, N Hari Babu and D A Cardwell “A Trapped Magnetic Field of 3 T in Homogeneous, Bulk MgB<sub>2</sub> Superconductors Fabricated by a Modified Precursor Infiltration and Growth Process” 2016 *Supercond. Sci. Technol.* **29** 035008.
- **A G Bhagurkar**, A Yamamoto, A R Dennis, J H Durrell, T A Aljohani, N Hari Babu, D A Cardwell “Microstructural Evolution in Infiltration-Growth Processed MgB<sub>2</sub> Bulk Superconductors” 2017 Accepted in *J. Am. Ceram. Soc.*

## Chapter 1. Introduction

### 1.1 Superconductivity and MgB<sub>2</sub>

MgB<sub>2</sub> has attracted a lot of attention within the scientific community in last 15 years. Not only it is an excellent choice for a practical application, but its unique two-band structure also offers further insights into the mechanism of superconductivity. This thesis is aimed at the fabrication of dense and complex shaped MgB<sub>2</sub> components, which are not easily achievable by conventional processing routes.

### 1.2 Basics of Superconductivity

Superconductivity was discovered in 1911 by a Dutch scientist Heike Kamerlingh Onnes [1]. He discovered that a few materials (first being Hg) lost electrical resistance rather abruptly at a certain temperature  $T_c$ , rather than following a continuously decreasing behaviour. These materials he named as superconductors. Highly pure metals are also expected to show zero resistance at 0 K. However, superconductors show a peculiar behaviour called the Meissner effect, suggesting that it's a different thermodynamic state. Meissner and Ochsenfeld [2] observed that when a superconductor is cooled in presence of small magnetic field, it expels the magnetic flux outside its body. A pure metal at 0 K is not expected to show such behaviour. It would rather try to retain the magnetic flux within itself by setting up eddy currents according to Faraday's law [3],

$$E = -\frac{d\phi}{dt} \quad (1.1)$$

Where  $E$  is induced electromotive force and  $\phi$  is magnetic flux.

A Magnetic field penetrates only a short distance inside a superconductor, known as penetration depth  $\lambda_c$ . Thus, any material needs to qualify two conditions to become a superconductor. First being zero resistivity and other being Meissner effect.

Moreover, superconducting material behaves as normal upon the application of a certain critical field  $H_c$  [4]. This too, is hard to explain for a pure metal showing 0 resistance at 0 K.  $H_c$ , is defined to be function of free energy difference between normal and superconducting state.

$$\frac{\mu_0 H_c^2(T)}{2} = f_n(T) - f_s(T) \quad (1.2)$$

The above equation is valid for long thin superconductor in a parallel field. This further implies that current carrying capacity in a superconductor is also limited. This is because critical currents  $I_c$  flowing in the wire, generate a self-field greater than  $H_c$  at the surface of superconductor.  $I_c$  is described by Silsbee's rule, where  $r$  is radius of wire [4]. This equation is valid only for zero external field.

$$I_c = 2\pi r H_c \quad (1.3)$$

Therefore superconductivity is not just a linear regime below  $T_c$ , but rather a volume bounded by  $J_c$  (Critical Current Density) and  $H_c$  (Critical Field) in a 3-D system  $T$ - $J$ - $H$ . The material is said to be in “superconducting state” within this volume and a “normal state” outside it. Thus, superconductor requires operating at limited temperature and magnetic field, and can carry large, although limited, amount of current.

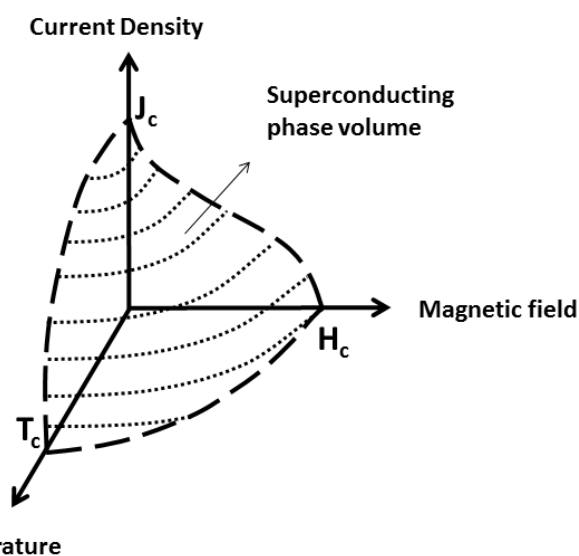


**Figure 1.1** Schematic showing Superconducting phase volume bounded by  $T_c$ ,  $J_c$  and  $H_c$ .

For most superconducting materials, superconductivity is explained by Bardeen-Cooper-Schrieffer theory [5]. The BCS theory attributes supercurrent to Cooper electron pairs. The electron pairs form due to interactions with phonons, vibration in the lattice of superconductors. This interaction gives rise to attractive potential between pairs of electrons, making it a slightly lower free energy system compared to a two free electron system. All the pairs exhibit a condensed momentum state described as  $(p=\hbar s)$  where  $s$  is momentum due to

supercurrent. These pairs exist over a length characterized by superconducting coherence length ( $\xi$ ).

This leaves energy a gap between them of the order of 1 meV. The energy gap  $2\Delta$  (0 K), although small inhibits the scattering with phonons that lead to resistivity. Therefore the superconductor exhibits zero resistivity when thermal perturbation is less the band gap. According to this theory,  $T_c$  is described as [6]

$$T_c = \frac{\Delta(0 K)}{1.8 k_B} \quad (1.4)$$

Where  $k_B$  is the Boltzmann constant ( $k_B=1.38 \times 10^{-23}$  J/K). Since the energy gap is small,  $T_c$  of BCS type superconductor is limited to about 30 K, the temperature after which thermal oscillations become significant, as shown in figure 1.2 for an Indium-Bismuth alloy.

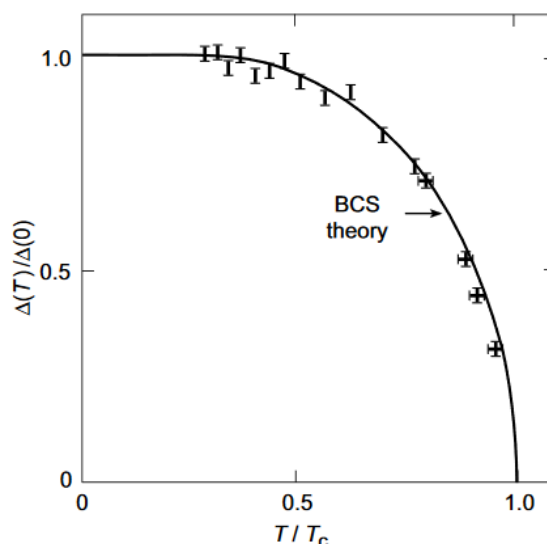


**Figure 1.2** Variation of superconducting energy gap with temperature. Experimental observation of energy gap are consistent with predictions of BCS theory [7].

Coherence length ( $\xi$ ) is also defined as the characteristic length of size of a Cooper pair, or statistically obtained average distance between two electrons in a Cooper pair. Coherence length can be affected by mean free path of electrons. In practical superconductors  $\xi$  can be estimated by following equations [6].

$$\frac{1}{\xi} = \frac{1}{\xi_0} + \frac{1}{l} \quad (1.5)$$

$\xi_0$  represents coherence length in a pure material without any defects. And  $l$  is mean free path of electrons.

Thus penetration depth and coherence length are two fundamental quantities in a superconducting material. These two terms together determine maximum critical current density  $J_D$ , also known as depairing current density, and critical field  $H_c$  as shown in following Ginzburg Landau equations. Moreover, their ratio ( $\kappa=\lambda/\xi$ ) decides the type of superconductor, i.e. type I or type II [7].

$$J_D = \frac{\phi_0}{3\sqrt{3}\pi\lambda_c^2\xi} \quad (1.6)$$

$$H_c = \frac{\phi_0}{\sqrt{2}\pi\lambda_c\xi} \quad (1.7)$$

Where  $\phi_0$  is the magnetic flux associated with single fluxon ( $h/2e$ ) ( $\sim 2 \times 10^{-15}$  Wb)

Solutions of Ginzburg Landau (G L) equations fall into two groups depending on the sign of energy of the normal state superconducting state interface [8]. Abrikosov noted that for the values of the Ginzburg Landau parameter ( $\kappa=\lambda_c/\xi$ )  $< 1/\sqrt{2}$ , surface energy is positive and Meissner effect is observed [9]. Such materials are termed as type I superconductors.

For the Ginzburg Landau parameter greater than  $1/\sqrt{2}$ , Abrikosov predicted that the magnetic flux would be expected to penetrate into the superconductors in the form of fluxons. As the surface energy in this case is negative, the lowest free energy configuration should have high normal-superconducting surface. Therefore system of large number of fluxons, each containing a flux quantum  $\phi_0$ , should be most stable. These materials are termed as type II superconductors. These fluxons are parallel to the direction of applied field and comprise of normal cylinders with radius equal to coherence length. Therefore, type II superconductors exhibit similar behaviour up to first critical field  $H_{c1}$ . Above  $H_{c1}$ , as flux penetrates into the material, the fluxons are screened by induced supercurrents. Above a second critical field  $H_{c2}$ , superconductivity ceases to exist. This is when normal areas associated with the fluxons overlap.

In a type II superconductor, repulsion between the fluxons forces them to arrange in a hexagonal array, called a flux lattice. In the presence of the transport current through such a



material, a Lorentz force  $\vec{F}_L = \vec{J}_c \times \vec{B}$  would force the fluxons to move in a perpendicular direction, generating a field gradient and a loss of zero resistance (Figure 1.3). Therefore superconductivity doesn't exist despite transport current density being lower than depairing current density,  $J_D$ .

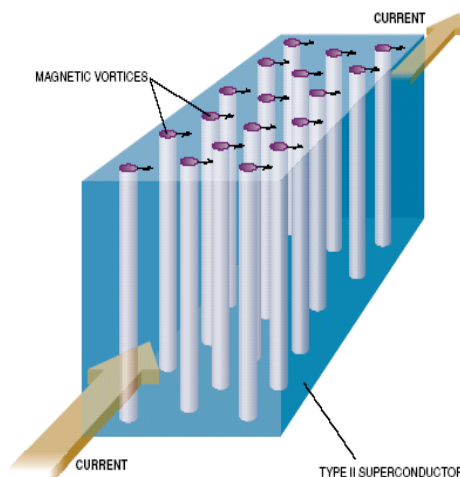


**Figure 1.3 Schematic showing origin of Lorentz force  $J_c \times B$**

To form a fluxon in a superconductor, extra energy has to be provided in order to transform the superconducting fluxon core into normal state. This is called condensation energy

$$\Delta G = \frac{1}{2} \mu_0 H_c^2 \pi \xi^2 \quad (1.8)$$

For the formation of fluxon in the normal region, condensation energy required to form a normal state fluxon core is reduced. Such a system thus attains a ‘‘Potential well’’, thus becomes more stable than the systems without pinning centres. Materials with strong pinning capability can therefore allow large current to pass, before it generates force  $F_l$  large enough to move fluxons. Flux pinning force is described as

$$F_p = J_c \times B \quad (1.9)$$

Many defects including precipitates, dislocations, stacking faults and grain boundaries can act as pinning centres. However, their pinning ability varies depending on the interaction between pinning centres and fluxons. Generally, for optimal pinning, the size of pinning centres should be comparable to the size of coherence length of fluxons. Dew-Hughes classified pinning centres based on their geometry. Their bulk overall pinning effect is described in following equations [10, 11]

$$\text{Normal core pinning } (d_i < a_i, b_i, c_i) \quad f(h) = h^0(1-h)^2 \quad (1.10)$$

$$\text{Normal surface pinning } (c_i < d_i < a_i, b_i) \quad f(h) = h^{0.5}(1-h)^2 \quad (1.11)$$

$$\text{Normal volume pinning } (a_i, b_i, c_i < d_i) \quad f(h) = h^1(1-h)^2 \quad (1.12)$$

Where,  $h=H/H_{irr}$  is reduced field ( $0 \leq h \leq 1$ ),  $f = f_p/f_{p(max)}$  is the normalized pinning force density,  $f_{p(max)}$  is the maximum pinning force.  $a, b$  and  $c$  are dimensions of pinning centre and  $d$  is inter-flux line spacing,  $d^2 = 0.17 \phi_0/B$ . Thus the reduced field dependence of normalised pinning force is determined entirely by flux pinning types, independent of materials or given temperature. If grain boundaries are dominant pinning centres in a material, pinning force  $f(h)$  is given by  $h^{0.5}(1-h)^2$  for all temperatures  $T < T_c$ .

Therefore the pinning force curves and reduced field at pinning force maxima can be used to determine the flux pinning mechanism of a superconductor. In practice, the normalised field  $h$  is often defined as  $H/H_{irr}$ , as  $H_{irr}$  is the field where  $J_c$  is practically zero. Finally it is noted that  $f_{p(max)}$  is dependent on density of pinning centres and increase in  $H_{c2}$  ensures that pinning centres can operate over a wider range of field. Thus  $H_{c2}$  enhancement and introduction of additional pinning centres are general approaches to improve flux pinning capability, and ultimately  $J_c$ , in a superconductor.

### 1.3 Superconducting materials of practical importance

Although thousands of materials are known to be superconducting, a vast majority of them are of little practical use owing to their very low critical transition temperatures and critical fields [12, 13]. Superconductors are generally characterized based on the  $T_c$ , namely Low temperature superconductors (LTS) (9-25 K) and high temperature superconductors (HTS) ( $\sim 90$  K). Typical commercial LTS materials, Nb, Nb-Ti, Nb<sub>3</sub>Sn, operate at temperatures  $< 20$  K which require extensive use of expensive liquid He [14]. HTS materials, YBCO and Bi-2223 can be operated above 77 K [15, 16]. This enables use of liquid nitrogen which is a relatively cheap resource.

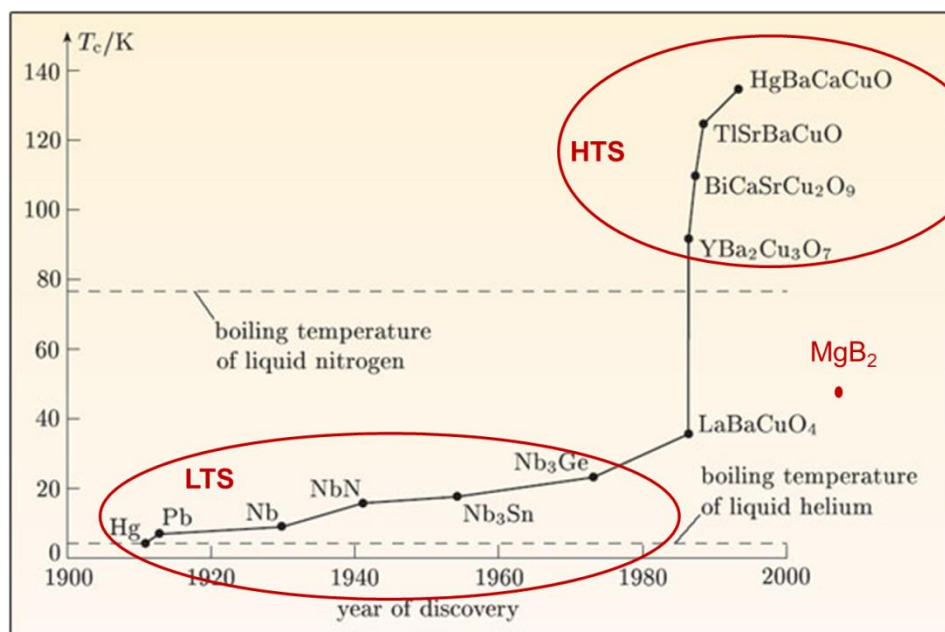


Figure 1.4. Timeline of discovery of superconductors in 20th century.

However, the necessity of high texture in these materials and inherent brittleness present considerable challenges in fabrication [17]. Therefore, their use in practical applications is largely limited. Another two new superconductors have been discovered in last 15 years,  $\text{MgB}_2$  [18] and Iron pnictide [19]. Figure 1.4 shows the timeline of practically important superconducting materials while table 1.1 summarizes their physical and magnetic properties.

Material	NbTi	Nb <sub>3</sub> Sn	YBCO	Bi-2223	Fe-122	MgB <sub>2</sub>
Crystal Structure	BCC	A15	Perovskite	Perovskite	Perovskite	Hexagonal
Anisotropy	Negligible	Negligible	7	50-100	Negligible	1.2-5
$T_c$ (K)	9	18	92	108	35	39
$H_{c2}(0\text{ K})$ (T)	15	30	>100	>100	>100	20
$H_{irr}$ (T)	11	24	--	--	--	--
$J_{c(max)}(77\text{ K})$ (A/cm <sup>2</sup> )	--	--	20000	1000	--	--
$J_{c(max)}(4.2\text{ K})$ (A/cm <sup>2</sup> )	3000	8000	40000	2000	1000	2000

Table 1.1 Superconducting properties of superconducting materials of practical importance [20].  $H_{irr}$

(only for this table) is the external field after which  $J_c$  is practically 0.

## Chapter 2. Literature Review

### 2.1 MgB<sub>2</sub>: Structure and Basic Properties

Although MgB<sub>2</sub> material was well known in 1953, it took five decades to realize its potential as a superconducting material. Jones *et al* studied the Mg-B system and identified the compound as MgB<sub>2</sub>, with alternate layers of Mg in a B honeycomb lattice (Figure 2.1), similar to AlB<sub>2</sub> [21, 22]. Lattice constants were found to be  $a = 3.083 \text{ \AA}$  and  $c = 3.5213 \text{ \AA}$ . It is characterized in  $P6/mmm$  space group, with Mg occupying (0, 0, 0) and B occupying (1/3, 2/3, 1/2) and (2/3, 1/3, 1/2) sites.

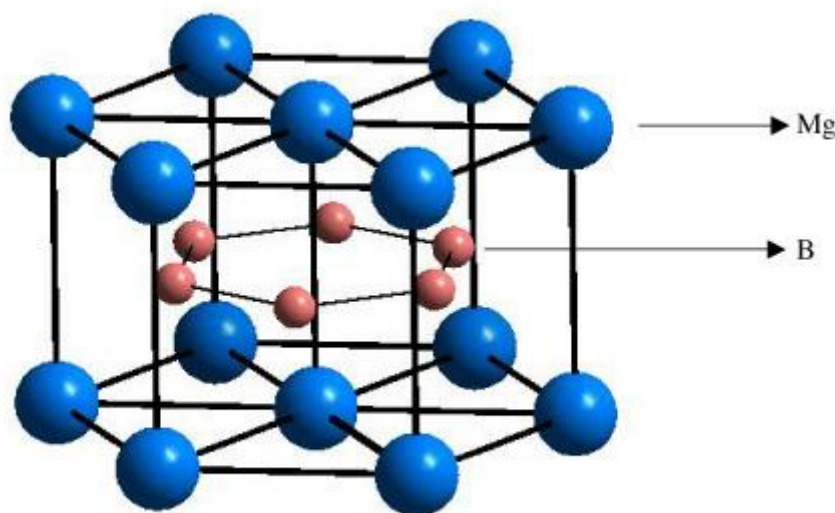


Figure 2.1 Schematic of crystal structure of MgB<sub>2</sub> [23].

A schematic of the crystal structure is shown in figure showing alternate layers of Mg in B honeycomb lattice. This feature results in anisotropy in superconducting properties. A specific heat study of MgB<sub>2</sub> was conducted by Swift and White in 1957. However, since the data was presented in tabular form the authors probably could not detect the  $C_p$ - $T$  transition typically observed in BCS superconductors [24]. The discovery was made much later in 2001 by Akimitsu *et al* [18]. It was realized that MgB<sub>2</sub> follows a conventional BCS mechanism, where electrons form Cooper pairs via electron-phonon interaction [25-29]. An Isotope effect presented another evidence for BCS driven superconductivity in MgB<sub>2</sub> [30]. In classical BCS theory, the isotope coefficient  $\alpha_{\text{BCS}}$  is defined as  $T_c \propto A_M^{-\alpha}$ , where  $A_E$  is atomic mass of element. When another, less common isotope of boron with atomic mass number 10 was used as reactant in the synthesis of MgB<sub>2</sub>, an increment of 1 K was observed in  $T_c$ . Interestingly,

Mg was observed to show a small isotope effect compared to boron, suggesting B atom vibrations are important for superconductivity [31]. The electronic structure in  $\text{MgB}_2$  can be described as a combination of a two dimensional planar network of  $\sigma$  bands within the B atomic layer and out-of-plane delocalized  $\pi$  bands throughout the unit cell [32]. Thus two distinct energy gaps are observed corresponding to different types of bands – the strongly coupled  $\sigma$  band with broad zero-temperature energy gap  $\Delta(0\text{K}) \sim 7$  meV and the weakly connected  $\pi$  band with  $\Delta(0\text{K}) \sim 2.2$  meV [33, 34]. The two-band nature of the electronic structure enables the  $T_c$  of  $\text{MgB}_2$  to go beyond the expected maximum as dictated by conventional BCS theory, reaching as high as 39 K.

## 2.2 Thermodynamics and reaction Kinetics

A phase diagram for the Mg-B binary system is shown in figure 2.2, whereas figure 2.3 shows temperature-pressure phase diagram for Mg-B system for Mg:B ratio greater than 0.5 [35]. Figure 2.2 shows three peritectic reactions (to form  $\text{MgB}_2$ ,  $\text{MgB}_4$  and  $\text{MgB}_7$  phase) and negligible solubility of each other in any other phase. However, additional B-rich borides like  $\text{Mg}_2\text{B}_{25}$ ,  $\text{MgB}_{20}$ ,  $\text{MgB}_{10}$  have also been reported in the literature, possibly formed because these are metastable phases or due different allotropes of boron used in the fabrication process. It can be seen from figure 2.3 that the  $\text{MgB}_2$  phase stability regime shrinks with drop in pressure. This can be explained by the high vapour pressure of Mg. The peritectic decomposition reaction temperature according to figure 2.2 is about 1500 °C at 1 atm, much higher than  $\text{MgB}_2$  synthesis temperature in any of the processing routes.

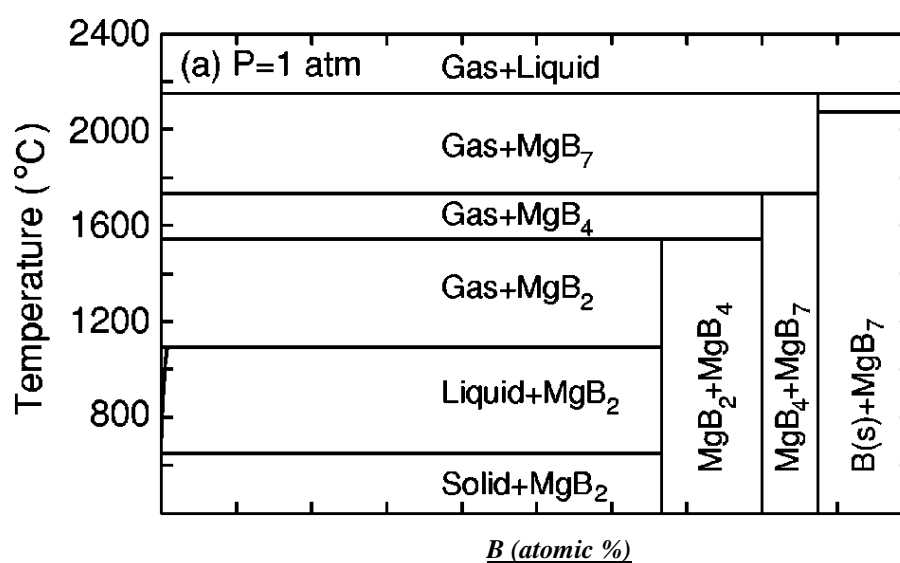


Figure 2.2 Equilibrium phase diagram of Mg-B system (with permission from [35]).

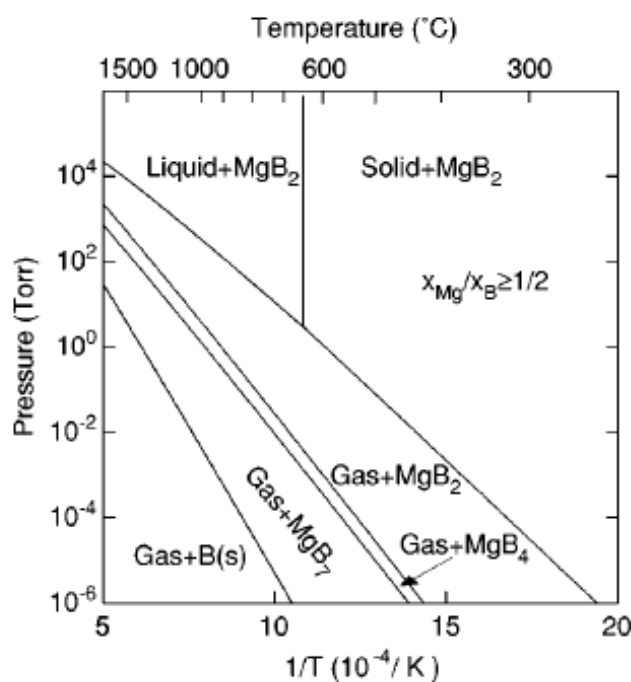


Figure 2.3 Temperature-Pressure phase diagram of  $\text{MgB}_2$  (With permission from [35]).

It is now realised that amorphous boron is much more reactive than crystalline boron. Dunand and DuFouw conducted *in situ* synchrotron radiation measurements and the activation barrier for crystalline and amorphous boron was found to be 360 and 108 kJ/mol respectively [36]. Ma *et al* measured *in situ* XRD patterns of sintered samples as they were heat treated at various constant temperatures [37]. Kim *et al* analysed TEM images of  $\text{MgB}_2$  thin films, where Mg vapour was reacted with B substrate at controlled temperature and suggested parabolic growth of  $\text{MgB}_2$  layer thickness with time [38]. All these studies suggested that the following reaction I occurred on phase/particle boundary forming a continuous  $\text{MgB}_2$  layer. Hence further progress was governed by diffusion of Mg through the  $\text{MgB}_2$  layer [39].



### 2.3 Anisotropy in Critical Field and Current Percolation

$\text{MgB}_2$  assumes a hexagonal crystal structure. Therefore its physical and superconducting properties differ in *a-b* and *c* direction. In the clean sample,  $H_{c2}$  is up to 5 times larger in the *a-b* plane compared to the *c* direction [40, 41] although this reduces to nearly 1 at temperatures approaching  $T_c$  as shown in figure 2.4. When grains are perfectly randomly oriented in a polycrystalline  $\text{MgB}_2$  material, the upper critical field distribution within the

material is shown in figure 2.5. Naturally, when a high magnetic field is applied, the material can be considered inhomogeneous. This is because grains oriented close to c-axis become normal under sufficiently high external fields [42]. Therefore

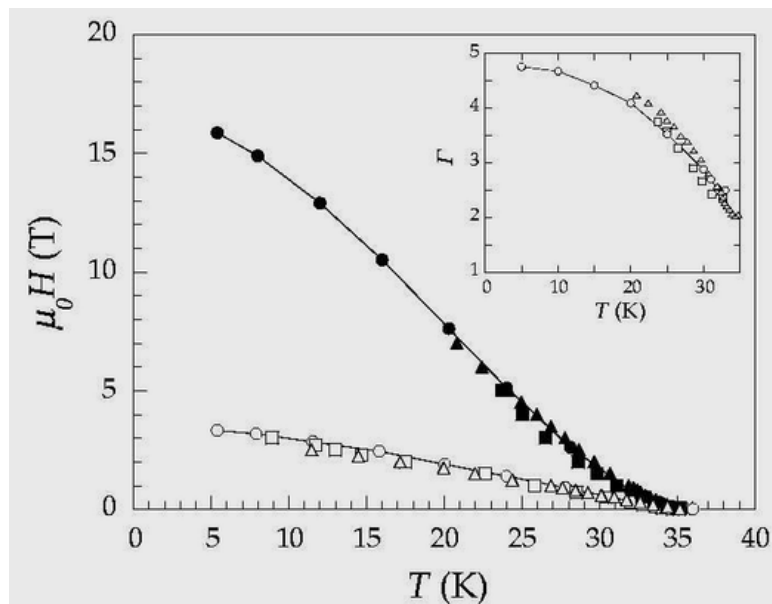


Figure 2.4 Anisotropy in  $H_{c2}(0 T)$  in  $\text{MgB}_2$  single crystals (With permission from [40]).

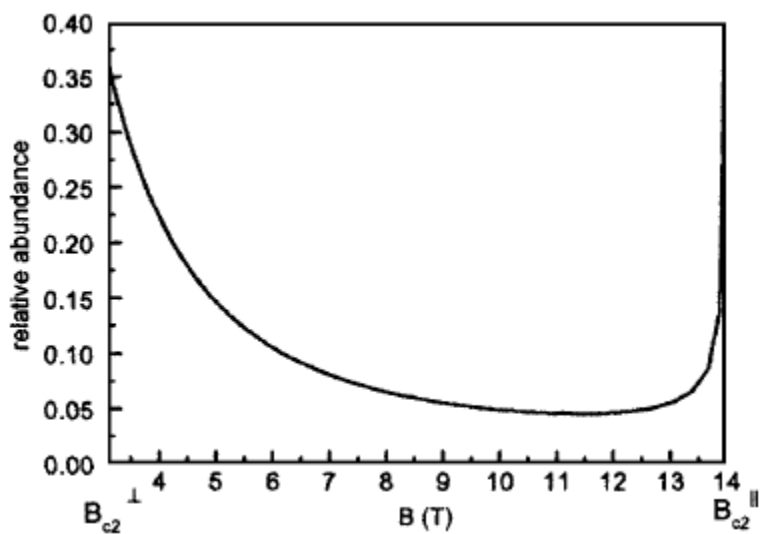


Figure 2.5 Distribution of upper critical field within the grains (With permission from [43]).

the critical current density in  $\text{MgB}_2$  continuously drops rather quickly with increasing external magnetic field until no macroscopic current path is present. The Dependence of overall  $H_{c2}$  with angle can be given by Ginzburg-Landau theory as [44]

$$H_{c2}(\theta_c) = \frac{H_{c2}^{ab}}{\sqrt{\gamma^2 \cos^2 \theta_c + \sin^2 \theta_c}} \quad (2.1)$$

Where  $\gamma$  is the anisotropy in the critical field ( $\frac{H_{c2}^{ab}}{H_{c2}^c}$ ) and  $\theta_c$  is the angle between external field and  $c$  axis the width of percolative transition at a fixed field  $H_0$  was given by Eisterer *et al* as [42]

$$\Delta T = \frac{\sqrt{(\gamma^2 - 1)p_c^2 + 1} - 1}{-\frac{\partial H_{c2}^{ab}}{\partial T}} H_0 \quad (2.2)$$

Whereas anisotropy-induced-irreversibility field ( $H_{\rho=0}$ ) is given as-

$$H_{\rho=0}(T) = \frac{H_{c2}^{ab}(T)}{\sqrt{(\gamma T^2 - 1)p_c^2 + 1}} \quad (2.3)$$

since loss of long range supercurrent here is caused by anisotropy rather than thermally activated depinning in HTS materials. Thus microscopic supercurrent flows only above  $p > p_c$ . Therefore, the effective cross sectional area  $A_p$ , can be defined as  $\sigma_p = A_p \sigma_0$ , over which current flows.

Polycrystalline MgB<sub>2</sub> is not an exact binary system and  $J_c$  distributed continuously depending on orientation angle. However, overall  $J_c$  can be estimated if the distribution function is known.

$$J_c = \int_0^\infty A_p p(J) dJ \quad (2.4)$$

Where  $p(J)$  is the fraction of grains exceeding  $J_c$ . The following power law fits the experimentally obtained data very well and the percolation threshold is estimated around 0.2 in dense samples.

$$A_p = \left( \frac{p - p_c}{1 - p_c} \right)^\alpha \quad (2.5)$$

Following on from the work of Zehetmyer *et al* which conclusively showed an increase of  $H_{c2}$  and decrease of anisotropy in MgB<sub>2</sub> single crystals upon neutron irradiation [45], Eisterer *et al* showed an enhanced  $J_c$ , with different  $J_c$ - $B$  slope, at higher fields in neutron irradiated MgB<sub>2</sub> tapes, which was attributed to changes in  $H_{c2}$  and anisotropy and calculated with a good fit as shown in figure 2.6 [43].



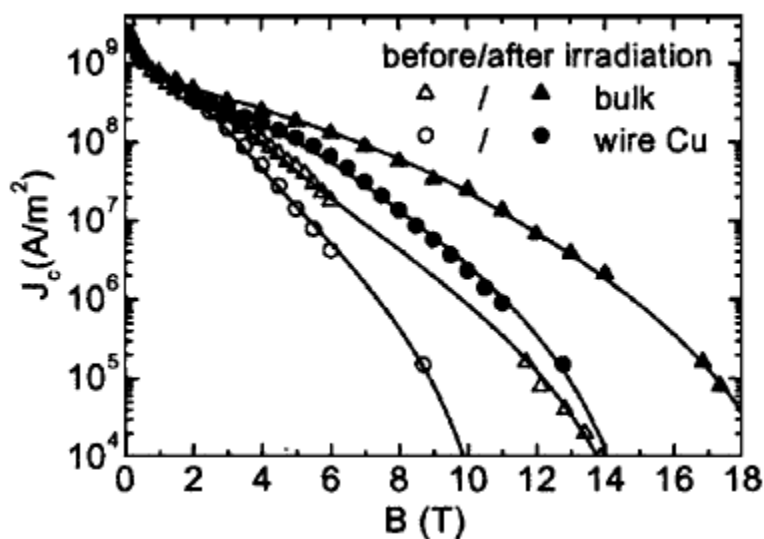


Figure 2.6 Measured  $J_c$ - $B$  before and after irradiation for  $\text{MgB}_2$  bulks and wires (With permission from [43]).

## 2.4 Flux pinning

It is important to have high flux pinning in a commercial superconductor. In a superconductor with high flux pinning ability, higher current can be driven. Hence it is an important feature

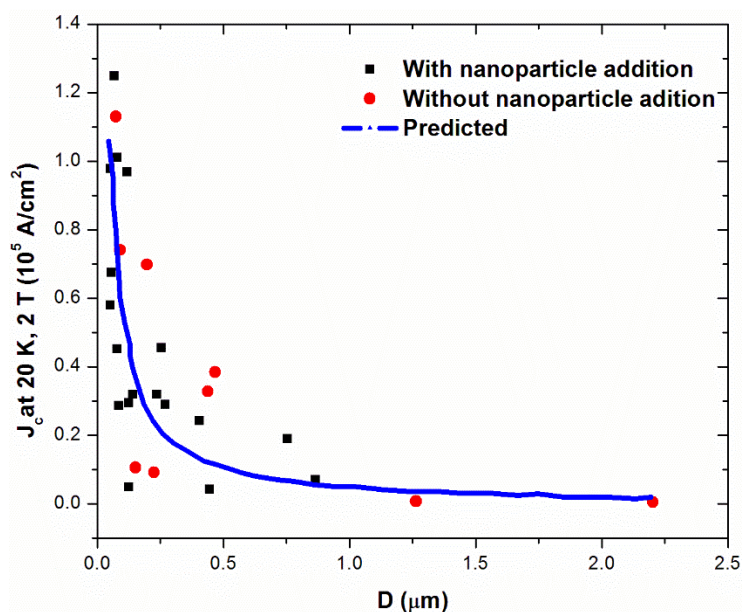


Figure 2.7  $J_c$  as a function of crystallite size as determined by EBSD (Reproduced from [50]).

to have especially in a commercial superconductor. Larbalestier *et al* [46], Kambara *et al* [47], Caplin *et al* [48] reported that grain boundaries are primary pinning sites in  $\text{MgB}_2$ . This was followed by series of works that aimed at increasing grain boundary density in  $\text{MgB}_2$  sample. Increased grain boundary density can be achieved by finer size of boron powder, ball milling the (Mg+B) powder mix to reduce particle size or by employing low temperature

sintering that inhibits grain growth. Notably Martinex *et al* [49] and Milkheenko *et al* [50] prepared samples of different grain sizes and observed an inverse dependence of  $J_c$  with grain size (Figure 2.7). It is noted that  $J_c$  steeply increased sharply below a grain size of 500 nm, above which it remained almost constant. This clearly suggests a dominant grain boundary pinning in MgB<sub>2</sub>. Martinez *et al* further stated that flux pinning force (per unit volume) in MgB<sub>2</sub> closely follows Hampshire-Jones equation [49].

$$F_{p0} = \frac{1}{21 \mu_0} \frac{1}{d} \frac{H_{c2}^2}{k_B} h^{1/2} (1 - h)^{1/2} \quad (2.6)$$

Where  $d$  is average grain size,  $h$  is the reduced field, and  $k_B$  is Boltzmann constant.

Thus it is necessary to enhance  $H_{c2}$  and/or decrease grain size to achieve optimum flux pinning.

In comparison with LTS materials (Nb based superconductors) and HTS materials, MgB<sub>2</sub> has a much lower  $H_{c2}$ , which is defined for a conventional single band superconductor as [51]

$$H_{c2}(0 K) = -0.69 T_c \left( \frac{dH_{c2}}{dT} \right)_{T < T_c} \quad (2.7)$$

However, owing to its two band structure, MgB<sub>2</sub> exhibits rather different  $H_{c2}$  vs  $T$  behaviour. Moreover,  $H_{c2}$  does not necessarily increase with normal state residual resistivity ( $\rho_0$ ). The bulk, tape and wire samples show a saturated  $H_{c2}$  at temperatures close to 0 K whereas thin film samples showed an increasing trend [52-54]. Gurevich explained this as the presence of two band superconductivity in MgB<sub>2</sub>, a double layer structure with  $\sigma$  band from in-plane B-B honeycomb and  $\pi$  band from out-of-plane Mg-B bonds. Thus overall  $H_{c2}$  is governed by the band with higher individual  $H_{c2}$ .

Thus according to Gurevich's equations, dirtier  $\sigma$  layer with respect to  $\pi$  layer would have higher  $H_{c2}$  and will dominate slope ( $dH_{c2}/dT$ ) at all temperatures. Whereas relatively dirtier  $\pi$  band would dominate  $H_{c2}$  near 0 K, causing a steep increase in  $H_{c2}$  close to 0 K, as shown in figure 2.8.

$$H_{c2}(\text{near } T_c) \propto \frac{1}{\lambda_{ep,1} D_\sigma + \lambda_{ep,2} D_\pi} \quad (2.8)$$

$$H_{c2}(0 K) \propto \frac{1}{\sqrt{D_\sigma D_\pi}} \quad (2.9)$$

Where  $\lambda_{ep}$  and  $D$  are respective electron-phonon coupling constants and charge carrier diffusivities for respective bands.

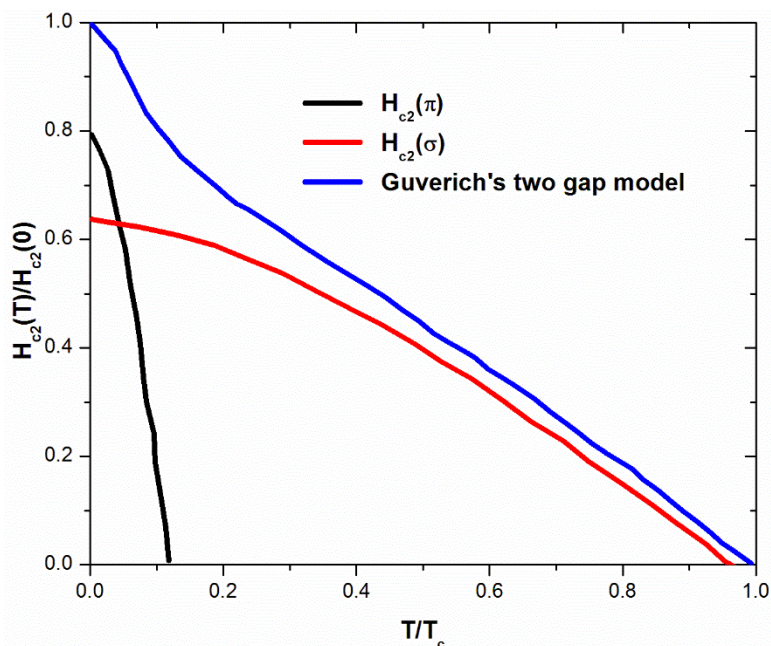


**Figure 2.8** The dotted curves show  $H_{c2}(T)$  calculated for  $\sigma$  and  $\pi$  films in the one-gap dirty limit. The solid curve shows  $H_{c2}(T)$  calculated from the two-gap dirty limit (Reproduced from [54]).

### 2.4.1 Improving $H_{c2}$

While approaches to reduce grain size are discussed previously, there are two main routes to increase  $H_{c2}$  of  $\text{MgB}_2$  namely doping and irradiation. Since the slope of the curve ( $dH_{c2}/dT$ ) is proportional to  $\rho_0$ , introducing defects (Irradiation) [55-57] and scattering centres (doping) has remained popular way of enhancing  $H_{c2}$  in LTS materials. On the other hand, when  $\text{MgB}_2$  is doped, either on substitutional or interstitial sites, it creates strains in the lattice. Such strains are also created when doping element forms a compound that has coherent or semi-coherent interface with the superconductor lattice. Thus far, any substitution on Mg site has only reduced  $T_c$  and  $H_{c2}$ . However, Oxygen, and more effectively carbon, substitution on B site have been successful in increasing  $H_{c2}$  of  $\text{MgB}_2$ . The effect of irradiation is briefly discussed here while doping effects on  $H_{c2}$  is discussed in separate section.

Irradiation is termed as bombardment of neutrons,  $\gamma$  rays, heavy ions (Ag, Au), and electrons at high enough velocities that can create defects in a microstructure. Irradiation may induce large scale and small scale defects. Large scale defects may be characterized as dislocations or stacking faults, which can act as pinning centres and thereby improves  $H_{iT}$ . Whereas small

scale defects like point defects may reduce mean free path which in turn reduces coherence length. This results in an increased  $H_{c2}$  [55-57].

## 2.5 Connectivity

It was realized soon after the discovery of  $\text{MgB}_2$  that grain boundaries don't form obstacles to supercurrent [46-48, 58-60]. This is a significant advantage over HTS materials where  $J_c$  decreases exponentially with grain boundary mis-orientation angle, hence special techniques are needed to achieve texture [17, 61]. However, the presence of impurity phases such as  $\text{MgO}$ , and  $\text{BO}_x$  can reduce critical current density in  $\text{MgB}_2$  [62-65]. Moreover, cracks [66-68], porosities [69-71] and other non-superconducting phases [72-74] can hinder the supercurrent flow.

The connectivity ( $K_c$ ) (or effective cross sectional area) can be estimated by phonon contribution to normal state resistivity, which is the ratio of the difference of resistivity between a single crystal ( $\rho_{sc}$ ) to that of a experimentally measured in a polycrystalline material ( $\rho_{exp}$ ) [63].

$$K_c = \frac{\Delta \rho_{sc}}{\Delta \rho_{exp}} \quad (2.10)$$

Note that  $K_c$  is estimated based on resistivity measurements in the normal state. The same cross section is believed to carry supercurrent in the superconducting state.  $\rho_{sc}$  is taken as  $\sim 6.3 \mu\Omega\text{cm}$  [75, 76]. The above equations are very useful to estimate connectivity in samples, typically with low resistivity. Thin films in particular show a direct relation between  $J_c$  and  $\rho_{exp}$  [64]. However, it is important to note that defects such as cracks or contaminants at grain boundaries may respond differently to normal current and supercurrent. Moreover, the presence of unreacted Mg or other conductive phases in the microstructure can alter the resistivity.

Porosity in  $\text{MgB}_2$  bulks is more prominent in *in situ* sintered samples. When one mole of Magnesium and 2 moles of boron react to form 1 mole of  $\text{MgB}_2$ , a 25% decrease in volume takes place. In addition, there is considerable porosity in the green precursor ( $\sim 25\%$ ) at the beginning of the process. Therefore *in situ* samples generally exhibit about 50% porosity [69-71].

## 2.6 Factors determining $J_c$

This section combines of all the factors discussed far and their impact on macroscopic long range  $J_c$ . The macroscopic  $J_c$  can be estimated taking (1) pinning mechanism and Pinning force, (2) Critical Field, (3) Anisotropy, (4) Percolation Threshold and (5) Connectivity into account-[77]

$$J_c(H) = A_{con} F_{p0} \frac{\left(1 - \frac{H}{H_{\rho=0}}\right)^2}{\sqrt{H_{\rho=0} H}} A_p \left(p_{max}(H) + \frac{p_c}{2.2}, p_c\right) \quad (2.11)$$

A small difference between  $H_{c2}$  and  $H_{irr}$  in single crystals is further narrowed by grain boundary pinning. It is noted that irreversibility in polycrystalline MgB<sub>2</sub> is caused by the lack of long range inter-grain supercurrent due to inherent anisotropy in the crystal, rather than flux motion as in the case of HTS materials. Therefore  $H_{irr}$  and  $H_{\rho=0}$  or ( $H_{irr}$  bulk) can't be improved significantly by pinning [77]. Also, field dependence of  $J_c$  is not strongly altered by pinning and is strongly suppressed by percolation ( $A_p$ ).  $J_c(B)$  dependence becomes weaker with decreasing  $\gamma$  and  $p_c$ . Finally,  $J_c$  is proportional to  $F_{p0}$  and  $K$ .

## 2.7 Alloying in MgB<sub>2</sub>

A superconductor is called 'Dirty' when presence of lattice defects or dopants cause degradation of crystallinity. These defects lead to reduction in mean free path ( $l$ ), associated with reduction in  $\xi$ ) as a result of enhanced intra-band and inter-band scattering. This allows larger flux to be accommodated in the material, thereby increasing  $H_{c2}$  [78]. Alloying also results in increased residual resistivity. Thus,  $H_{c2}(0 K)$  is correlated directly with residual resistivity [79];

$$H_{c2}(0 K) = 3 \rho_0 \gamma_v T_c \quad (2.12)$$

Where  $\gamma_v$  is electronic specific heat coefficient per volume. Despite a simple crystal structure, superconducting properties of MgB<sub>2</sub> are proven difficult to modify through doping unlike its HTS counterparts [80-85]. Moreover, non-stoichiometry (vacancy doping) is practically non-existent in MgB<sub>2</sub> fabricated using contemporary techniques [86]. Thus, although a series of elements such as Li[87], Si[88], Zn [89], Cu[90], Cr[91], Co[92], Ni[93], Ag[94], Sc[95], Ir[96], Ca[97], Au[98] are attempted so far, only Mn[99], Zr[100] and particularly aluminium [101-110] and carbon substitutions [111-115] have shown significant solubility into MgB<sub>2</sub>

lattice. Barring C, Be[116], F[117] and Cr[91], all the substitutions occurred on the Mg site and all of them resulted in reduction of  $T_c$ .  $T_c$  drop was rather rapid in B substitution than Mg substitution. C substitution on the B site significantly improved  $H_{c2}$  and this route has often been exploited to achieve high in-field performance.

### 2.7.1 Aluminium Substitution

Aluminium probably was the first choice to dope  $\text{MgB}_2$  because of its close atomic size to Mg, similar electronic structure and large solid solubility of Al into Mg [101]. Al substitutes the Mg site in  $\text{MgB}_2$  hexagonal unit cell. The resulting  $\text{Mg}_{1-x}\text{Al}_x\text{B}_2$  ternary compound has shortened  $a$  and  $c$  lattice constants, with  $c$  having a strong dependence on  $x$  relative to  $a$ . However, this seemingly single phase solid solution breaks into two phase mixture with distinct individual  $c$  between  $0.1 \leq x \leq 0.25$  [101]. Furthermore, TEM analysis at compositions  $x = 0.5$  revealed the existence of a superlattice. The origin of ordering was believed to be alternate layers of Mg and Al planes with lattice constants  $a$  and  $2c$  [108]. However, detailed analysis suggested the extension of superstructure to 10 nm in  $a$ - $b$  plane [108].  $T_c$  was found to drop steadily with  $x < 0.1$  from 39 K to 36 K in the single phase region with the transition remaining sharp. In two phase region however,  $T_c$  broadens significantly due to the increased concentration of non-superconducting phase and bulk superconductivity is lost thereafter [101]. Most experiments investigating the Mg-Al-B system were carried out by sintering. Powders were taken in the ratio according  $\text{Mg}_{1-x}\text{Al}_x\text{B}_2$  final compound. It is not clear which mechanism Al accommodates itself within the lattice. It is probably underlying assumption that first  $\text{MgB}_2$  phase forms followed by Al substitution to Mg site [118]. Reports of Al substitution on  $J_c$  are contradictory. Most reports indicate degradation in  $J_c$  with Al addition, for instance [88]. However, only a few have suggested increased  $H_{c2}$ , and a resultant increase in  $J_c$ , as a result of intra-band scattering [119].

### 2.7.2 Carbon Substitution

Uniform doping of C in  $\text{MgB}_2$  is now realized, particularly with a clever choice of dopant like  $\text{B}_4\text{C}$ , where C is already distributed uniformly on atomic level [120, 121]. Since C in graphite form is difficult to dope in  $\text{MgB}_2$  SiC, C-nanotube, nano diamond and organic compounds are often used to achieve uniform doping. The maximum limit for solubility of C in  $\text{Mg}(\text{B}_{1-x}\text{C}_x)_2$  is found to be 0.15 [122].  $H_{c2}(0)$  values for low C addition increased at 5 T/%C. This suggests that the  $H_{c2}(0)$  of 40 T is achievable [111], which is significantly higher

than a clean reference value of 17 T [123]. Furthermore, thin films on the other hand have shown a very high  $H_{c2}$  of 70 T.

C doping in  $\text{MgB}_2$  was found to increase  $H_{c2}$ . Enhancement in  $H_{c2}$  of C- added bulks was attributed to the formation of defects in the  $\text{MgB}_2$  lattice. C doping is accompanied by considerable lattice parameter change in-plane B-C distance whereas out-of-plane Mg-C remained almost unchanged [124, 125]. In single crystals, as  $T_c$  decreased with increased carbon doping,  $H_{c2}$  (0 K) continuously increased with respect to the undoped crystal. Increased  $H_{c2}$  as a result of scattering (particularly in  $\sigma$  band [126]), degradation of the crystallinity [113], enhanced vortex and  $\Delta k$  pinning (pinning arising from compositional fluctuations in superconductor) [114], reduced anisotropy [127] and the formation of a defect structure as a result of electron addition [128] are some of the mechanisms explaining much improved  $J_c(B)$  performance in C-doped  $\text{MgB}_2$  bulks.

### 2.7.3 Oxygen doping

Oxygen was believed to substitute the B site in a  $\text{MgB}_2$  lattice. Oxygen doping in  $\text{MgB}_2$  thin films resulted in considerably enhanced  $H_{c2}(0\text{ K})$ , expected up to 57 T, associated with an increased resistivity and reduced electron mean free path and coherence length [129]. A large number of compounds were added to  $\text{MgB}_2$ . Most of them did not substitute in the  $\text{MgB}_2$  hence did not alter the inherent superconducting properties. However, they reacted with Mg or B to form fine nanoscale precipitates that provided additional pinning and a resultant improvement in  $H_{irr}$ . For instance, the addition of  $\text{Dy}_2\text{O}_3$  during in situ  $\text{MgB}_2$  synthesis yielded additional pinning centres in the form of precipitates of  $\text{DyB}_4$  that resulted in up to 4 fold increase in  $J_c$  [130]. Similarly, almost 50% increase in  $H_{irr}$  was observed upon addition of  $\text{Y}_2\text{O}_3$  [131]. Increased flux pinning is also observed in the  $\text{MgB}_2$  bulk alloyed with  $\text{ZrB}_2$  [132],  $\text{Nb}_x\text{B}_2$  [133],  $\text{TiB}_2$  [134],  $\text{Bi}_2\text{O}_3$  [135], Sm [136].

## **2.8 $\text{MgB}_2$ Bulk Fabrication**

This section describes major fabrication routes adopted for  $\text{MgB}_2$  bulk synthesis. Powder synthesis, *in situ* or *ex situ*, has been the popular and rather easy way followed by a novel infiltration route. Sintering refers to processes involved in heat treatment of powder compacts at elevated temperatures, where diffusional mass transport is appreciable. This applies to both *in situ* and *ex situ* sintering routes. The driving force of sintering is the excess energy

associated with the solid/vapour interfaces. Therefore the system attains a configuration by creating grain boundaries to obtain solid/solid interface through reducing solid/vapour interface (Figure 2.9). Reduction in surface to volume ratio occurs and the particles size increases. In the initial stages of sintering, the neck formation occurs, resulting in concave curvature at neck. In the intermediate stage, neck grows through material transport. The densification, however, occurs only when the particles centres can move closer together. Therefore atoms migrating from grain boundary region to neck region (Red) lead to densification and atoms migrating from surface to neck don't (Blue). In the final stage, the atoms move to the neck region due to difference in vapour pressure arising from the convex shaped particle and concave shaped neck.

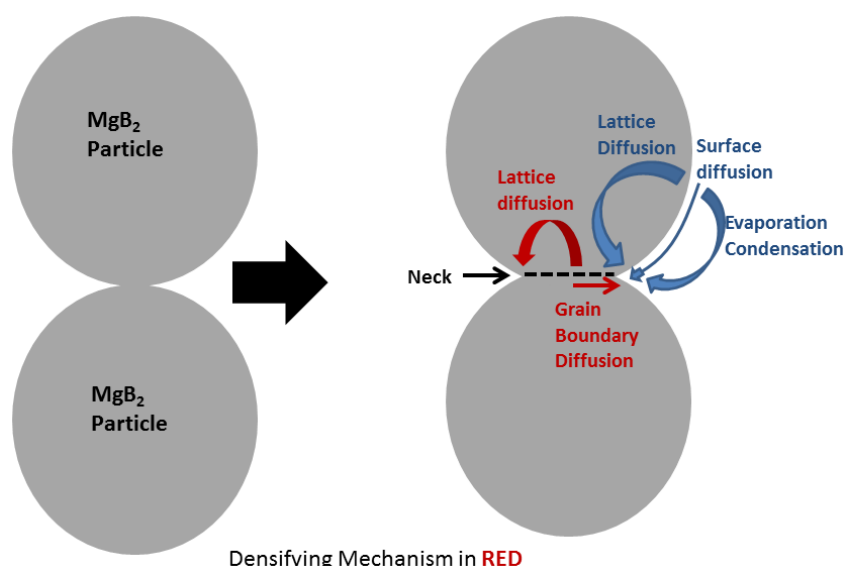


**Figure 2.9** A Schematic showing neck formation during sintering in either *in situ* or *ex situ*.

### 2.8.1 In situ Technique

When a precursor made from mixture of stoichiometrically required Mg and B powder is heat treated, typically between 600 °C to 800 °C, to obtain MgB<sub>2</sub>, it is known as *in situ* technique [69-71, 137-141]. Samples fabricated by this technique are about 50% dense [137-141]. This is primarily due to the shrinkage associated in MgB<sub>2</sub> formation from B and Mg powder and secondarily due to the volatility of Mg. This technique is performed under inert atmosphere to suppress the formation of MgO (MgO is stable under oxygen partial pressure of 10<sup>-23</sup> Torr [142]), since vacuum may result in loss of Mg through evaporation. However, such samples show low residual resistivity and high electrical connectivity. This is because grain boundaries formed in MgB<sub>2</sub> processed by this technique are cleaner, as they are formed by



freshly formed  $\text{MgB}_2$  surfaces [139]. As a result, *in situ* sintered bulks often show sharp superconducting transitions [143] and can carry larger current than *ex situ* sintered bulks [139]. Bulks fabricated by such technique typically show connectivity of  $\sim 20\%$  and a low value of residual resistivity ( $\sim 15\text{-}50 \mu\Omega\text{cm}$ ). This technique, when used to fabricate wires, is also known as the *Powder in Tube* (PIT) technique. In PIT,  $\text{Mg+B}$  powder mix is packed together and then reacted [144-146].

### 2.8.2 *Ex situ* Technique

When a precursor made from pre-synthesized  $\text{MgB}_2$  powder is heat treated, at a relatively high temperature, to obtain bulk  $\text{MgB}_2$ , it is known as *ex situ* technique. Samples fabricated by such technique are quite dense and this has been main motivation for using the *ex situ* route. This is because problems such as volatility of Mg and reaction induced shrinkage are not associated with this process [147-156]. Notably, Grasso *et al* showed  $J_c$  exceeding  $10^5 \text{ A/cm}^2$  in unsintered  $\text{MgB}_2$  tapes [147]. However, Dancer *et al* pointed observed very little evidence of sintering beyond loss of volatile matter and inter-particle adhesion [148]. Therefore higher temperature ( $\sim 1000 \text{ }^\circ\text{C}$ ), pressure [156], other heating methods such as resistive sintering [157] or spark plasma sintering [153] and ball milling [152, 154] are often employed to enhance reaction kinetics. Since the surface of pre-synthesized  $\text{MgB}_2$  powder invariably contains thin nano-scale layers of oxides such as  $\text{MgO}$  and  $\text{BO}_x$  [63], *ex situ* samples typically exhibit low connectivity ( $\sim 10\%$ ). Therefore although relative density of

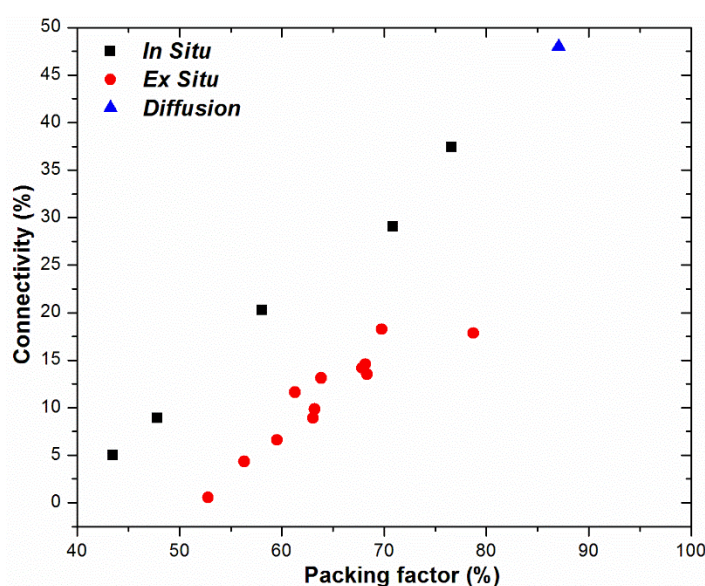


Figure 2.10 Connectivity as a function of packing factors for  $\text{MgB}_2$  bulks fabricated by various techniques (Reproduced from [139]).

such samples is higher (up to 90% of theoretical), it doesn't reflect in improving self-field  $J_c$ . This finding was further confirmed by reports of Mizutani *et al* [151] Tanaka *et al* [155], who used freshly prepared  $\text{MgB}_2$  powder for *ex situ* synthesis and observed high connectivity (20%) and  $J_c$  of up to  $200 \text{ kA/cm}^2$  at 20 K. It is however noted that,  $\text{MgB}_2$  is prone to decomposition at higher reaction temperature, resulting in boron rich borides such as  $\text{MgB}_4$  [148].

### 2.8.3 A Novel Approach: Infiltration and Growth

The infiltration and Growth (IG), impregnation or Reactive Liquid Infiltration (RLI) process was developed to counter difficulties such as porosity and poor sinterability associated with conventional processing routes. In this approach, B powder is packed to form a green body followed by infiltration with liquid Mg. The infiltration route for processing  $\text{MgB}_2$  fibres (of diameter  $160 \mu\text{m}$ ) was first reported by Canfield *et al* which involved exposing B fibres to Mg vapour at  $950 \text{ }^\circ\text{C}$  [158]. Later, Dunand *et al* reported the synthesis of Mg- $\text{MgB}_2$  composites by infiltrating liquid Mg under pressure at  $800 \text{ }^\circ\text{C}$  into a B preform [159, 160]. Improved versions of this process were reported subsequently by Giunchi *et al* [161] (RLI) for the fabrication of state-of-the art bulk  $\text{MgB}_2$  artefacts, in which Mg bulk and B powder are placed in a metallic container. A crystalline variety of boron (particle size  $< 100 \mu\text{m}$ ) is used in this process. The container is then welded closed and heat-treated at  $950 \text{ }^\circ\text{C}$  for up to 3h to obtain dense, bulk  $\text{MgB}_2$ , with the initial arrangement of B and Mg bulk in the container being used to define the geometry of the final product [162]. Infiltration processing when used to fabricate wires is known as internal Mg diffusion process [163, 164].

## **2.9 Factors Affecting Growth of $\text{MgB}_2$**

### 2.9.1 Crystallinity and Purity

Although  $\text{MgB}_2$  is chemically inert to most of the elements, its superconducting properties are adversely affected with impure powder. Impurities like B and Mg oxides that segregate at the grain boundaries obstruct the flow of supercurrent [165]. Thus, increased purity in B powder directly correlated in increased  $J_c$  as a result of improved connectivity accompanied with reduced residual resistivity and increased residual resistivity ratio [166-168].  $\text{MgB}_2$  prepared from pure B powder shows a 3 fold enhancement in  $J_c$  relative to impure powders [167].

Moreover, the crystallinity of boron powder has been an important factor in  $\text{MgB}_2$  synthesis [168, 169, 170]. It has been realized from synchrotron measurements that a larger activation barrier exists for crystalline boron compared to amorphous boron [36]. As a result,  $\text{MgB}_2$  phase formation with the use of crystalline boron often occurs via the formation of non-equilibrium phases such as  $\text{Mg}_2\text{B}_{25}$  [169]. Thus crystalline boron is often reacted at higher temperatures (900 °C), while amorphous boron undergoes complete reaction at a relatively low temperature of 600 °C.

### 2.9.2 Particle size

The particle size distribution of B and Mg is an important contributing factor in the green density of precursor, which ultimately determines final density [171]. Moreover, the diffusion distance of B in Mg is limited [172], therefore the use of coarse powder may have considerable fraction of non-superconducting higher boride ( $\text{MgB}_{2+x}$ ). Moreover, since grain boundary pinning is the dominant mechanism in  $\text{MgB}_2$ , finer particle size for B and Mg leads to higher performance. Maeda *et al* found in a systematic study that use of fine Mg powder led to higher lattice strain, better connectivity and enhancement in  $J_c$ . Similarly Wang *et al* stated finer Mg particles reacted quickly and uniformly [173]. Thus samples fabricated with 10 micron sized Mg particles showed an order of magnitude increase in  $J_c$  than ones fabricated using 40 and 70  $\mu\text{m}$ .

Since commercially available fine nano-sized boron powder is considerably expensive, it is common practice to ball-mill micron sized powder to obtain finer size. According to Hassler *et al*, energy transferred from balls per unit mass of sample ( $E/m$ ) is estimated by [174]

$$\frac{E_T}{m} = c \beta_B \frac{(w_p r_p)^3}{r_v} t \quad (2.13)$$

Where  $\beta_B$  is ratio of mass of balls to mass of powder,  $W_p$  is angular frequency,  $r_p$  is radius of sun disk,  $r_v$  is radius of vial,  $t$  is time and  $c$  is dimensionless constant of the order of 0.1. Numerous reports on  $\text{MgB}_2$  synthesis from ball milled powder [174-178] are consistent in following ways.

- Significant fraction of  $\text{MgB}_2$  is observed in as milled Mg and B powder mixture due to high milling energy in mechanical alloying process.

- $T_c$  is reduced with increasing milling, because of strain induced from milling energy or contamination. For instance, Sugino *et al* reported C contamination in milled B powder and for the same reason,  $H_{c2}$  is increased as a result of scattering in such cases [176].
- Significant increase in  $H_{irr}$  is observed with respect to reference value as a result of enhanced grain boundary pinning.
- Residual resistivity increased with energy input, RRR (Residual Resistivity Ratio) decreased while connectivity remained unaltered.
- One order of difference compared to reference value is observed in  $J_c$ . MgB<sub>2</sub> bulks with one of highest  $J_c$  obtained so far are fabricated by milling/mechanical alloying method [177, 178].

### 2.9.3 Pressure

Use of pressure can be categorized in two ways. First, while preparing a green body precursor and second, during heat treatment. While making a green body, the highest pressure employable is often used to minimise porosities and to achieve more particle-particle contact, especially during *in situ* and *ex situ* sintering methods. In infiltration processing however, it is crucial to leave certain porosities which can later be occupied by stoichiometric amount of Mg as required by the reaction (I) [20, 39, 131]. Moreover, geometry and distribution of porosities determine depth of liquid Mg infiltration. Li *et al* have shown that loosely pressed powder in *AIMI* wires (Advanced Internal Mg Infiltration) shows 100 micron MgB<sub>2</sub> layer, whereas powder pressed with larger load shows thinner MgB<sub>2</sub> layer of about 30 microns [20, 39].

Use of pressure during heating cycle results in a further increase in density in *in situ* and *ex situ* sintered bulks [179, 180, 148]. *In situ* sintered bulks fabricated without application of pressure contain about 50% porosity. Use of pressure can not only contain Mg vapour within the die and minimise shrinkage porosities by means of powder flow, but also induce defects in the structure that can act as pinning centres [181]. Final density of high pressure sintered bulk increases with pressure, although the relation is not linear.

### 2.9.4 Reaction temperature

Temperature determines rate of reaction, diffusivity, sintering and recrystallization behaviour in MgB<sub>2</sub> bulk processing. Although optimised reaction temperature appears to be different in

*in situ*, *ex situ* and infiltration-growth routes. Grasso *et al* reported a high  $J_c$  of 105 kA/cm<sup>2</sup> in a MgB<sub>2</sub> tape fabricated *ex situ* route without any heat treatment. Cold welding of MgB<sub>2</sub> grains that occurred during rolling possibly contributed to this high  $J_c$  [147]. Dancer *et al* have pointed out that a higher reaction temperature (>1000 °C), coupled with the application of pressure is essential to achieve any significant sintering between MgB<sub>2</sub> particles in *ex situ* sintering [148]. The accelerated decomposition of MgB<sub>2</sub> at high temperatures places the upper limit on reaction temperature. Brutti *et al* observed evaporation of Mg at a temperature as low as 425 °C. This resulted in the formation of higher borides such as MgB<sub>4</sub> and MgB<sub>7</sub> [182, 183].

The optimised reaction temperature varies with particle size in *in situ* sintering and is generally low, about 800-900 °C [137, 139]. However, higher reaction temperature results in higher crystallinity of MgB<sub>2</sub> and a coarser crystallite size. Therefore, a relatively low reaction temperature (600 °C) is found to be useful to obtain MgB<sub>2</sub> with degraded crystallinity and refined structure, although a longer reaction time is needed for complete transformation into MgB<sub>2</sub> [60, 184]. In such an approach, a loss of Mg occurring as a result of its high vapour pressure is minimised, since the Mg evaporation rate is higher at a higher reaction temperature [185-187]. Notably Rogado *et al* fabricated MgB<sub>2</sub> bulks at 500 °C [187]. Yamamoto *et al* observed increased  $H_{c2}$  and  $H_{irr}$ , as a result  $J_c$  at higher external fields is significantly enhanced [184]. Moreover higher residual resistivity and lower  $RRR$  was observed in such samples. This low temperature reaction, or solid-solid reaction, approach is particularly important during the synthesis of MgB<sub>2</sub> from nano-powders [67]. This is because nano-particles are prone to coarsening at higher temperature.

In infiltration-growth processing, a higher reaction temperature (900 °C) is necessary to ensure complete transformation. Boron used in IG processing is relatively coarse to achieve the required pore geometry. Therefore higher temperature (>900 °C) is often needed to enhance kinetics and thereby ensure complete transformation into superconducting MgB<sub>2</sub>.

## 2.10 Advancements in Conventional Methods

Given that there are certain respective challenges in each of the processing routes, several approaches adopted by the researchers are discussed in this section.

### 2.10.1 Non-Stoichiometric Composition

Both compositions on either side of ‘‘line compound’’  $\text{MgB}_2$  have been investigated. Zeng *et al* reported that use of excess Mg ( $\text{Mg}_{1+x}\text{B}_2$ ,  $x < 0.1$ ) starting compositions allowed oxygen incorporation in the  $\text{MgB}_2$  lattice, reduced MgO fraction and resulted in significantly improved low field  $J_c$  due to improved connectivity [188]. In a comparative study of mechanically alloyed  $\text{MgB}_2$  across both Mg rich and Mg poor sides of  $\text{MgB}_2$ , Perner *et al* concluded that a Mg rich composition yielded superior low field  $J_c$  performance and a homogeneous microstructure, whereas Mg poor samples showed better high field  $J_c$ , microstructure comprised of higher borides and inhomogeneous grain size [189]. The reason for improved low field  $J_c$  was stated that the loss of Mg is almost unavoidable owing to its volatility, thus compensation is needed for Mg. In another study of a Mg deficient  $\text{Mg}_{1-x}\text{B}_2$  composition, it was realised that the B in-plane lattice constant  $a$  decreased while out-of-plane lattice constant  $c$  decreased.  $T_c$  decreased by 2 K for sample with  $x = 0.6$ . Finally Jiang *et al* pointed out in the synthesis of  $\text{MgB}_2$  tapes that Mg rich compositions yield in a greater crystallinity, grain growth and better connectivity. While in Mg poor compositions, crystallinity is poor and grain growth is restricted which results in finer grain size. Therefore Mg poor compositions display superior high field performance [190].

### 2.10.2 Different Precursors: $\text{MgH}_2$ , $\text{MgB}_4$

$\text{MgH}_2$ : Since Mg exhibits a great affinity towards oxygen to form MgO, its formation is practically unavoidable in *in situ* sintering. Therefore Mg is introduced in reacted form as  $\text{MgH}_2$  [191-193]. This compound decomposes into Mg and  $\text{H}_2$  at 566 °C below 25 MPa. Thus liberated  $\text{H}_2$  gives a reducing atmosphere which inhibits oxidation of Mg, thereby giving a pure phase well connected  $\text{MgB}_2$ .

$\text{MgB}_4$ : Volume shrinkage of 25% associated with reaction I is one of the two important reasons for reduced density and connectivity in *in situ* sintered bulks. Thus Mg is introduced in the form of  $\text{MgB}_4$ . Reaction of  $\text{MgB}_4$  with Mg generates less volume contraction (15%) therefore resulting in reduced porosity [194-197].  $\text{MgB}_4$  can be fabricated by the decomposition of  $\text{MgB}_2$  under controlled Mg partial pressure. Further reaction of  $\text{MgB}_4$  with Mg to obtain  $\text{MgB}_2$  yields improved packing factor, improved grain connectivity and as a result, enhanced  $J_c$ .

### 2.10.3 Sintering Aids

The connectivity for sintered samples is reported to be around 15% due to reasons discussed in previous sections and there is scope for its improvement. Researchers have used various compounds through which Mg atoms can diffuse efficiently and thereby promote reaction kinetics. Notably Chen *et al* added GaN to Mg+B powder mixture. Mg-Ga formed a low melting eutectic, which yielded a reduction in MgO content with a 3-4 times increase in  $J_c$  [198]. Later, Shcherbakova *et al* used Mg-Ga alloy and observed a similar impact on  $J_c$  [199]. Similarly, Zhao *et al* found that Ni nanoparticle formed Mg-Ni eutectic that promoted the diffusion of Mg and B [200]. Kumar *et al* have stated that silver in Mg and B mixture traps Mg atoms by forming a liquid phase mixture of Mg-Ag, thereby reducing tendency of MgO formation and vaporization. Such material therefore carried larger currents relative to undoped MgB<sub>2</sub> [201]. Cheng *et al* observed an order of magnitude difference in Ti added MgB<sub>2</sub>. They speculated that the Ti addition resulted in partial doping occurs on Mg<sub>1-x</sub>Ti<sub>x</sub>B<sub>2</sub> which promoted sintering and grain connectivity [202].

In an *ex situ* sintering study with up to 10% addition of Nb, Ti, Zr, Hf, W and, Kovac *et al* found that  $J_c$  is substantially improved. The reason for such behaviour was reported to be improved quench stability as a result of electrically and thermally conductive metals and reactive nature of added elements that preferentially react with impurities such as H and O to allow formation of phase pure MgB<sub>2</sub> [203].

## **2.11 Aim of the Thesis**

Chapter 2 summarised major contributions in the development of MgB<sub>2</sub> in last 15 years since its discovery in 2001. Various synthesis techniques have been developed to obtain high density defect free MgB<sub>2</sub> and realize its potential. Techniques like diffusion processing (Figure 2.10) or use of pressure assisted techniques successfully generate highly dense samples. However, these techniques tend to be difficult to scale-up to form large MgB<sub>2</sub> components, as the use of pressure represents significant practical limitation, or shapes with complex geometries (e.g. Microwave Cavity Structure).

Thus there appears to be a large scope to improve density and connectivity in MgB<sub>2</sub> by a process that could be easily scalable to different shapes and sizes. The primary purpose of the thesis is to explore “Infiltration and Growth” method as a potential solution to this problem. It includes identifying merits and challenges associated with the process, establishing

microstructure-property correlations and to use doping as a means to further enhance superconducting properties.



### Chapter 3. Methodology

This chapter describes the inspiration behind the IG process and processing route adopted to synthesize bulk MgB<sub>2</sub>.

#### 3.1 Inspiration and Adaptation of IG process

Infiltration processing is an established route to fabricate dense ceramics Ceramics/Ceramic Matrix Composites (CERMETS) as well as Metal Matrix Composites. Various infiltration based techniques such as Melt infiltration [204], Sol-gel infiltration [205], Polymer Infiltration and Pyrolysis [206, 207], Directed oxidation [208], Reaction bonding [209] have been developed to enable dense near-net shape processing of materials like SiC, Al<sub>2</sub>O<sub>3</sub>, B<sub>4</sub>C-Co, TiC-Co, WC-Co.

During the past two decades, infiltration and Growth process has been successfully used to synthesize large single grains Y-Ba-Cu-O (YBCO) superconductors. The process, as depicted schematically in figure 3.1, involves infiltrating Ba-Cu-O liquid into porous Y<sub>2</sub>BaCuO<sub>5</sub> (Y-211) preform followed by a controlled peritectic reaction to yield the target superconducting YBa<sub>2</sub>Cu<sub>3</sub>O<sub>7-δ</sub> (Y-123) phase [61, 210, 211].

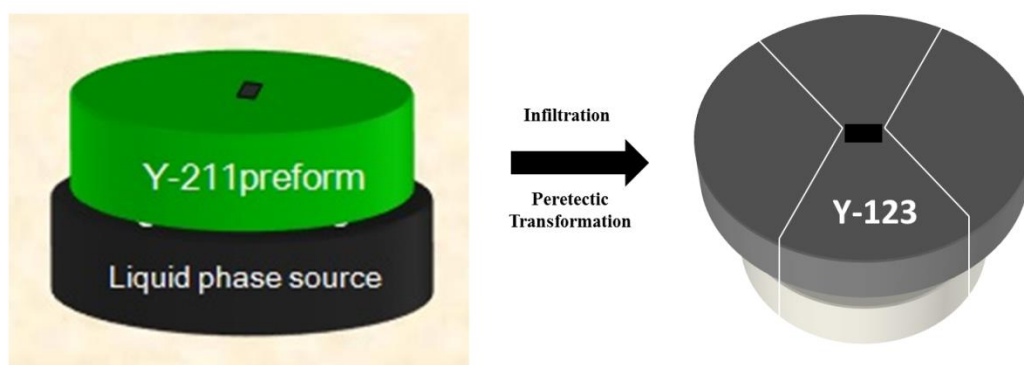
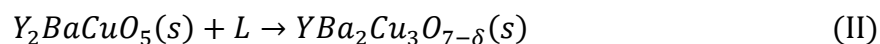


**Figure 3.1** Schematic representation of Infiltration and Growth process during the synthesis of YBCO bulk superconductors.

the use of a seed crystal provides an oriented Y-123 heterogeneous nucleus and by slowly cooling (0.1–0.3 °C/h) the melt below the peritectic transformation temperature promotes the growth of Y-123 nucleus whilst suppressing formation of homogeneous nuclei elsewhere in the melt. Thus heterogeneous nucleation of Y-123 takes place on the seed crystal (with low

misfit) mimicking the atomic arrangement that resulted in a highly textured microstructure [61, 210]. The Y-123 single grain bulk superconductor processed using the IG process exhibits reduced porosity and finer Y-211 inclusions in the Y-123 matrix that is not achievable by conventional melt-growth process. Therefore the objective here is to adopt this process for MgB<sub>2</sub> synthesis using B(s) and Mg(l) as the starting materials. The infiltration and growth process offers significant advantages for the Mg-B system due to its lower reaction temperature and the inherent capability of MgB<sub>2</sub> fabricated in polycrystalline form to carry large current, eliminating the need of texture [46-48, 58-60].

### 3.2 Sample Preparation

Disc shaped boron precursor bodies (figures 3.2(b) and (c)) are prepared from boron powder using a SPECAC Hydraulic Pellet Press with load of 5-10 MPa (Figure 3.2(a)). The green density of the precursor pellet was engineered to be around 40% of the theoretical value, so that the residual pores in the bulk microstructure could be infiltrated by liquid Mg during processing to satisfy the overall compositional stoichiometry, as calculated in table 3.1.

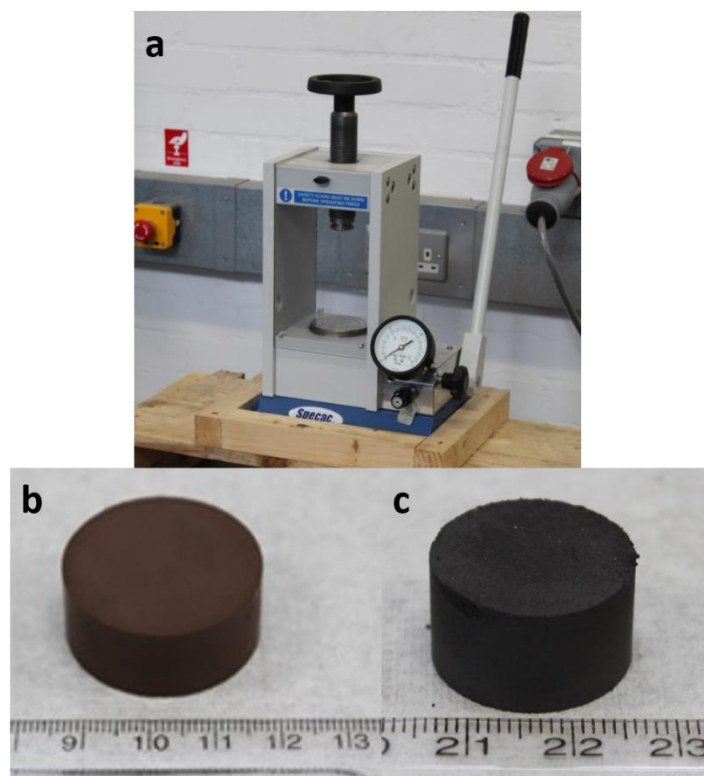


**Figure 3.2 (a) SPECAC hydraulic pellet press. (b) and (c) show preforms prepared using amorphous and crystalline boron powder respectively.**

A boron pellet was sandwiched initially between Mg blocks of commercial purity, as shown in figure 3.3(a). Mg, 99.9% pure with minor metallic impurities, was sourced from

Magnesium Elektron Ltd and was used in the synthesis of all the samples in this study. A variety of B sources were used in this study and their characteristics are described in table 4.1.

The Mg-B-Mg sandwich configuration was then melted at a temperature ( $T > T_m(650^\circ\text{C})$ , Mg melting temperature) in a graphite crucible for and held there for desired time.

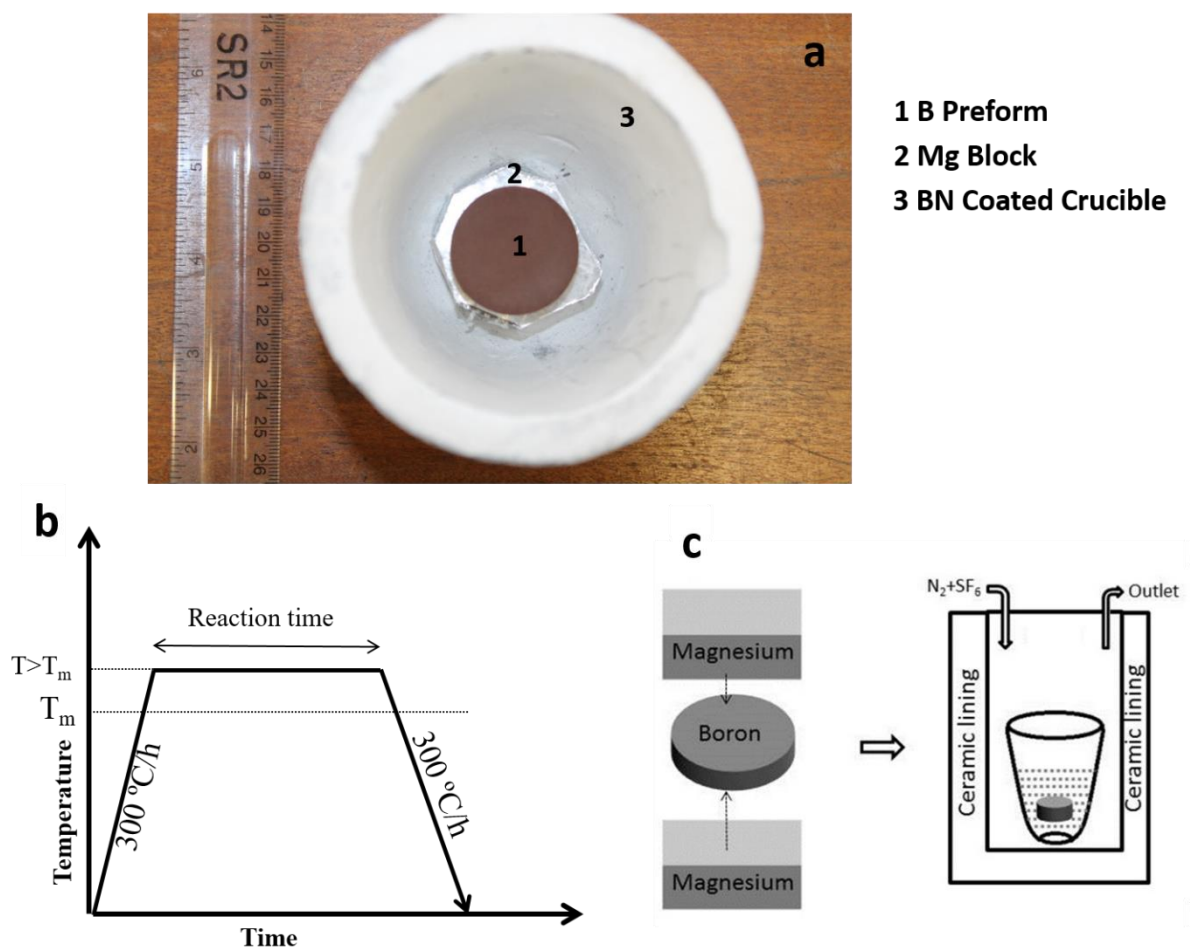


**Figure 3.3 (a) BN coated graphite crucible containing B preform on Mg block. Another Mg block is placed on B preform to make Mg-B-Mg sandwich geometry (b) Heating cycle used in IG process. (c) A sandwich arrangement when heat treated, Mg melted and surrounded B preform from all sides.**

The heating conditions used during the process are shown in figure 3.3(b). Excess liquid Mg was used in this process in view of its high vapour pressure and to maintain a positive fluid pressure aid to infiltration. A controlled, continuous flow of gas of a mixture of  $\text{N}_2 + \text{SF}_6$  was maintained over the sample during processing to minimize oxidation of Mg.  $\text{SF}_6$  gas is known to react with Mg(l) to form  $\text{MgF}_2$ , which fills the pores in otherwise porous MgO film on the melt surface [212]. This forms a continuous impervious MgO/ $\text{MgF}_2$  layer on the melt

surface which protects underlying Mg from oxidation. The excess Mg was removed from the sample by machining after cooling to room temperature and the MgB<sub>2</sub> disc recovered. This procedure slightly varies from reactive liquid infiltration method adopted by Giunchi *et al*, where Mg bulk and B precursor were placed in a metallic container. It was later welded prior to heat-treatment to obtain dense, bulk MgB<sub>2</sub> [161]. The density of these samples was 2.4-2.45 g/cm<sup>3</sup>, which was calculated by measuring weight and dimensions of bulk sample. The samples that are analysed in Chapter 4 were fabricated this method, whereas subsequent synthesis of MgB<sub>2</sub> samples was carried out by a *Modified IG* process which is discussed in following section.

	Mg	B
<b>Volume</b>	60%	40%
<b>Density (g/cc)</b>	1.74	2.34
<b>Mass (g)</b>	1.044	0.93
<b>Moles</b>	0.0435	0.084
<b>Mole ratio</b>	1	2

Table 3.1 60% porosity is maintained initially in the precursor. When these are occupied by Mg, final Mg/B molar ratio of 1:2 can be obtained after completion of reaction  $Mg+2B \rightarrow MgB_2$ .

### 3.3 Modifications to the Infiltration and Growth Process

The standard IG process was modified in order to minimise the machining which was required to retrieve the reacted product surrounded by large amount of Magnesium metal.

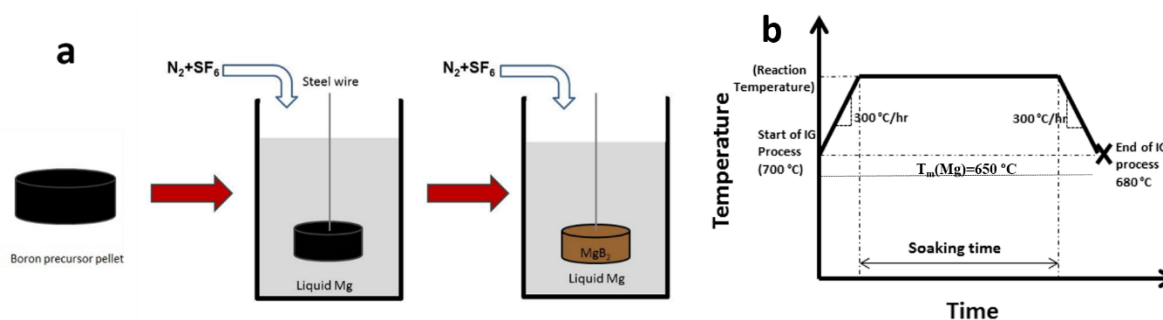


Figure 3.4 (a) illustrating modification to the IG process. The reacted product was taken out of the Mg melt at 700 °C, avoiding significant machining. (b) Heating conditions employed during the process. Note that process starts finishes above Mg melting temperature.

In the modified IG process, Mg(l) was melted separately in a graphite crucible and held at 700-750 °C in a graphite crucible. The precursor pellet, which was contained in a perforated steel enclosure, was transferred slowly using a steel wire to the crucible containing the liquid Mg at 700-750 °C (Figure 3.4(a)). Since Fe has almost negligible solubility with Mg even up to 1000 °C, use of steel in the processing is not expected to alter the composition of Mg(l)

significantly [213]. The porous steel vessel ensured that that no part of the precursor pellet came into contact with the walls of the crucible and that it did not float on the Mg melt, which could result potentially in a non-uniform infiltration process. The column height of Mg(l) was maintained at 10 cm above the precursor to obtain a hydrostatic pressure of approximately 1.7% of atmospheric pressure, which was found to be necessary to achieve a uniform infiltration process. The crucible containing the submerged preform in Mg(l) was then subjected to the thermal profile as shown in figure 3.4(b) and heat treated at a desired temperature for desired time. After the end of thermal cycle (at 680-750 °C), the perforated steel enclosure containing reacted product was taken out from the melt. The thin layer of Mg surrounding the sample after processing was removed by slight grinding to recover the bulk specimen. Wherever a powdery reacted product was obtained, all the powder was carefully collected. The reacted sample obtained after such an infiltration and growth process is hereafter referred to as *MgB<sub>2</sub>-IG*.

### 3.4 Sample Characterization

#### 3.4.1 Optical Microscopy

*Carl Zeiss AxioScope A 1* optical microscope was used to capture images of the polished MgB<sub>2</sub>-IG sample surface. The microscope was equipped with 2.5x - 100x objective lenses with bright field and polarization field mode. An *AxioCam MRm* digital camera was located at the top of the microscope to record the images.

#### 3.4.2 X-Ray Diffraction

XRD pattern was measured by *Bruker D8 Advance* (Detector: *LYNXEYE* high resolution energy-dispersive 1-D), operated at a generator voltage of 40 kV and a current of 50 mA, with Bragg-Brentano geometry on a polished surface of sample using Cu-K<sub>α</sub> source (Figure 3.5(a)). 2θ was set between 5° and 80°. A step size of 0.009° and scanning speed of 0.001°/s was used.

*DIFFRACT. EVA* software package was used in order to identify phases corresponding to XRD peak positions. Phase quantification was performed by using a computational programme called '*Powder Cell*'. This software accounts for both the positions and types of atoms in the structure generates calculated pattern as output.

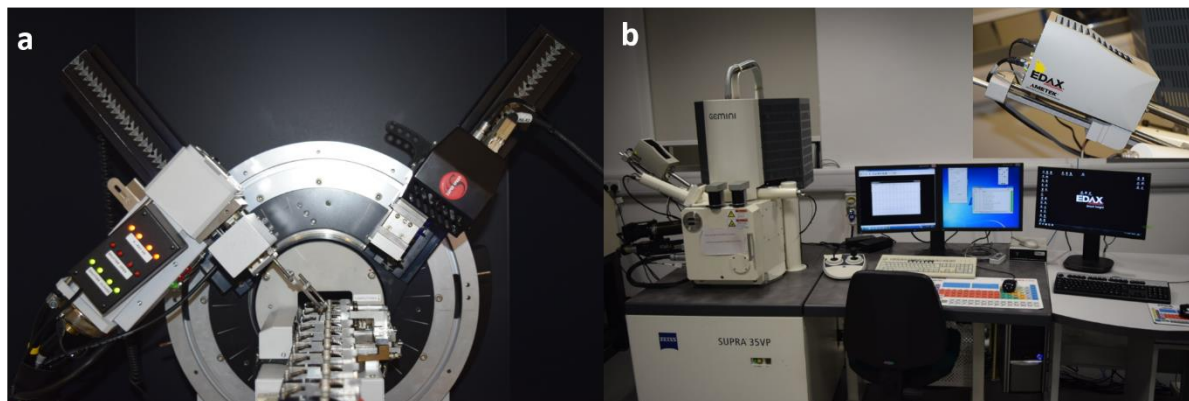


Figure 3.5(a) Bragg-Brentano geometry in Bruker X Ray diffractometer and (b) Scanning electron microscope (Bruker D8 Advance) with EDS detector shown in inset.

### 3.4.3 Electron Microscopy

#### 3.4.3.1 Scanning Electron Microscope

A Zeiss Supra 35 field-emission gun SEM was used to capture secondary and back scatter electron images. Energy dispersive X-ray spectroscopy (EDS) (Oxford Instruments, UK), fitted to the SEM, was used to obtain EDS point analysis, line scans and maps (Figure 3.5(b)).

#### 3.4.3.2 Transmission Electron Microscopy

In order to further investigate the crystal orientation, identify possible defect structure and Mg/MgB<sub>2</sub> or MgB<sub>2</sub>/Mg<sub>2</sub>B<sub>25</sub> interface, thin cross-sectional foil specimens were prepared by mechanical grinding, and further thinned by focus ion beam (FIB) using a FEI Helios 600i system at 30 kV. TEM and HRTEM examinations were carried out using a Tecnai G2s-Twin microscope operating at 200 kV, with the point resolution 0.24 nm.

### 3.4.4 Vickers Hardness Measurements

Microhardness was used to measure the hardness of the MgB<sub>2</sub>-IG samples. A 0.1 kg load and 5 s dwell time (*Buehler Micromet 5101*) was employed in order to estimate the hardness of an individual phase. A 20 kg load and 10 s dwell time (*Wilson Hardness*) was employed to obtain a relatively larger indent. Such value would represent combined hardness of individual phases, as well as the bonding of interfaces between them.

### 3.4.5 Physical Property Measurements

A quantum Design *MPMS-XL 7 T* Superconducting Quantum Interference Device at the University of Cambridge was used to measure magnetic moment generated in small samples (2\*2\*3 mm<sup>3</sup>). *SQUID* was equipped with the optional reciprocating sample and low temperature measurement options allowing a nominal sensitivity of 1x10<sup>-8</sup> emu and measurements from room temperature down to 1.9 K.  $T_c$  was defined as the temperature at which the  $M-T$  curve in the zero field cooled mode starts to deviate, i.e. onset of diamagnetism.

The critical current density ( $J_c$ ) throughout the thesis was calculated from measured magnetic moment hysteresis loops using the extended Bean model for a rectangular cross ( $a < b$ ) section in a perpendicular, applied magnetic field [214].  $J_c$  is calculated from the width of the hysteresis loop as shown in figure 3.6(a). A typical sample used for such measurements is shown in figure 3.6(b) and external field direction is maintained parallel to longer edge. The small cut sample was taken from central region of the bulk, so that any variation of properties could be attributed to experimental parameters.

$$J_c = \frac{20 \Delta M}{a \left(1 - \frac{a}{3b}\right)} \quad (3.1)$$

$$\Delta M = M^+ - M^- \quad (3.2)$$

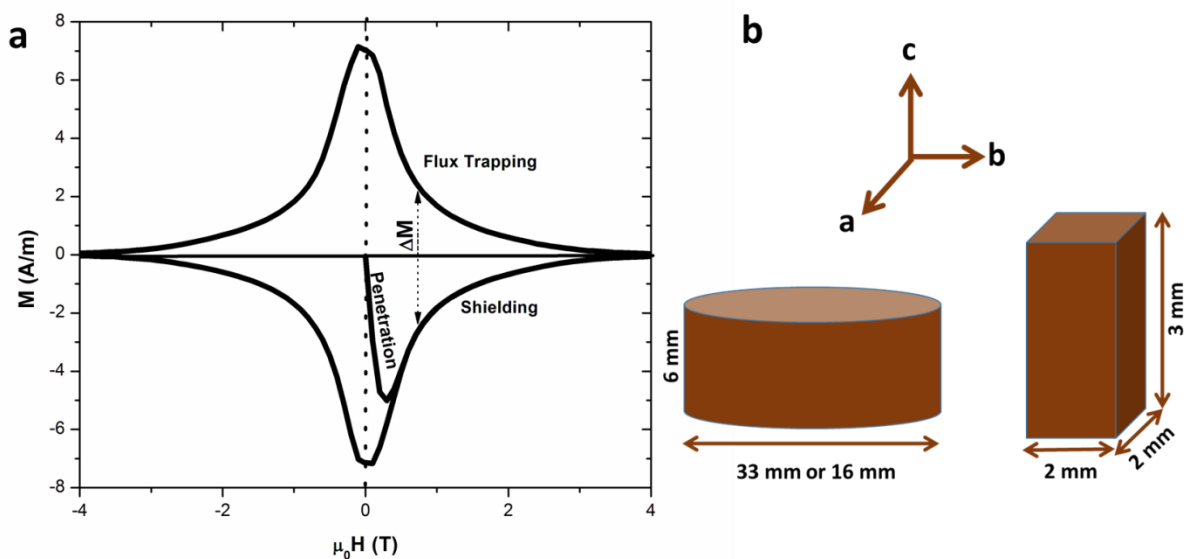


Figure 3.6 A typical  $M-H$  loop measured for MgB<sub>2</sub>-IG sample at 5 K and (b) Orientation of small cut sample used for such measurement relative to parent bulks.

The  $M$ - $T$  and  $J_c$ - $B$  plots presented in this thesis for each representative bulks were measured at least twice to ensure reliability of the data.

### 3.4.6 Resistivity Measurements

Resistivity measurements were performed by the conventional four-point probe method with ac current of 15 Hz using a physical property measurement system (*PPMS*; Quantum Design PPMS Model 6000) at University of Tokyo. The resistivity measurements were made in order to calculate: (1) Normal state electrical connectivity; and (2) Critical fields  $H_{irr}$  and  $H_{c2}$  of MgB<sub>2</sub>-IG.  $H_{irr}$  and  $H_{c2}$  as a function of temperature was estimated by measuring the resistivity-temperature curve at fields up to 9 T. 10% and 90% of the resistive transition was used to estimate  $H_{irr}$  and  $H_{c2}$  respectively [16].

### 3.4.7 Trapped field Measurement

The field Cooled Magnetization (*FCM*) method was used to measure trapped magnetic flux density in a single MgB<sub>2</sub> bulk and combinations of MgB<sub>2</sub>-IG samples.

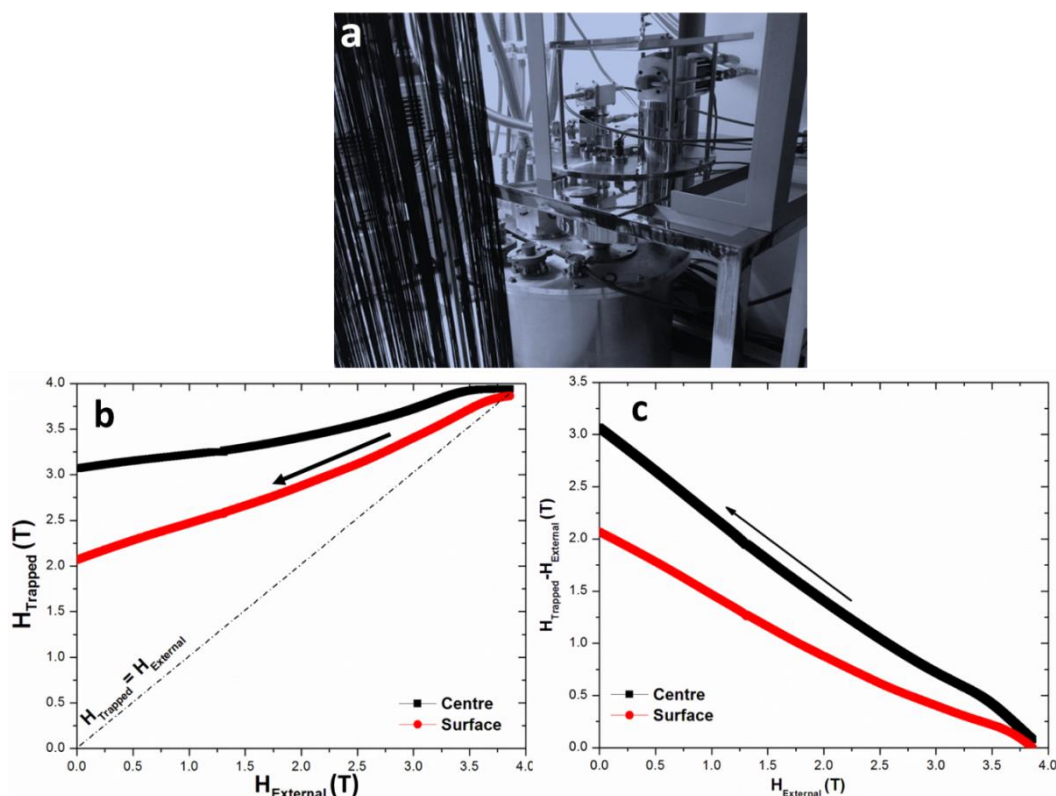


Figure 3.7(a) FCM set-up used to measure trapped fields in MgB<sub>2</sub> bulks. (b) Variation of trapped field as a function of external field (c) Difference between trapped magnetic flux density and external field as a function of external field for two-sample-stack arrangement discussed in section 5.7.1



FCM, although not as practical as pulsed field magnetization method, can reveal the maximum obtainable trapped flux density in the material.

The measurements involved cooling down the sample or sample arrangement to 5 K under an external magnetic field of 5 T/6 T applied perpendicular to the top surface of the sample using a *Gifford–McMahon* (GM) cryocooler (*CRTHE05-CSFM, Iwatani Gas*) (Figure 3.7(a)). The external magnetic field was then reduced very slowly to zero at a rate of 1.8 T/h to minimise any loss of trapped flux from the sample(s), as shown in figures 3.7(b) and (c). The sample(s) was then heated slowly at 0.1 K/min and the trapped magnetic flux density was measured at temperatures up to 40 K by cryogenic hall sensors (*HGCT-3020, Lake Shore*).

#### 3.4.8 Thermal Conductivity Measurements

Thermal conductivity measurements were carried out using the Quantum Design Physical Property Measurement System (*PPMS*) using the *Thermal Transport Option* [215, 216]. Copper leads were attached to the sample with silver epoxy resin. A constant heat input to the sample of dimensions  $1 \times 1 \times 10 \text{ mm}^3$  was maintained using a heater attached to the top. Lateral contacts simultaneously recorded the temperature difference using *Cernox* sensors screwed to the lateral. A thermal radiation screen was anchored thermally to this sample to provide a thermal sink. Data were recorded for several temperatures between 5 K and 10 K. The thermal transport option allowed numerical correction for radiation losses, depending on sample emissivity, geometry, average temperature and temperature gradient.

## Chapter 4. 1<sup>st</sup> Generation IG Processed MgB<sub>2</sub>

### 4.1 Introduction

In the past 15 years of MgB<sub>2</sub> research, it is now realised that the nature of the boron powder is one of the key parameters in the synthesis of MgB<sub>2</sub>. Crystallinity, particle size distribution and purity of the boron powder greatly determine final superconducting properties of MgB<sub>2</sub>. Therefore this chapter is aimed at identifying the boron powder which best suits the IG experiments; establish experimental parameters to produce reproducible results and finally present a complete characterization of synthesised MgB<sub>2</sub> bulk revealing merits or challenges in the IG process. To begin with, a variety of Boron powders are used in initial experiments to test which ones result in optimum performance in the IG process. The transition temperature,  $T_c$ , and the width of  $M-T$  transition are used to determine reactivity of Boron powder with Mg. The phases observed in resultant samples were analysed using XRD, SEM and hardness measurements. Finally resistivity measurements were performed to estimate critical fields and effective current carrying cross-section.

### 4.2 Fabrication and characterization MgB<sub>2</sub> bulk obtained from various B powders

Four different varieties of powder have been used in the MgB<sub>2</sub> synthesis to observe impact of various parameters on MgB<sub>2</sub> phase formation. Their purity, crystallinity and particle size is summed up in table 4.1. The Boron precursor pellets with diameter 16 mm weighing 1 g were prepared from these powders and were subject to various heating conditions. MgB<sub>2</sub> obtained using the particular boron source is hereafter referred to as (MgB<sub>2</sub>-Source), for example MgB<sub>2</sub>-AA (Alpha Aesar).

#### 4.2.1 Reactivity of powders

In order to estimate reactivity of powders with Mg, five precursor pellets made from four varieties were subjected to a temperature of 700 °C and soaking time of 2 h, as per experimental procedure described in section 3.2. The physical appearance of the recovered sample after processing is tabulated in table 4.2. Figure 4.1(a) shows the magnetic moment of MgB<sub>2</sub> bulks, cooled down to 5 K under zero field followed by application of 20 Oe external field, as a function of temperature. MgB<sub>2</sub> processed using the amorphous powders (MgB<sub>2</sub>-AA) showed strong superconducting transition, although very broad; with onset at 37.5 K suggesting partial MgB<sub>2</sub> phase formation. MgB<sub>2</sub>-NM, MgB<sub>2</sub>-HCC and MgB<sub>2</sub>-HCA showed a

very weak diamagnetic signal suggesting negligible quantity of superconducting MgB<sub>2</sub> phase in the reacted product. Although a higher activation barrier associated with crystalline boron explains negligible MgB<sub>2</sub> formation in MgB<sub>2</sub>-NM and MgB<sub>2</sub>-HCC, the low reactivity of HCA with Mg is not fully understood at this stage [36].

Supplier	Particle size	Crystallinity	Purity (%)
Alfa-Aesar (AA)	< 44 micron	Amorphous	99.99
HC Starck (HCA)	< 1 micron	Amorphous	97
New Met (NM)	< 44 micron	Crystalline	99
HC Starck (HCC)	< 38 micron	Crystalline	98

**Table 4.1** Summarizing particle size, crystallinity and purity of various boron powder, as provided by supplier, used in the IG synthesis.

Supplier	Reacted Product
Alfa-Aesar (AA)	Powdery product (MgB <sub>2</sub> -AA)
HC Starck (HCA)	Powdery product MgB <sub>2</sub> (MgB <sub>2</sub> -HC Starck)
New met (NM)	Powdery product without colour change. Probably unreacted (MgB <sub>2</sub> -NM)
HC Starck (HCC)	Powdery Product. No colour change. Possibly Unreacted (MgB <sub>2</sub> -HCC)

**Table 4.2** Physical appearance of product obtained after IG process.

Figure 4.1(b) compares XRD patterns of reacted powdery samples revealing small amount of MgB<sub>2</sub> and Mg<sub>2</sub>B<sub>25</sub> phases along with unreacted B. It is noted that the presence of Mg in the case of MgB<sub>2</sub>-NM is caused by Mg contamination in the sample during sample recovery. It can be seen from MgB<sub>2</sub> (101) reflection at 42.5 °C that only MgB<sub>2</sub>-AA and MgB<sub>2</sub>-HCA show partial MgB<sub>2</sub> formation. It is interesting to note that although Mg(l) infiltration within the porous body was insignificant, MgB<sub>2</sub> formed in MgB<sub>2</sub>-HCA and MgB<sub>2</sub>-AA, while B-rich boride formed in MgB<sub>2</sub>-HCC and MgB<sub>2</sub>-NM. XRD did not detect presence of B-rich boride in MgB<sub>2</sub>-AA. This may be the consequence of a reaction between the B particles and Mg vapor, since Mg has a high vapor pressure.

The B-rich Mg<sub>2</sub>B<sub>25</sub> impurity is a non-equilibrium metastable phase and has been previously observed by Giunchi *et al* in MgB<sub>2</sub> synthesis by RLI [169, 217-219]. Therefore, owing to the higher reactivity towards Mg, AA and HCA powders are considered for further analysis. One

variety of crystalline boron (HCC), is also considered to observe any potential impact of crystallinity on IG processed MgB<sub>2</sub>.

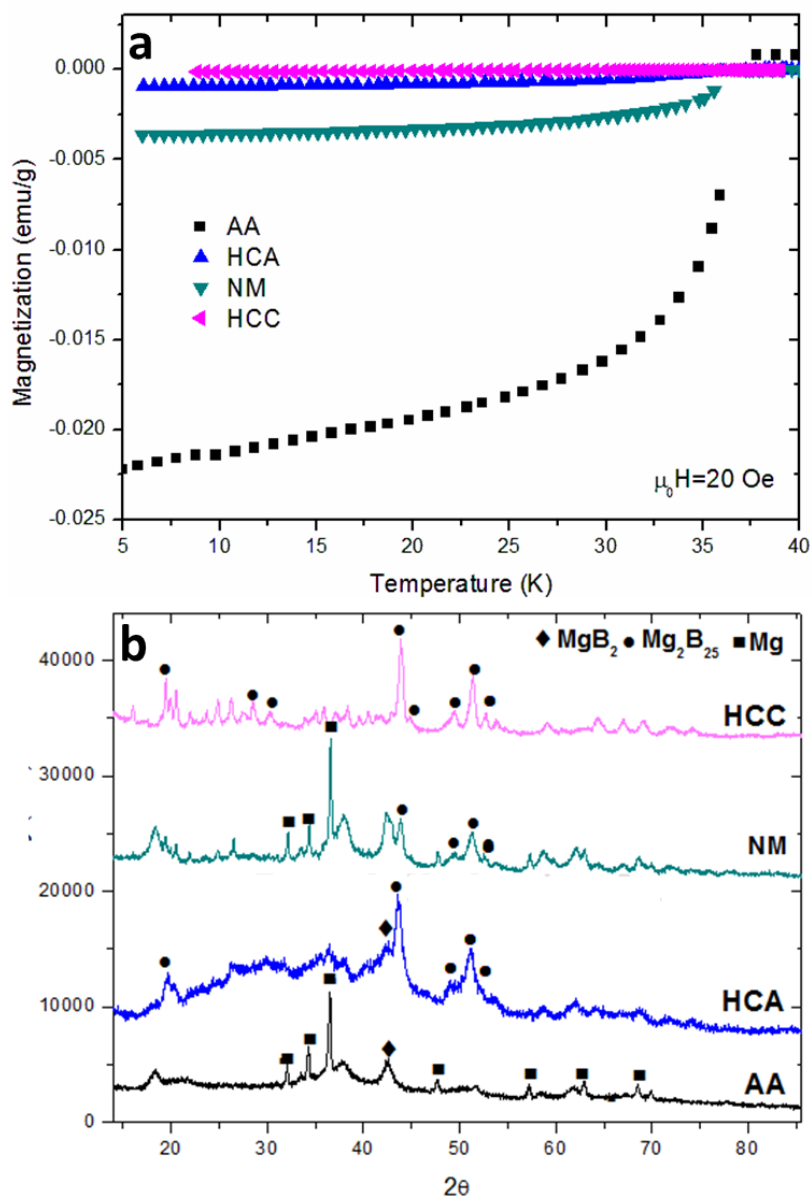


**Figure 4.1(a)** Magnetization response of MgB<sub>2</sub> product, obtained from using different boron sources listed in Table 4.3 but processed under identical processing conditions, as a function of temperature and (b) the corresponding XRD patterns.

#### 4.2.2 Effect of Reaction Temperature

The previous section gave a good indication of the reactivity of various powders. Therefore,

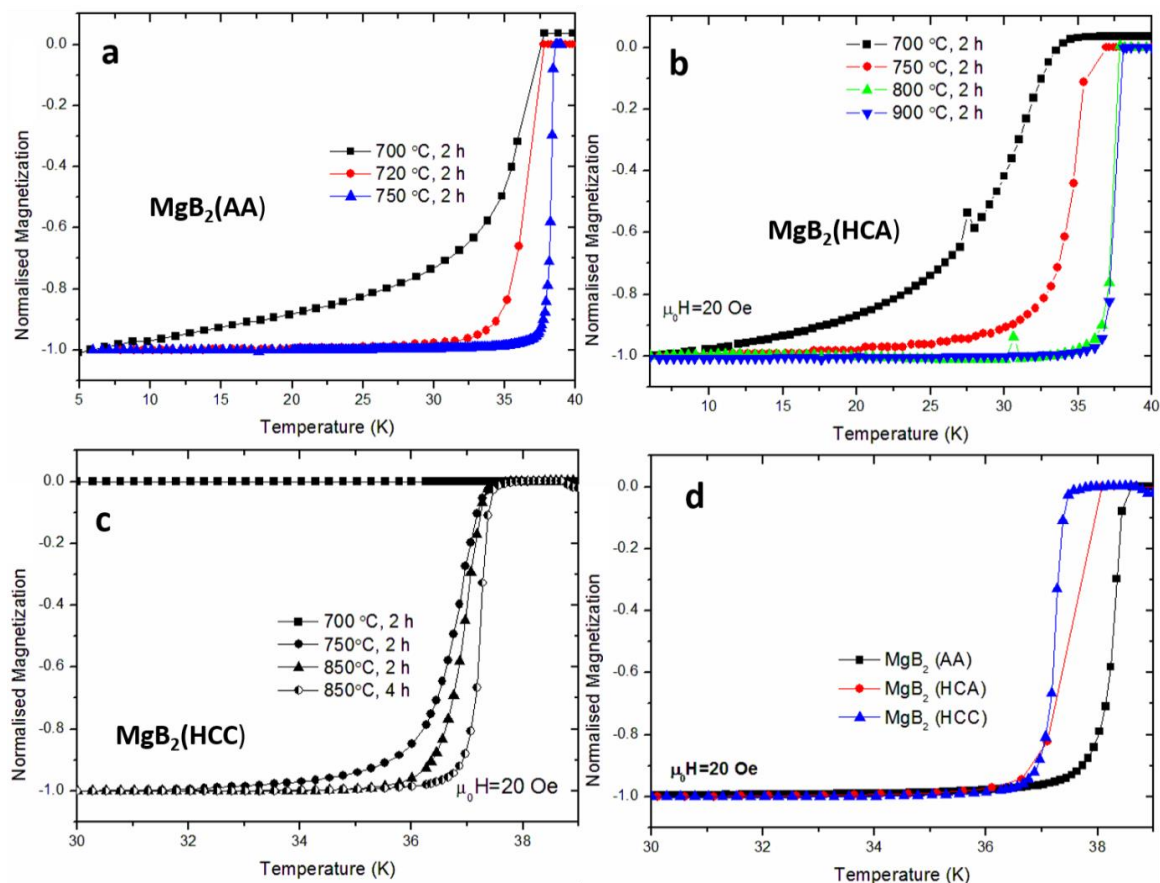


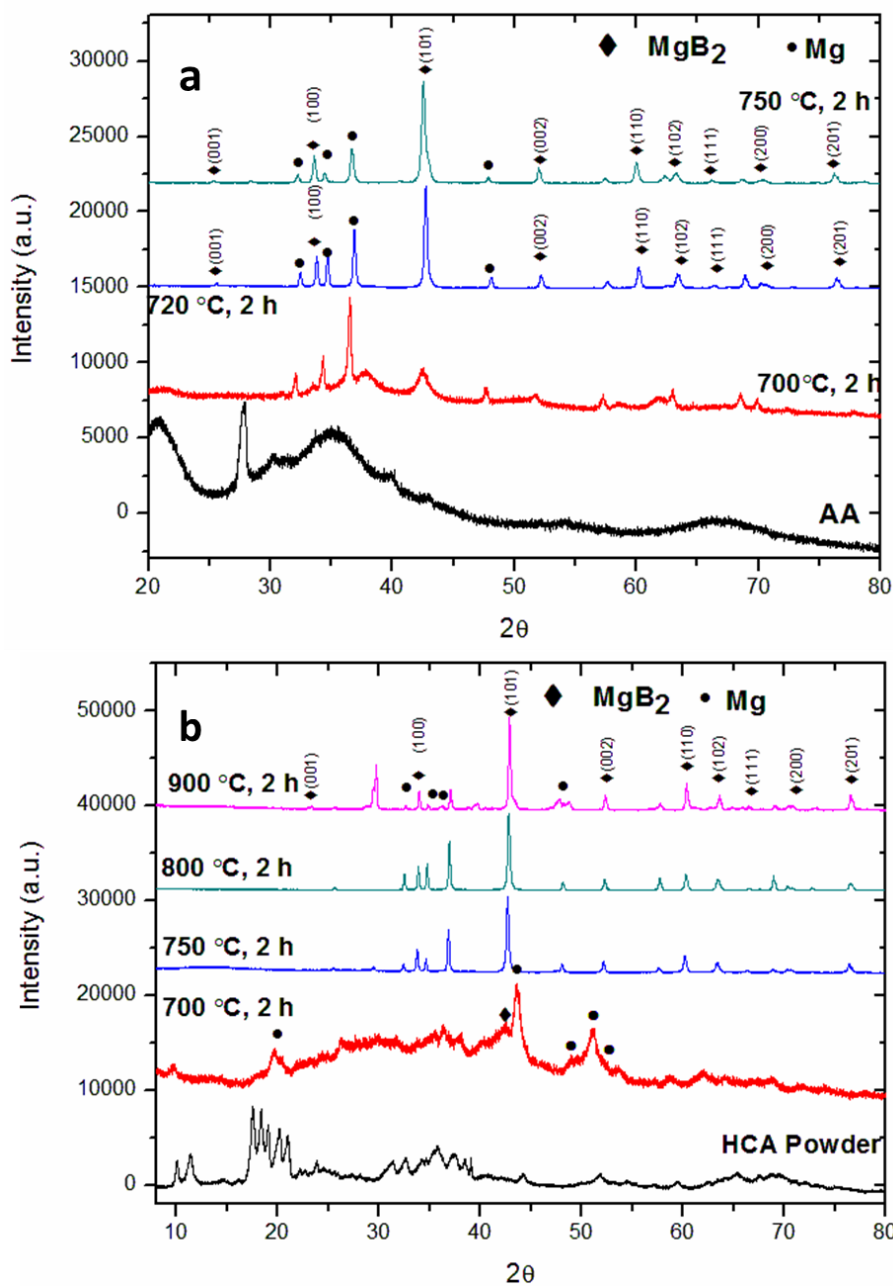
**Figure 4.2** Normalised magnetization as a function of temperature for (a) MgB<sub>2</sub> (AA), (b) MgB<sub>2</sub> (HCA) and (c) MgB<sub>2</sub> (HCC) processed at different temperatures. (d) Comparison of magnetization data of transformed MgB<sub>2</sub> with the sharpest transition in each case.

to examine the effect of the reaction temperature on MgB<sub>2</sub> transformation, further experimental studies were conducted at higher reaction temperature. Two amorphous varieties of boron (AA & HCA) and crystalline boron (HCC) were selected for this analysis. Figures 4.2(a), (b) and (c) show normalised magnetic moment as a function of temperature for MgB<sub>2</sub> samples fabricated under a different reaction temperature. A maximum reaction temperature of 750 °C, 900 °C and 850 °C was used for the synthesis of MgB<sub>2</sub>-AA, MgB<sub>2</sub>-HCA and MgB<sub>2</sub>-HCC respectively. MgB<sub>2</sub>-AA, MgB<sub>2</sub>-HCA and MgB<sub>2</sub>-HCC, under an optimised reaction temperature, showed sharp  $M$ - $T$  transition with onset at 38.8 K, 38.2 K and 37.8 K small  $\Delta T_c < 1$  K. The sharpest  $M$ - $T$  transitions obtained with the use of three B powder sources is compared in figure 4.2(d). MgB<sub>2</sub>-HCA showed a relatively high  $T_c$  despite low purity of HCA whereas MgB<sub>2</sub>-HCC showed slightly reduced  $T_c$  despite 98% purity. It can be seen that all the curves show increase in  $T_c$  and diminishing width of transition ( $\Delta T_c$ ) with increase in the reaction temperature. This clearly is an indication of increasing degree of crystallinity with increasing reaction temperature, since the diffusivity of Mg atoms increases exponentially with temperature. While a higher reaction temperature for crystalline boron is

expected as it is observed, it is rather surprising to note that finer ( $< 1 \mu\text{m}$ ) amorphous boron required a much higher temperature for complete transformation than a coarser ( $< 44 \mu\text{m}$ ) amorphous boron.

#### 4.2.3 Phase Analysis

XRD patterns in figures 4.3(a), (b) and (c) describe XRD patterns of MgB<sub>2</sub>-HCA, MgB<sub>2</sub>-AA and MgB<sub>2</sub>-HCC samples prepared with varying heating conditions, respectively. For a comparison, XRD patterns of boron powders (AA, HCA and HCC) are also plotted.



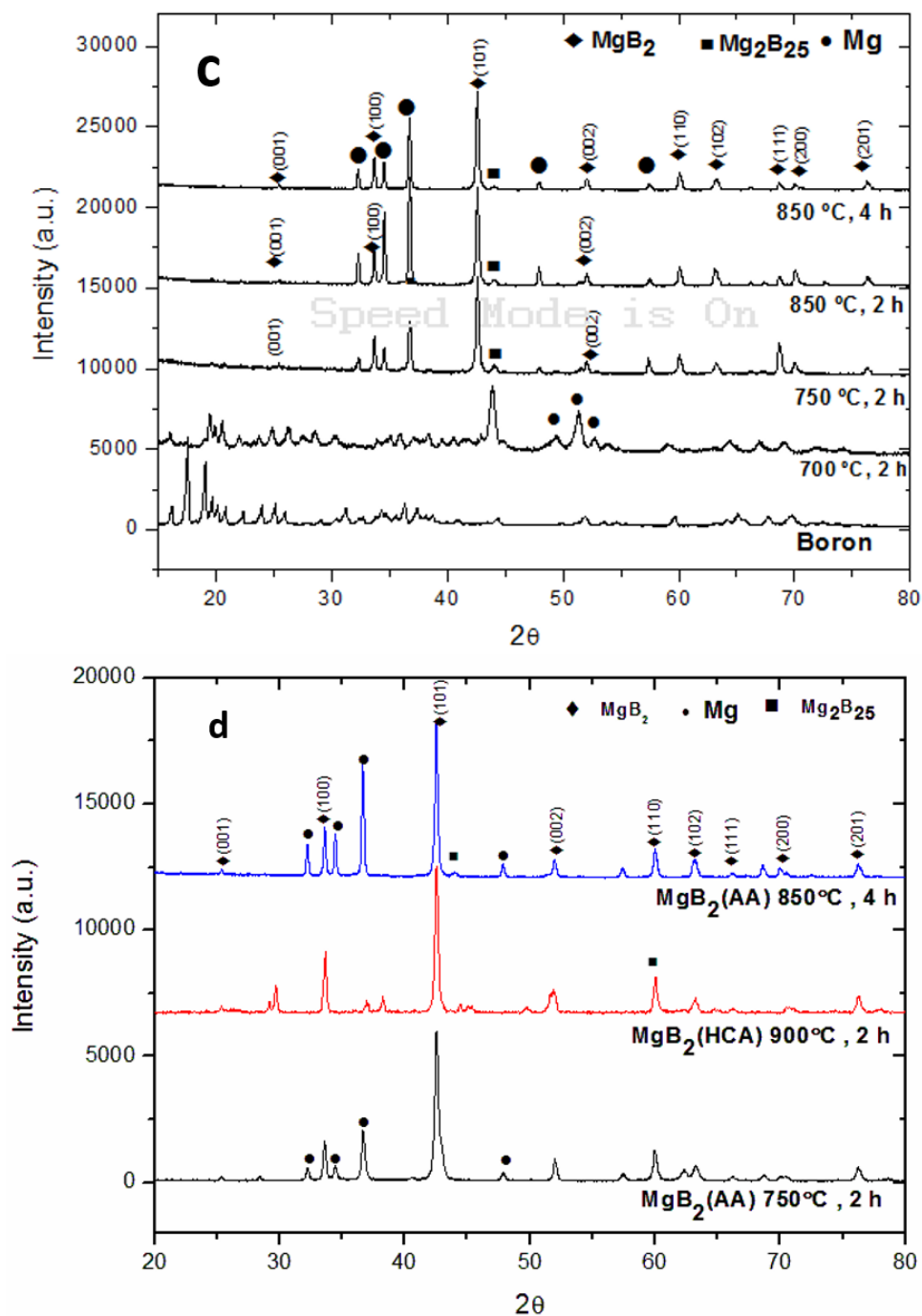


**Figure 4.3** XRD patterns of obtained product reacted at various temperatures using (a) AA (b) HCA and (c) HCC boron powders. (d) Comparison of XRD patterns of transformed MgB<sub>2</sub> obtained in each case under optimum conditions.

The presence of a majority MgB<sub>2</sub> phase is confirmed under the highest processing temperature in each case and is compared in figure 4.3(d). XRD patterns for AA and HCA suggests these powders are predominantly amorphous with small traces of crystalline phases. The presence of multiple halos in the XRD pattern indicates several type of boron atoms clusters that exhibit different characteristic short range order. It is apparent that the

mechanism of phase evolution is rather different in MgB<sub>2</sub> fabricated using amorphous and crystalline powders. With the increase in reaction temperature for AA and HCA, the amorphous halo vanishes and MgB<sub>2</sub> peak sharpens suggesting formation of crystalline MgB<sub>2</sub>. Clearly, the reaction kinetics for amorphous boron is generally faster and MgB<sub>2</sub> forms without the formation of any intermediate phase, unlike crystalline powder (Figures 4.3(a) and (b)). HCA (partial crystalline Boron) and HCC which were reacted at 700 °C for 2 h, show little signs of infiltration, resulting in a powdery specimen, with the majority of the sample consisting of lesser known Mg<sub>2</sub>B<sub>25</sub> phase. Its fraction progressively decreased with increase in reaction temperature as seen from figure 4.3(c). This confirms that Mg<sub>2</sub>B<sub>25</sub> is probably one of the intermediate phases stable at room temperature that forms during the MgB<sub>2</sub> phase transformation process. Mg<sub>2</sub>B<sub>25</sub> phase detection was first reported by Giunchi *et al.* in the RLI process [169, 217-219]. This further underlines the low reactivity of crystalline boron relative to amorphous boron. The evolution of superconducting MgB<sub>2</sub> from  $\beta$ -boron is discussed in detail in chapter 6.

Another common feature in XRD patterns of MgB<sub>2</sub>-HCA, MgB<sub>2</sub>-AA and MgB<sub>2</sub>-HCC samples is the presence of residual Mg. No evidence of texture was observed in IG processed MgB<sub>2</sub> bulk, as suggested by the unaltered relative peak intensities in both bulk and milled powder X-Ray patterns (not shown here), although there is contamination in the form of MgO which formed during the milling stage. The presence of Mg is commonly observed in MgB<sub>2</sub> samples produced by infiltration and growth process. The presence of residual Mg is attributed to the dense packing of the MgB<sub>2</sub> unit cell, which results in the creation of voids due to volume shrinkage upon reaction between Mg and B and these voids are later become filled by surrounding Mg during infiltration (assuming MgB<sub>2</sub> nucleation occurs everywhere simultaneously). The amount of Mg is estimated to be around 15% from the XRD patterns. Interestingly, the amount of MgO, which could be detrimental to the electrical connectivity of the bulk sample, is below the detection limit of XRD.

#### 4.2.4 Microstructures

Figure 4.4(a) shows an SEM image of the polished surface of the MgB<sub>2</sub>-AA sample. The sample shows a surprisingly fine grained structure, which doesn't reflect a maximum Boron particle size of



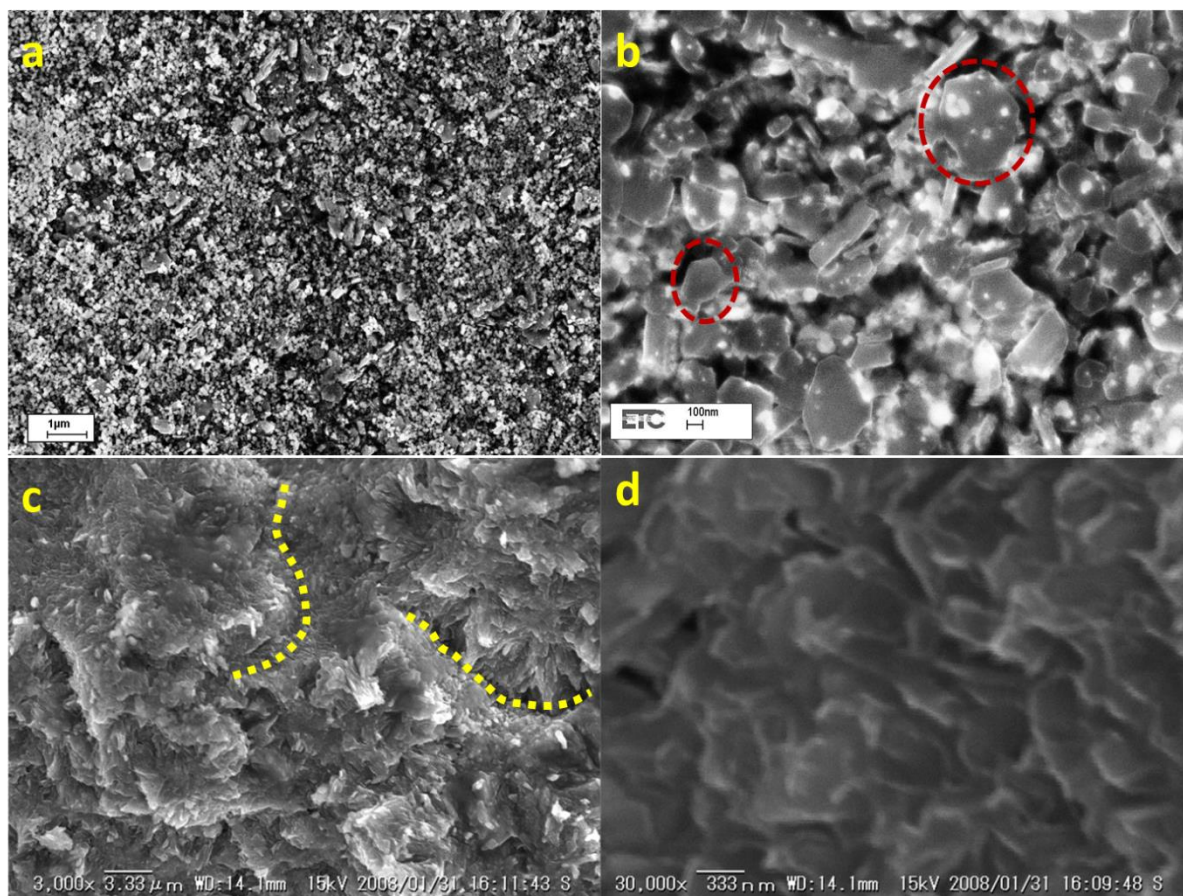


**Figure 4.4(a) and (b) SEM images (In-lens detector) of polished surface. Red circles in (b) are contaminants (possibly colloidal silica) introduced during polishing stage. (c) and (d) show secondary electron images of fracture surface of MgB<sub>2</sub>-AA (750 °C, 2 h). Yellow dotted lines show MgB<sub>2</sub> particle-particle interface.**

44 μm in AA precursor. A higher magnification image (Figure 4.4(b)) shows the crystallite size is of the order of 200 nm. Figures 4.4(a) and (b) also showed bright-in-the-contrast contaminants on the surface, which possibly were introduced during preparation of the polished surface. To ensure that these are not from the material itself, MgB<sub>2</sub>-AA bulk was intentionally fractured and the fracture surface was observed with SEM as shown in figures 4.4(c) and (d). The fracture surface appears free from contaminants, confirming that bright-in-contrast regions probably were introduced during the polishing stage. Since fracture has taken place at the inter-particle interface, these can be clearly observed in figure 4.4(c) as shown by yellow dotted line. Figure 4.4(c) also shows a dense microstructure and clean inter-particle interface. Significantly, no impurities or porosity are observed in this image. Such a homogeneous microstructure is attributed to the presence of excess Mg during the reaction, which is known for improving grain connectivity, the elimination of micro-cracks, facilitating recrystallization and avoiding B-rich impurities [188, 189]. The fracture surface (Figure 4.4(d)) also shows number of hexagonal plate-like crystals. This is due primarily to the rapid

crystal growth parallel to the *a-b* plane; such geometry is typical of hcp borides that exhibit faceted growth.

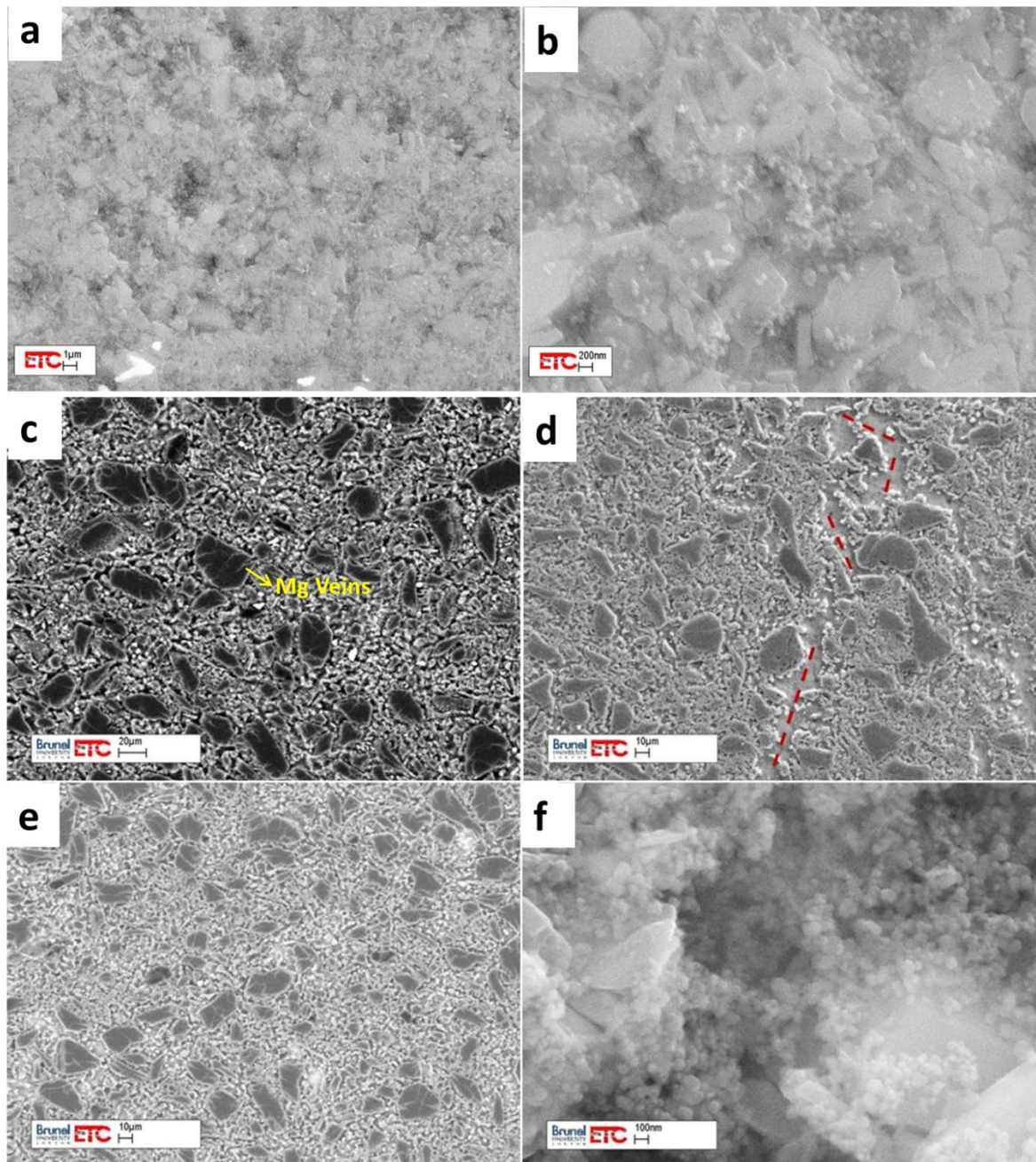


**Figure 4.5(a) and (b)** secondary electron images of polished surface of MgB<sub>2</sub>-HCA bulk (900 °C). Scanning electron micrographs of infiltrated and grown MgB<sub>2</sub>-HCC reacted at (c) 750 °C, 2 h 1000x in BSE mode, (d) 850 °C, 2 h at 1000x in SE mode and (e) 850 °C, 4 h at 1000x in BSE mode. (f) 20-50 nm size precipitates in the inter-particle region in sample reacted at 850 °C, 4 h. Non-superconducting continuous Mg channel, a defect in IG MgB<sub>2</sub>, shown by red dotted line in figure (d).

Similarly, MgB<sub>2</sub> fabricated using HCA (Figure 4.5(a) and (b)) shows plate-like MgB<sub>2</sub> crystals with size of about 1 micron in size, clearly resembling the initial particle size. Many finer crystals of size 10-20 nanometer can also be seen in Figure 4.5(b). Notably, all the crystallites are of uniform particle size and no grain growth appears to have taken place even after a heat

treatment at 900 °C. Such microstructures of IG process samples are in contrast with the ones observed in sintering techniques, which invariably contain large amount of porosity arising as a result of shrinkage in reaction I and high Mg vapor pressure.

MgB<sub>2</sub> synthesized using crystalline boron on the other hand shows rather different microstructures (Figure 4.5(c-f)). Many dark-in-contrast particles of size of the order of 30 μm can be observed, reminiscent of maximum particle size of crystalline boron. All the images show a relatively dense microstructure and no large pores or voids can be seen. Figures 4.5(c), (d) and (e) show larger MgB<sub>2</sub> particles and finer (~1 μm) sized grains, that are embedded between them. Such a bimodal grain size distribution was also observed previously and could be explained by a bimodal distribution of precursor boron powder itself (not shown here). The population of larger MgB<sub>2</sub> particles in a given area and their individual size is found to be unaffected, which suggests that grain growth has not taken place after 4 h processing at 850 °C. However, these larger particles exhibit a number of distinctive features. Figures 4.5(c), (d) and (e) show a number of bright Mg veins across the particle from its surface to the interior (clearly seen in figure 6.5). The reason for such behavior is discussed in detail in section 6.3. Its effect is clearly to decrease the distance the Mg atoms need to diffuse in order to achieve complete phase transformation. An EDS (Energy Dispersive Spectroscopy) profile measured along the diameter of particle is shown in figure 4.6. The scan clearly suggests that dark-in-contrast areas are composed of B-rich phases whereas the Mg concentration is significantly increased in the outer areas as well as in the veins.

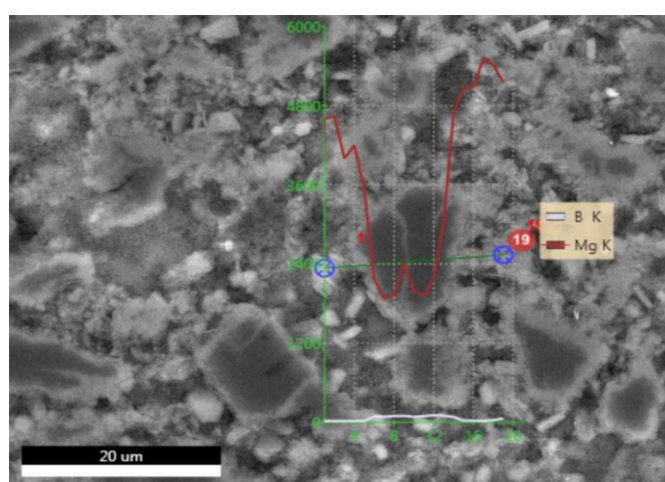


Figure 4.6 EDS line profile of Mg and B across particle.

Finally, Figure 4.5(f) shows a higher magnification image of MgB<sub>2</sub>-HCC produced at 850 °C for 4 h. The image was captured in the region between two adjacent MgB<sub>2</sub> particles. The

image shows a large density of 20–50 nm thin crystals. An EDS analysis in this area identifies the constituent elements to be Mg and B. These particles therefore probably are comprised of both Mg and MgB<sub>2</sub>. Such fine precipitates are potentially effective magnetic flux pinning centers in the MgB<sub>2</sub>-HCC bulk superconductor.

#### 4.2.5 Defects in IG MgB<sub>2</sub>

Figure 4.5(d) shows a continuous, 10 μm Mg wide channel (dotted red line) originating from

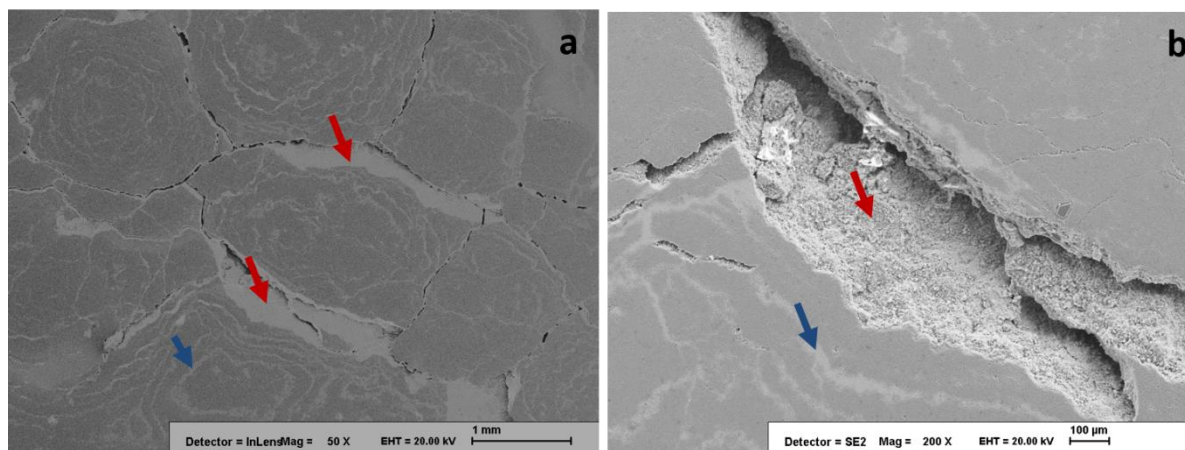


**Figure 4.7(a) and (b) low magnification images of MgB<sub>2</sub>-HCA (850 °C, 4 h). The defects in the microstructure, i.e. regions where Mg(l) has not fully infiltrated, are indicated by red arrows. Blue arrows indicate fine continuous, often concentric, Mg channels.**

the surface of the sample. Such channels are observed at numerous locations in all the samples. the effect of these on the performance of MgB<sub>2</sub>-IG bulk is discussed in the following chapter (Chapter 5). Similar continuous Mg channels (indicate by red arrows) were also observed in MgB<sub>2</sub>-HCA, although these were much finer and large in population with concentric contour geometry, as indicated by blue arrows in Figures 4.7(a) and (b).

Furthermore, these figures also show numerous locations in the microstructure that appear to be pores (Figure 4.7 Red arrows). A careful look suggests that these are parts of the sample where complete Mg(l) infiltration has not taken place despite reaction at higher temperature (900 °C). This can be explained by fine pore geometries that are formed in the precursor as a result of the fine particle size of the HCA boron. Washburn's model for a capillary action suggests that infiltration depth is an increasing function of capillary diameter [220]. Therefore time taken for completion of infiltration is higher when fine boron is used. Recently, Li *et al* also have pointed out that AIMI wires fabricated using nano-boron show a small Mg infiltration layer and a small resultant MgB<sub>2</sub> layer [39]. Therefore, keeping in view

the fabrication of larger MgB<sub>2</sub> bulks, only 40 μm size powders (AA and HCC) are used in further work.

#### 4.2.6 Resistivity Measurements

Since MgB<sub>2</sub>-HCC contained a considerable amount of secondary phases such as B-rich boride, its contribution to resistivity makes the determination of connectivity and critical fields more difficult.

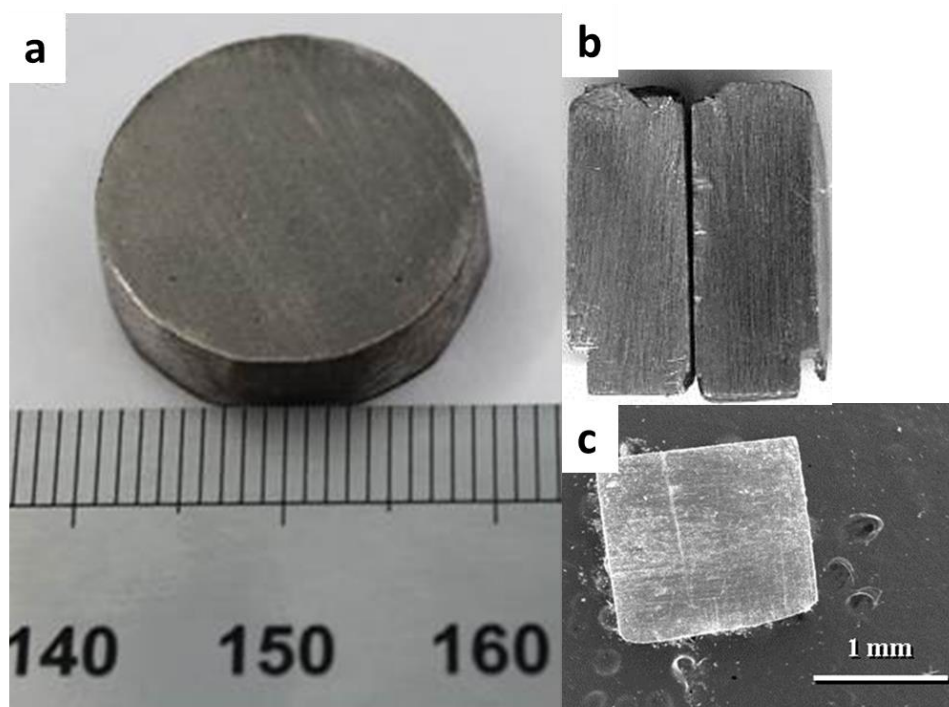


**Figure 4.8(a)** A typical image of MgB<sub>2</sub>-AA bulk and **4.8(b)** A uniform and dense looking MgB<sub>2</sub> bulk cross section and **(c)** a small cut section used to measure resistivity and critical current density in figures 4.9, 4.10 and 4.11.

Therefore determination of connectivity and critical fields may not be representative of MgB<sub>2</sub>-IG. Hence MgB<sub>2</sub> fabricated from AA boron powder was used in this analysis, so that it represents Resistivity-Temperature characteristics of IG processed MgB<sub>2</sub> bulk. A typical image of MgB<sub>2</sub>-AA 20 mm Dia bulk sample, processed at 750° C for 2h, is shown in figures 4.8(a), (b) shows cross-section and (c) shows the small sample used for resistivity measurements.

In order to estimate the normal state electrical connectivity and critical field, variation of resistivity with temperature for the MgB<sub>2</sub> bulk sample, fabricated using AA powder, was measured between 300 K and 5 K in an applied external field up to 9 T (Figure 4.9(a)). For a

comparison, normalised zero field cooled (ZFC) magnetic transition is also plotted (Figure 4.9(a) inset). Although  $T_c$  offset is slightly reduced (difference of 0.4 K) in inductive mode,  $T_c$  onset is quite close (difference is  $\approx 0.02$  K). Such behaviour has previously been observed and is attributed to the transport current path in resistive measurement that preferentially chooses good quality grains i.e. path of least resistance [221].

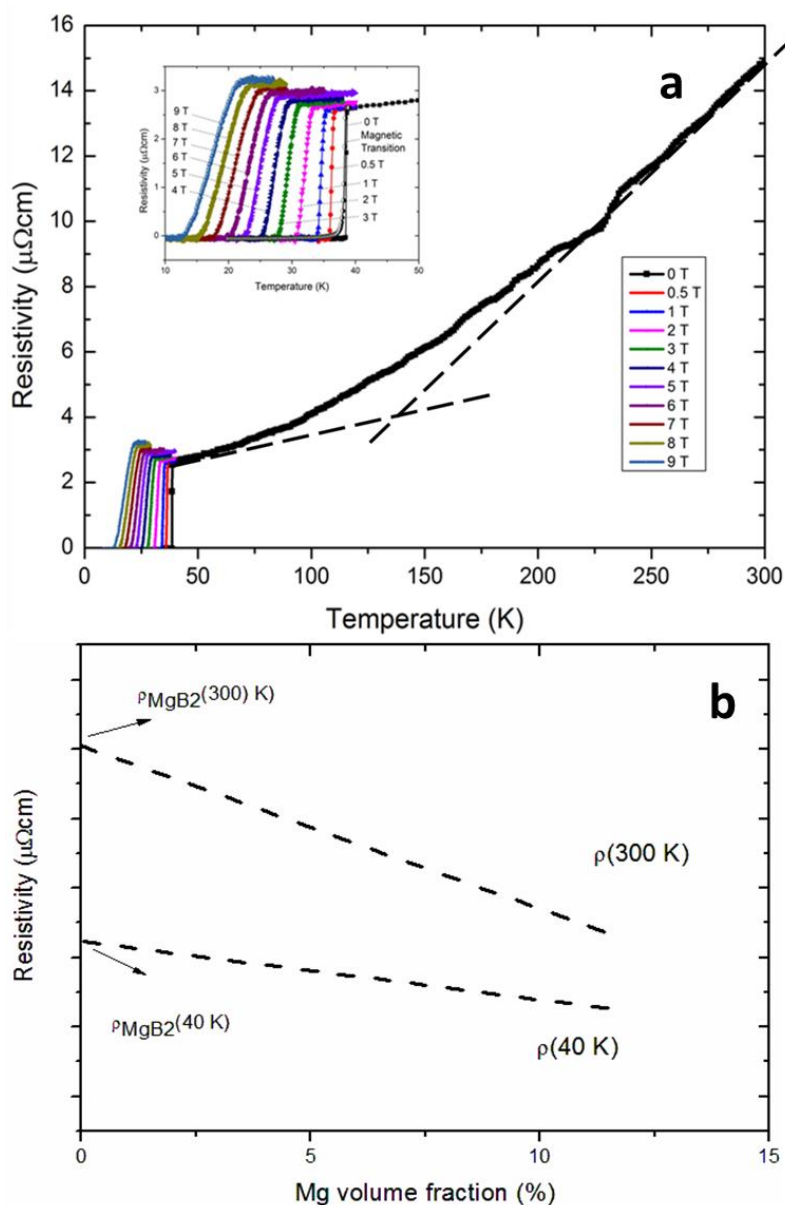


**Figure 4.9(a)** Variation of resistivity as a function of temperature under external magnetic fields up to 9 T. inset shows magnified images and compares resistive and inductive superconductive transition. **(b)** Schematic illustration of expected resistivity of MgB<sub>2</sub> with respect to residual Mg content.

This is in contrast to the inductive measurement where current loop passes through the surface of the material which includes good and poor quality grains. Good quality grains can be described as grains with fully transformed highly crystalline of MgB<sub>2</sub>, with higher  $T_c$  that

can support relatively large supercurrent. Whereas poor quality grains are grains where MgB<sub>2</sub> transformation is incomplete, or contains impurities which result in reduction in  $T_c$ . The observed low difference in measured  $T_c$  by two separate techniques suggests that the material is indeed homogeneous.

The sample exhibits a very low residual resistivity of 2.64  $\mu\Omega\text{cm}$  and a residual resistivity ratio (RRR) of 5.63, which is comparable to values observed for single crystal MgB<sub>2</sub> samples (typically 1-2  $\mu\Omega\text{cm}$  measured in-plane), as reported previously [75, 76]. In addition, the observed increase in resistivity with external field at a given temperature indicates that the bulk MgB<sub>2</sub> sample exhibits significant magneto resistive effects. The normal state electrical connectivity  $K_c$  (or effective cross sectional area), which is defined by Rowell [62] as the ratio of difference of resistivity between a single crystal to that of a poly-crystal, is calculated for the MgB<sub>2</sub> bulk sample from the following expression:

$$K_c = \frac{\rho_{sc}(300\text{ K}) - \rho_{sc}(40\text{ K})}{\rho(300\text{ K}) - \rho(40\text{ K})} = 51.8\% \quad \begin{array}{l} \rho_{sc}(300\text{ K}) - \rho_{sc}(40\text{ K}) = 6.32\ \mu\Omega\text{cm} \\ \rho(300\text{ K}) - \rho(40\text{ K}) = 12.2\ \mu\Omega\text{cm} \end{array} \quad (4.1)$$

where  $\rho_{sc}$  is the resistivity of an MgB<sub>2</sub> single crystal averaged over random orientations and  $\rho$  is the resistivity of MgB<sub>2</sub> fabricated by infiltration and growth. The difference of resistivity of a single crystal between 300 K and 40 K ( $\rho(300\text{ K}) - \rho(40\text{ K})$ ) is taken as 6.32  $\mu\Omega\text{cm}$  based on predictions of mean field theory in [137]. The connectivity obtained here is significantly higher than that observed in bulk MgB<sub>2</sub> samples synthesized by both *ex situ* ( $\sim 10\%$ ) and *in situ* ( $\sim 30\%$ ) ambient pressure processing routes [139]. Note that XRD did not detect the presence of MgO and BO<sub>x</sub> type impurities that are known to reduce the effective current carrying cross section.

It is important to note that the transport properties of the present sample are altered by residual magnesium metal within the infiltrated grown sample. The  $\rho$ - $T$  plot for pure MgB<sub>2</sub> shows a plateau near 80 K, whereas the  $\rho$ - $T$  curve for Mg exhibits a linear decrease till 40 K [223]. Magneto-resistance is other evidence for the contribution of residual magnesium on current transport [223]. Magnetoresistance indicates a Mg volume fraction in the material of about 15%. This is reasonably accurate estimation, as the contribution is generated from bulk of Mg inside the IG sample. On the other hand, the powder XRD might have contaminants introduced during milling process, whereas bulk XRD reveals only surface chemistry.

It is evident from figure 4.9(a) that the  $\rho$ - $T$  curve obtained here has characteristics of MgB<sub>2</sub> as well as Mg. The  $\rho$ - $T$  curve for MgB<sub>2</sub> tends to flatten near 80 K, whereas the  $\rho$ - $T$  curve for Mg has a linear decrease till 40 K. Thus it is likely that  $\rho(300\text{ K})$  and  $\rho(40\text{ K})$  are underestimated whereas  $RRR$  and connectivity are overestimated in the present case.

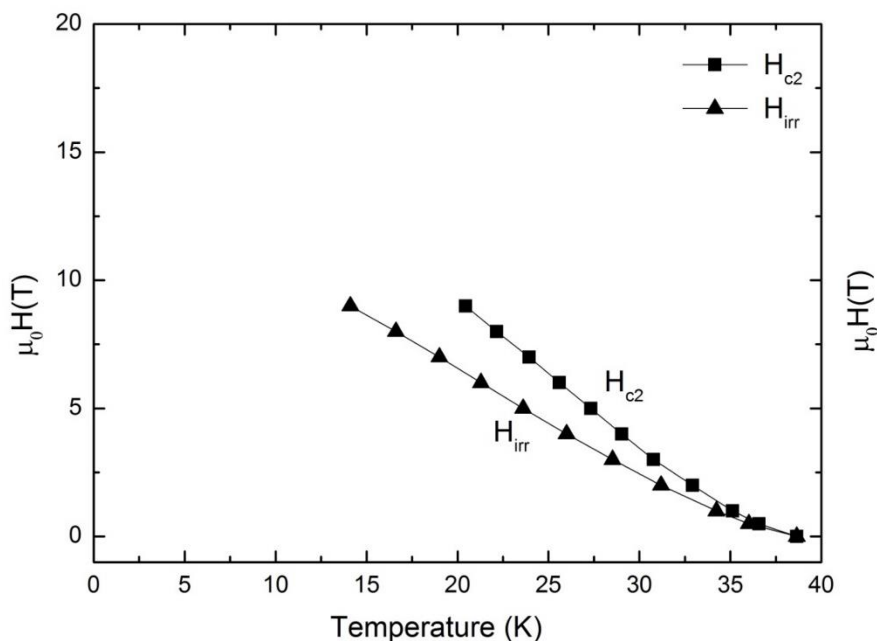


**Figure 4.10** dependence of  $H_{c2}$  and  $H_{irr}$  of infiltrated bulk MgB<sub>2</sub> with temperature. Values estimated using 90%-10% of the normal-state resistivity.

A prediction of connectivity in such a case would require numerous samples with a known amount of excess Mg. The intercept of extrapolated  $\rho(T)$  versus excess Mg curves would yield a fairly good value of  $\rho(300\text{ K})$  and  $\rho(40\text{ K})$  excluding any effects by Mg (Figure 4.9(b)). These values can then be used to estimate the corrected value of connectivity. Naturally, the samples selection should be in a relatively small range of Mg concentration. This would make the assumption, ‘Change in resistivity being entirely due to Mg concentration and addition of Mg not altering inherent MgB<sub>2</sub>-MgB<sub>2</sub> connectivity’, reasonable.

Figure 4.10 shows the variation of upper critical field,  $H_{c2}$ , and irreversibility field,  $H_{irr}$ , with temperature, both of which have been estimated using the 90%-10% definition of the resistive transition. Although  $\rho$ - $T$  is affected by the remaining magnesium content, at this temperature range between 0-40 K, Mg shows very weak temperature dependence. Therefore the resistive transitions are mostly dominated by superconducting MgB<sub>2</sub>. Thus the 90%-10% criterion to define  $H_{c2}$  and  $H_{irr}$  is not compromised by absolute value. It can be



seen that both  $H_{c2}$  and  $H_{irr}$  vary linearly at temperatures below around 34 K (i.e. slightly below  $T_c$ ). Equation 2.7 yields a value of  $H_{c2}$  at 0 K of 17 T. This is rather lower than that obtained for polycrystalline MgB<sub>2</sub> [224] and is close to the value of  $H_{c2}$  for a single crystal (15 T in the  $a$ - $b$  plane) [225]. This suggests that the sample fabricated in the present study is transformed fully into highly crystalline MgB<sub>2</sub> and is in clean limit.

#### 4.2.7 Critical Current Density

Figure 4.11 shows the variation of critical current density,  $J_c$ , as a function of applied field at

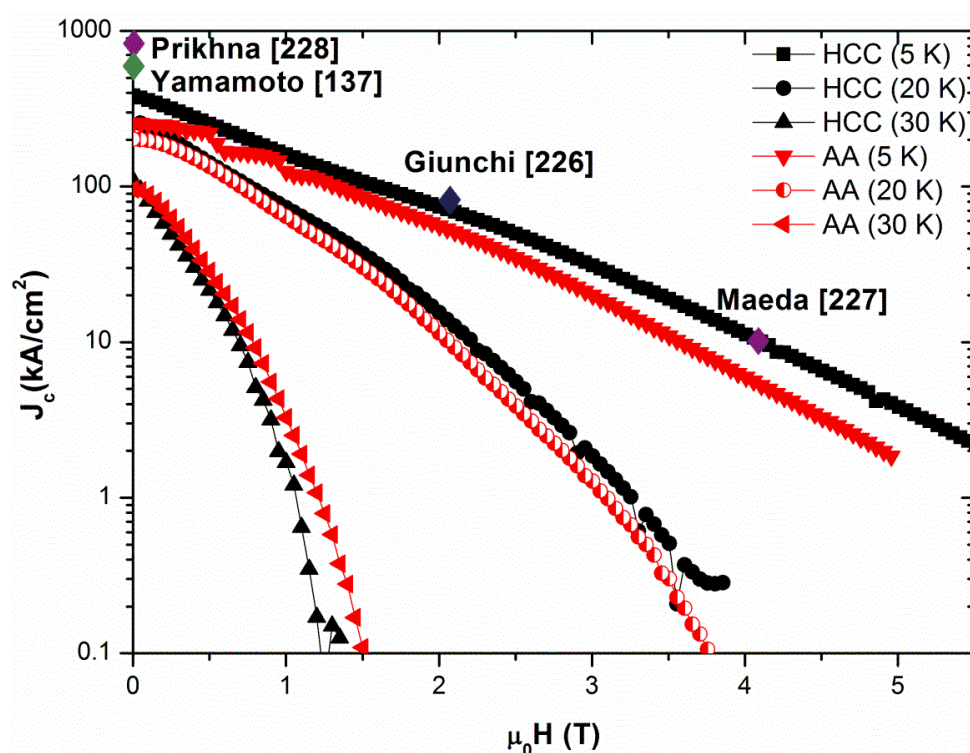


Figure 4.11 A comparison of critical current density between MgB<sub>2</sub>-AA and MgB<sub>2</sub>-HCC, as a function of external magnetic field. Other researcher's data shown is measured at 20 K.

5 K, 20 K and 30 K. A large population of residual Mg channels in the microstructure did not allow exact estimation of  $J_c$  in MgB<sub>2</sub>-HCA.  $J_c$  at 5 K and 20 K under self-field is as high as 260  $\text{kA/cm}^2$  and 200  $\text{kA/cm}^2$ , respectively, for MgB<sub>2</sub> fabricated using AA powder. While MgB<sub>2</sub> fabricated using HCC shows relatively high self-field  $J_c$  of 380  $\text{kA/cm}^2$  and 280  $\text{kA/cm}^2$ .

This suggests that the sample is well connected with a relatively large current carrying cross sectional area.  $J_c$  expectedly decreases in higher applied field, which is indicative of weak flux pinning in this field regime in clean limit MgB<sub>2</sub> sample.  $J_c$  in MgB<sub>2</sub> fabricated from

HCC is higher than MgB<sub>2</sub> fabricated using AA at low temperatures and lower at higher temperatures. Although a lower  $J_c$  at higher temperature is expected since  $T_c$  is MgB<sub>2</sub> (HCC) is lower by 1 K, the observed higher  $J_c$  at low temperature is not fully understood. Moreover MgB<sub>2</sub>-HCC shows a better  $J_c(B)$  dependence relative to MgB<sub>2</sub>-AA at 5 and 20 K. Giunchi *et al* obtained slightly high  $J_c$  of 80 kA/cm<sup>2</sup> (20 K, 2 T) with RLI process [226]. Similarly Maeda *et al* (10<sup>3</sup> A/cm<sup>2</sup>, 20 K, 4T) [227], Yamamoto *et al* (600 kA/cm<sup>2</sup>, self-field 20 K) [137] reported high  $J_c$  in ambient pressure in-situ sintering route. Prikhna *et al* recently reported very high  $J_c$  of 900 kA/cm<sup>2</sup> (Self field, 20 K) using high pressure [228]. Obtained  $J_c$  here, although modest when compared to these data, is relatively high taking into account residual Mg content. This is likely to be due to the very low fraction of MgO in MgB<sub>2</sub>-IG.

#### 4.2.8 Microhardness

The Semi-micro hardness, i.e. one measured using relatively higher load of 20 Kg, for MgB<sub>2</sub>-HCC bulk samples figure 4.12(a). Indentations along cross section were made at 7 equally spaced points between edges of specimen from top to bottom. Hardness measured at each point is plotted against geometrical location of the indent. Length of diagonal of indent was between 300–500  $\mu$ m, depending on hardness at each location.

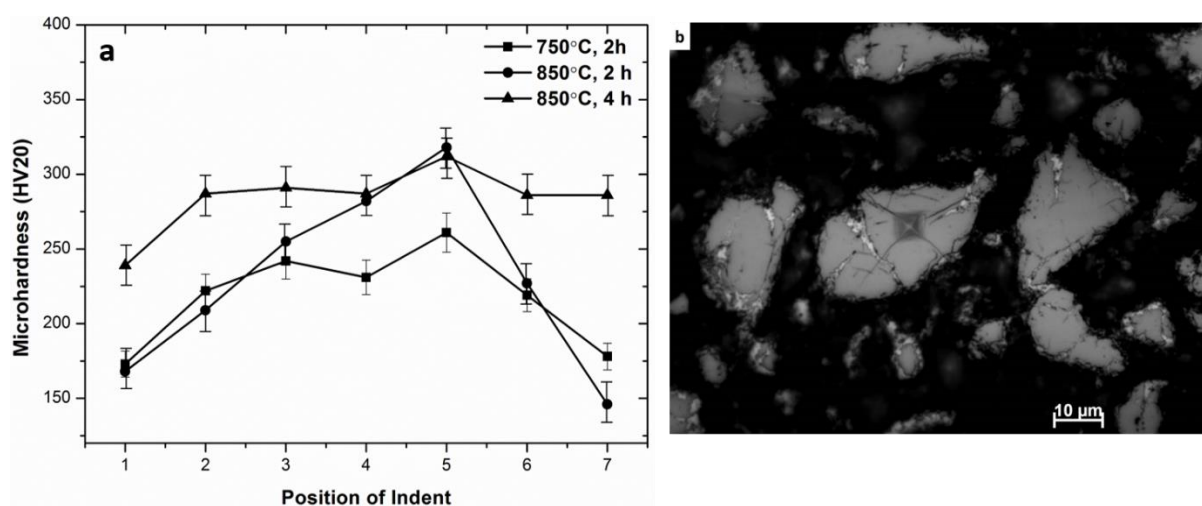


**Figure 4.12** Hardness of MgB<sub>2</sub>-HCC samples (a) Semi-microhardness of MgB<sub>2</sub>-HCC samples measured along the cross section with Load = 20 kg, dwell time = 10 s and (b) Microhardness performed on a particle (850 °C, 4 h) with load = 0.1 kg, dwell time = 5 s.

It is evident that hardness increased with increase in reaction temperature by a constant value along the entire cross-section. This demonstrates clearly that an increase in the MgB<sub>2</sub> phase fraction results in increased hardness of the bulk superconductor, and, therefore, hardness can be interpreted generally as the extent of MgB<sub>2</sub> phase formation. Notably, samples reacted for 750 °C, 2 h and 850 °C; 2 h show a rather interesting behaviour. The peak value of hardness

for these samples is observed at the center of each specimen and decreases with distance from the center. The hardness at the edges of the samples increases significantly as the soaking time is increased in the IG process, while the maximum hardness at center remains the same. This probably suggests that the superconducting phase first forms at the center of the sample, while the edges are partially transformed during the initial 2 h processing period.

Finally, the micro-hardness of individual larger particles was measured on sample processed at 850 °C for 4 h. After the indentation, cracks invariably formed along either side of both diagonals in all measurements and propagated towards the surface of the particle as shown in figure 4.12(b). The calculated average value of hardness over 4 particles was 33 GPa, although this might be slightly underestimated due to the formation of cracks upon application of the load and contribution from material underneath the particle with indent. Maximum hardness in MgB<sub>2</sub> samples is reported as 35 GPa [229], which is in good agreement with our measurements. The presence of Mg<sub>2</sub>B<sub>25</sub> phase inside the larger MgB<sub>2</sub> grains is reported to be the reason for such high hardness [229]. As expected, the hardness measurements across the Mg veins inside MgB<sub>2</sub> particles show a reduced value of 20 GPa.

### 4.3 Summary

The primary objective of this study so far was to identify the suitable choice of boron and to examine the effect of temperature on the IG process. The fabrication of dense and highly connected bulk MgB<sub>2</sub> by an infiltration and growth process is demonstrated. This relatively simple technique is performed at ambient pressure and is therefore potentially scalable to the fabrication of larger bulk MgB<sub>2</sub> samples of more complex geometries. X-Ray diffraction analysis revealed that the MgB<sub>2</sub> phase was the main phase with minor quantities of Mg. When  $\beta$ -boron was used Mg<sub>2</sub>B<sub>25</sub> phase formation was also observed. Densification mechanism in this study differs significantly from conventional solid state sintering of MgB<sub>2</sub>, in which the porosity is typically retained during processing resulting in poorly connected grains. This is remarkable considering that thick sections and complex shapes can be fabricated with this method while the process not requiring expensive high pressure apparatus.  $J_c$  of the bulk MgB<sub>2</sub> samples in the self-field is 400 kA/cm<sup>2</sup> (MgB<sub>2</sub>-HCC) and 260 kA/cm<sup>2</sup> (MgB<sub>2</sub>-AA) at 5 K. This is relatively high considering the high residual Mg content. The good microstructural and superconducting properties of bulk MgB<sub>2</sub> fabricated by the infiltration and growth process are attributed to the presence of dense, fine grains and a pore free MgB<sub>2</sub> bulk microstructure. An upper critical field of 17 T has been observed for this

sample, which is close to a single crystal value and which indicates that the bulk material is operating in the clean pairing limit for superconductivity. Finally, HCC boron was selected as source of boron for future studies, since MgB<sub>2</sub>-HCC showed greatest promise.

## Chapter 5. Fabrication of Homogeneous MgB<sub>2</sub>-IG Bulks

### 5.1 Introduction

Chapter 4 described Infiltration-Growth synthesis and the characterization of the resultant MgB<sub>2</sub> sample with various techniques. It was demonstrated that critical current density in IG samples is very high and comparable to the best of the samples fabricated elsewhere. For a bulk superconductor to be used in an engineering application, the macroscopic current flowing over a range of several centimetres is an important design parameter. Numerous reports in extant literature show a wide variation between locally measured  $J_c$  (typically 1mm) and  $J_c$  measured from relatively long range currents [230, 231]. This may arise from inhomogeneous microstructure and defects like porosities, micro-cracks, non-superconducting phases, texture etc., since probability of current obstruction, due to the aforementioned factors, increases with longer current path. Therefore, it is vital to understand defects and understand their impact on the overall superconducting properties of MgB<sub>2</sub>. This chapter identifies frequently occurring defects in the IG process and their impact on bulk superconducting properties.

### 5.2 Continuous Mg Channels: A Challenge

A large number of reports [159-163] indicate that all infiltration processes generate a considerable amount of residual Mg, up to 20%, in the fully processed sample microstructure. This is attributed primarily to 25% volume shrinkage in MgB<sub>2</sub> during the phase formation process. This makes way for the surrounding liquid Mg during the primary phase formation process, assuming that MgB<sub>2</sub> nucleates everywhere simultaneously in the precursor and that the sample doesn't shrink overall. Moreover, once complete Mg infiltration has occurred, Mg transport is governed by diffusion. Therefore the microstructure may contain unreacted Mg pockets as shown in figure 5.1. Such discrete residual Mg pockets may have a limited impact on superconducting properties, particularly  $J_c$ , of MgB<sub>2</sub>. In addition, MgB<sub>2</sub>-IG samples show a large number of continuous Mg channels. Few are of the order of several tens of micrometres (as shown in figure 4.5(d)) and many extend from the surface of bulk MgB<sub>2</sub> sample to its centre, as illustrated in figure 5.2(a). Giunchi *et al.* also observed the presence of residual Mg both in the form of discrete, fine inclusions between large MgB<sub>2</sub> particles and as thread-like structures (~20  $\mu\text{m}$  long) in individual MgB<sub>2</sub> particles in the Reactive Liquid Infiltration (RLI) process [161].

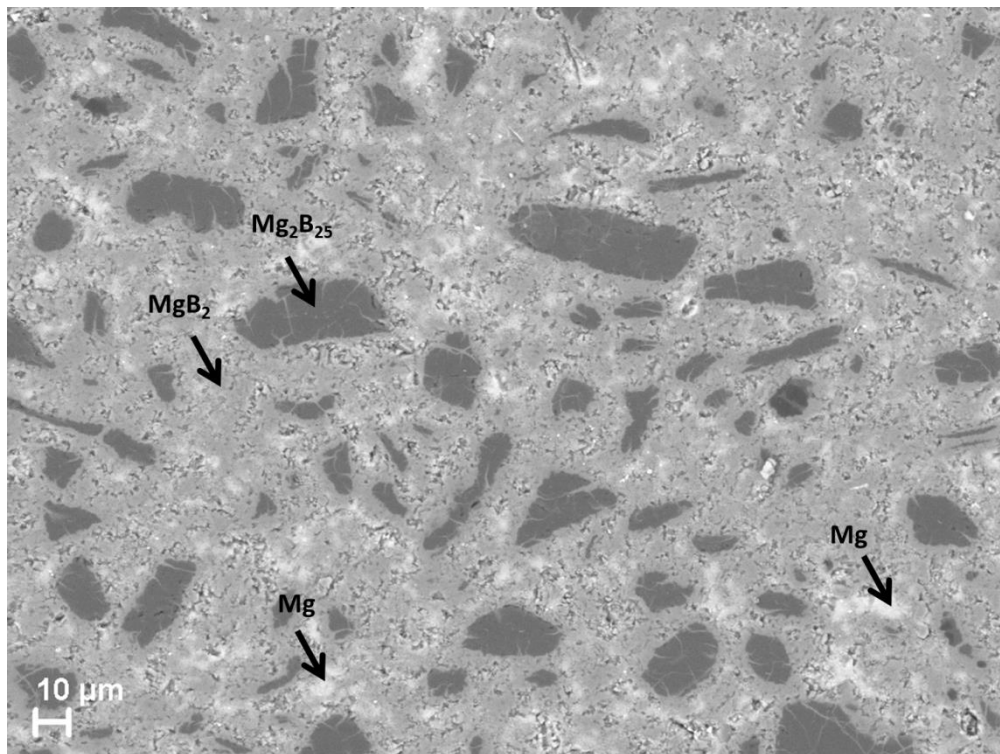


Figure 5.1 Residual Mg pockets in the final IG processed  $\text{MgB}_2$  microstructure as shown. Sample processed at 900°C, 4 h

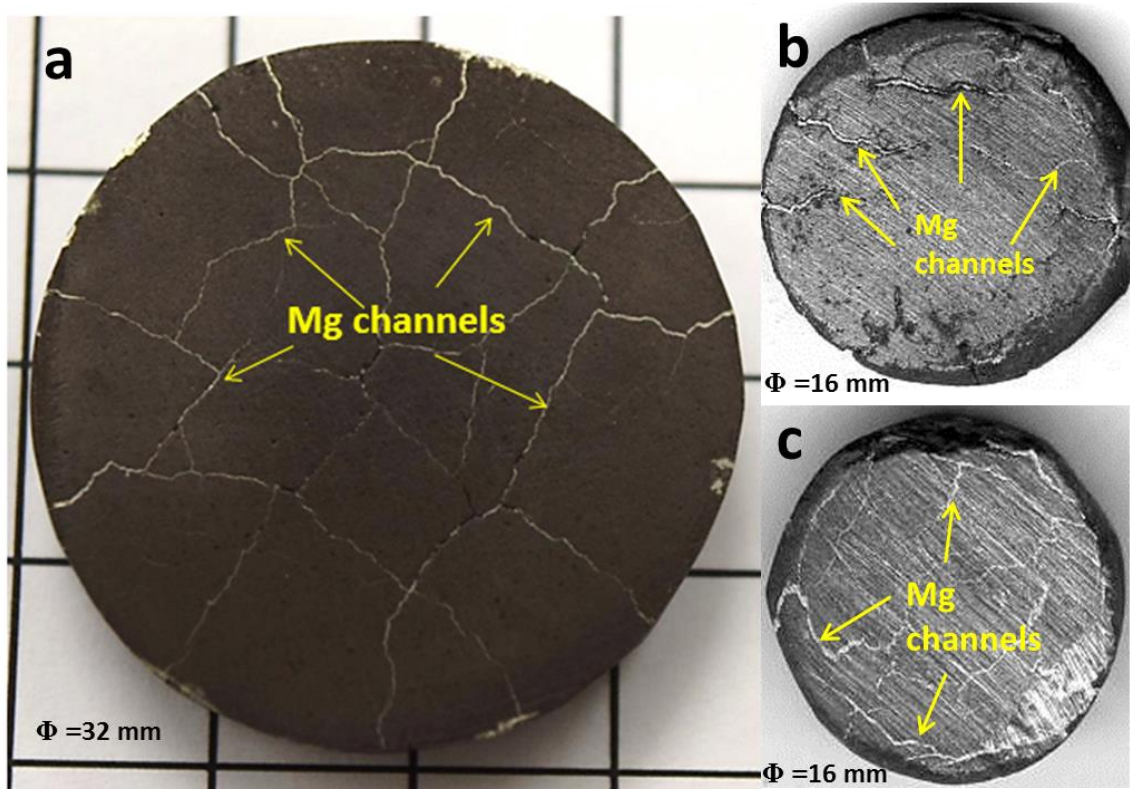
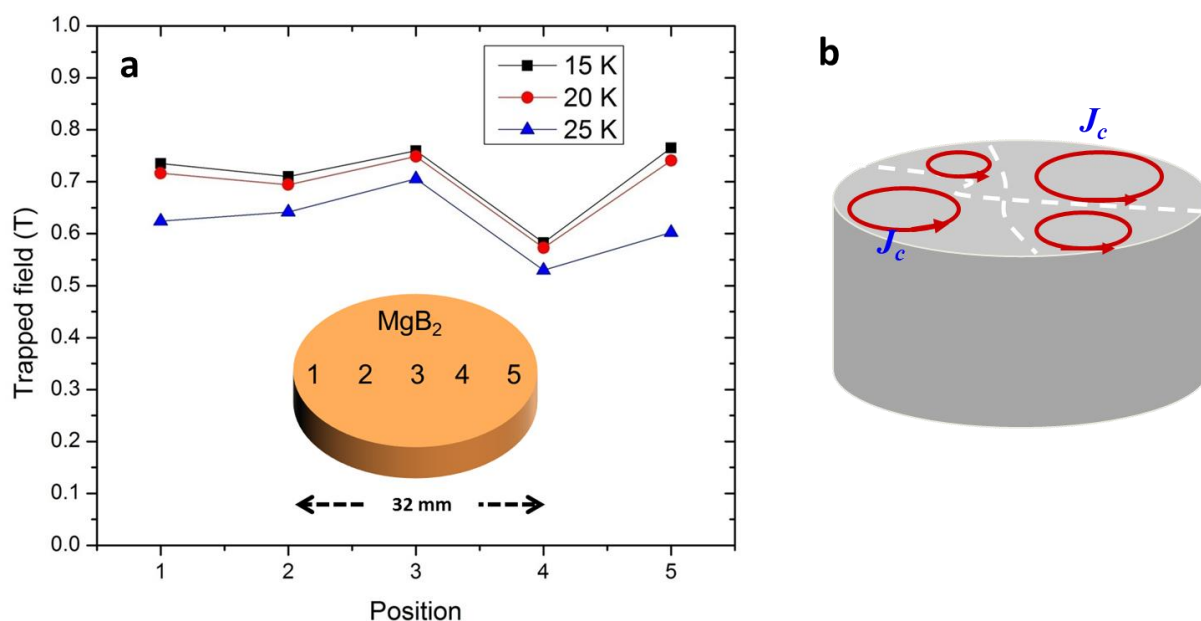


Figure 5.2 Continuous Mg channels in  $\text{MgB}_2$ -IG samples of various dimensions.

The formation of continuous Mg channels in IG processing are believed to form due primarily to poor wetting between B(s) and Mg(l), which is further accentuated by volume shrinkage (by up to 25%) that occurs as a consequence of reaction (I) and hydrostatic pressure exerted by the Mg(l) column on to the precursor during the infiltration process.

The trapped field of bulk superconductor with such Mg channels can be severely compromised despite superior local properties. This is due to the impediment of concentric current loops, which form in the superconductor, caused by these non-superconducting Mg channels. It is apparent, therefore, that the presence of residual Mg, especially in the form of continuous channels, may have an adverse effect on the trapped field performance of MgB<sub>2</sub> bulk superconductors fabricated by an infiltration and growth process. Figure 5.3(a) shows trapped field measured on a bulk containing Mg channels. The trapped field measured along the diameter of sample is nearly constant, while Biot-Savart law suggests a conical profile is expected in a homogeneous cylindrical sample. Such a profile is the direct consequence of multiple non-concentric loops operating within the sample due to impediment from continuous non-superconducting Mg (Figure 5.3(b)).



**Figure 5.3(a)** Trapped field measured as a function of locations along the diameter as shown in inset and **(b)** schematic illustration of multiple non-concentric current loops that result in such a trapped field profile. The sample was processed at 850°C, 4 h.

In RLI processed samples, Naito *et al.* suggested casing the precursor with a stainless steel to curb any expansion of sample in the radial direction [232]. This approach ameliorated the problem of continuous unreacted Mg in the bulk. This chapter attempts at limiting the

formation of residual continuous Mg channels through the incorporation of various powders as wetting enhancers (namely Mg, AlB<sub>2</sub> and MgB<sub>2</sub>), thereby enabling fabrication of large and complex shaped MgB<sub>2</sub> bulk superconductors. The idea behind incorporation of Mg/AlB<sub>2</sub>/MgB<sub>2</sub> into the precursor is to enhance the overall wettability with Mg(l), which ensured a uniform influx of Mg(l) into the porous preform. Moreover, the mixing Mg/AlB<sub>2</sub>/MgB<sub>2</sub> powder with B in the precursor is observed to provide sufficient strength to withstand the compressive hydraulic stresses exerted by the Mg liquid. Also, the presence of a wetting enhancer in the precursor pellet allows the precursor powder to be packed under higher uniaxial load, which directly benefits sintering and can potentially result in high density of the processed sample. Finally, the trapped field measurements were performed to demonstrate the ability to generate high magnetic fields in the samples that are free from Mg channels.

### 5.3 Mg addition

The effect of Mg addition on the formation of continuous Mg channels was investigated by preparing a precursor (100- $x$ )% B +  $x$ % Mg (weight %), hereafter written as B- $x$ % Mg, containing Mg powder levels of  $x = 10, 20$  and  $30$  (wt.) and subjecting these to Mg(l) infiltration at  $850\text{ }^{\circ}\text{C}$ ,  $4\text{ h}$ . Mg powder,  $99.8\%$  pure, was sourced from Alpha Aesar with particle size of  $-325$  mesh. Mg is probably the ideal candidate to act as wetting enhancer in an infiltration process involving liquid Mg. When a composite precursor containing B + Mg powder mixture is introduced into the Mg melt, Mg particles in the precursor melt and form multiple pathways that facilitate the influx of Mg, as schematically illustrated in figure 5.4(a). The proposed mechanism of Mg infiltration with AlB<sub>2</sub> and MgB<sub>2</sub> powder addition is also depicted in figure 5.4(b) and (c). Many studies have been conducted which studied MgB<sub>2</sub> formation with excess Mg addition. However unlike in this study, the objective there has been to explore the possibility of forming Mg<sub>1+ $\delta$</sub> B<sub>2</sub> type compound that may have superior superconducting properties or to compensate for volatility of Mg and thereby encourage sintering [188, 189, 233].

Figure 5.5(a), (b) and (c) show  $M-T$  plots,  $J_c-B$  plots and XRD patterns respectively for samples with nominal Mg additions up to  $30\%$ . Figure 5.5(d) shows homogeneous MgB<sub>2</sub> bulk obtained using  $x = 20$  Mg addition although several Mg channels can still be seen. This suggests that enrichment of Mg in the precursor has enabled uniform Mg(l) infiltration which has significantly minimized continuous Mg channels. Mg addition, up to  $x = 30$ , resulted in



drop in  $T_c$  by 2 K while the superconducting transition still remaining sharp, as seen from figure 5.5(a).  $J_c$  however, suffered from 380  $\text{kA/cm}^2$  for undoped sample to 270, 240, 160  $\text{kA/cm}^2$  for  $x = 10, 20$  and  $30$  respectively. Such degradation of the superconducting properties can be explained by high Mg content in the microstructure and presence of considerable  $\text{MgO}$ , as seen from XRD patterns in figure 5.5(c).

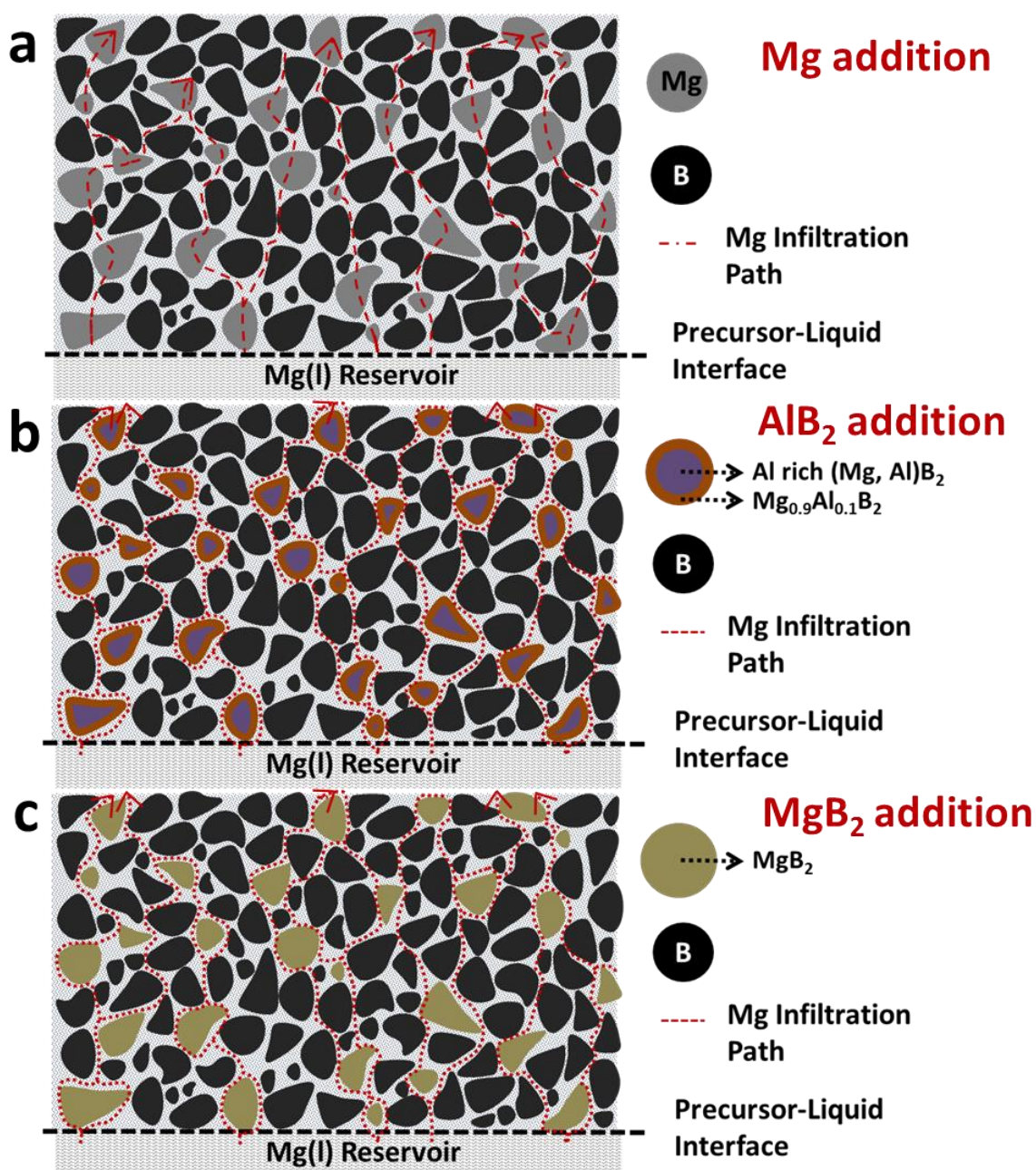


Figure 5.4 Schematically illustrating infiltration of liquid Mg facilitated by 5.4(a) Mg (b)  $\text{AlB}_2$  and (c)  $\text{MgB}_2$  respectively.

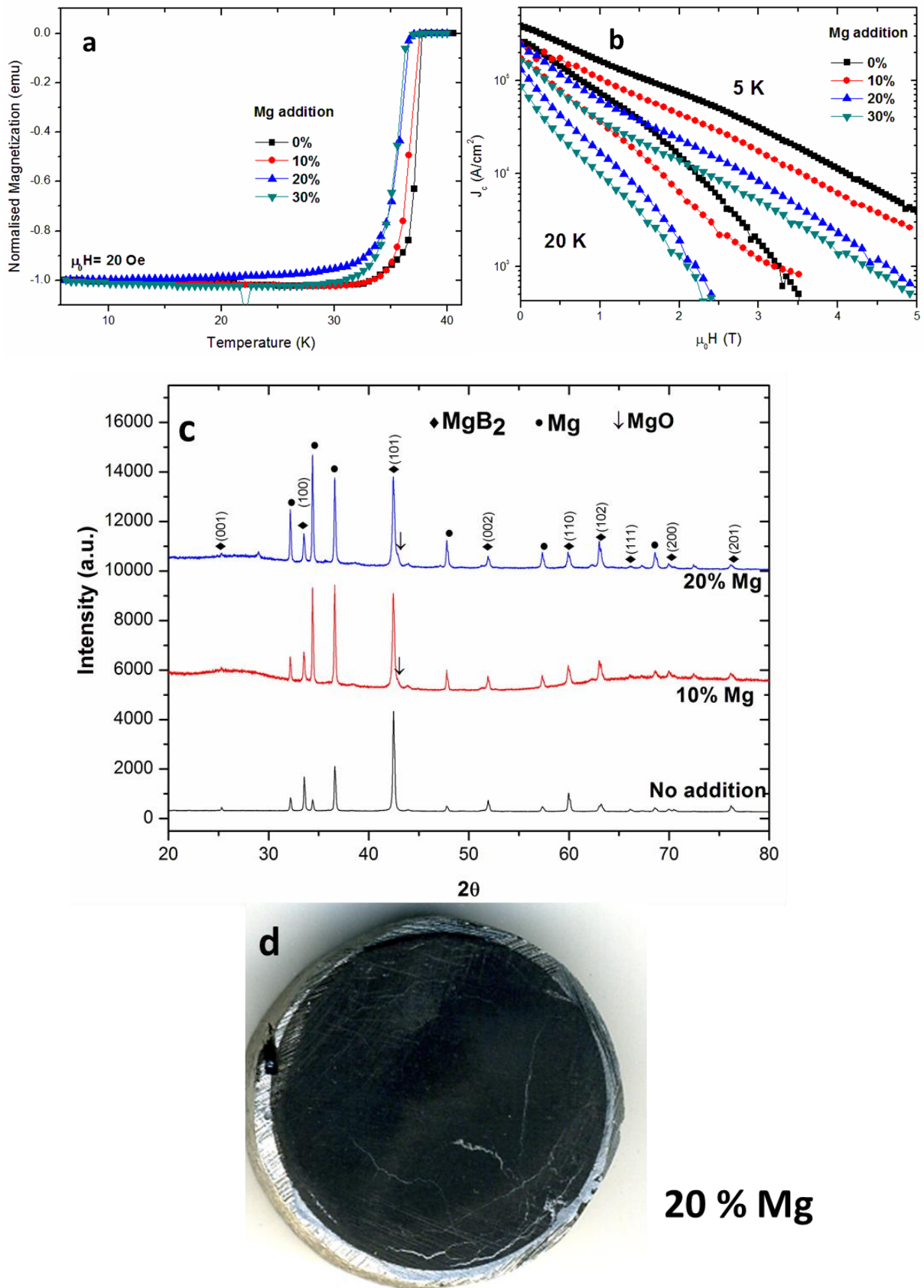


Figure 5.5(a) Normalised magnetization-temperature plots (b)  $J_c$  as a function of external field and (c) XRD patterns for samples with varying nominal Mg addition. Figure (d) showing images of sample with 20% Mg addition with fewer Mg channels.

#### 5.4 AlB<sub>2</sub> addition: Reactive wetting

Effect of AlB<sub>2</sub> addition on the formation of continuous Mg channels was investigated by preparing a composite precursor containing AlB<sub>2</sub> powder to levels of  $x = 2.5, 5, 7.5, 10$  and  $20$  (wt.) and subjecting those to Mg(l) infiltration at  $850\text{ }^\circ\text{C}$ ,  $4\text{ h}$ . The current work, as is discussed below, showed that reaction of AlB<sub>2</sub> with Mg results in Mg substitution on Al sites in AlB<sub>2</sub>. Such reaction allows AlB<sub>2</sub> to be ‘reactively wetted’ by Mg(l) and for the same reason AlB<sub>2</sub> was chosen as a candidate for ‘wetting enhancer’. AlB<sub>2</sub> is well characterized boride and commonly observed as a precipitate in Al and Mg alloys grain refiners [234] or as ceramic reinforcement in Al/Mg matrix composites [235]. Results show bulk diffusion of Mg to occur into AlB<sub>2</sub> particles to an extent that 98% of Al sites are substituted by Mg. This is somewhat unusual considering such displacement reaction is rare in rather stable borides. A study by Calderon *et al* indicated diffusion of Mg in AlB<sub>2</sub> particle [235]. A similar displacement of Mg in MgB<sub>2</sub> by Ti is reported by Wilson *et al*, where Ti-4MgB<sub>2</sub> powders are high energy ball milled to  $\sim 20\text{ nm}$  and then subject to heat treatment [236]. In order to analyse the interactions between Mg and AlB<sub>2</sub>, a precursor pressed from AlB<sub>2</sub> was infiltrated with Mg(l) using exact same procedure as in typical IG process as described in ‘Chapter 3: Methodology’. AlB<sub>2</sub> powder, 99% pure, was sourced from Sigma Aldrich with particle size of -325 mesh. Five such samples were prepared by reaction at constant temperature of  $700\text{ }^\circ\text{C}$  for soaking time of  $1, 2, 3, 4$  and  $6\text{ h}$ . Two more samples were prepared by infiltrating AlB<sub>2</sub> precursor at  $750\text{ }^\circ\text{C}$  and  $900\text{ }^\circ\text{C}$  for  $4\text{ h}$ . The reaction of AlB<sub>2</sub> with Mg is studied with use of XRD, SEM and EDS analysis. The obtained samples were further characterized with  $M-T$  and  $J_c-B$  measurements. Trapped field measurements were also performed on such sample with Dia  $16\text{ mm}$ . Finally, the effect of varying the amount of AlB<sub>2</sub> addition on superconducting properties, mainly  $J_c$ , is studied.

##### 5.4.1 Interactions between Mg and AlB<sub>2</sub>

A typical sample ( $16\text{ mm Dia}$ ) obtained by infiltrating a precursor prepared from AlB<sub>2</sub> with Mg(l) is shown in figure 5.9(a) inset. Almost negligible change in the dimensions of the fully processed samples was observed with respect to the pressed precursor pellets, although Mg substitution on Al should result in expansion of  $a$  and  $c$  axes. More importantly, no continuous Mg channels were observed in these samples unlike ones shown in figure 5.2. This is achieved by virtue of ‘reactive wetting’ of AlB<sub>2</sub> particles by liquid Mg, as will be

shown in the following section. This unique feature enables homogeneous infiltration of Mg(l) in the preform, as schematically shown in figure 5.4(b).

### 5.4.1.1 XRD analysis

XRD patterns for four samples reacted at varying temperature along with AIB<sub>2</sub> and MgB<sub>2</sub>

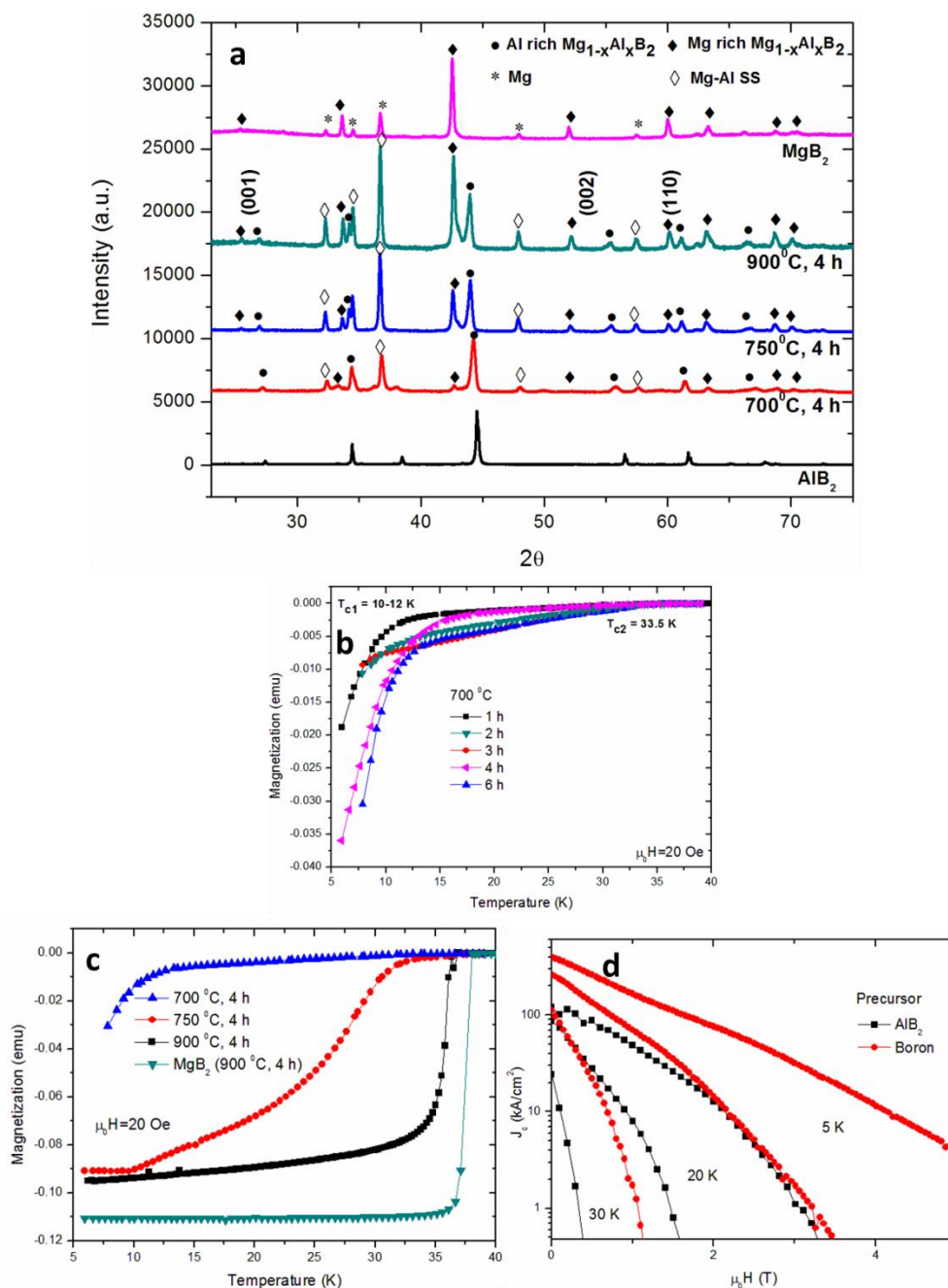


Figure 5.6(a) and (b) showing  $M$ - $T$  plots and XRD patterns respectively for AIB<sub>2</sub> precursor reacted at 700 °C, 750 °C and 900 °C. Data for AIB<sub>2</sub> and MgB<sub>2</sub> also shown for comparison in (c) Magnetization vs temperature plots for AIB<sub>2</sub> precursor infiltrated with Mg(l) at constant temperature and varying soaking time. (d) Comparing  $J_c$ - $B$  (5, 20 and 30 K) for B and AIB<sub>2</sub> precursor infiltrated with Mg(l) at 900°C for 4 h.

powder are shown in figure 5.6(a). All the samples show two separate AlB<sub>2</sub> type structures (with distinct  $a$  and  $c$ ) and Mg-Al solid solution following infiltration. This suggests that Al sites in AlB<sub>2</sub> are partially substituted by Mg and two distinct Mg<sub>1-x<sub>i</sub></sub>Al<sub>x<sub>i</sub></sub>B<sub>2</sub> type phases form with two distinct  $x_i$  values. Interestingly, both these phases become richer in Mg with enlarged  $a$  and  $c$  axes, which is consistent with many other reports on Al doping in MgB<sub>2</sub>, with increased temperature as evident by steady peak shifts to lower angle [101, 110, 237-240]. However, the shift is more subtle in (110) reflections owing to the rigid B-B in-plane bonds. Also, relative amount of Mg rich Mg<sub>1-x<sub>i</sub></sub>Al<sub>x<sub>i</sub></sub>B<sub>2</sub> ternary phase increases with reaction temperature. This is attributed to higher diffusivities of Al and Mg as a result of increased temperature. Displaced Al atoms from AlB<sub>2</sub> particles appear to dissolve in the surrounding liquid Mg during the progress of reaction as shown by Mg-Al solid solution peaks in XRD pattern.

#### 5.4.1.2 Magnetization Measurements

Figure 5.6(b) shows the dependence of the zero field cooled magnetic moment with temperature for the AlB<sub>2</sub> sample reacted at 700 °C for varying soaking times. Almost all samples showed a step in the  $M$ - $T$  curve at  $\sim 11.5$  K. It appears that the diamagnetic contribution has come from two types of Mg<sub>1-x<sub>i</sub></sub>Al<sub>x<sub>i</sub></sub>B<sub>2</sub> phases, each with distinct  $x_i$ . Phase-1 loses superconductivity at 11.5 K after which contribution comes only from the other Phase-2. Thus in all the samples  $T_c$  onset remained almost unchanged. Such a step was not observed in samples reacted at higher reaction temperature (Figure 5.6(c)). This is probably due to the relatively large fraction of Phase-2 (Figure 5.6(a)) present in such samples, which can carry all the screening current, unlike the 700 °C reacted sample. The sample reacted at 900 °C, 4 h showed a relatively sharp superconducting transition at 36.6 K. Comparing  $M$ - $T$  (Figure 5.6(b) and (c)) data obtained for these samples with Mg<sub>1-x<sub>i</sub></sub>Al<sub>x<sub>i</sub></sub>B<sub>2</sub> single crystals available in literature suggests  $x$  is  $\sim 0.3$  (Phase-1) and 0.02 (Phase-2) for Mg poor and Mg rich Mg<sub>1-x<sub>i</sub></sub>Al<sub>x<sub>i</sub></sub>B<sub>2</sub> respectively [102, 103, 241]. Both the phases, can therefore be viewed as Al substituted MgB<sub>2</sub>. The reduced  $T_c$  (Figure 5.6(c)) is due to the electron addition to the structure with Al substitution on Mg.

#### 5.4.1.3 $J_c$

$J_c$  vs.  $B$  plots for infiltrated AlB<sub>2</sub> samples is shown in figure 5.6(d). The self-field  $J_c$  of 120, 80 and 25 kA/cm<sup>2</sup> was obtained in these samples, at 5, 20 and 30 K respectively. It is noted

that both types of  $\text{Mg}_{1-x}\text{Al}_x\text{B}_2$  phases contribute to  $J_c$  at 5 K whereas only Mg rich  $\text{Mg}_{1-x}\text{Al}_x\text{B}_2$  phase contributes to  $J_c$  at 20 and 30 K. The  $H_{irr}$  is reduced relative to  $\text{MgB}_2$ -IG due to reduction of  $H_{c2}$  in  $a$ - $b$  direction upon Al doping.

#### 5.4.1.4 SEM and EDS

SEM images and phase maps for sample reacted at 900 °C, 4 h are shown in figure 5.7 Phase map (Figure 5.7(c)) on relatively large particles shows concentric shells of  $\text{Mg}_{0.98}\text{Al}_{0.02}\text{B}_2$  on

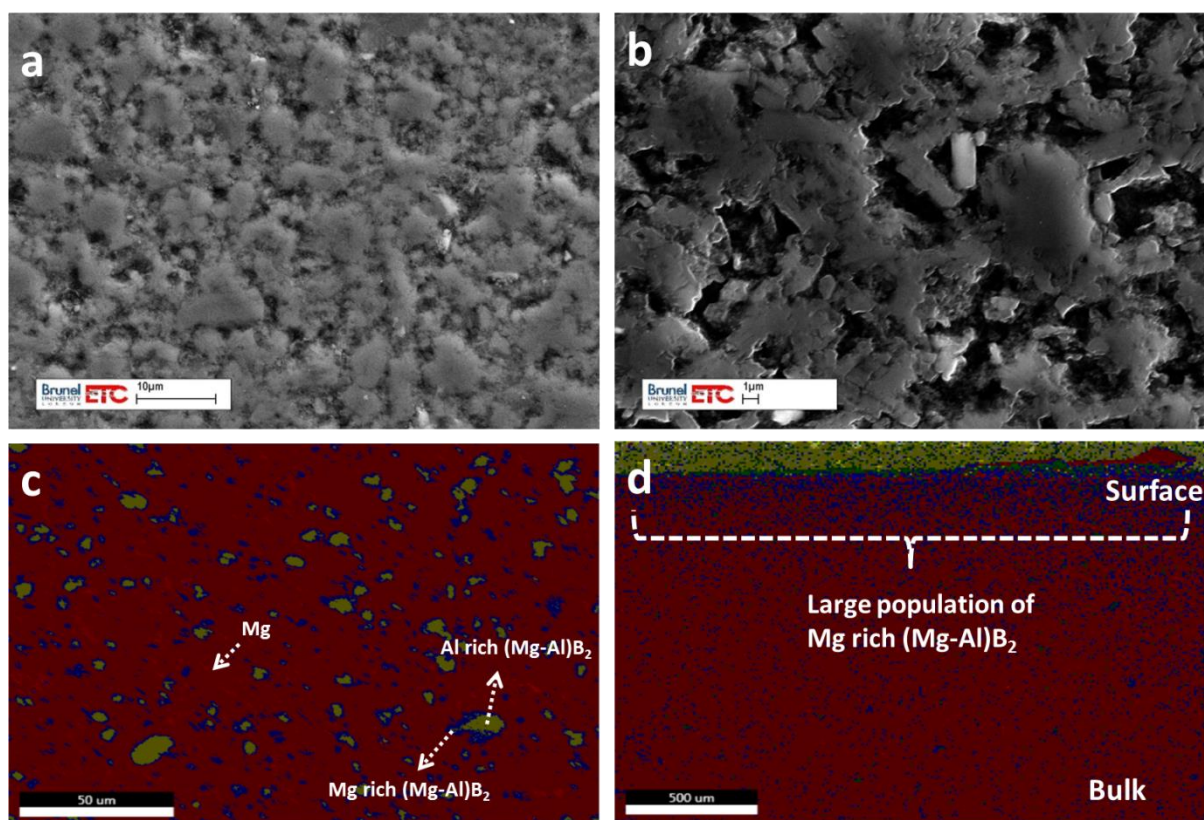
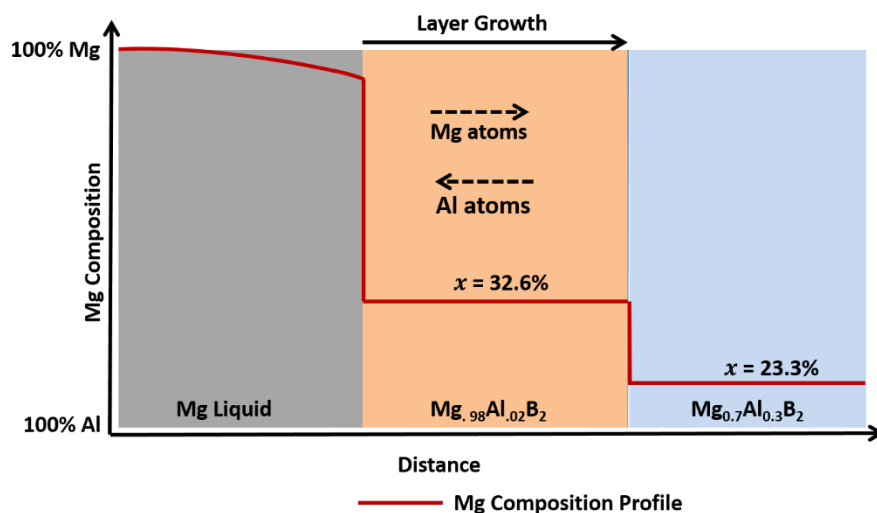


Figure 5.7(a) and (b) SEM images of polished surface of  $\text{AlB}_2$  precursor reacted at 900 °C, 4 h. (c) Mg and Al EDS maps superimposed on one another. A shell like structure is seen in all the particles, indicative of clear difference in Mg concentration. (d) EDS map on the cross section of reacted sample showing large fraction of  $(\text{Mg}, \text{Al})\text{B}_2$  phase near the surface and reducing towards the centre.

the inner core of Al rich  $\text{Mg}_{0.7}\text{Al}_{0.3}\text{B}_2$ . The expected Mg concentration gradient within such particles is schematically shown in figure 5.8. The Mg rich shell of  $\text{Mg}_{1-x}\text{Al}_x\text{B}_2$  grows inward with the progress of reaction which is primarily controlled by counter-diffusion of Al and Mg. The ‘shell like’ structure could not be observed in smaller particles, since the shell thickness is probably less than resolution of EDX. Therefore all such particles have been incorrectly identified by EDX as Mg. It is rather interesting to note such dual phase distribution within a particle with distinct contrast between Mg and Al rich regions while

steady state diffusion would suggest a linear decrease in concentration from surface to centre of grain. Figure 5.7(d) shows EDS map for Mg on cross-section of same sample. A large fraction of  $\text{Mg}_{0.98}\text{Al}_{0.02}\text{B}_2$  phase can be seen in top 100  $\mu\text{m}$  layer on the surface of sample, which is clearly due to the higher concentration of Mg near the surface.



**Figure 5.8** Schematic of expected Mg concentration within an  $\text{AlB}_2$  particle (surface to centre) during the reaction with Mg.

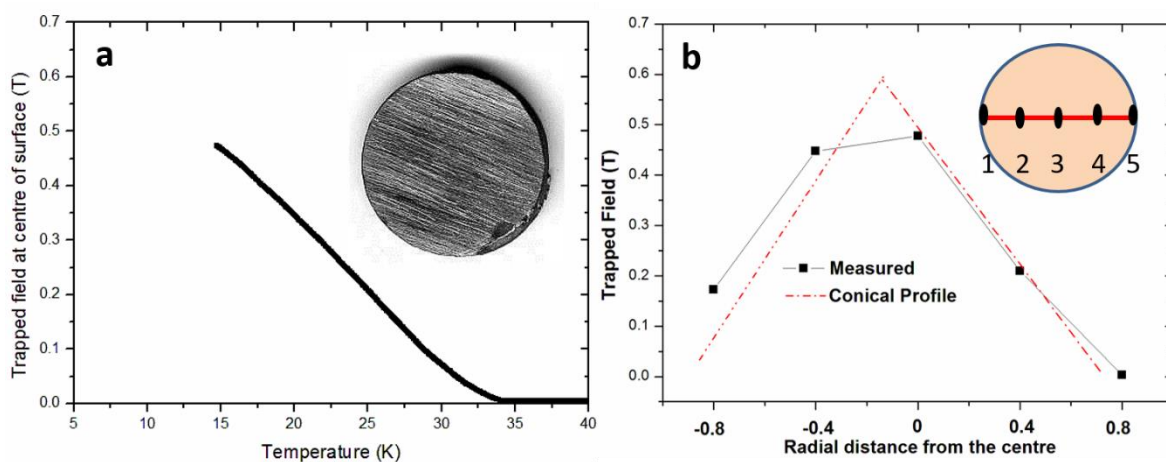


**Figure 5.9**(a) Variation of trapped field with temperature measured at the centre of surface and (b) Variation of magnetic flux density along the diameter for sample obtained by infiltrating  $\text{AlB}_2$  precursor with  $\text{Mg}(\text{l})$  at  $900\text{ }^\circ\text{C}$ , 4 h. The 16 mm Dia sample and location of hall sensors in (a) and (b) insets.

#### 5.4.1.5 Trapped Field

The trapped field measured at the centre of surface of  $900\text{ }^\circ\text{C}$ , 4 h reacted sample is shown in figure 5.9(a). The trapped field increased almost linearly with a drop in temperature and a maximum of 0.48 T was measured at 15 K at the centre of surface. Furthermore, the measured magnetic flux density along the diameter of surface of sample followed a near-conical profile, which is indicative of long range concurrent current loops along the axis

passing through centre of sample (Figure 5.9(b)). Biot-Savart law suggests a current of 10000 A/cm<sup>2</sup> must flow to generate such magnetic field. This value is appreciably high considering that the contribution, presumably, comes from only Mg<sub>0.98</sub>Al<sub>0.02</sub>B<sub>2</sub> phase. Also, this value suggests that Mg rich Mg<sub>1-xi</sub>Al<sub>xi</sub>B<sub>2</sub> phase is well connected in the bulk of the sample, as it forms selectively at the outer cores of particle.

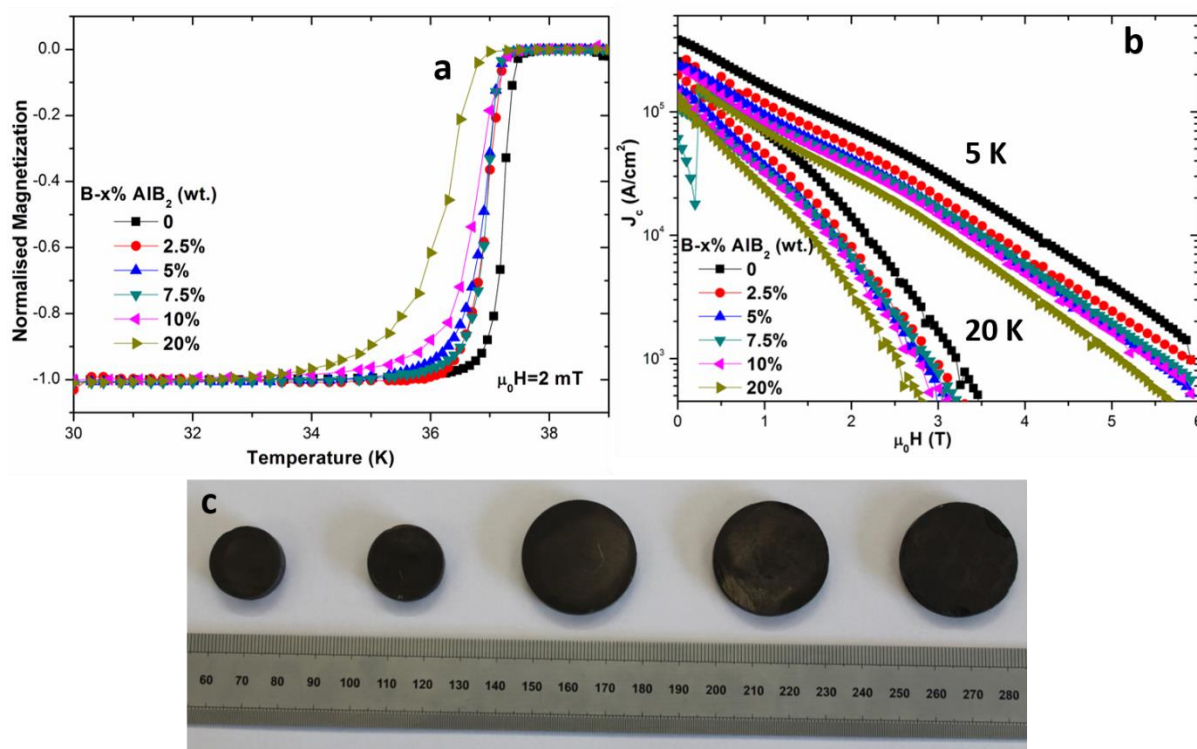


Figure 5.10(a) Magnetization response with respect to temperature under external field of 2 mT and (b)  $J_c$  (5, 20 K) as a function of external field for AlB<sub>2</sub> addition up to  $x=20\%$ . (c) Variety of homogeneous MgB<sub>2</sub> bulks fabricated by AlB<sub>2</sub> enrichment of 20%.

#### 5.4.2 B+AlB<sub>2</sub> Composite precursor

Normalised magnetization as a function of temperature and  $J_c$ - $B$  plots are shown in figure 5.10(a) and (b) for samples with nominal AlB<sub>2</sub> additions up to  $x=20$ . Figure 5.10(c) shows a number of homogeneous MgB<sub>2</sub> bulks of different dimensions obtained by infiltrating a precursor prepared by mixing B and AlB<sub>2</sub> powder in weight ratio 80:20. This clearly demonstrates that improved wetting of Mg with AlB<sub>2</sub> enables fabrication of near-net-shaped samples without any defects such as Mg-channels or cracks. The  $T_c$  reduced to 36.8 K in the sample with AlB<sub>2</sub> addition of  $x=20$  from 37.8 K ( $x=0$ ), while self-field  $J_c$  (5 K) degraded to 50% in comparison to sample with  $x=0$ .



### 5.5 MgB<sub>2</sub> addition

The effect of enriching B powder with MgB<sub>2</sub> prior to processing has been reported by Iwayama *et al.* [242] an *in situ* sintering study. This approach is known to suppress the formation of voids

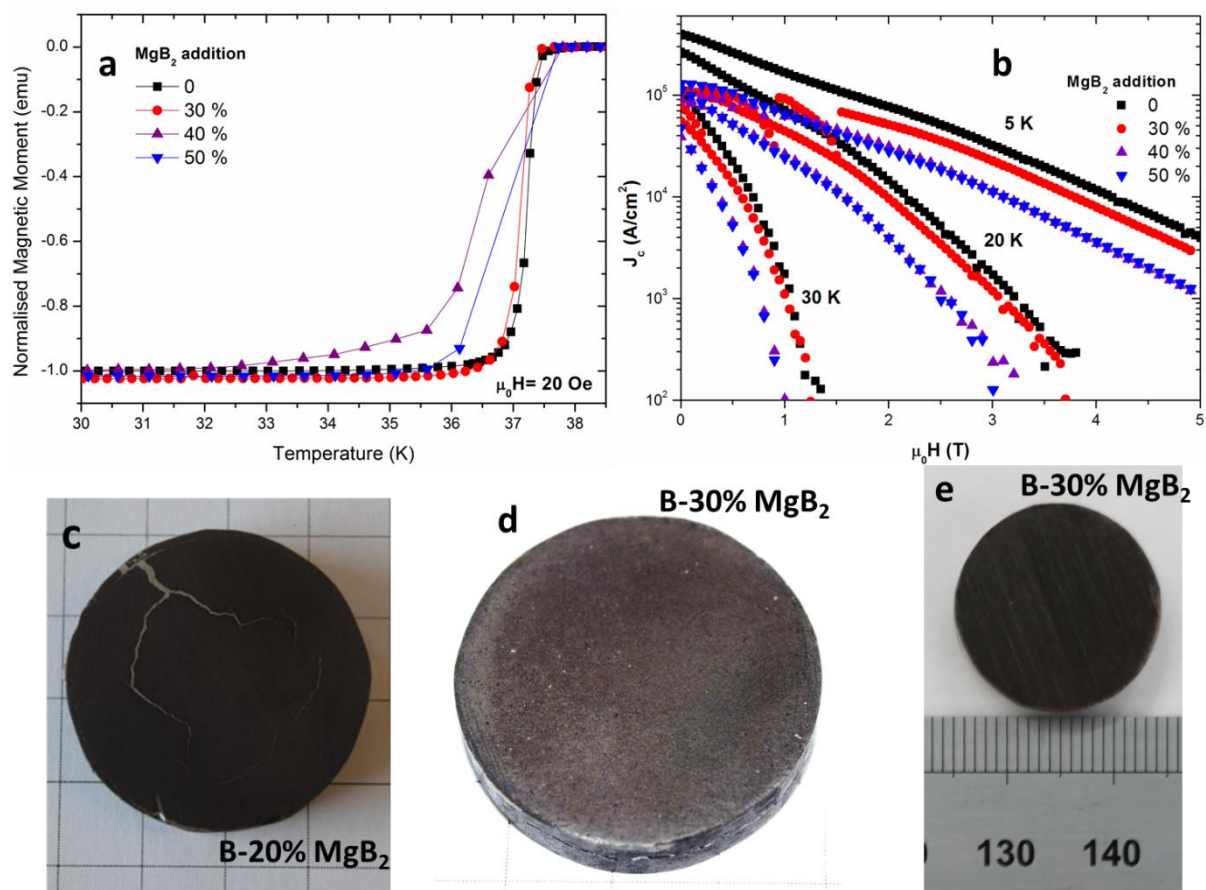


**Figure 5.11**(a) Magnetization as a function of temperature under external field of 2mT and (b)  $J_c$  as a function of external field for varying MgB<sub>2</sub> addition up to  $x=50$ . Image of MgB<sub>2</sub> samples with 32 mm Dia prepared with MgB<sub>2</sub> powder additions of (c)  $x=20$ , (d)  $x=30$  and (e)  $x=30$ .

and cracks that form during the process, as a result of low and inhomogeneous filling density of boron powder [137, 242, 243]. In this study, the MgB<sub>2</sub> addition was primarily made primarily to allow uniform Mg(l) infiltration as described in and schematically represented in figure 5.4(c).  $M-T$  and  $J_c-B$  plots are shown in figure 5.11(a) and (b) for samples with nominal MgB<sub>2</sub> additions of  $x=30$ , 40 and 50. Figure 5.11(c), (d) and (e) show MgB<sub>2</sub> bulks obtained by infiltrating a composite precursor prepared by mixing B and MgB<sub>2</sub> powder. Mg powder, 99% pure, was sourced from Pavezyum with a particle size of -325 mesh. The sample with  $x=20\%$  showed one large Mg-channel, or possibly a large crack in the sample, although the number of Mg-channels was considerably reduced. Subsequent higher additions

( $x=30$ ) yielded highly uniform MgB<sub>2</sub> bulks without the formation of large defects, clearly demonstrating the advantages offered by the enrichment of MgB<sub>2</sub>. The  $T_c$  onset remained nearly constant (Figure 5.11(b)) with a gradual decrease in  $T_c$  (offset) with MgB<sub>2</sub> addition of up to  $x=50\%$ . The sample with  $x=30$  maintained reasonably high self-field  $J_c$  (250 kA/cm<sup>2</sup> at 5 K), which degraded with further addition. (Further discussion on  $J_c$  in section 5.5.2).

### 5.5.1 Scanning Electron Microscopy

Figures 5.12(a-d) show the SEM images of the polished surfaces of MgB<sub>2</sub> bulk samples fabricated by the MPIG process. Figure 5.12(a), (b) and (d) show the presence of two types of

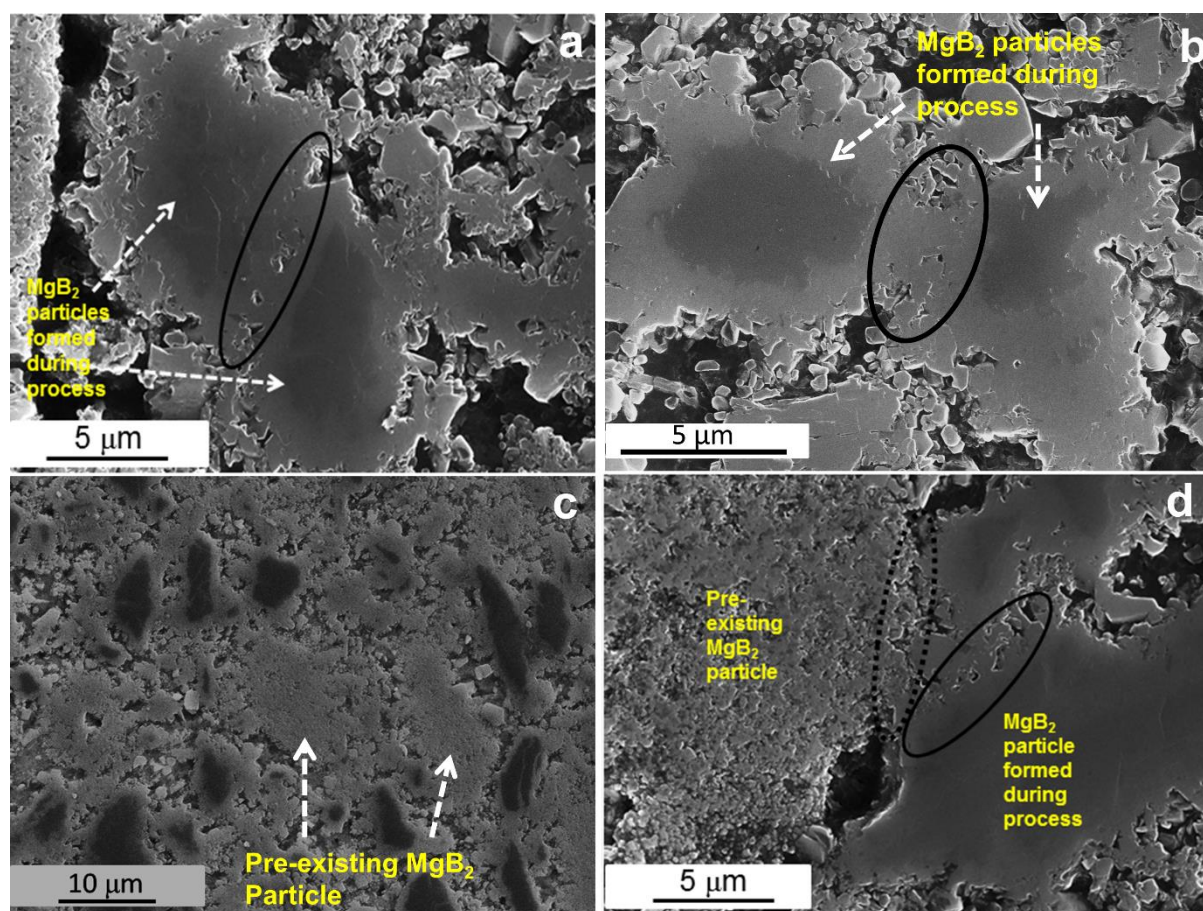


Figure 5.12 Secondary electron images showing different regions of the polished surface of MPIG processed bulk MgB<sub>2</sub> sample. Continuous contours (in (a), (b) and (d)) indicate significant sintering between newly formed MgB<sub>2</sub> particles while dotted contours (b) show little inter-particle coupling between pre-existing MgB<sub>2</sub> particle with other particles. (c) Distinguishes pre-existing MgB<sub>2</sub> particles from the ones formed during processing.

MgB<sub>2</sub> particles. One with a smooth surface and dark inner core and other that appears rough and bright. The particles with a dark-in-contrast boron rich, inner core comprise of a B-rich intermediate (Mg<sub>2</sub>B<sub>25</sub>) phase [169, 217-219]. Since Mg<sub>2</sub>B<sub>25</sub> is an intermediate phase formed during the reaction of crystalline B with Mg(l), it is plausible that these are formed during the

process, while the bright-in-contrast are pre-existing, unreacted MgB<sub>2</sub> particles. A lower magnification image of the same sample showing number of such particles is shown in figure 5.12(c).

When a boron particle undergoes a reaction to transform into MgB<sub>2</sub>, (i.e. 2 moles of B giving 1 mole of MgB<sub>2</sub>), the original B particle almost doubles in volume, due to an associated volume expansion ( $\text{MgB}_{2(\text{molar volume})}/2 * \text{B}_{(\text{molar volume})} \approx 2$ ). The growing MgB<sub>2</sub> particles then impinge upon each other and sinter simultaneously. This is evidenced by a large contact area between MgB<sub>2</sub> particles in the area shown by continuous contours in figures 5.12(a), (b) and (d). Similar features were also observed elsewhere in the microstructure. However, such a large contact area was not observed between newly formed MgB<sub>2</sub> and pre-existing powder particles (dotted contours in figure 5.12(b)). This could be due to the fact that newly formed MgB<sub>2</sub> surface is free from impurities and therefore likely to sinter readily, whereas nano-scale impurities such as MgO and BO<sub>x</sub> are more likely to be present on the surface of pre-existing MgB<sub>2</sub> particles [63].

As seen from figures 5.5, 5.9 and 5.10, all the additions to the precursor in the form of Mg/AlB<sub>2</sub>/MgB<sub>2</sub> ( $20 < x < 30$ ) successfully yielded large homogeneous bulk MgB<sub>2</sub> samples. Moreover, the reproducibility of MPIG technique was confirmed by synthesizing several bulk samples with identical experimental parameters and Mg/AlB<sub>2</sub>/MgB<sub>2</sub> powder addition. A comparison of  $M$ - $T$  and  $J_c$ - $B$  plots for samples fabricated with various powder additions indicates that MgB<sub>2</sub> enrichment showed greatest promise. Firstly, the MgB<sub>2</sub> addition did not cause any loss in  $T_c$ , unlike Mg and AlB<sub>2</sub> addition. This is crucial considering that lower  $T_c$  is likely to result in inferior  $J_c$  at ~20 K, a temperature easily attainable by cost effective cry-cooler. Moreover, MgB<sub>2</sub> addition showed highest self-field  $J_c$  of 250 kA/cm<sup>2</sup> at 5 K, as opposed to 180 kA/cm<sup>2</sup> (AlB<sub>2</sub>) and 220 kA/cm<sup>2</sup> (Mg) respectively. For these reasons, the technique of ‘MgB<sub>2</sub> addition’ is adopted in further work wherever long range (several cm) microstructure homogeneity is of primary importance, rather than local (1-2 mm) superior properties. The method of fabrication, based on a composite precursor containing boron and MgB<sub>2</sub> powder, is referred to subsequently as the *Modified Precursor Infiltration and Growth* (MPIG) method, whereas Infiltration and Growth (IG) is used to describe any method that uses a precursor pressed purely from boron powder. Sections 5.5.1 and 5.5.2 describe careful ‘SEM analysis’ and ‘Spatial variation in  $T_c$ / $J_c$ ’ in such sample ( $x=30$ ).

Finally, it is noted that contact angle measurements are important to establish wettability of ceramic particles (AlB<sub>2</sub>, MgB<sub>2</sub>) with liquid Mg, although experimental observations indicate the strong possibility of efficient wetting. Thus far, such measurements seem to be eluded owing to difficulties associated with oxidation tendency of Mg(l).

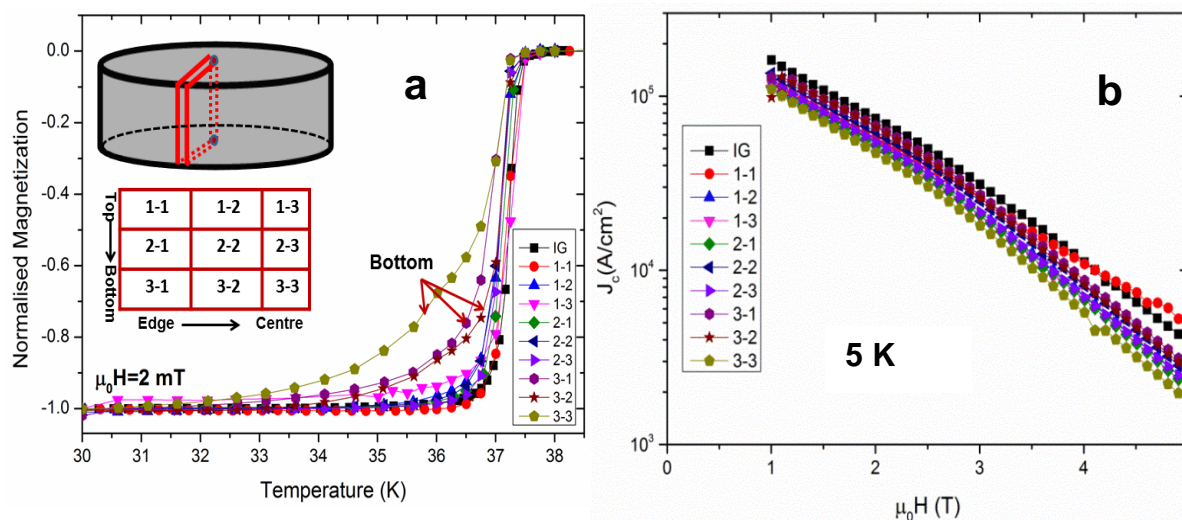


Figure 5.13(a) Normalised  $M-T$  and (b)  $J_c(B)$  (5 K) characteristics for nine samples cut from the locations in the parent bulk shown in the inset of (a) inset. The IG sample was cut from a location corresponding to 1-1, as shown in (a).

### 5.5.2 Spatial variation in MPIG samples

The uniformity of the superconducting properties throughout the volume of the MgB<sub>2</sub> cylinder, which is required to generate high trapped fields, was investigated by cutting nine, relatively large (4 mm x 3 mm x 2 mm) rectangular samples from various positions within the MPIG bulk. Figure 5.13(a) shows the normalized magnetization of these samples as a function of temperature, measured using a SQUID magnetometer. Typical magnetization data for IG-processed samples are also plotted for purposes of comparison. The measurements were made using a small, applied external magnetic field of 2 mT and normalized to the value at 30 K, with the position of the sample in the parent bulk indicated in the inset of figure 5.13(a). The IG processed sample exhibits a  $T_c$  of 37.50 K, whereas the samples cut from the MPIG bulk exhibit  $T_c$  that vary between 37.25 and 37.40 K. Also, samples cut from rows 1 and 2 of the parent MPIG bulk exhibit very similar  $M-T$  curves with a sharp transition, whereas all the samples from row three (bottom surface) exhibit relatively broader transitions. XRD analysis (not shown here) on MPIG bulk shows presence of MgB<sub>2</sub>, Mg and Mg<sub>2</sub>B<sub>25</sub> phases with similar phase fraction on both top and bottom surfaces. Such  $M-T$  behaviour could be due possibly to the fact that slightly denser MgB<sub>2</sub>, in comparison to

boron, tends to settle preferentially towards the bottom of the precursor powder prior to palletisation.

Figure 5.13(b) shows the dependence of external magnetic field on  $J_c$  for the MPIG specimens cut from the various sample locations. The geometrical location in the parent MPIG bulk sample appears to have little effect on  $J_c$ , which doesn't change appreciably across the volume of the bulk investigated. All the samples in MPIG bulk show  $J_c$  (5 K, 1 T) within the close range of  $\pm 10\%$  of average  $J_c$ . This doesn't correlate directly to broad transitions observed in some of the samples (Figure 5.13(a)). This is because, at lower temperatures (5 K in this case), difference in ratio  $T/T_c$  is small enough in each sample to leave  $J_c$  almost unaltered from sample to sample, according to following equation [244]

$$J_c = \alpha \left[ 1 - \left( \frac{T}{T_c} \right)^2 \right]^{1.5} \quad \alpha \text{ being } J_c \text{ extrapolated to 0 K} \quad (5.1)$$

MPIG and IG samples exhibit similar  $J_c(B)$  dependence up to  $\sim 3$  T, after which MPIG samples show a strong  $J_c(B)$  behaviour (except 1-1). Magneto optical studies on such *in situ* sintered bulks fabricated from pre-added MgB<sub>2</sub> powder by Polyanskii *et al.* reveal that MgB<sub>2</sub> particles in microstructure have lower  $J_c$  than surrounding matrix. Origins of low  $J_c$  are reported to be weaker connectivity and lower  $H_{c2}$  that results in poor flux pinning strength [243].

These findings are consistent with SEM observations (Figure 5.12) and  $J_c(B)$  data reported here, which shows reduced  $J_c$  in MPIG bulk sample compared to IG sample. This suggests that the inter-grain electrical coupling between newly-formed MgB<sub>2</sub> particles (from boron during the processing) and pre-existing MgB<sub>2</sub> particles in the MPIG process is probably inferior compared to the coupling between two newly-formed MgB<sub>2</sub> particles. These boundaries, therefore, probably form weak links at higher fields resulting in reduced  $J_c$ .

## 5.6 Fabrication of near-net complex shape

Complex ceramic structures are required in a variety of engineering applications e.g. heat engine components, recuperates, insulators, nozzles, metal matrix composites etc. This has been a challenge, unlike their metallic counterparts, where lower melting temperature and higher plasticity has a relatively easy fabrication of different shapes.

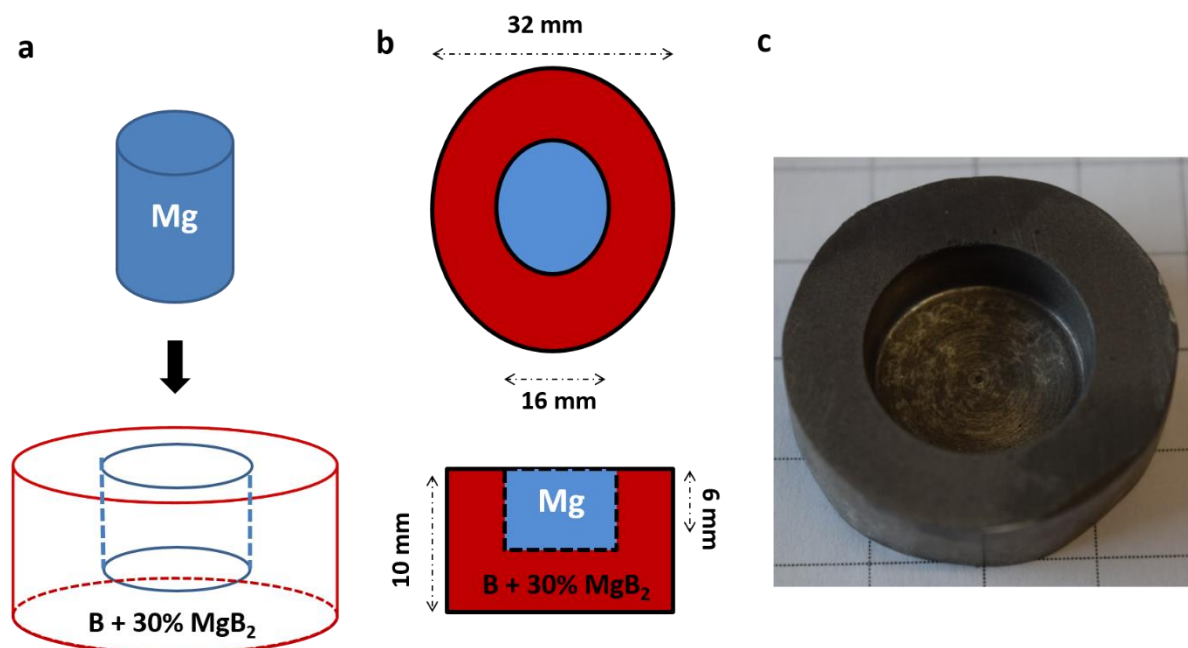


**Figure 5.14(a) and (b) Design of composite precursor containing Mg and  $(\text{B}+\text{MgB}_2)$ . (c) A closed-ended cavity. Mg in (a) and (b) melted away during infiltration giving a near-net-shape.**

The conventional method of producing such shapes can be described as ‘Reductive Manufacturing’- which is known as the physical removal of material by operations such as milling, grinding to obtain desired shapes. Therefore novel methods of ceramic fabrication like Infiltration or ‘Polymer Derived Ceramics’ have attracted considerable attention over last 3-4 decades [204-209]. The key step in both processes lies in preparing a ‘Preform’, which determines the final shape, followed by a heat treatment. On the other hand, reductive manufacturing not only results in loss of valuable material, but machining may also induce defects in the finished component, given the inherent brittleness in ceramics. This is particularly important keeping in view fabrication of superconducting radio frequency (RF) Cavity, where a very high surface finish is desired.

Here we demonstrate that the IG process could be adopted to produce a complex superconducting  $\text{MgB}_2$  RF cavity. At first, a Magnesium powder preform is prepared of 16 mm Dia and 5 mm thickness and this is later embedded with a larger preform of (Dia 32 mm and 10 mm thickness) coaxially as shown in figure 5.14(a) to obtain a configuration in figure 5.14(b). When such a complex precursor is infiltrated with  $\text{Mg(l)}$ , the Mg powder (blue regions) was melted away, thus generating a cavity as shown in figure 5.14(c). The as-processed cavity structure had slightly larger outer diameter of 33 mm, as opposed to

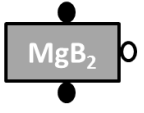
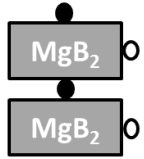
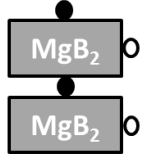
precursor diameter of 32 mm). No change in inner diameter and height was observed. A slight machining was required to obtain a smooth inner surface.

### 5.7 MgB<sub>2</sub>: Quasi-permanent Magnet

The ability of a type II bulk superconductor to trap magnetic field is a direct indication of the presence of strong flux pinning, and hence high critical current density,  $J_c$ , within the sample microstructure. In general, the magnitude of the field trapped by a bulk superconductor is determined by the product of the sample radius,  $r$ , and  $J_c$ , assuming that the current flows homogeneously throughout the volume of the sample. As a result, superconducting “permanent magnets” have the potential to generate magnetic fields that are significantly higher than conventional Nd-Fe-B magnets, which are limited generally to less than 1.5 T. MgB<sub>2</sub> superconductors have already been used to generate trapped fields of greater than 5 T. A significant increase in the trapped field has been reported recently for sintered MgB<sub>2</sub> bulk samples. Notably, Fuchs *et al.* and Yamamoto *et al.* reported high trapped fields of 5.4 T (12 K) and 3.72 T (5 K) respectively, in nano-crystalline MgB<sub>2</sub> samples [245, 246]. In addition, Yamamoto *et al.* reported a trapped field of 4 T at 10 K in an *in-situ* sintered MgB<sub>2</sub> sample and Naito *et al.* obtained 4.6 T in a Ti-doped MgB<sub>2</sub> bulk at 14 K [247, 248]. Finally, Durrell *et al.* reported 3 T at 17.5 K in a sintered, hot-uniaxially-pressed MgB<sub>2</sub> bulk sample fabricated by an *ex-situ* technique [249]. This recent data represents a significant improvement over the previous reports of the field trapping ability of MgB<sub>2</sub> of Vznichenko *et al.*, Murlidhar *et al.*, Naito *et al.*, Perini *et al.* and Giunchi *et al.* [250-253]. However these levels of field have not yet been realized in samples fabricated by an infiltration technique [254, 255], although samples processed by the infiltration route are denser and the local critical current density in samples fabricated by the two methods is comparable.

#### 5.7.1 Trapped Field Measurement

Three separate trapped field measurements were made, one on individual MgB<sub>2</sub> (A) bulk sample, second and third on a two-sample stack using bulks A-B and C-D respectively. A two-sample stack arrangement was made primarily to minimize the demagnetization effect, which is more severe in the case of a single bulk, whereas two measurements on two different MPIG bulks were performed (M-2 and M-3) in order to examine the reproducibility of the IG process. Table 1 describes the arrangement of hall and temperature sensors in each of the measurements.

Measurement	Arrangement of Hall Sensors and Temperature Sensors	Bulk
M-1		A
M-2		A B
M-3		C D

**Table 5.1** Arrangement of cylindrical  $\text{MgB}_2$  bulks and location of hall sensors (black circles) and temperature sensors (hollow circles) and  $\text{MgB}_2$  bulks used in each of the three measurements.

The Hall sensors were placed at the centre of the top and bottom surfaces of two individual bulk samples to enable the trapped field to be measured simultaneously in the initial two measurements. In the third measurement, one Hall probe was positioned at the centre of the top surface of the upper sample in a two sample stack, with the second probe used to measure the trapped field between the sample pair.

The measured trapped field as a function of temperature for a single bulk (M-1) and a stacked pair of MPIG processed bulk samples (M-2, M-3) are shown in figures 5.15(a), (b) and (c) respectively. A difference of less than 0.5% in the magnitude of the trapped field recorded at the top and bottom surface of the single bulk confirms its homogeneity, given that any cracks, porosity or non-superconducting regions would impede the flow of supercurrent throughout the volume of the bulk. These measurements are consistent with the narrow range of  $J_c$  (Figure 5.13(b)) observed in the MPIG bulk. Although sample 3-3 (centre of bottom surface, Figure 5.13(a)) shows broad transition and low  $J_c$  amongst all samples, it is not likely to alter trapped field performance of the MPIG bulk greatly. This is because the trapped field in the bulk is mainly governed by the low field  $J_c$  in the outer regions of the bulk, as the current loop is largest. Recently, numerical simulations, based on a novel  $2D$  axisymmetric  $\mathbf{H}$ -formulation, have been performed for a single MPIG bulk sample using  $J_c(B)$  of single sub-



specimen as an input for the model [256]. The model assumed, essentially, that the  $J_c(B)$  characteristics of the small specimen extended over the entire volume of the bulk sample. The results of the simulation reproduced the experimental results extremely well, confirming the homogeneity of the samples fabricated by the MPIG technique.

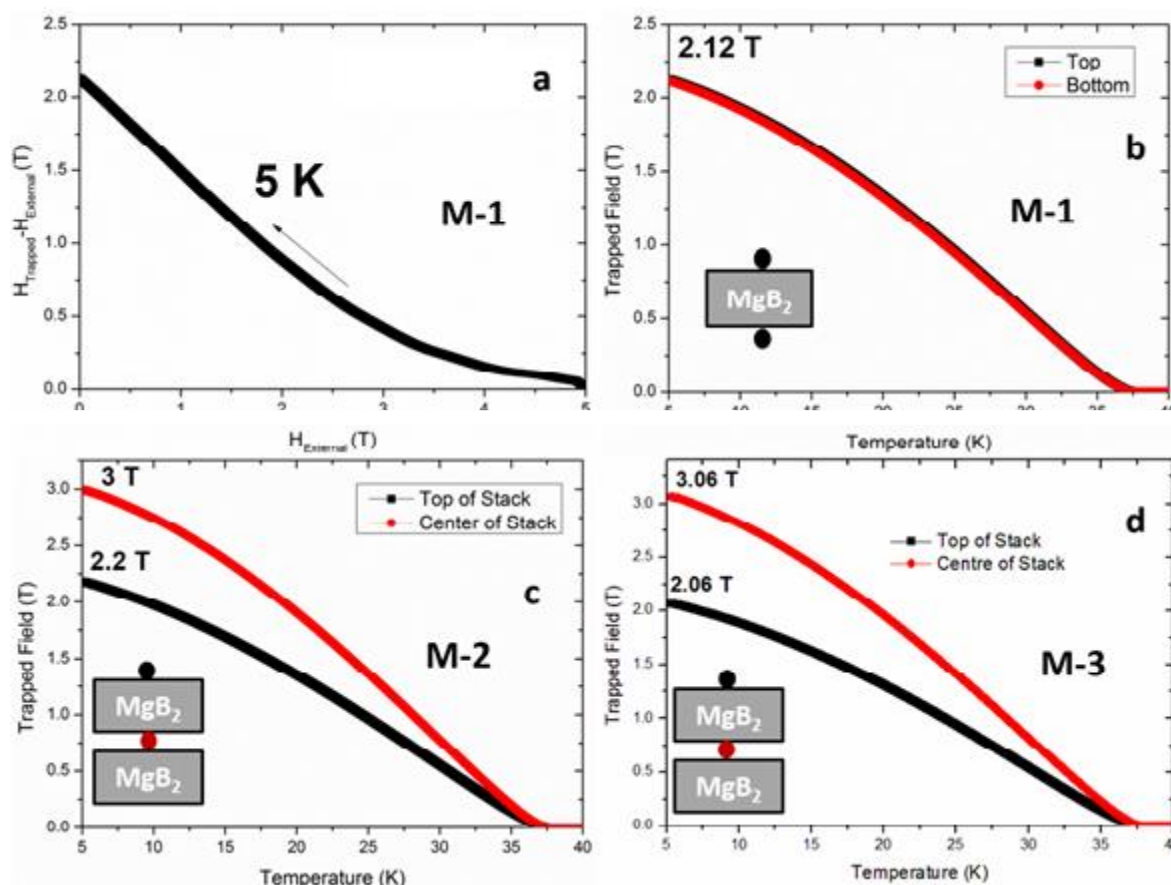


**Figure 5.15(a)** Difference between trapped magnetic flux density and external field as a function of external field for the  $\text{MgB}_2$  bulk samples fabricated by MPIG. (b) Trapped magnetic field as a function of temperature for single bulk (a) A and two-sample stack of (b) A-B and (c) C-D (Table 5.1). The locations of the Hall and temperature sensors are shown in the insets.

The maximum trapped fields of 2.12 T/2.06 T (M-2/M-3) and 3 T/3.06 T (M-2/M-3) were recorded for a single bulk and stacked pair of bulk samples, respectively. This is indicative of very good reproducibility of highly homogeneous  $\text{MgB}_2$  bulks in the IG process. At 20 K, temperature that can easily be achieved with cryogen free cost effective cryo-coolers, a 1.35 T and 2 T/1.96 T (M-2/M-3) trapped field was recorded in a single bulk and centre of stack, respectively.

In comparison, for single bulk at 20 K, RLI processed sample trapped 1.1 T (55 mm Dia, 15 mm thick) [253]. Yamamoto *et al* reported 1.9 T (30 mm Dia, 10 mm thick) and Muralidhar

*et al.* reported 1.4 T (20 mm Dia, 7 mm thick) in *in-situ* sintered samples [251, 257]. Hot isostatically pressured samples showed 2 T (23 mm Dia, 24 mm thick) [252]. Nanostructured bulk trapped 3.2 T (20 mm Dia, 8 mm thick) and 2.2 T (30 mm Dia, 10 mm thick) as reported by Fuchs *et al.* and Sugino *et al.* [176, 245]. Similarly Naito *et al.* reported 2.8 T (40 mm Dia, 20 mm thick) in Ti-doped bulk MgB<sub>2</sub> sample [248]. Whereas trapped field at the centre of 2 sample stack is reported 2.6 T in *ex-situ* hot pressed, 2.9 T in *in-situ* sintered and 3.6 T in Ti-doped MgB<sub>2</sub> bulk samples [247-249].

The Biot-Savart law suggests that trapped field is directly proportional to  $J$  and a dimensionless geometrical factor  $k_G$ , which depends on the radius of bulk sample;

$$B = \mu_0 \cdot J_c \cdot r \cdot k_G \quad (5.2)$$

$$k_G = \frac{t_B}{2r} \ln \left( \frac{r}{t_B} + \sqrt{1 + \left( \frac{r}{t_B} \right)^2} \right) \quad (5.3)$$

Where  $t_B$  and  $r$  are the thickness and radius of the sample, respectively [258]. Assuming  $J_c$  3 be the same for both samples, therefore, any change in the trapped field can be attributed to a variation in  $k_G$ . The ratio of fields measured at the centre to the top of the two sample stack,  $B_{(\text{centre})}/B_{(\text{top})}$ , is 1.36 while predicted value (from equations 1 and 2) is 1.56 (a difference of 15%). This deviation from the measured values is due to the fact that the Biot-Savart law assumes a constant current density everywhere in the bulk sample whereas, in reality, central regions of the bulk are likely to have reduced  $J_c$  due to the relatively strong  $J_c$ - $B$  dependence for MgB<sub>2</sub>. It is also interesting to note that the magnitude of the trapped field at the top of the stack (2.2 T) is similar to that observed at the top of a single bulk, suggesting that the increase in thickness of the MgB<sub>2</sub> sample contributes relatively little to the trapped field (i.e. the sample thickness of the single bulk has already reached the trapped field saturation limit). Significantly, no flux avalanches were observed to occur in the MPIG samples down to a minimum measurement temperature of 5 K, despite a relatively high trapped field.

The trapped field in the bulk MPIG samples fabricated in the current study is likely to be limited by moderate intrinsic values of  $J_c$ , at least compared to recently reported values in the order of MA/cm<sup>2</sup> in bulk MgB<sub>2</sub> fabricated by other processes [228], and a strong  $M$ - $H$  dependence. This also explains why only a 36% increase in the trapped field was observed at the centre of the two-sample stack compared to a single bulk.

### 5.7.2 Flux Creep

A loss of flux from the material can be explained by Lorentz force (Figure 1.2) when  $J > J_c$ . In addition, flux also ‘leaks’ at  $J < J_c$ , since there is definite probability of flux lines overcoming potential well (Pinning) above 0 K. Such decay is called thermally activated flux motion, which is logarithmic in LTS materials and rather rapid in HTS. Here, the stability of trapped magnetic flux in the MgB<sub>2</sub> bulk samples is investigated by performing additional magnetic moment measurements at 10 K following field cooling at 5 T. Figure 5.16(a) shows the variation of the trapped field with time for a single MgB<sub>2</sub> disc of diameter 32 mm. The trapped field after initial magnetization was measured to be 1.94 T, which decreased subsequently to 1.92 T (1% decay) and 1.91 T (1.5% decay), after 1 hour and 1 day, respectively.

This behaviour is characteristic of logarithmic flux creep in type II superconductors (i.e. high initially and then decreasing rapidly to almost a linear variation after  $\sim 2$  min) [259]. The flux creep behaviour of the sample measured in figure 5.16(a) can be expressed by the following equation;

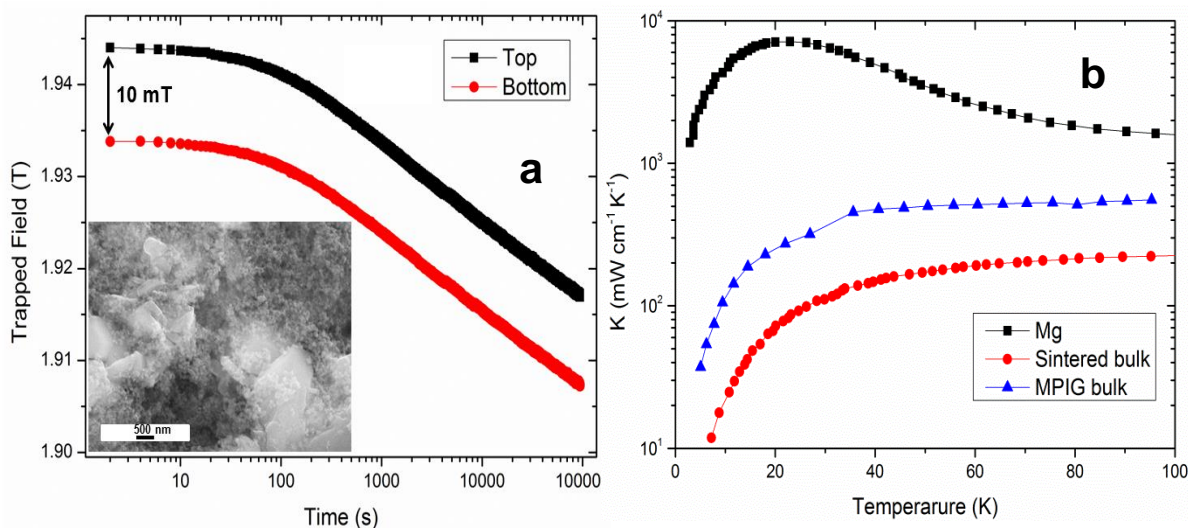


**Figure 5.16(a)** Time dependence of magnetic field trapped in a bulk-MgB<sub>2</sub> sample fabricated by MPIG at 10 K and inset showing fine distribution of Mg and MgB<sub>2</sub> grains in inter-particle region (b) Comparison of thermal conductivity of as processed MPIG [256], sintered MgB<sub>2</sub> [Reproduced from Ref. 260] bulk and pure magnesium [Reproduced from Ref. 261] as a function of temperature.

$$B_{Normalised} = -0.004 \log(t) + 1 \quad (\text{For } t > 100 \text{ s}) \quad (5.4)$$

The rate of loss of flux for these samples is relatively high compared to a recent report by Yamamoto *et al*, where the negative slope of  $B_{(normalised)}$  vs  $\log(t)$  plot was as low as  $4 \times 10^{-6}$

[247]. During trapped field measurements, especially at low temperatures, dissipative flux motion can result in sudden local temperature rise. If this heat is not conducted away quickly enough, then it can potentially result in loss of trapped magnetic flux. Thus a higher thermal conductivity is highly desirable in these quasi-permanent superconducting magnets [262].

Figure 5.16(b) describes measured thermal conductivity for MPIG bulk. Mg and sintered MgB<sub>2</sub> data are also plotted for a comparison. It is evident that thermal conductivity of MPIG bulk is significantly higher than a sintered bulk measured within 5-100 K. This is attributed to uniform distribution fine Mg grains in the inter-particle region (Figure 5.16(a)(inset)) that possess orders of magnitude higher thermal conductivity than MgB<sub>2</sub>. Detail SEM observation and EDS analysis suggests that such inter-particle regions (Figure 5.16(a) inset) comprise of both MgB<sub>2</sub> and Mg grains.

As a result, it can be seen that thermal stability of samples has been increased and no flux avalanches were observed down to 5 K and the magnetized bulk showed a low trapped field decay rate.

## 5.8 Summary

Continuous Mg channels are major defects in IG processed samples and their presence limits long range current flow. These channels are eliminated by incorporating Mg or AlB<sub>2</sub> or MgB<sub>2</sub> powder in the precursor as wetting enhancer to facilitate in-flux of Mg, leading to a more uniform infiltration process, thereby enabling the fabrication of near-net shaped MgB<sub>2</sub> bulk superconductors. Effect of addition of Mg/AlB<sub>2</sub>/MgB<sub>2</sub> was analysed only qualitatively. The Mg channels are 2-D in nature and are quite inhomogeneous throughout the bulk, which make their quantification quite challenging. Interactions of AlB<sub>2</sub> with Mg(l) suggested that it is reactively wetted by liquid Mg and Mg substituted Al sites to form two types of Mg<sub>1-xi</sub>Al<sub>xi</sub>B<sub>2</sub> phases, as indicated by SEM, XRD and magnetic measurements. A moderate trapped field of 0.48 T demonstrates good connectivity of Mg<sub>0.98</sub>Al<sub>0.02</sub>B<sub>2</sub> phase.

MPIG process (MgB<sub>2</sub> powder enrichment in the precursor) was adopted to produce quasi-permanent MgB<sub>2</sub> magnets, since it showed greater promise than Mg or AlB<sub>2</sub> powder additions. An almost identical value of trapped magnetic flux was measured at the top and bottom surfaces of a single bulk sample suggest that MgB<sub>2</sub> bulk samples fabricated by the MPIG method are homogeneous. A stack of two MgB<sub>2</sub> bulk samples trapped a field of 3 T at the centre of the stack at 5 K. These values of trapped field are the highest obtained for a

single bulk MgB<sub>2</sub> sample or a combination of bulk samples fabricated by an infiltration growth process reported to date. A moderate  $J_c$  values and a strong  $J_c(B)$  dependence limits the overall trapped field performance of MgB<sub>2</sub> bulk superconductors fabricated by MPIG. The introduction of additional pinning centres to improve  $J_c$  in an applied magnetic field, therefore, is necessary for further improvement in the trapped field performance of MgB<sub>2</sub> bulk fabricated by this technique. Finally, this study has demonstrated clearly that the infiltration and growth method has significant potential for fabrication high quality, MgB<sub>2</sub> superconducting magnets for high field applications.

## Chapter 6. Investigation of IG Process Mechanism

### 6.1 Introduction

Infiltration and Growth is proven to be a promising route for the fabrication of  $\text{MgB}_2$  bulk superconductors, typically involving the impregnation of liquid magnesium,  $\text{Mg(l)}$ , into a porous solid boron,  $\text{B(s)}$ , preform. The resultant product is essentially an  $\text{MgB}_2$ -Mg ceramic matrix composite, with Mg levels up to 15%. The relative density of IG processed  $\text{MgB}_2$  is significantly higher (>90%) than samples fabricated using conventional sintering techniques, with the process requiring no high pressure apparatus. Moreover, near-net complex shapes can be fabricated with the infiltration route that are not easily achievable by conventional sintering method [159-163].

Significant advances have been made to the IG process to enable fabrication of high quality bulk samples. Recently Naito *et al* have reported fabrication of defect free IG bulks only a few reports have commented on the underlying mechanism of the process [232]. However, DeFauw *et al* proposed a diffusion based model for  $\text{MgB}_2$  growth in boron fibres [263]. They observed radial and circumferential growth of  $\text{MgB}_2$ , via the formation of intermediate phases, including  $\text{MgB}_7$  and  $\text{MgB}_4$ . Radial growth of the  $\text{MgB}_2$  phase occurred mainly due to the formation of radial cracks due to an associated volume expansion. More recently Li *et al* have suggested that the thickness of the first layer of  $\text{MgB}_2$  formed at the  $\text{Mg(l)}$ - $\text{B(s)}$  interface is critical in determining the overall fraction of  $\text{MgB}_2$  in the final reacted IG processed  $\text{MgB}_2$  wires [20]. They accounted for this as being due to the fact that Mg atoms needed to diffuse through the  $\text{MgB}_2$  layer in order to react with the B. For this study, the devised experiments were aimed at understanding the growth mechanism of the superconducting  $\text{MgB}_2$  phase during the Infiltration and Growth process. The resultant microstructural evolution in the samples is discussed via the analysis of series of samples. Finally, a possible mechanism for the growth of superconducting  $\text{MgB}_2$  is proposed.

Crystalline  $\beta$ -boron (98% pure, HC Starck, < 40  $\mu\text{m}$ ), weighing 1.5 g, was pressed uniaxially into cylindrical precursor pellets of diameter 16 mm and thickness 6 mm under a load of 20 MPa. SEM images of  $\beta$ -B powder (not shown here) suggested a bimodal particle size distribution with most particles with sizes of 5-10  $\mu\text{m}$  and  $\sim 30 \mu\text{m}$ . A total of 10 such boron precursor pellets were prepared. Seven of the Boron precursors were subjected to IG process at a fixed temperature of 750  $^\circ\text{C}$  for durations of 5 min, 10 min, 20 min, 40 min, 1 h, 2 h and

4 h. To study the influence of reaction temperature, the remaining 3 precursors were reacted with a constant soaking time of 4 h and varying reaction temperatures of 800 °C, 850 °C and 900°C. The reacted product from IG process, when in the form of hard bulk, was slightly ground to remove Mg metal on the bulk surface. Wherever powdery reacted product was obtained, especially for soaking time < 20 min, all the powder was carefully collected. Weights of all the samples were recorded to estimate Mg intake, since the weight of starting B precursor was kept constant at 1.5 g

## 6.2 Infiltration and Growth: A Three Stage process

From our observations we divide the overall growth of superconducting  $\text{MgB}_2$  in the IG process into 3 stages as follows.

### 6.2.1 Stage 1: Initiation of cracks in the Boron particle: $\text{Mg}_2\text{B}_{25}$ phase formation process

The SEM images of samples reacted isothermally at 750 °C at 5 min, 10 min, 20 min and 40 min are shown in figures 6.1(a), (b), (c) and (d), respectively.

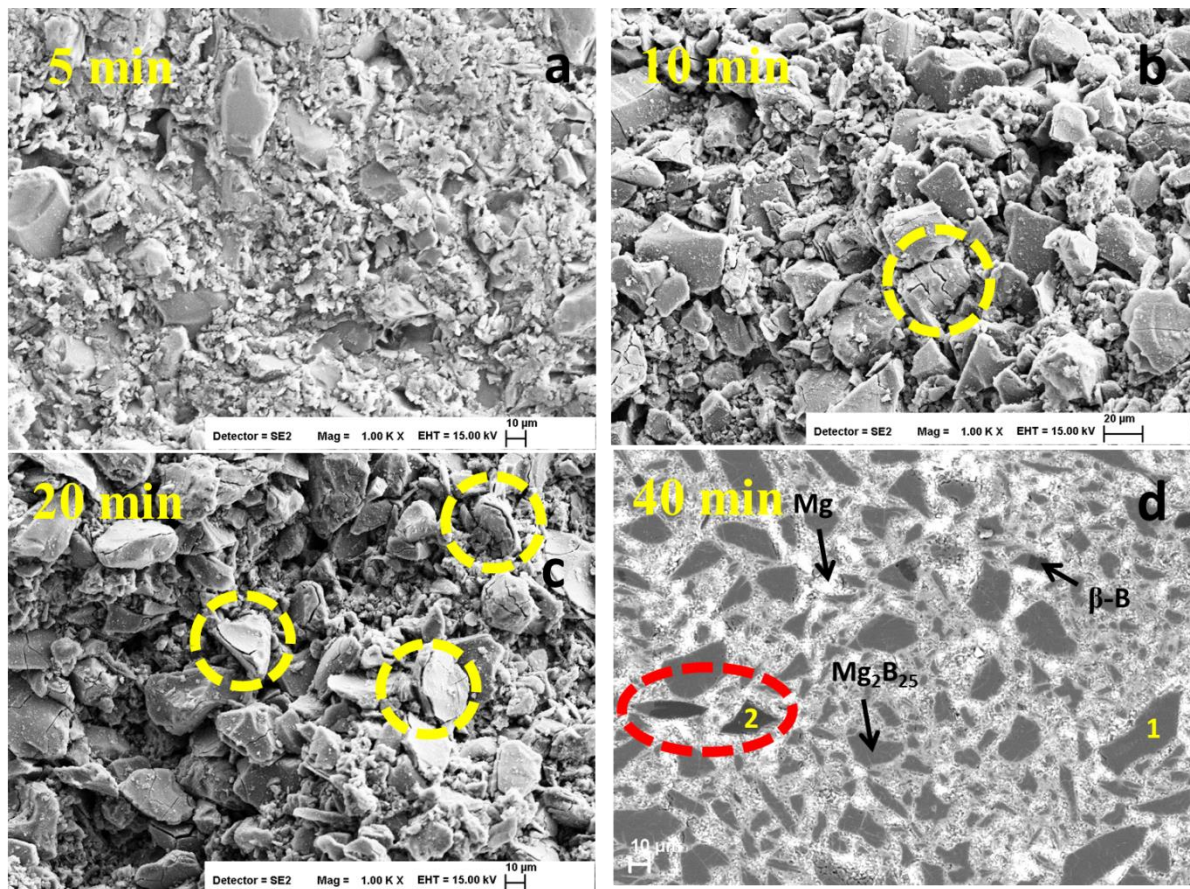


Figure 6.1 Back scatter electron images of samples reacted at 750 °C for (a) 5 min, (b) 10 min, (c) 20 min and (d) 40 min, respectively.

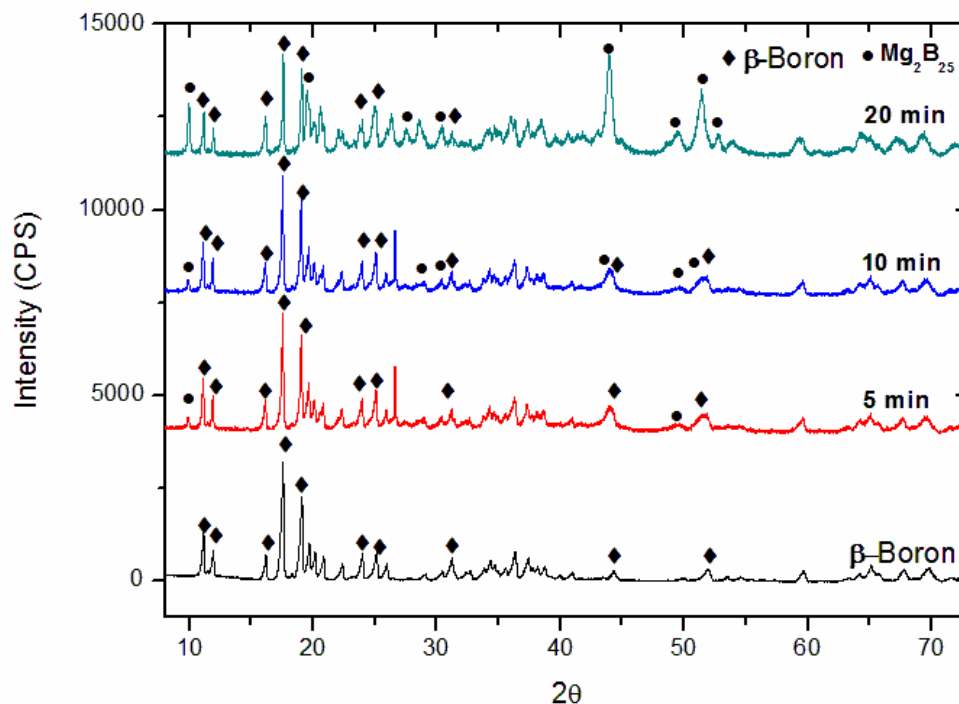


Figure 6.2 XRD patterns for the samples reacted for 5, 10 and 20 min, respectively, at 750 °C. Plot for  $\beta$ -boron also shown for comparison.

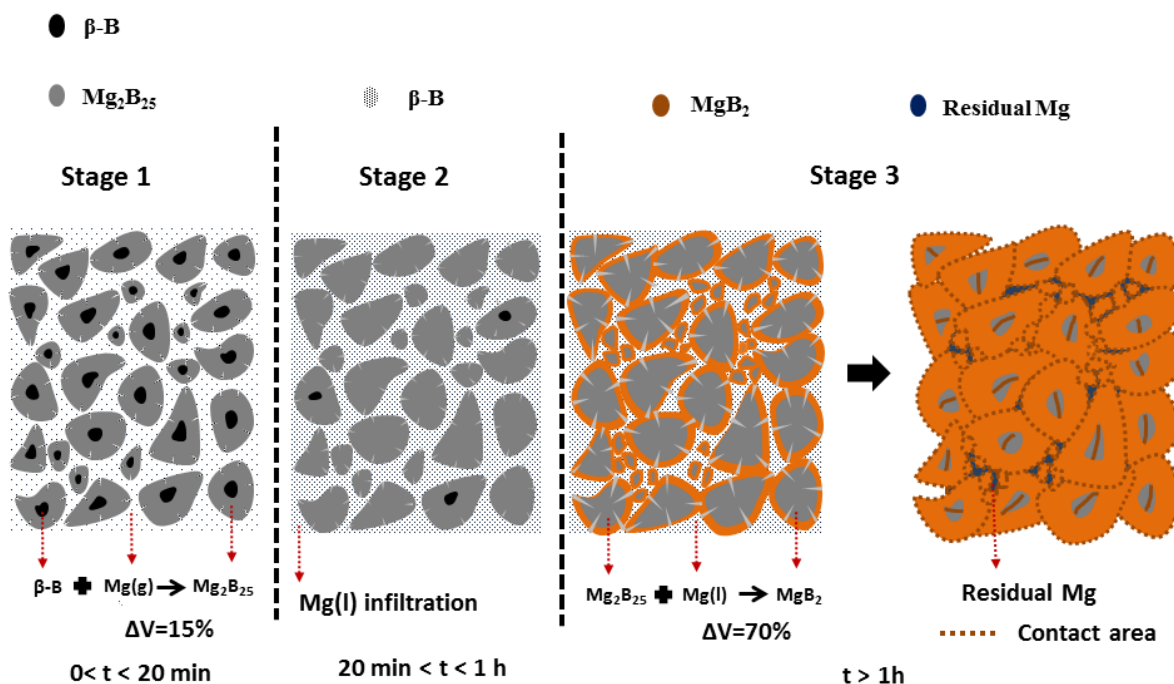


Figure 6.3 Schematic illustration of microstructure and phase evolution during the IG process.

The sample reacted for 5 min is observed to be free from Mg with no sign of phase transformation. The sample reacted for 10 min, however, shows the initiation of cracks in some of the particles (indicated in figure 6.1 by yellow dashed circles), whereas almost all the



B particles in sample reacted for 20 min show radially inward multiple cracks, exposing fresh B region to Mg vapour.

The XRD patterns of these samples, shown in figure 6.2, reveal an increasing appearance of  $Mg_2B_{25}$ , a recently discovered phase, in the sample reacted for 10 and 20 min, suggesting a strong correlation between cracking and transformation of the  $\beta$ -rhombohedral into  $Mg_2B_{25}$  [169, 217-219]. This is illustrated as stage 1 in schematic of IG process in figure 6.3.

### 6.2.2 Stage 2: Mg uptake in the porous precursor

The overall weight gain in the precursor as a function of reaction time at a fixed temperature (750 °C), plotted in figure 6.4, enables the study of rate of influx of Mg with time (Figure 6.3, Stage 2). Given that XRD did not detect any traces of MgO (Figure 6.2), all the gain in weight of the sample can be attributed to liquid Mg only.

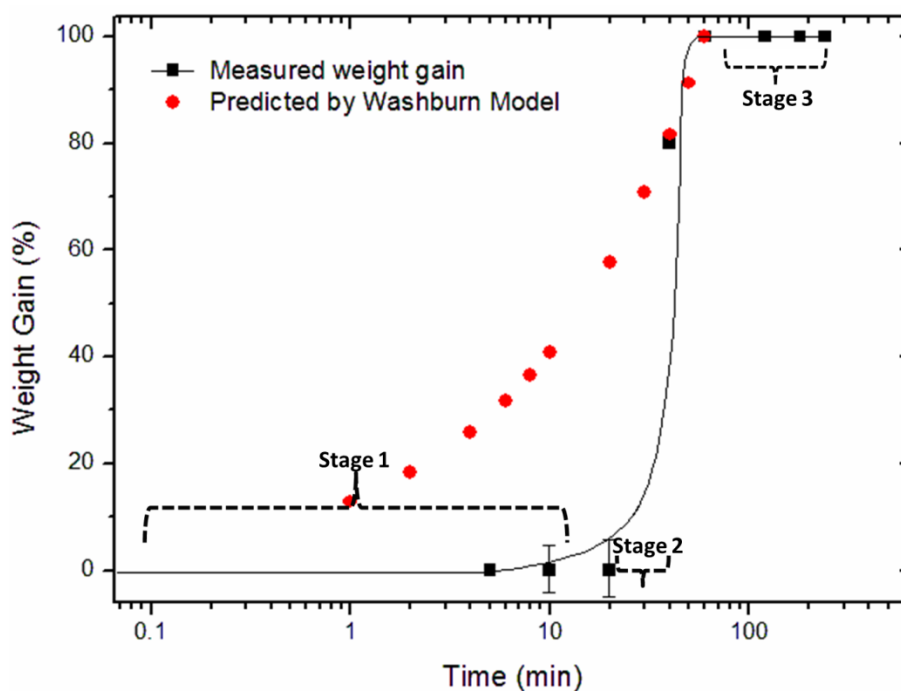


**Figure 6.4** Measured weight gain in IG sample compared with that predicted by classical capillary infiltration, as a function of reaction time. The 5% error for samples reacted for 10 and 20 min accounts for losses associated with the handling of powdery reacted product.

Mg uptake into the precursor pellet could only be observed after 40 min of reaction. Samples reacted for 5, 10 and 20 min showed no detectable weight gain. Conversely, the sample reacted for 40 min showed an 80% weight gain while the 1 h sample exhibited a doubling in weight. It is noted that doubling (100% weight gain - 1.5 g Mg) also satisfies the

stoichiometric requirement of the quantity of Mg needed to react with B in the precursor. The sample reacted for longer than 1 h showed no further uptake of Mg.

### 6.2.3 Stage 3: Transformation of $Mg_2B_{25}$ to $MgB_2$ : Rate determining step

The following 3 phenomenon are observed concurrently in the final stage IG process.

#### 6.2.3.1 Propagation of primary cracks in $Mg_2B_{25}$ particles and fragmentation

Figures 6.5(a) and (b) show back scatter electron images of samples reacted at 750 °C for 40 min and 2 h, respectively.

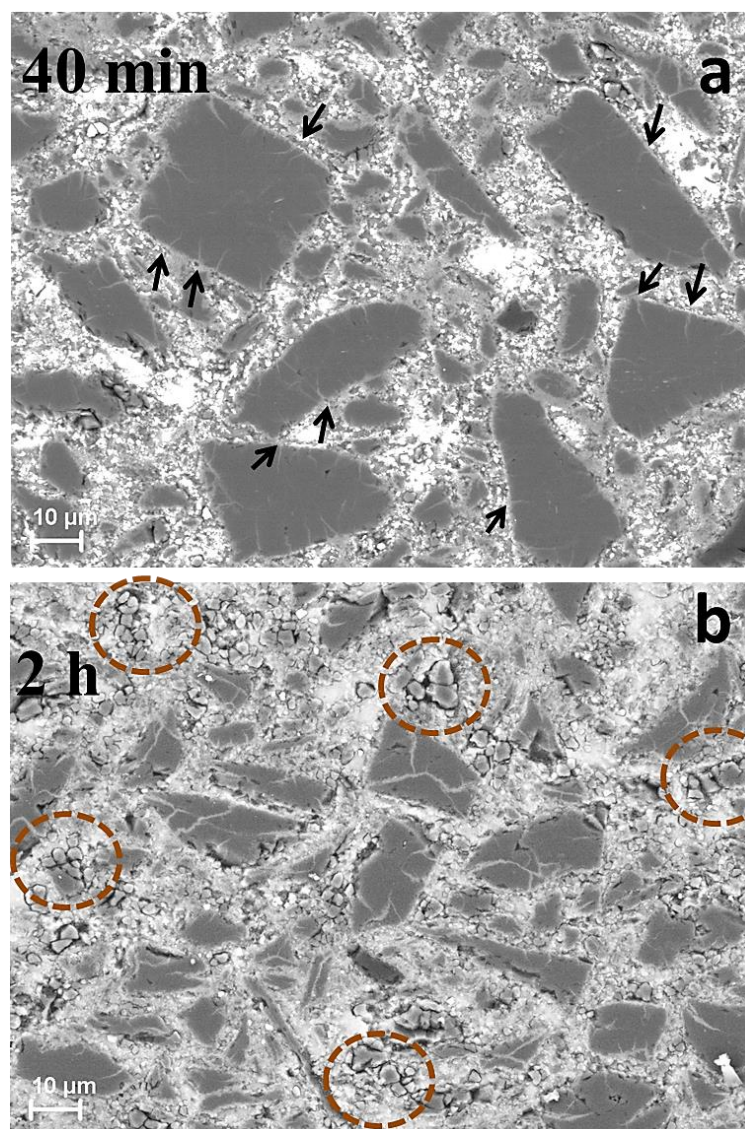


**Figure 6.5** Back scatter electron images of IG processed samples. (a) The sample reacted for 40 min shows a smaller crack length (shown by arrows) (b) The sample reacted for 2 h shows the propagation of cracks and ultimate fracture in the  $Mg_2B_{25}$  particles (indicated by dotted circles).

The sample reacted for 40 min shows the presence of Mg (bright in contrast) within pores in the precursor and radial cracks that formed during Stage 1 (as shown by black arrows). It is quite apparent that cracks in the sample reacted for 2 h are deeper in to the particle than that of particles in the sample reacted for 40 min. These cracks propagated through the  $Mg_2B_{25}$  particle, and even extend throughout the entire particle cross-section, as can be seen from figure 6.5(b). Consequently, these cracks resulted in fracture and fragmentation in some of the particles (indicated by red dashed circles) during Isothermal heat treatment at 750 °C. XRD analysis (not shown here) indicates that samples reacted at 750 °C for 40 min and 2 h contained  $Mg_2B_{25}$  phase of up to 40% and 30% (volume) respectively.

#### 6.2.3.2 Diffusion controlled $MgB_2$ growth

Figures 6.6(a) and 6(b) compare the microstructures of samples reacted for 4 h at 750 °C and 900 °C respectively.

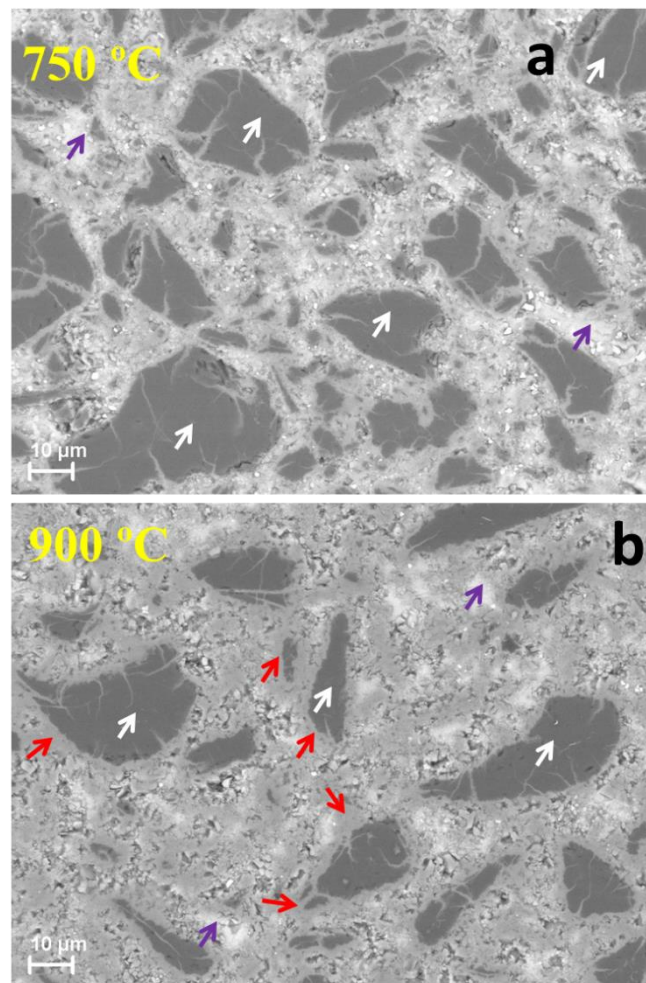


**Figure 6.6** Back scatter electron images of samples reacted for 4 h at (a) 750 °C and (b) 900 °C. The red arrows indicate the “Diffusion zone”. The purple arrows indicate unreacted Mg and the white arrows indicate the  $Mg_2B_{25}$  phase.

High residual Mg content and a large amount of  $\text{Mg}_2\text{B}_{25}$  phase is present in the sample reacted at 750 °C. The sample reacted for 900 °C shows a large depth of  $\text{MgB}_2$  layer thickness on individual particles or “diffusion zone”, indicating the Mg diffusion distance into  $\text{Mg}_2\text{B}_{25}$  particle. The expected concentration profile of Mg within a particle is schematically shown in figure 6.7. Moreover, smaller particles of size 5  $\mu\text{m}$  appear to have completely transformed into a different phase. XRD patterns and the corresponding estimated phase contents at each temperature (750 °C, 800 °C, 850 °C and 900 °C) are shown in figures 6.8(a) and (b), respectively. Phase quantification of various phases shown in figure 6.8(b) was performed using a computational tool ‘Powder Cell’. An example of fitting is shown in figure 6.8(c) for the sample reacted at 750 °C for 4 h.. Phase content of  $\text{Mg}_2\text{B}_{25}$  and Mg at 750 °C is estimated to be about ~26% and 33% respectively. It is reduced progressively as the temperature increases and reaches ~12% and 14% respectively at 900 °C, which clearly suggests that growth of the superconducting  $\text{MgB}_2$  phase occurs at the expense of  $\text{Mg}_2\text{B}_{25}$  and Mg phase consumption.

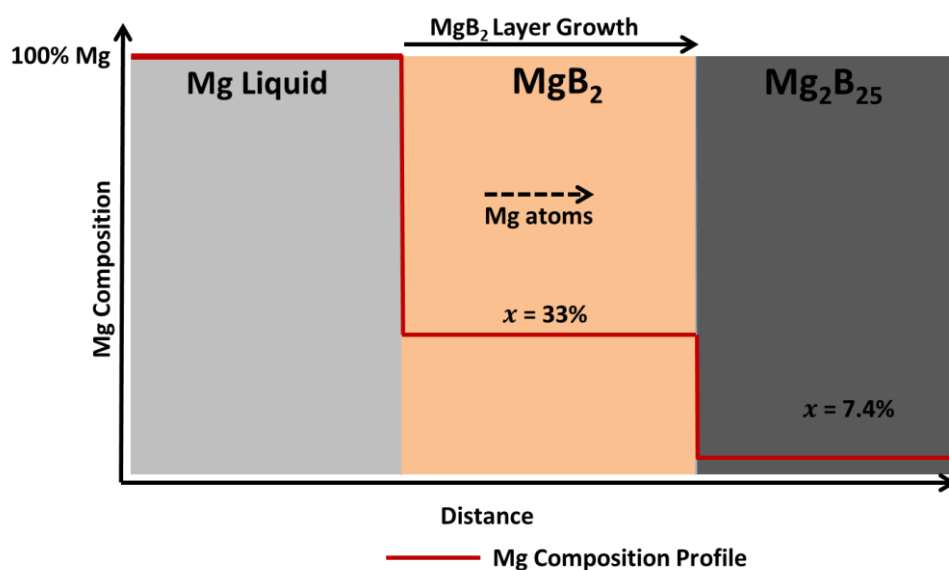


**Figure 6.7** Schematic representation of compositional profile from surface of the  $\text{MgB}_2$  particle towards center.

### 6.2.3.3 Simultaneous sintering

Figure 6.9 shows the variation of bulk hardness and critical current density as a function of reaction temperature. It is evident that critical current density increases with the reaction temperature. The growth of  $\text{MgB}_2$  occurs radially inwards in the boron particles and this superconducting layer undergoes almost 2 fold volume expansion. These growing particles

impinge on one another and sinter simultaneously (Figure 6.3, Stage 3), as evident in the SEM images shown in figure 5.12. The sintering process enhances the grain connectivity and is responsible for the observed increased  $J_c$  as a function of soaking temperature. Increased hardness as a function of temperature also suggests increased grain connectivity by the sintering process.

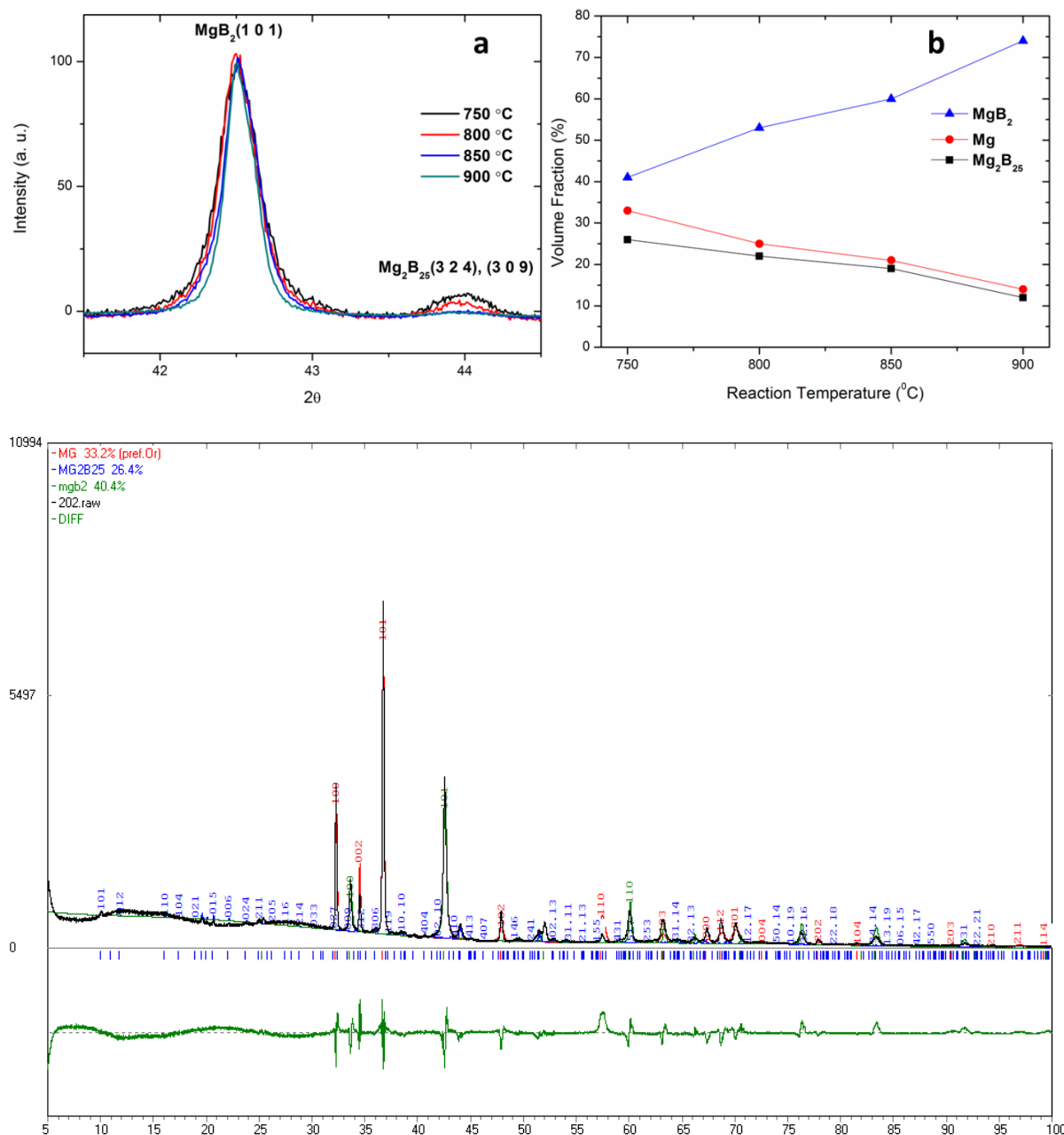


**Figure 6.8.** (a) XRD patterns of samples reacted for 4 h at 750 °C, 800 °C, 850 °C and 900 °C. Note that changing the relative amount of  $MgB_2$  and  $Mg_2B_{25}$  phases varies depending on the temperature. (b) Estimated volume fraction phases ( $MgB_2$ , Mg and  $Mg_2B_{25}$ ) as a function of reaction temperature. Figure (c) shows fitting of XRD pattern performed using Powder Cell for sample prepared at 750 °C, 4h. Notable texture in (101) can be seen in residual Mg, possibly resulting from unique growth direction of Mg during cooling the sample.

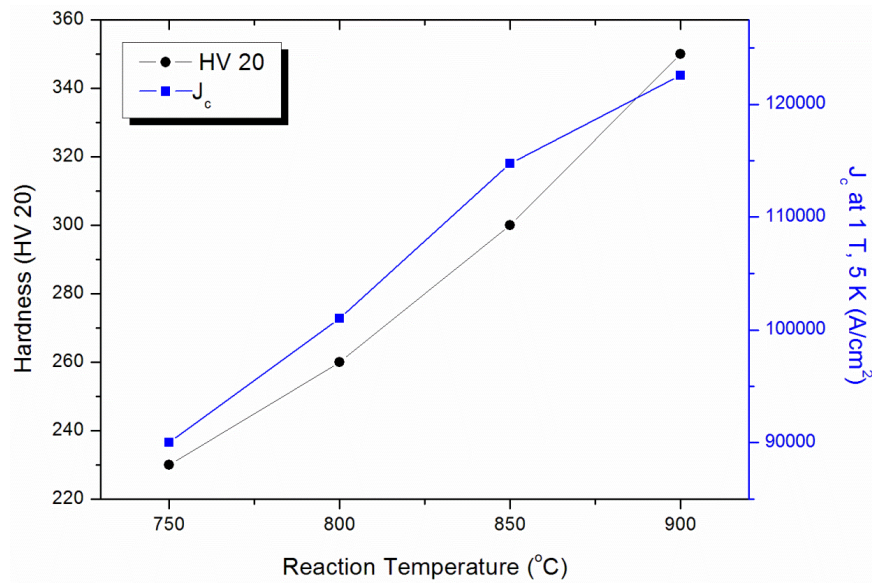


Figure 6.9 Variation of critical current density and hardness plotted as a function of reaction temperature.

### 6.3 Mg<sub>2</sub>B<sub>25</sub> Formation

It is clear from Stage 1 that Mg<sub>2</sub>B<sub>25</sub> is a non-equilibrium intermediate phase that formed during transformation into MgB<sub>2</sub>.

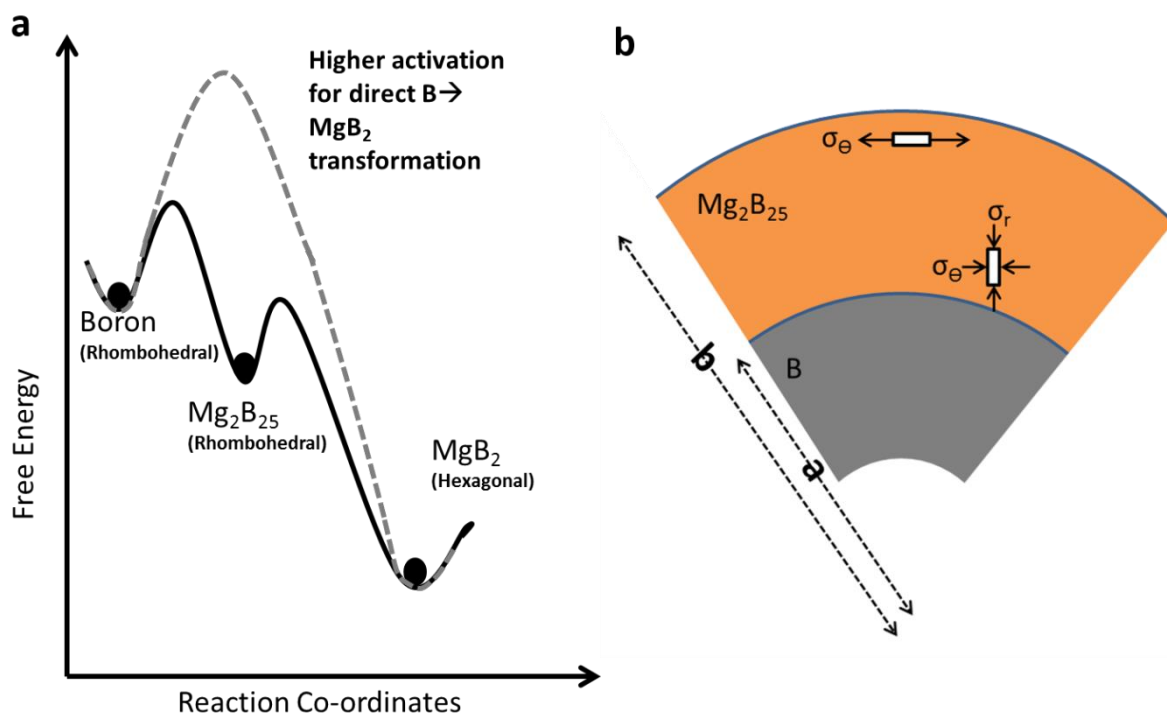
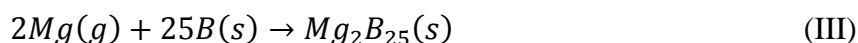


Figure 6.10(a) Schematic illustration of a progressing Mg<sub>2</sub>B<sub>25</sub> front and the generation of stress and (b) Schematic depiction of transformation of B → Mg<sub>2</sub>B<sub>25</sub> → MgB<sub>2</sub>, which probably involves lesser activation barrier.

The crystal structure of the  $Mg_2B_{25}$  phase can be described as partial occupancy of Mg atoms (7.4 atomic %) at interstitial sites (namely A, D, E and F) in a complex rhombohedral unit cell of  $\beta$ -boron comprising of 105 atoms. Thus major structural rearrangement of  $\beta$ -boron is not necessary, although lattice constants are slightly enhanced [217, 218]. The transformation of  $\beta$ -B directly to  $MgB_2$  probably involves larger activation (Figure 6.10(a)). As a result, the reaction  $\beta$ -B  $\rightarrow$   $MgB_2$  proceeds via the formation of a metastable phase, whose crystal structure closely resembles  $\beta$ -B.

Given that the influx of Mg(l) is below detectable limits in the initial stages of the infiltration process it is likely that the Mg atoms that are transported from liquid source to individual  $\beta$ -boron particles to form  $Mg_2B_{25}$  are in the vapour phase. A quick transformation of B (~20-40 min) to form boron rich boride according to following reaction suggests that the reaction kinetics are favourable.



When a B particle reacts with Mg vapour, the  $Mg_2B_{25}$  phase initially forms on the surface of boron particle (Figure 6.3, Stage 1), as shown in figure 6.10(b). At this stage, an element of  $Mg_2B_{25}$  at the periphery of B particle experiences compressive tangential stresses. This is primarily because B (Molar volume ( $V_B$ )= 4.7 cm<sup>3</sup>) particle undergoes volume expansion after transforming into  $Mg_2B_{25}$  (Molar volume ( $V_{Mg_2B_{25}}$ )= 129.7 cm<sup>3</sup>) according to reaction (III). The peripheral region is pushed away from the centre upon subsequent growth of the  $Mg_2B_{25}$  layer, which unloads elastically and then experiences tensile tangential stress as illustrated schematically in figure 6.10(b). This stress leads to the initiation of a radial crack due to the negligible plasticity of  $Mg_2B_{25}$ . This phenomenon has been observed previously and reported as ‘‘Lithiation induced fracture’’ within the context of the diffusion of lithium in silicon particles [264-268].

When elastic strain is small compared to reaction induced strain (11%), radial ( $\sigma_r$ ) and tangential ( $\sigma_\theta$ ) stresses at any distance  $R$  from the centre of a spherical  $\beta$ -B particle upon formation of a thin  $Mg_2B_{25}$  shell can be described as [264];

$$\sigma_r = -2\sigma_y \log\left(\frac{b}{R}\right) \quad (6.1)$$

$$\sigma_\theta = \sigma_y - \sigma_y \log\left(\frac{b}{R}\right) \quad (a \leq R \leq b) \quad (6.2)$$

Where  $b$  is the outer the radius of sphere and  $a$  is the radius of an unreacted  $\beta$ -B sphere.

$b$  is also expressed as a function of initial radius of particle prior to reaction ( $b_i$ ) as

$$b = [a^3 + \beta(b_i^3 - a^3)]^{1/3} \quad (6.3)$$

The above equation takes relative volume expansion  $\beta$  (ratio of molar volume of  $\text{Mg}_2\text{B}_{25}$  to  $\beta$ -B) into consideration. The hoop stress is tensile in nature at the periphery ( $b = R$ ) with a maximum value equal to the yield strength  $\sigma_y$ . Given the brittle nature of  $\text{Mg}_2\text{B}_{25}$ , the hoop stress ( $\sigma_\theta = \sigma_y$ ) is likely to initiate fracture of the particle by the generation of a crack [264]. It is noted that residual stresses can remain compressive in a particle with flat surface. Thus, curvature is critical for the initiation of cracks at the surface of a particle.

This stress  $\sigma_y (> \sigma_c)$  would propagate the crack [264] if the crack size is such that

$$G = Z \frac{\sigma_c^2}{E} b_c \quad (6.4)$$

Where  $\sigma_c$  is the critical stress required to propagate a crack of length  $2b_c$  and  $Z$  is a geometrical factor.  $E$  is elastic modulus of  $\text{Mg}_2\text{B}_{25}$  and  $G$  is the energy release rate. Although  $\sigma_y$  is clearly sufficiently high to propagate a crack for a short distance (as apparent from figure 6.5(a)), the cracks do not propagate freely inwards since the tensile hoop stress decreases steadily, eventually becoming compressive towards the centre [264, 268].

### 6.3.1 EDX Analysis

Figure 6.11(a) shows a SEM image of  $\text{MgB}_2$  bulk (800 °C, 4 h) while figures (b) and (c) show elemental maps of boron and magnesium respectively. Expectedly, the Mg concentration is lower in larger particles ( $\text{Mg}_2\text{B}_{25}$ ) and is higher in the ‘matrix’, which is composed of finer  $\text{MgB}_2$  particles. On the contrary, B concentration is higher in larger particle and lower in the matrix. Moreover, relatively higher concentration of Mg can clearly be seen within the cracks in  $\text{Mg}_2\text{B}_{25}$  particles. Energy dispersive X-ray analysis at locations 1 and 2 in figure 6.1(d) confirms the  $\text{Mg}_2\text{B}_{25}$  phase formation and the corresponding EDAX patterns are shown in figure 6.11(d). At this stage a considerable amount of Mg has occupied the pores in the boron precursor.



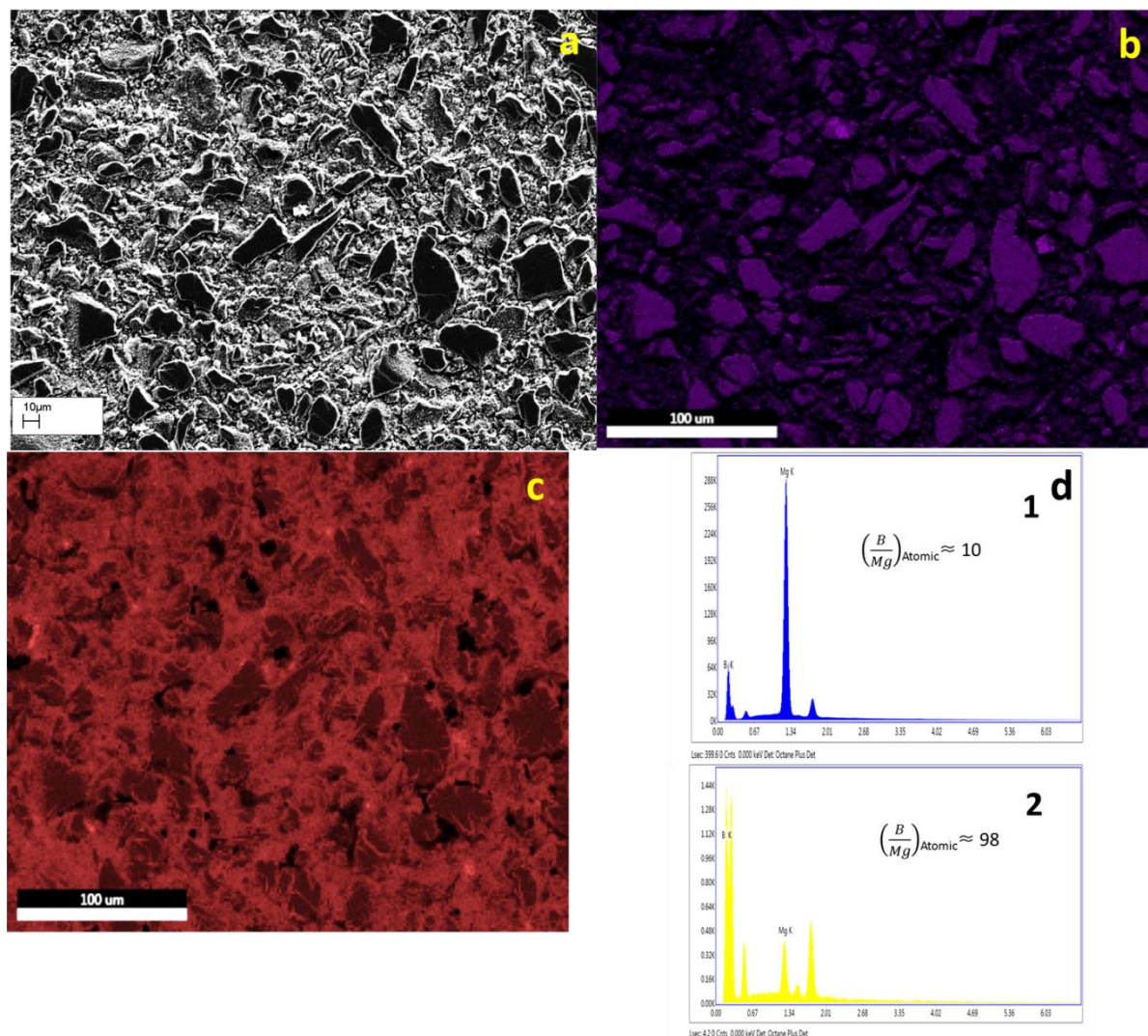


**Figure 6.11(a)** Secondary electron SEM image of polished surface of sample reacted at 800 °C, 4 h. **Figure 10(b)** and **(c)** show EDS maps of boron and magnesium respectively. **(d)** EDS point analysis on locations 1 and 2, shown in figure 6.1(d).

It is evident from figure 6.2 that significant portion of B powder is transformed into  $Mg_2B_{25}$  within the first 20 min of soaking time and that no detectable amount of superconducting  $MgB_2$  is observed. Several particles in the microstructure (Figure 6.1(d)), appearing dark in contrast indicated by a red dashed circle, represent unreacted  $\beta$ -Boron particles with B/Mg ratio of 98 (e.g. location 2) that have not yet transformed into  $Mg_2B_{25}$ . The relatively lighter in contrast particles (location 1) are confirmed as  $Mg_2B_{25}$  particles. EDS analysis on several random points within such areas suggests a B/Mg atomic ratio of 10 as opposed to an ideally expected ratio of 12.5. The slight underestimation of this ratio is attributed to the interaction volume of the penetrating electron beam, some of which probes Mg metal beneath the particle.

### 6.4 Mg(l) Infiltration

The Mg infiltration depth ( $\chi_0$ ) into the porous boron preform can be expressed by following Washburn's equation in the Stage 2 of the IG process [220],

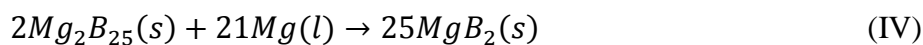
$$\chi(0) = \left( \frac{r_p \gamma_s \cos \theta_w}{2\eta} \right)^{1/2} \cdot t(0)^{1/2} \quad (6.5)$$

$r_p$ ,  $\gamma_s$ ,  $\theta_w$  and  $\eta$  represent the radius of cylindrical porous channels, surface tension, wetting angle between  $\beta$ -B(s) - Mg(l) and viscosity of Mg melt, respectively, whereas  $\chi$  and  $t$  represent infiltration depth and time taken. Since rise in infiltration depth is associated with rise in mass in linear proportion, weight gain can be directly to  $\chi$ , equation 6.5 suggests a parabolic dependence of weight gain (dotted line in figure 6.4) with time. A deviation from Washburn's model is expected in the present case as the pores are of irregular shapes and sizes. Moreover, other mechanisms such as gravity, hydrostatic fluid pressure and negative pressure (from volume shrinkage in MgB<sub>2</sub> phase formation) are also expected to contribute to the uptake of Mg. The predicted and measured weight gain with reaction time is compared in figure 6.4. Note that due to the unknown contact angle ( $\theta_w$ ), Washburn infiltration is assumed to reach completion after 1 h, and weight gain from 0 to 1 h is predicted. Li *et al.* observed that, at 675 °C, Mg infiltrates to a depth of 40  $\mu\text{m}$  in 1 h in MgB<sub>2</sub> wires synthesized from nano-boron powder [20]. Even after suitable correction for pore radius (assumed proportional to particle size), and a small change in viscosity, the rate of Mg uptake appears much more rapid in the present study. It is therefore suggested that apart from liquid infiltration and other aforementioned mechanisms, vapour diffusion could also be another mode of transport of Mg from the liquid reservoir since Mg is known for its high vapour pressure. The vapour diffusion process explains the observed phase transformation of B into Mg<sub>2</sub>B<sub>25</sub> everywhere within the sample and the absence of Mg phase in the initial 20 minutes of the process. During this period, Mg atoms are adsorbed everywhere on the  $\beta$ -B particle surface and react according to reaction (III) to form Mg<sub>2</sub>B<sub>25</sub>, creating further driving force for Mg vapour influx. Mg pick-up from classical Washburn liquid infiltration is likely to be limited to the edges of sample during initial 20 min of the soaking period.

### 6.5 MgB<sub>2</sub> formation on Mg<sub>2</sub>B<sub>25</sub> particle

In the 3<sup>rd</sup> and final stage of the process, the propagation of cracks, formation of an MgB<sub>2</sub> diffusion layer and sintering all occurred simultaneously. Mg(l) entered the cracks and

reacted with  $Mg_2B_{25}$  at the crack tip/surface to form  $MgB_2$  as schematically shown in figure 6.12. This chemical reaction can be expressed as;



$$\varepsilon_V = \frac{2V_m^{Mg_2B_{25}} - 25V_m^{MgB_2}}{2V_m^{Mg_2B_{25}}} \sim 70\% \quad (6.6)$$

where  $V_m$  is molar volume and  $\varepsilon_V$  and  $\varepsilon_L$  are volumetric and linear strains, respectively. Under the isotropic volume expansion, the linear strain  $\varepsilon_L$  is given by,

$$\varepsilon_L = \frac{\varepsilon_V}{3} \sim 23\% \quad (6.7)$$

Thus the stress at the tip of the crack is given as

$$\sigma_{crack\ tip} = E_{MgB_2}\varepsilon_L \sim 65\text{ GPa} [269] \quad (6.8)$$

Although such a volume expansion ahead of the crack tip is expected to blunt the tip and hinder crack propagation, as in the case of yttria stabilized zirconia [270, 271], experimental

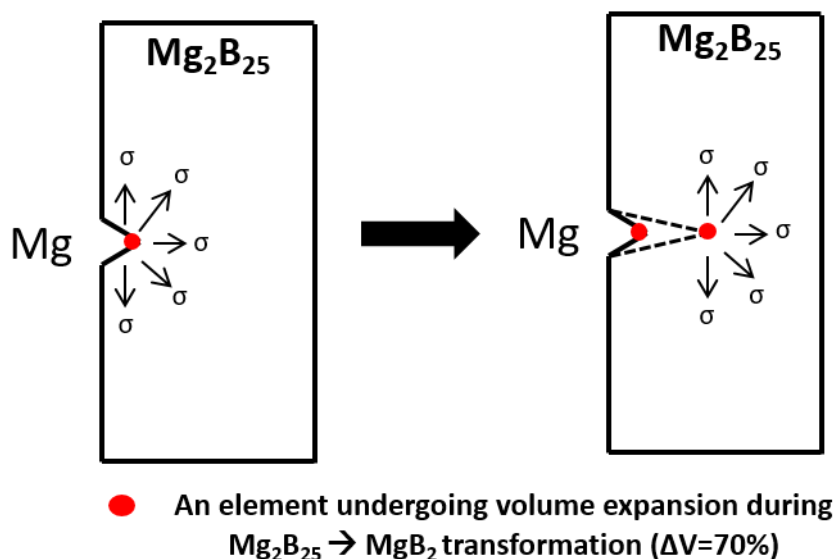


**Figure 6.12** Schematic illustration of volume expansion at the tip of crack. This is believed to lead to crack extension.

evidence suggests that the continuous formation of  $MgB_2$  can impart a stress larger than the one that can be sustained elastically by  $Mg_2B_{25}$ . Therefore, the crack propagates further exposing fresh  $Mg_2B_{25}$  to  $Mg(l)$ . DeFaw *et al.* also observed such time dependent crack

growth in  $\text{MgB}_2$  synthesis from boron fibres [263]. As a result, cracks propagate radially inward, often resulting in the fragmentation of particles. Formation and propagation of these cracks play a vital role in formation of  $\text{MgB}_2$  channels passing through the non-superconducting  $\text{Mg}_2\text{B}_{25}$  phase. This provides an added supercurrent path in the fully processed bulk material.

$\text{MgB}_2$  phase formation closely resembles a peritectic reaction where the reaction occurs only on the surface and is governed by the diffusion of various chemical species. Therefore, the reaction doesn't often reach completion, as is observed frequently in the fabrication of YBCO superconductors, where the final microstructure invariably contains a considerable amount of unreacted phase (Y-211) [61, 272]. A decrease of  $\text{Mg}_2\text{B}_{25}$  phase content (12%) is observed as a result of  $\text{Mg(l)}$  reaction with  $\text{Mg}_2\text{B}_{25}$  phase and enhanced kinetics at higher temperature. Similarly, XRD patterns (Figure 6.8(a)) also show a diminishing phase content of  $\text{Mg}_2\text{B}_{25}$  with increasing reaction temperature. It is also worth noting that  $\text{MgB}_2$  formed at a lower temperature is "dirtier", as indicated by broader peaks in samples reacted at low temperature.

The so-called Deal and Grove model has been adopted to describe the Mg diffusion process in the growth of  $\text{MgB}_2$  [273, 274]. In this model, it is assumed that all boron particles are spherical and of equal diameter, and that the diffusion process is a steady state. It is assumed that no reaction has taken place while  $\text{Mg(l)}$  occupies all the porous sites in the precursor.

According to Fick's first law:

$$J_{Mg} = D \frac{(C_{Mg-MgB_2} - C_{MgB_2-Mg_2B_{25}})}{x} \quad (6.9)$$

Where  $D$  is the diffusivity of Mg in  $\text{MgB}_2$ ,  $C_{Mg-MgB_2}$  represents the concentration at Mg- $\text{MgB}_2$  interface,  $C_{MgB_2-Mg_2B_{25}}$  is the Mg concentration at the  $\text{MgB}_2$ - $\text{Mg}_2\text{B}_{25}$  interface,  $J_{Mg}$  is in-flux of Mg atoms and  $x$  is thickness of the  $\text{MgB}_2$  layer.

For mass balance, the influx of Mg ( $J_{Mg}$ ) should be equal to the rate of  $\text{MgB}_2$  formation given that the number of moles of Mg diffusing through the  $\text{MgB}_2$  layer is the same as that reacting with  $\text{Mg}_2\text{B}_{25}$  to form  $\text{MgB}_2$ . Assuming a first order reaction,

$$J_{Mg} = KC_{MgB_2-Mg_2B_{25}} \quad (6.10)$$

Where  $K$  is reaction constant in equation 6.10

Combining equations (6.9) and (6.10) yields

$$C_{MgB_2-Mg_2B_{25}} = \frac{(D C_{Mg-MgB_2})}{D+xK} \quad (6.11)$$

$$J_{Mg} = \frac{K(D C_{Mg-MgB_2})}{(D+xK)} \quad (6.12)$$

Assuming that the  $MgB_2$  layer grows by an infinitesimally small length  $dx$  in time  $dt$ , the number of moles of Mg crossing a unit cross sectional area in  $dt$  is therefore  $J_{Mg}dt$ . These are number of Mg atoms reacting to form  $MgB_2$  with a volume of cuboid equaling unit area and length  $dx$  ( $V_{Mg}^{MgB_2}$ ). Note that 21 moles of Mg are required to form 25 moles of  $MgB_2$ . (Reaction IV)

$$21 J_{Mg} dt = 25 V_{Mg}^{MgB_2} dx \quad (6.13)$$

$$dt = \frac{25 (D+xK)}{21 0(K D C_{Mg-MgB_2})} V_{Mg}^{MgB_2} dx \quad (6.14)$$

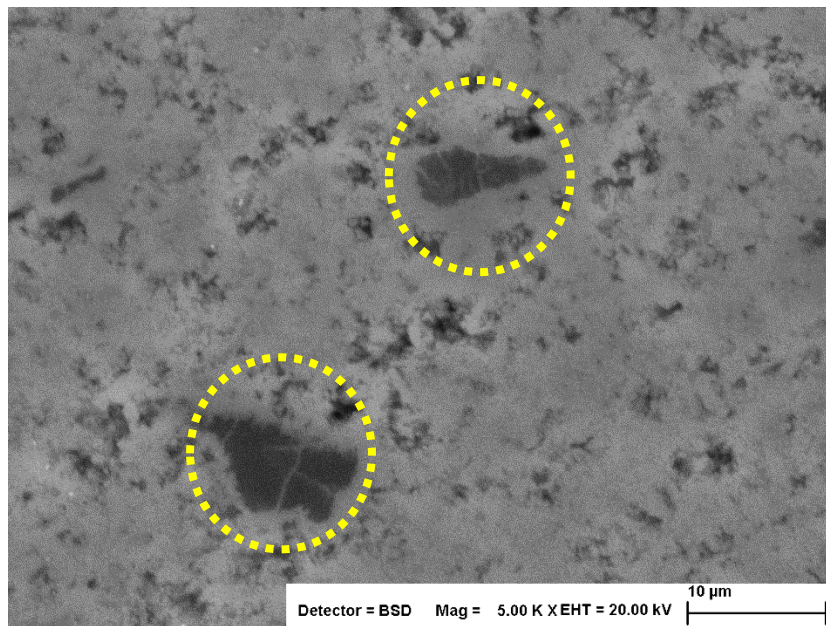
Invoking the assumption that the overall reaction is controlled by diffusion rather than reaction rates, equation (6.14) yields

$$\int_{t=0}^{t=t^*} dt = \frac{25 V_{Mg}^{MgB_2}}{21} \int_{x=0}^{x=20 \times 10^{-6}} \left( \frac{x}{D C_{Mg-MgB_2}} \right) dx \quad (6.15)$$

Where  $t^*$  is the time necessary to complete reaction II (stage 3) at 900 °C. The upper limit of  $x$  is chosen as the radius of the reacting particle. Values of  $D= 10^{-14} \text{ m}^2/\text{s}$  (900 °C) [263],  $C_{Mg-MgB_2}=6.6 \times 10^4 \text{ mol/m}^3$ , yields  $t^*=6 \text{ h}$ .  $V_{Mg}^{MgB_2}=5.6 \times 10^4 \text{ mol/m}^3$  Similarly, to ensure completion of reaction at 900 °C at 4 h (When the time taken for completion of stage 1 and 2 is  $\sim 1 \text{ h}$ ), a uniform particle size of  $\sim 14 \mu\text{m}$  would be required for this process.

As the  $MgB_2$  layer forms on the surface of particle, it almost doubles in volume, leading to impingement of particles on one another. A large contact area between the particles presents clear evidence of sintering between the particles (Figure 5.12). The critical current density is essentially a function of  $MgB_2$  phase fraction and degree of sintering between the particles. These two factors together form  $A_f$ , the effective cross-sectional area. Therefore,  $J_c$  increases almost linearly with the reaction temperature, as expected (Figure 6.9).

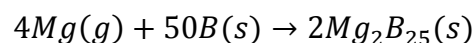
Relative density can only be increased by removal of porosity and growth of neck region by material transport to the pores (Figure 1). In other words, increase in relative density is closely associated with growth of grain boundaries (GB). A relationship between degree of sintering and hardness is demonstrated by Mukhopadhyay *et al* [275] and more recently by Dancer *et al* in  $MgB_2$  [148]. As more GBs form, more inter-particle supercurrent paths are created. In this study, these GBs are less likely to contain significant amount of non-superconducting phases, since these are created by freshly formed  $MgB_2$ . Therefore, hardness can be co-related to connectivity in this case. Thus an observed increase in hardness of these samples with temperature gives independent evidence of sintering between the  $MgB_2$  particles. Finally, in order to conclusively show that the mechanism of  $MgB_2$  phase formation varies significantly in  $\beta$ -B compared to amorphous B, a SEM image of the polished surface of  $MgB_2$ -HCA is shown. HCA powder contained primarily amorphous B with a small amount  $\beta$ -B (Figure 4.3(b)). The particles in figure 6.13 indicated by yellow dotted circles show all the familiar cracks that were so far observed in this study, and are distinctly different from other particles. Clearly, these yellow dotted particles were transformed from  $\beta$ -B.

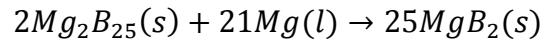


**Figure 6.13** SEM images of microstructure of  $MgB_2$ -HCA. Particle indicated by yellow dotted circles are formed from  $\beta$ -B while other particles are formed from amorphous boron.

## 6.6 Summary

It can be concluded that  $MgB_2$  phase formation in the IG process is a 3 stage process that can be summarized by the following chemical equations.





With the formation of the intermediate phase  $Mg_2B_{25}$  and associated volume expansion, cracks were initiated in all boron particles. These cracks propagated radially inwards, originating from crack tip stresses, resulting in fracture and disintegration in a number of particles and thereby offering better kinetics by exposing a large surface area for reaction. Mg infiltration in the precursor was rapid, aided probably by vapour phase transport. This was followed by  $MgB_2$  layer growth, limited by the diffusion of Mg atoms, and simultaneous sintering together to form grain boundaries. Despite reaction at a high temperature (900 °C, 4 h), the samples contained residual intermediate boride ( $Mg_2B_{25}$ ). Therefore, an optimized particle size, of sufficient size to create pore geometries to facilitate Mg(l) infiltration, yet small enough to ensure complete diffusion of Mg atoms to the center and to provide grain boundary pinning, could be the way forward for the fabrication of high performance IG processed  $MgB_2$  bulk superconductors.

## Chapter 7. Carbon Doping in MgB<sub>2</sub>

### 7.1 Introduction

Over the last 15 years, various methods have been developed and optimised to obtain dense high performance MgB<sub>2</sub> bulks by techniques such as high pressure sintering [148, 179, 180, 181], spark plasma sintering [276] or Infiltration [161, 162]. The high density is associated with the high effective current carrying cross section which results in high  $J_c$ . However, its rapid drop with external field is proven to be Achilles heel of MgB<sub>2</sub>, although self-field  $J_c$  as high as  $10^6$  A/cm<sup>2</sup> has been obtained (Figure 7.1).

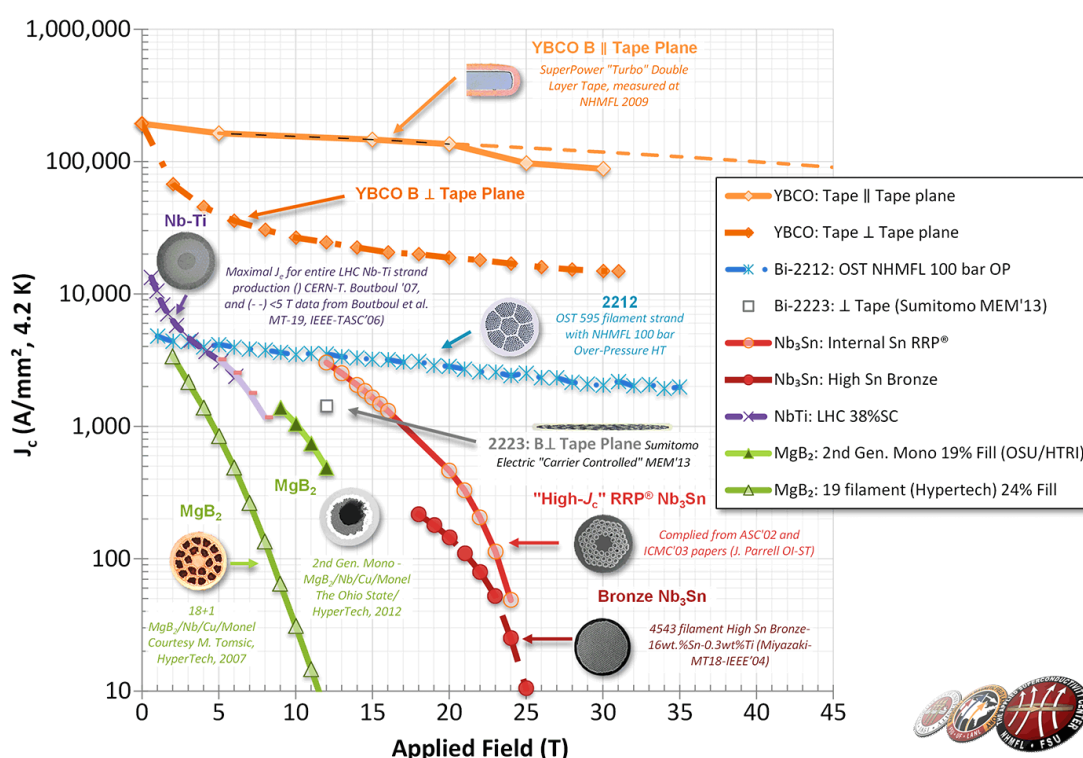


Figure 7.1 Comparison of  $J_c$ - $B$  (4.2 K) plots for a variety of commercial superconductors [277].

Furthermore, the inherent anisotropy in the critical fields of MgB<sub>2</sub> results in low  $H_{irr}$  in random polycrystalline MgB<sub>2</sub> samples [40-43]. Therefore, it is extremely important to enhance the in-field performance of MgB<sub>2</sub> in order to replace currently used Nb based LTS materials, which require expensive He as a coolant during operation.

Performance of MgB<sub>2</sub> is generally enhanced by an increase in flux pinning and  $H_{irr}$  by using fine starting powders (Mg and B) [174-178]. Other approaches include irradiation of gamma particles, neutrons and heavy metal ions at high velocities [55-57]. This creates defects in the microstructure which may induce defects such as dislocations or stacking faults that can act



as pinning centres and thereby improve  $H_{irr}$ . Another practical method includes enhancement in  $H_{c2}$ , which is a thermodynamic property which depends only on the electronic structure, by means of doping. Carbon in particular, is proven to be a promising candidate to enhance  $H_{c2}$  in MgB<sub>2</sub>. Carbon doping is also accompanied by a degradation of crystallinity [113],  $\delta T_c$  pinning [114] and reduced anisotropy [127], all of which contribute to the enhancement in field  $J_c$ . The effect of C doping on structure and properties of MgB<sub>2</sub> have been summarised in section 2.8.2.

In the present work, B<sub>4</sub>C (99.9% purity) has been used as a source of carbon, since B<sub>4</sub>C is a rich source of B (80% atomic) and C is already distributed uniformly on the atomic level. The effect of addition of B<sub>4</sub>C was studied initially by Yamamoto *et al* in *in situ* sintered MgB<sub>2</sub> [120]. Moreover, a higher reactivity of B<sub>4</sub>C with Mg allows the use of a relatively lower reaction temperature, thus inhibiting grain growth and thereby enhancing grain boundary pinning. [120]. Four precursors were pressed of size Dia 32 mm, 6 mm thick by mixing B and B<sub>4</sub>C powders as (100- $x$ )% B- $x$ % B<sub>4</sub>C (hereafter mentioned as B- $x$ % B<sub>4</sub>C) with  $x$  varying as 10, 20, 60 and 100, in weight proportion. For the purpose of comparison, one precursor with SiC addition ( $x=10$ ) was also prepared, since SiC has also proven to be potential candidate for C doping. The precursors were then infiltrated with Mg(l) and reacted at 850 °C for 4 h as per the procedure described in Chapter 3. The carbon substitution and changes in lattice parameters were then studied in resultant samples and their effect on superconducting properties was analysed. Finally, homogeneous MgB<sub>2</sub> bulk samples were fabricated using MPIG technique described in chapter 5 and trapped field measurements were performed.

## 7.2 Effect on $T_c$

Figure 7.2(a) shows normalised magnetization as a function of temperature for samples with  $x=10$  SiC,  $x=10$  B<sub>4</sub>C and un-doped sample. Effective carbon addition (atomic%) to the precursor in  $x=10\%$  SiC is 2.9%, in comparison with 2.13% in  $x=10\%$  B<sub>4</sub>C. Both the SiC and B<sub>4</sub>C addition of 10% resulted in a reduction of  $T_c$  (onset) from 37.9 K (un-doped) to 36.2 K. Such reduction of  $T_c$  arises from  $\sigma$  band filling by electron doping, since boron exhibits three electrons in valance shell while carbon exhibits four. Electron doping reduces the number of holes at the top of the  $\sigma$  bands together with a reduction in the electronic density of states [115,125]. Moreover, the B<sub>4</sub>C added sample shows a relatively sharp superconducting transition while the SiC added sample shows a very broad transition. This suggests that

carbon doping has been non-uniform upon SiC addition and uniform with B<sub>4</sub>C addition. This can be explained by the homogeneous distribution of C on an atomic level in the case of B<sub>4</sub>C.

Figure 7.2(b) shows normalised magnetization-temperature plots for samples added with varying amount of B<sub>4</sub>C, from  $x = 0, 10, 20, 60$  and  $100$ . All samples showed a reasonably sharp transition with  $T_c$  (Onset) reducing from  $37.9$  K ( $x = 0$ ) to  $25.9$  K ( $x = 100$ , C = 20 atomic %). This clearly is an indicator of decreasing  $T_c$  as a result of C doping in MgB<sub>2</sub>. The superconducting transition for the sample added with 10% B<sub>4</sub>C was sharp, whereas further additions showed two noticeable  $T_c$ , as seen from black arrows in figure 7.2(b). For instance, sample  $x=20$  show  $T_c$  at  $36.95$  K and  $32.08$  K, Sample  $x=60$  showed  $T_c$  at  $36$  K and  $31.6$  K while sample  $x= 100$  showed  $T_c$  at  $25.67$  K and  $22.1$  K. The appearance of two  $T_c$  can be directly correlated to two types of Mg(B<sub>1-x</sub>C<sub>x</sub>)<sub>2</sub> phases with distinct  $x_i$ . Since single crystals of Mg(B<sub>1-x</sub>C<sub>x</sub>)<sub>2</sub> do not show such a phase separation, as discussed in the next section, this variation might have originated from the slightly inhomogeneous doping of C for higher additions of B<sub>4</sub>C.

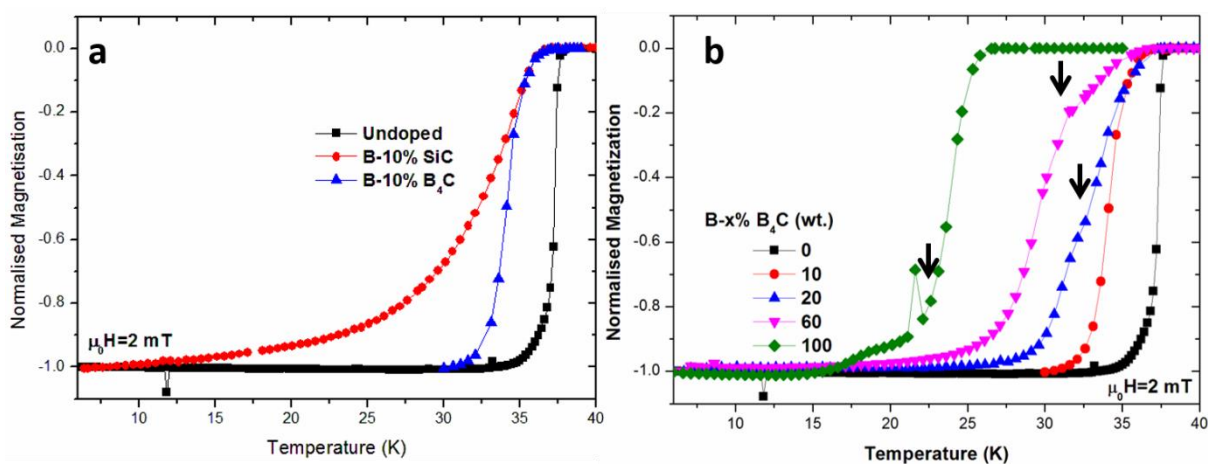
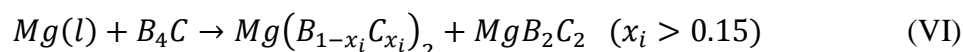
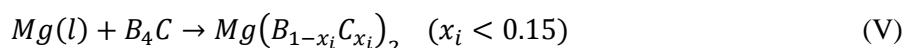


**Figure 7.2(a)** Magnetization response with respect to temperature under external field of 2mT shown for (a)  $x=10\%$  SiC and  $10\%$  B<sub>4</sub>C and (b) for varying B<sub>4</sub>C addition from  $x=0$  to  $x=100$  B<sub>4</sub>C. Black arrows indicate multiple observed  $T_c$ .

### 7.3 Phase Analysis

Figure 7.3(a) compares XRD patterns obtained for B<sub>4</sub>C added samples ( $x = 10, 20, 60$  and  $100$ ) with undoped sample. The un-doped sample shows the presence of familiar phases: highly crystalline MgB<sub>2</sub>, residual Mg and small amount of metastable Mg<sub>2</sub>B<sub>25</sub>. On the other hand, B<sub>4</sub>C ( $x = 100$ ) infiltrated with Mg(l), shows superconducting Mg(B, C)<sub>2</sub>, MgB<sub>2</sub>C<sub>2</sub> and small unreacted B<sub>4</sub>C phases. The reaction of B<sub>4</sub>C with Mg has been studied before and is known to result in MgB<sub>2</sub> according to the following chemical equation [278].



A detailed analysis by Wilke *et al* suggests that MgB<sub>2</sub>C<sub>2</sub> phase begins to appear when carbon saturation is reached, i.e. when C can no longer be accommodated in the MgB<sub>2</sub> lattice. It is therefore precipitated in the form of MgB<sub>2</sub>C<sub>2</sub> [278]. Analysis of C doped MgB<sub>2</sub> single crystals show that C saturation occurs at about  $x_i = 0.15$  [279]. Therefore MgB<sub>2</sub>C<sub>2</sub> was only observed for  $x = 60$  and 100 in the present study. Moreover, presence of unreacted B<sub>4</sub>C is indicative of the fact that not all the carbon introduced in the precursor is doped in the MgB<sub>2</sub> lattice. Samples for lower B<sub>4</sub>C additions ( $x = 10\%$ ,  $20\%$ ) show a majority of MgB<sub>2</sub>, without phase separation, with residual Mg.

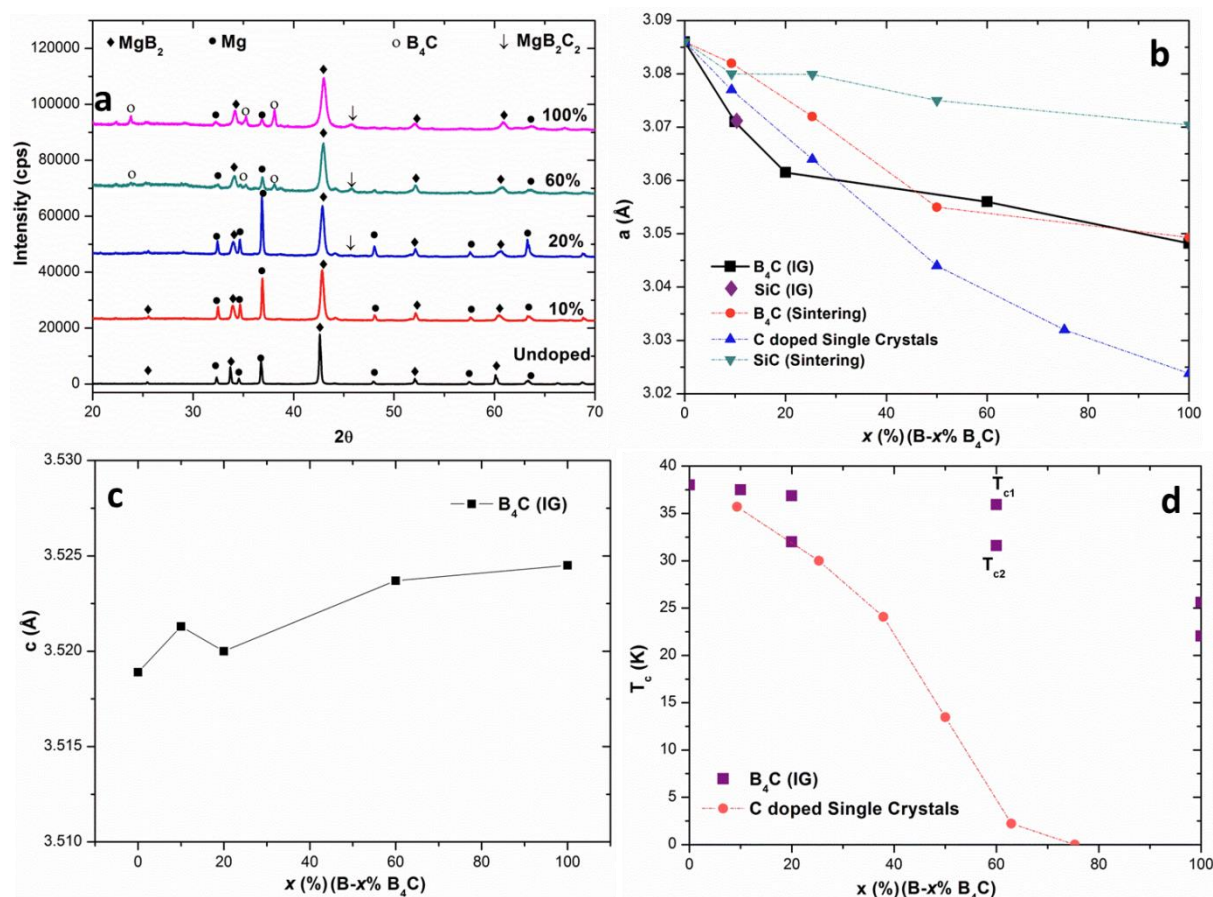


Figure 7.3(a) XRD patterns for un-doped sample and B<sub>4</sub>C added samples ( $x = 10, 20, 60$  and  $100$ ). Figure (b) and (c) show obtained lattice parameters,  $a$  and  $c$  respectively, after carbon doping. Single crystal data obtained from reference [279]. (d) Obtained  $T_c$ (Onset) in various C doped samples along with  $T_c$  of C doped MgB<sub>2</sub> single crystals.

Figure 7.3(a) offers significant insights into carbon doping in MgB<sub>2</sub>. In B<sub>4</sub>C added samples, the peaks corresponding to the plane, which possess a component of plane normal in  $a$ - $b$

plane, show a consistent and significant shift towards higher angles with considerable broadening. In addition, peak positions corresponding to the planes parallel to basal (001) plane remains almost unchanged. This clearly suggests, and is in good agreement with previously observed studies [111, 113, 120], that carbon doping induces strain in the  $a$ - $b$  plane only. Figure 7.3(b) shows the calculated in-plane lattice parameter as a function of B<sub>4</sub>C addition. Obtained data is compared with C-doped MgB<sub>2</sub> single crystals and along with C the introduction with B<sub>4</sub>C and SiC through the sintering route under similar reaction conditions [120]. It is quite apparent from the change in ' $a$ ' that B<sub>4</sub>C addition is more efficient than SiC. SiC addition led to change in ' $a$ ' from 3.086 Å (undoped) to 3.0703 Å ( $x = 100$ ), whereas B<sub>4</sub>C addition through an IG or sintering process led to significant change in ' $a$ '. Both techniques showed an in-000plane lattice parameter  $a = 3.048$  Å for  $x = 100\%$ . In comparison, carbon doped single crystals show  $a = 3.023$  Å for  $x = 100\%$ . Interestingly, carbon doping for samples with  $x = 10\%$  and  $x = 20\%$  appears to be higher than obtained data for C-doped single crystals. This could be due to the fact that about 15% boron is present in the form of intermediate boride Mg<sub>2</sub>B<sub>25</sub> and not fully transformed into superconducting MgB<sub>2</sub>. This possibly resulted in an apparent increase in carbon concentration in MgB<sub>2</sub>. Similarly, Figure 7.3(c) shows the calculated lattice parameter ' $c$ ' from (002) reflection as a function of nominal B<sub>4</sub>C addition. A small change in ' $c$ ' was observed from 3.518 to 3.524 Å from undoped to  $x = 100\%$  respectively. The actual carbon substitution from the B site in Mg(B<sub>1-x</sub>C<sub>x</sub>)<sub>2</sub> after B<sub>4</sub>C addition can be estimated from figure 7.3(a). Therefore samples added with 60% and 100% B<sub>4</sub>C can be estimated to have  $x \sim 0.07$  and  $x \sim 0.09$  respectively. Figure 7.3(d) shows the variation of  $T_c$  (onset) with B<sub>4</sub>C addition. A systematic decrease in  $T_c$  with B<sub>4</sub>C addition was seen, indicative of the suppression of  $T_c$  as a result of C substitution. A comparison of measured  $T_c$  with C-doped single crystals suggests a C substitution of up to 8.6%, which is in fairly good agreement with 9% C substitution as suggested by Figure 7.3(b). The  $T_c$  changed from 38.1 K to 25.62 K from undoped to  $x = 100$ .

#### 7.4 EDS Analysis - C distribution

A sample with 20% nominal addition was analysed using the SEM in order to observe the distribution of carbon within the microstructure. The back scatter electron image (Figure 7.4(a)) shows reacted B<sub>4</sub>C particles/agglomerates, which are distinctively different from other particles that exhibit Mg veins. The particle also shows fine dark-in-contrast inclusions,

which are probably  $\text{MgB}_2\text{C}_2$  or unreacted  $\text{B}_4\text{C}$  phases. The larger particles in figure 7.4(a) with Mg veins are  $\text{Mg}_2\text{B}_{25}$  particles, characterized in detail in chapter 6.

The EDS map shows special distribution of carbon in figure 7.4(a). Clearly, carbon is distributed relatively homogeneously in  $\text{MgB}_2$  (gray contrast) and no significant segregation can be seen to the resolution limit of EDS. A small amount of C can also be seen in  $\text{Mg}_2\text{B}_{25}$  particles. This suggests that  $\text{B}_4\text{C}$  addition can indeed result in uniformly C doped  $\text{MgB}_2$  phase. Further analysis is required to understand the exact mechanism of C-doping in  $\text{MgB}_2$  via  $\text{B}_4\text{C}$ .

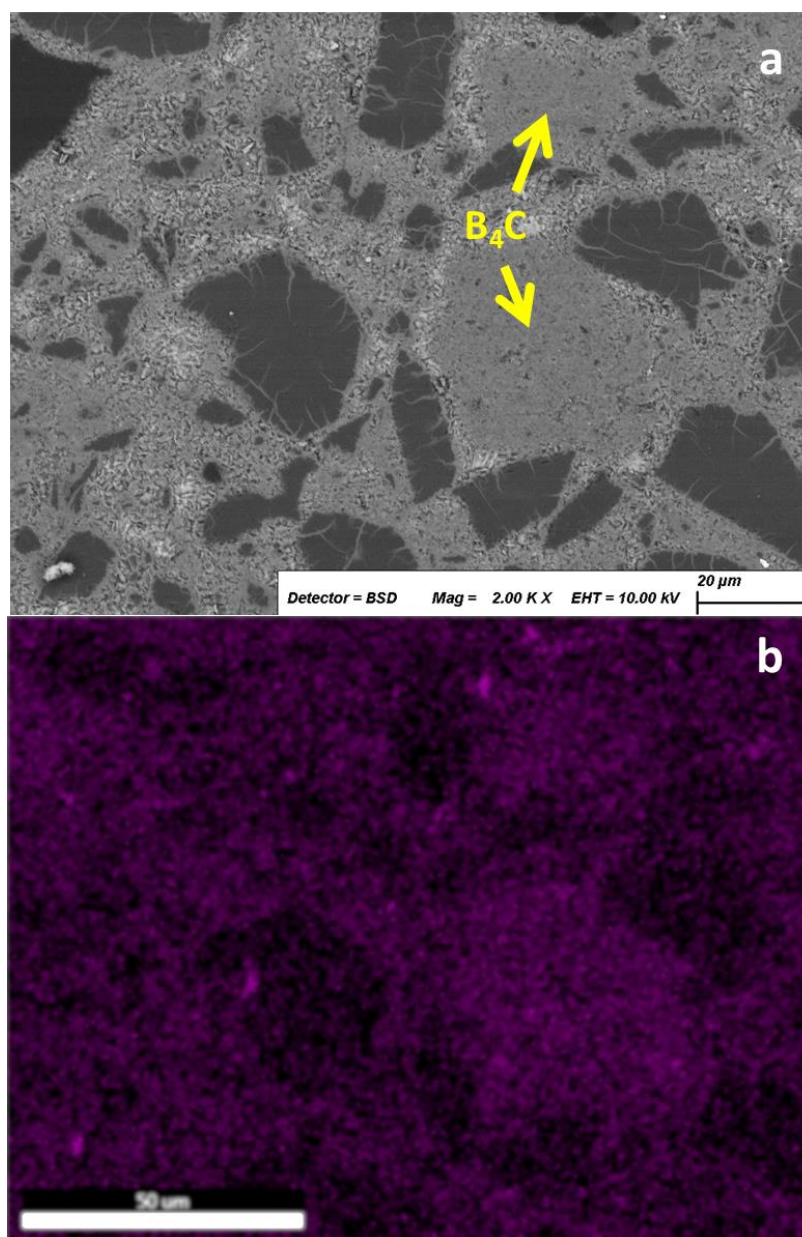


Figure 7.4(a) BSE image of sample with 20% nominal  $\text{B}_4\text{C}$  addition and (b) EDS map for C.

## 7.5 Strain Analysis

Figures 7.5(a), (b) and (c) show the magnified peak positions of (101), (100) and (002) peaks while (d) shows full width at half maximum (FWHM) of various reflections as a function of

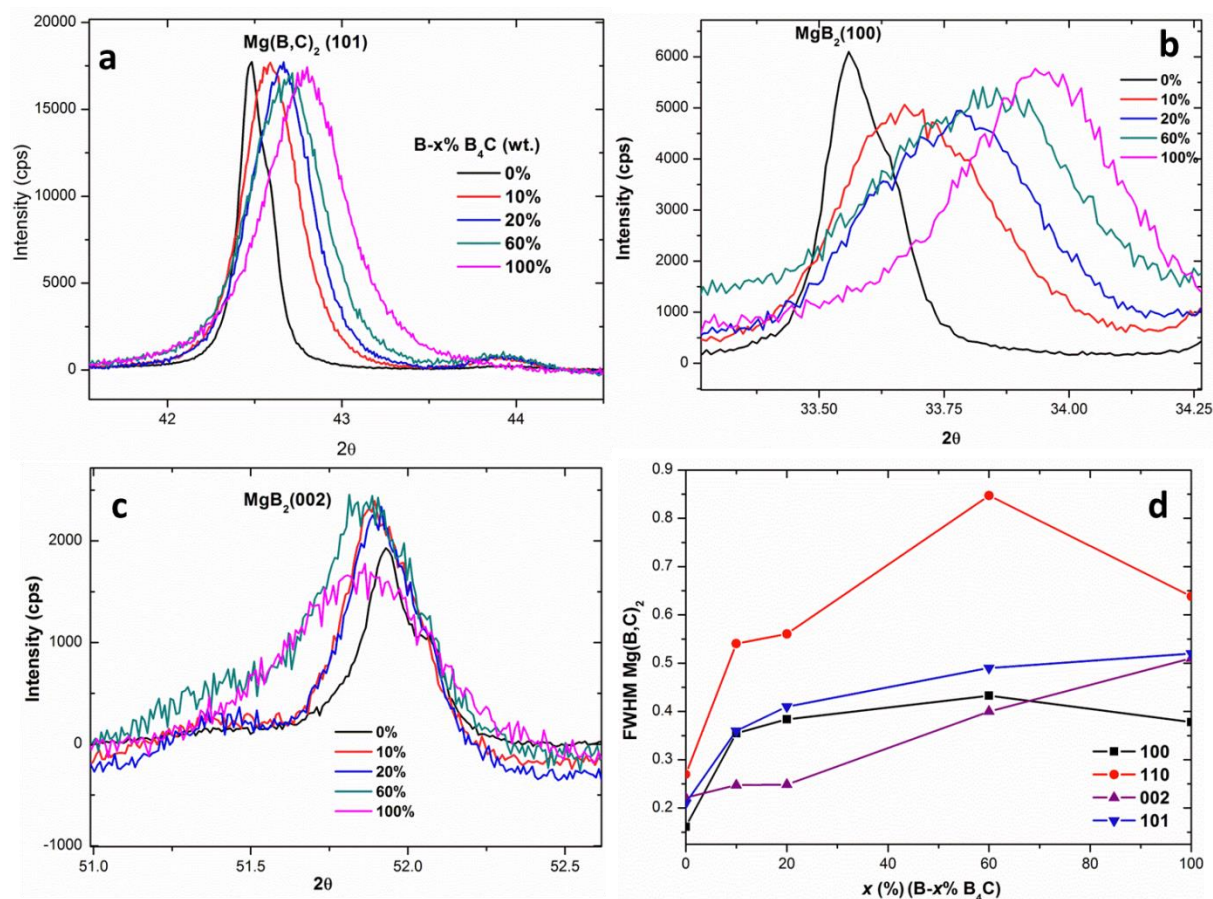


Figure 7.5 XRD patterns of un-doped and carbon doped samples showing (a) (101) (b) (100) and (c) (002) reflections. (d) showing observed FWHM in various planes.

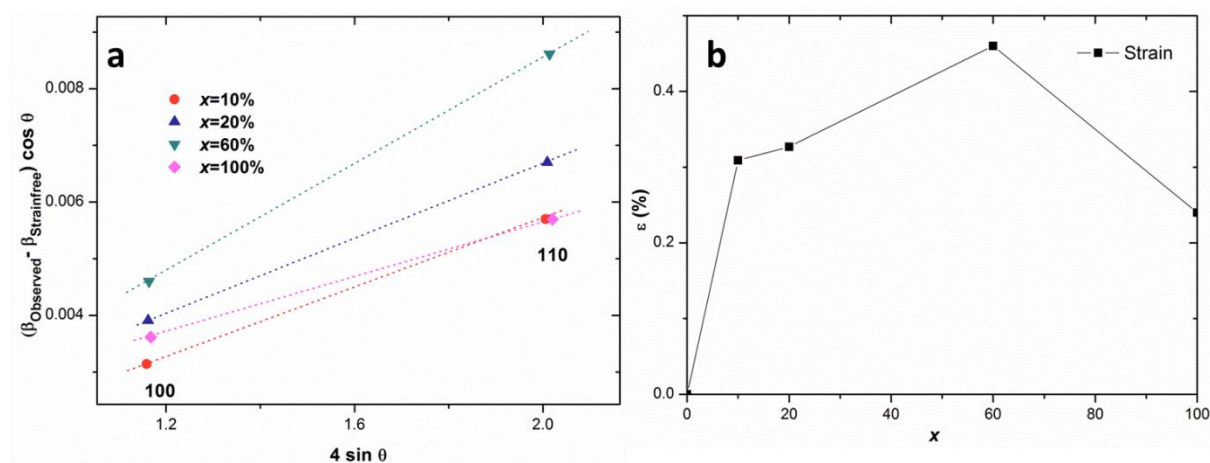


Figure 7.6(a) Williamson-Hall plot for samples with varying carbon doping and (b) non-uniform strain computed from WH plot as a function of B<sub>4</sub>C addition.

nominal B<sub>4</sub>C addition. It is quite apparent that carbon doping has induced a large amount of lattice strain/distortion and degradation of crystallinity in MgB<sub>2</sub>, mostly in the *a-b* direction, as evidenced by an increase in FWHM of (100) and (110) reflections (Figure 7.5(a) and (b)). In comparison, FWHM of (002) reflection appears rather small (Figure 7.5(c) since a small peak shift is observed for (002) reflections (Figure 7.3(c)). The strain/distortion in the MgB<sub>2</sub> lattice can be quantified by a Williamson-Hall (W-H) plot according to the following equation [280]

$$(\beta_{Observed} - \beta_{Instrumental}) \cos \theta = \frac{K_s \lambda_{X Ray}}{L} + 4\epsilon_N \sin \theta \quad (7.1)$$

Where  $\beta_{Observed}$  and  $\beta_{Instrumental}$  are the observed and instrumental broadening in radian.  $K_s$  is the Scherrer constant determined by crystallite size ( $\sim 1$ ),  $\lambda_{X Ray}$  and  $L$  are wavelength of X-ray and size of diffracting domain in Å respectively.  $\epsilon_N$  is the non-uniform strain. Here,  $\beta_{instrumental}$  is approximated to be FWHM of the undoped sample. Also, since strain is present only in *a-b* plane, only (100) and (110) reflections are considered for strain analysis and the WH plot is shown for nominal B<sub>4</sub>C additions (Figure 7.6(a)). Samples with nominal B<sub>4</sub>C additions of 10%, 20%, 60%, 100% showed an overall average strain of 0.1%, 0.08%, 0.35% and 0.22% respectively (Figure 7.6(b)).

### 7.6 Effect on $J_c$

Figure 7.7(a) compares  $J_c$  at 5 and 20 K as a function of external fields for samples added with  $x = 10$  (SiC),  $x = 10$  (B<sub>4</sub>C) and un-doped MgB<sub>2</sub> sample. It can be seen that carbon doped samples, both with SiC and B<sub>4</sub>C addition, show a marked difference in  $J_c$ - $H$  behaviour, especially at 5 K. These samples also showed much weaker  $J_c$ - $H$  dependence compared to the un-doped sample. The B<sub>4</sub>C added sample in particular, showed a much enhanced self-field  $J_c$  of 600 kA/cm<sup>2</sup> (5 K) and 350 kA/cm<sup>2</sup> (20 K), which represents 50% and 36% increase with respect to undoped sample. Moreover, in-field  $J_c$  (5 T, 5 K) as high as 50 kA/cm<sup>2</sup> was measured in this sample, which is nearly 10 times more than the undoped sample at 5 T (5 K). This clearly suggests that flux pinning, especially at higher external fields, was significantly enhanced as a result of carbon doping. On the other hand, the SiC added sample did not show a similar increment in  $J_c$  since C doping was quite inhomogeneous (Figure 7.2(a)), although  $J_c$ - $B$  behaviour was similar to the B<sub>4</sub>C added sample. Moreover, the SiC reaction with Mg is known to lead to the formation of non-superconducting Mg<sub>2</sub>Si inclusions,

which reduces the effective current carrying cross section [113, 281]. The SiC added sample showed almost similar self-field  $J_c$  at 5 K while the self-field  $J_c$  was reduced to 50% at 20 K with respect to un-doped sample.

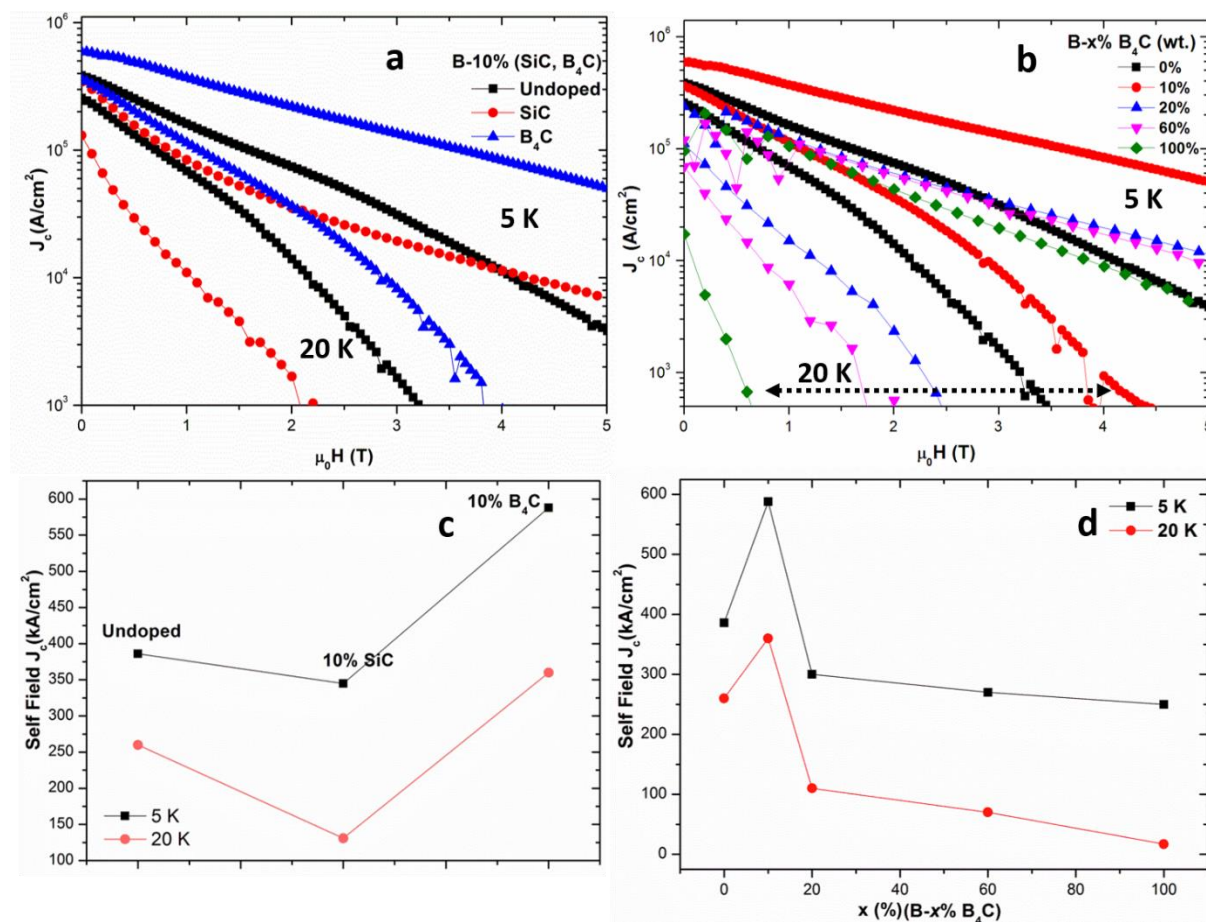


**Figure 7.7**  $J_c$  as a function of external field for samples added with (a)  $x = 10$  SiC and B<sub>4</sub>C and (b) varying B<sub>4</sub>C additions from  $x = 0$  to  $x = 100$ . The self-field  $J_c$  for samples added with (c)  $x = 10$  SiC and B<sub>4</sub>C and (d) varying B<sub>4</sub>C additions from  $x = 0$  to  $x = 100$ .

In order to observe the change in  $J_c$  with carbon doping,  $J_c$ - $H$  plots for samples with varying B<sub>4</sub>C additions are shown in figure 7.7(b). The sample with nominal B<sub>4</sub>C addition  $x = 100$  showed a quite high self-field  $J_c$  of 250 kA/cm<sup>2</sup> at 5 K despite low  $T_c$  (22 K). This together with the  $M$ - $T$  plot (Figure 7.2(a)) and XRD for  $x = 100$  (Figure 7.3(a)) suggests that B<sub>4</sub>C is not only highly reactive towards Mg, but the effective current carrying area is also reasonably high. This sample also showed better in field  $J_c$  ( $> 5$  T) at 5 K compared to un-doped sample. The sample with 10% B<sub>4</sub>C showed optimum  $J_c(B)$  performance, while  $J_c$  gradually degraded with subsequent additions of B<sub>4</sub>C. This clearly demonstrates a ‘trade-off’ between enhanced pinning and reduction in  $T_c$  as a result of C doping. Also, a relatively lower  $J_c$  is observed at 20 K in B<sub>4</sub>C added samples, which can be explained by equation 5.1.



Samples with nominal B<sub>4</sub>C additions of  $x = 20, 40, 60$  and  $100$  showed a gradually decreasing self-Field  $J_c$  of  $300 \text{ kA/cm}^2, 266 \text{ kA/cm}^2, 250 \text{ kA/cm}^2$  at  $5 \text{ K}$  and  $108 \text{ kA/cm}^2, 71 \text{ kA/cm}^2, 17 \text{ kA/cm}^2$  at  $20 \text{ K}$  (Figure 7.7(d)).

### 7.7 Pinning Force

Figure 7.8(a) and (b) show the variation of pinning force with magnetic field (Kramer's plot) for varying nominal B<sub>4</sub>C additions at  $5 \text{ K}$  and  $20 \text{ K}$  respectively [282]. Linear dependences of pinning force with the magnetic field for all the samples suggests the flux pinning mechanism is governed by pinning sites which are planar such as grain boundaries. Moreover, all the samples with B<sub>4</sub>C additions showed a weaker dependence of Kramer's pinning force  $F_k$  with field, strongly suggesting the enhancement of pinning as a result of C doping sites.

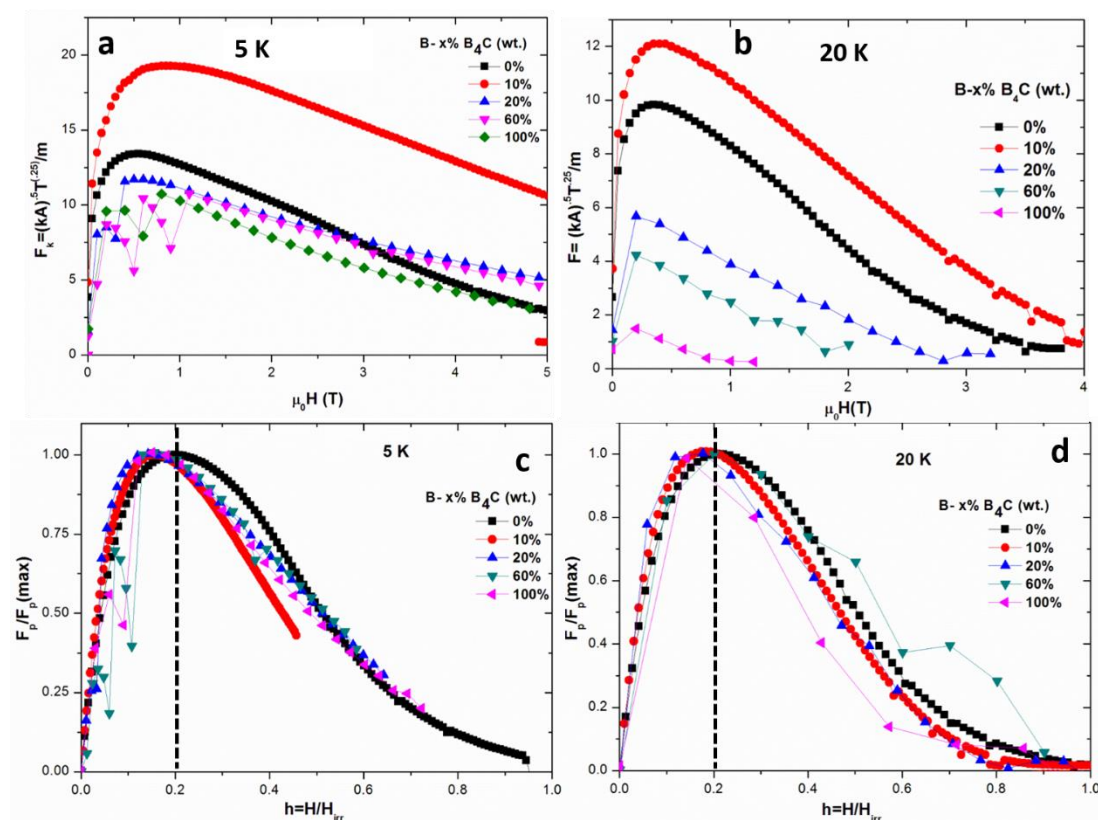


**Figure 7.8** Kramer's plot at (a)  $5 \text{ K}$  and (b)  $20 \text{ K}$  for undoped and B<sub>4</sub>C added samples MgB<sub>2</sub> samples as a function of magnetic field. Pinning force ( $JxB$ ) for undoped and B<sub>4</sub>C added MgB<sub>2</sub> samples at (c)  $5 \text{ K}$  and (d)  $20 \text{ K}$ .

The samples  $x = 0, 10, 20, 40, 100$  showed  $-dF_k/dH$  ( $\text{kA}^2 \text{T}^{-0.75} \text{m}^{-1}$ ) values of  $2.62, 2.32, 1.5, 1.67, 2.11$  at  $5 \text{ K}$  and  $3.48, 3.44, 2.19, 2.43, 1.85$  at  $20 \text{ K}$ . This data indicates that extra pinning mechanism may be operative in the carbon doped samples along with grain boundary pinning. Moreover, the slope of pinning force co-relates very well with the strain analysis

from figure 7.6(b). For example, the sample with B<sub>4</sub>C addition of  $x = 60\%$  exhibited maximum strain and also showed weakest field dependence of pinning force. Therefore, increased pinning force together with  $H_{irr}$  is clearly a result of induced strain in the lattice, or degradation in crystallinity of MgB<sub>2</sub>. Such defects are believed to enhance the intra-band scattering and reduce the electron mean free path  $l$  and coherence length  $\xi$  according to the equation  $1/\xi = 1/l + 1/\xi_0$ . Shortening in  $\xi$  allows a larger flux to be accommodated in the sample, which results in increased  $H_{c2}$ .

The variation of normalised pinning force  $F_p/F_p(max)$  with normalised field ( $h=H/H_{irr}$ ) is shown in figure 7.8(c) and (d) for undoped and C doped samples.  $H_{irr}$  is defined as field at which  $J_c=10^2$  A/cm<sup>2</sup>.

It is worth recalling the expression proposed by Dew-Hughes on the summation of pinning forces [10].

$$F_p(h) = F_p/F_{p(max)} \propto h^p(1 - h)^q \quad (7.2)$$

The parameters  $p$  and  $q$  are material constants. Dew-Hughes suggested six different pinning mechanisms using the above equation (2). (1)  $p = 0, q = 2$ : normal core pinning, volume pins; (2)  $p = 1, q = 1$ :  $\Delta k$ -pinning, volume pins (3)  $p = 1/2, q = 2$ : normal core pinning, surface pins; (4)  $p = 3/2, q = 1$ :  $\Delta k$ -pinning, surface pins; (5)  $p = 1, q = 2$ : normal core pinning, point pins; and (6)  $p = 2, q = 1$ :  $\Delta k$ -pinning, point pins.

For the sample with dominant surface pinning, the maximum of the normalized pinning force is expected at  $h = 0.2$ , as evidenced by the plot for undoped MgB<sub>2</sub> in figure 7.8(c) and (d). Such pinning is also observed in Nb based superconductors where grain boundaries are dominant pinning sites [11]. In B<sub>4</sub>C added samples, the normalised pinning force maxima is shifted to lower fields at both 5 and 20 K. For instance, Samples with 10% and 20% nominal B<sub>4</sub>C addition show maximum pinning force at  $h = 0.15$  and  $h = 0.14$  respectively at 5 K. At 20 K, samples 10% and 20% B<sub>4</sub>C addition showed a maxima at  $h = 0.18$  and 0.15 respectively. A similar feature was also observed by Matsushita *et al* in MgB<sub>2</sub> bulk samples [283]. This suggests the presence of flux pinning centres other than the ‘Surface’ in C doped samples, such as volume pinning, as  $p$  approaches 0. Fine precipitates in the microstructure such as MgB<sub>2</sub>C<sub>2</sub> or B<sub>4</sub>C probably contributed towards volume pinning. The contribution to pinning from inclusions was reported by Dou *et al* in Mg(B,C)<sub>2</sub> addition with SiC addition

[114]. Alternatively, such shift of pinning force maxima towards lower field could also result from inhomogeneous carbon doping, and a resultant distribution of  $H_{c2}$ , in the microstructure. Moreover, increases in  $H_{irr}$  are also attributed to reduced anisotropy in  $H_{c2}$  in C-doped MgB<sub>2</sub>, as shown by Eisterer *et al* [43]. Numerous reports also reaffirm the presence of strengthened grain boundary pinning at higher reduced fields, since intra-band scattering in C doped MgB<sub>2</sub> should not alter pinning mechanism [120, 286].

### 7.8 Fabrication of High Performance homogeneous C-doped samples

The above analysis on small C-doped MgB<sub>2</sub> samples strongly suggests a significant improvement in  $J_c(B)$  performance, especially in the in-high field regime. This shows a great prospect for fabricating the high performance C-doped MgB<sub>2</sub> bulks, which can trap higher magnetic flux. Most of characterization techniques used to plot  $J_c$ - $B$ ,  $M$ - $T$  or resistivity relationships involve the small representative specimen of size of dimensions 3mm × 2mm × 2mm, as used in the current study. Extrapolation of the properties measured in small samples to estimate bulk properties can often be inaccurate as the number of defects, which increase with sample size, have a significant impact on properties of MgB<sub>2</sub>. In the present study, the presence of continuous Mg channels in bulk MgB<sub>2</sub> is quite well known and their effect is studied in detail in chapter 5. Therefore, to realize the advantage offered carbon doping on a larger scale, larger bulks (32 mm Dia × 6 mm thick) were fabricated by combining carbon doping and the Modified Precursor Infiltration and Growth (MPIG) technique, as described in chapter 5. Thus B+B<sub>4</sub>C powder mix is further enriched with pre-reacted MgB<sub>2</sub> powder (10% mole) in order to achieve uniform infiltration and a homogeneous Mg-channel free microstructure. For instance 4.725 g of B (63%), 0.75 g B<sub>4</sub>C (10%) and 2.02 g MgB<sub>2</sub> (27%) were taken to prepare a porous preform in order to fabricate homogeneous carbon doped MgB<sub>2</sub> bulks. Three such bulks were fabricated, one with 5% and two with 10% nominal B<sub>4</sub>C addition. Such homogeneous carbon doped bulks are subsequently referred to as  $x\%$  B<sub>4</sub>C (MPIG), where  $x$  is weight % of B<sub>4</sub>C in the preform prior to infiltration.

Figure 7.9(a) shows the normalised magnetization for un-doped, 10% B<sub>4</sub>C and 10% B<sub>4</sub>C (MPIG) sample, which showed  $T_c(\text{onset})$  at 36.4 K and 34.1 ( $T_{c2}$ ) K respectively. The apparent difference between 10% B<sub>4</sub>C and 10% B<sub>4</sub>C (MPIG) superconducting transitions suggests that C-doping has not taken place in the pre-reacted MgB<sub>2</sub> particles in the bulk. As a result, carbon doping in MgB<sub>2</sub> is higher in the MgB<sub>2</sub> which formed during the processing from B powder.

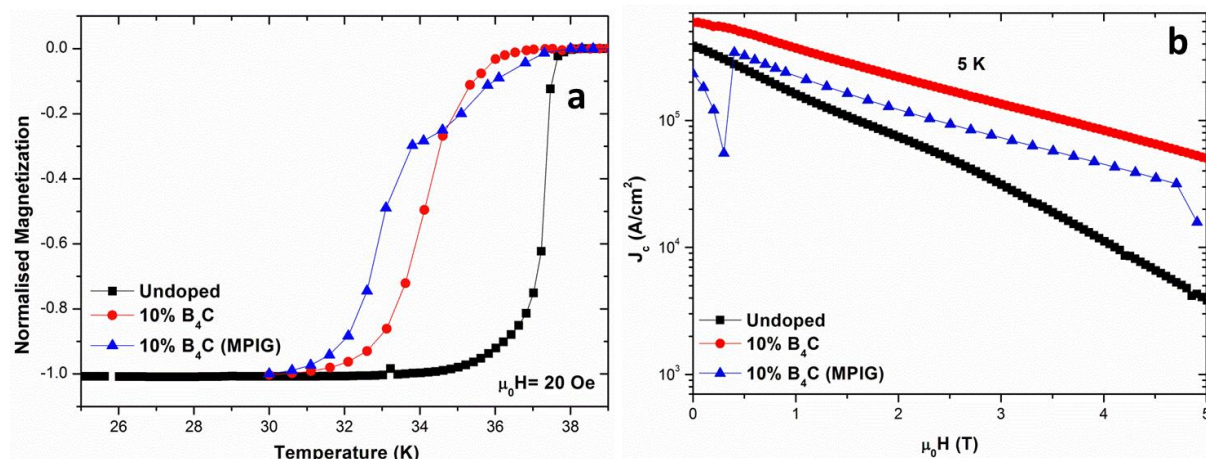


**Figure 7.9(a)** Superconducting  $M-T$  transition and **(b)**  $J_c$ - $B$  (5 K) plots for un-doped 10% B<sub>4</sub>C and 10% B<sub>4</sub>C (MPIG) samples.

A comparison of critical current density of undoped, 10% B<sub>4</sub>C doped and 10% B<sub>4</sub>C (MPIG) sample is shown in figure 7.9(b). Each undoped, 10% B<sub>4</sub>C doped and 10% B<sub>4</sub>C (MPIG) sample showed a self-field  $J_c$  of 380, 440 and 600 kAcm<sup>2</sup> respectively. Although the magnitude of  $J_c$  is reduced in 10% B<sub>4</sub>C (MPIG) sample with respect to 10% B<sub>4</sub>C while still maintaining quite high value in comparison to the undoped sample, the field dependence of  $J_c$  remained very similar. The reduced  $J_c$  in 10% B<sub>4</sub>C (MPIG) is clearly a result of weakly linked grain boundaries formed by the pre-reacted MgB<sub>2</sub> particle, as demonstrated in section 5.5.1 and also reported by several researchers [36].

### 7.8.1 Trapped Field Measurements

The ‘Field cooled magnetization’ method was used to obtain a trapped field on C-doped MgB<sub>2</sub> bulks as described in Chapter 3. Three sets of measurements were performed on, (1) 5% B<sub>4</sub>C (MPIG) (Figure 7.10(a)), (2) two sample stack of 10% B<sub>4</sub>C (MPIG) MgB<sub>2</sub> (Figure 7.10(b)) and (3) five sample stack (Figure 7.10(c)). The arrangement of bulks and location of hall probes for the first two measurements is shown in their respective insets and in figure 7.10(d) for 5 sample stack (hereafter referred to as Stack-5). Measurements (2) (Figure 7.10(b)) and (3) (Figure 7.10(c)) were made in order to keep demagnetization effects to a minimum. The measurements involved cooling down the sample or sample arrangement to 5 K under an external magnetic field of 6 T (5 T for two sample stack of 10% B<sub>4</sub>C (MPIG)), applied perpendicular to the top surface of the sample. Measurement (2) was repeated with an external field of 6 T and had very little effect on magnetic flux density measured in both in the centre and surface of two-sample stack.

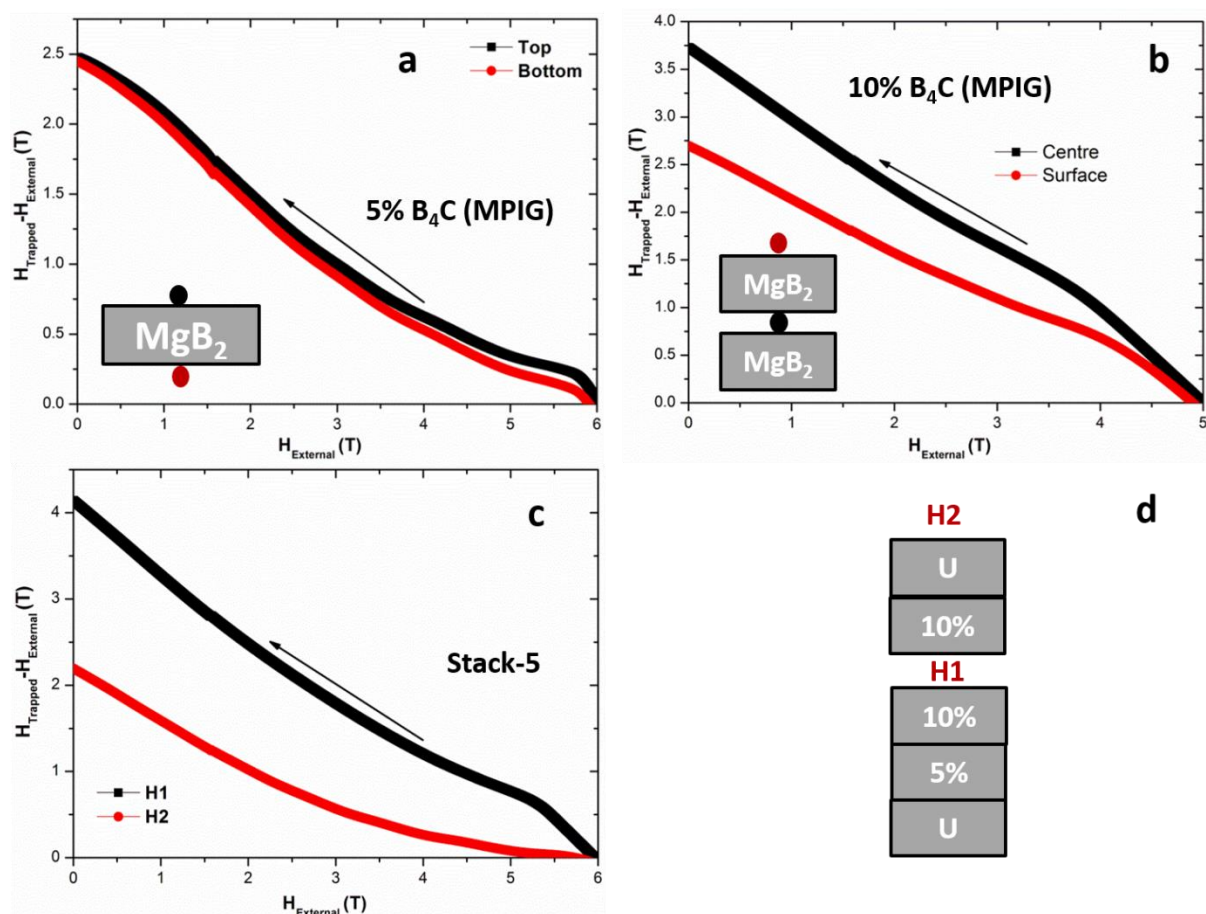


**Figure 7.10** Difference between trapped magnetic flux density and external field as a function of external field for figure (a) a single 5% B<sub>4</sub>C (MPIG), (b) two sample stack of 10% B<sub>4</sub>C (MPIG) and (c) Stack-5. Location of hall sensors shown in (a) and (b) inset. (d) Arrangement of bulks and location of Hall sensors in stack-5. U stands for undoped bulk.

The obtained trapped field as a function of temperature for a single 5% B<sub>4</sub>C (MPIG), two sample stack of 10% B<sub>4</sub>C (MPIG) is shown in figures 7.11(a) and (b) respectively. For the purpose of comparison, the trapped field at the centre of the surface of a single undoped bulk is shown in figure 7.11(a), while the trapped field at the centre and surface of two-sample-stack of undoped bulks is shown in figure 7.11(b). A magnetic field of 2.47 T and 2.44 T was recorded at 5 K on the centre of the top and bottom surfaces of 5% B<sub>4</sub>C (MPIG) bulk respectively, confirming a high degree of uniformity in the sample. This value of the trapped field represents a 16% increase over the one measured on undoped sample, which decreased with temperature reaching 0 T at 36.2 K. The two-sample stack of 10% B<sub>4</sub>C (MPIG) bulks trapped 3.75 T and 2.7 T at the centre and surface respectively at 5 K, which is a 23% increase over the trapped field in undoped bulks of the same configuration (Figure 7.11(b)), and dropped fairly quickly to reach 0 T at 34.6 K. Thus the rate of change of trapped field with temperature ( $-dB/dT$ ) increased with carbon doping.

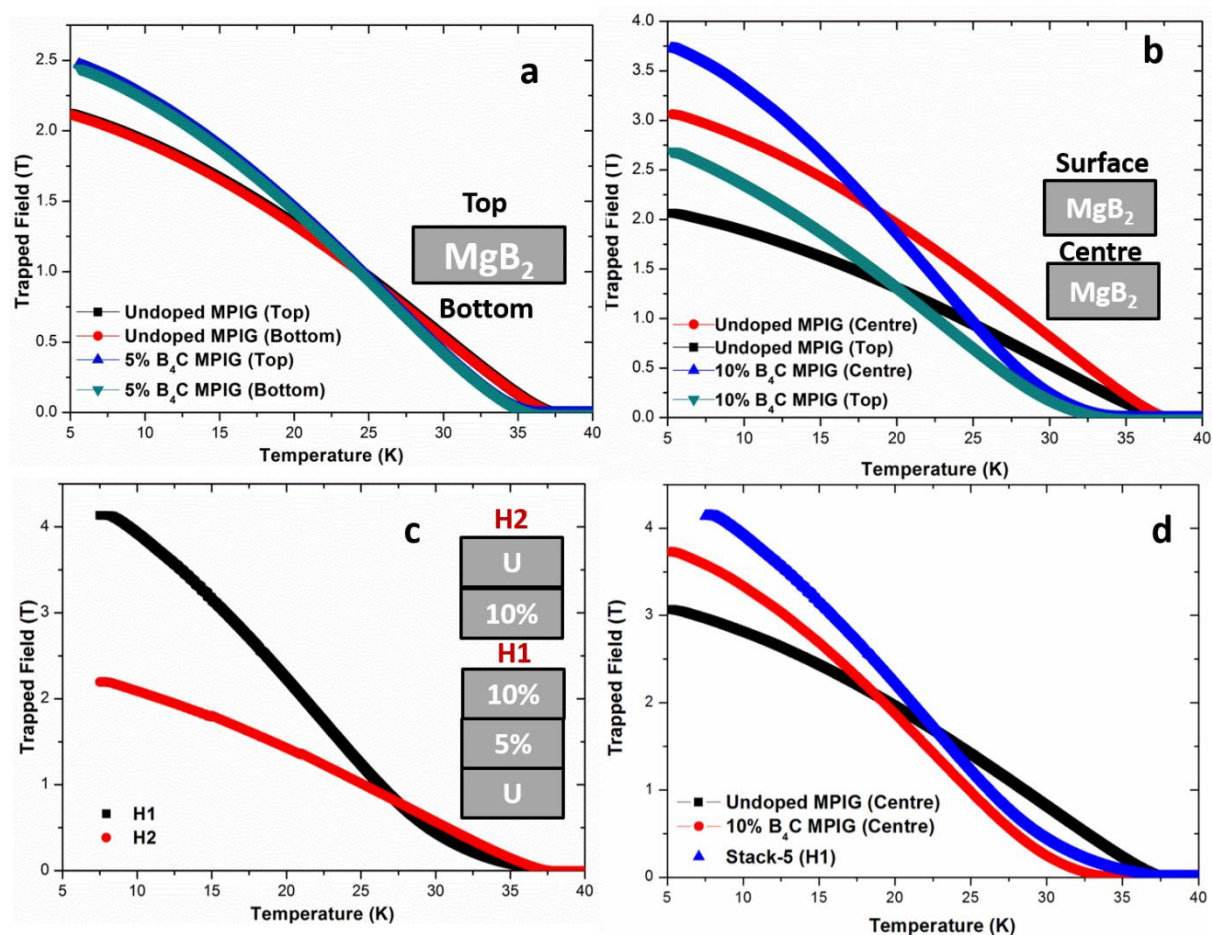


**Figure 7.11** Variation of trapped field with trapped magnetic field for (a) a single bulk MgB<sub>2</sub> sample, (b) a two-sample and (c) stack-5 geometry. (d) comparing trapped field obtained at position H1 and the centre of stack of two samples in undoped and 10% B<sub>4</sub>C (MPIG).

Such behaviour of the trapped field from undoped  $\rightarrow$  5% B<sub>4</sub>C (MPIG)  $\rightarrow$  10% B<sub>4</sub>C (MPIG) is attributed to a higher  $J_c$  at lower temperature, and a lower  $J_c$  at higher temperature, is clearly a result of increased doping (Figure 7.7(b)).

Thus far, an enhancement in trapped field has been achieved by means of ‘‘Grain Refinement’’ of MgB<sub>2</sub>. For instance, Fuchs *et al* and Yamamoto *et al* used high energy ball milled nano-scale Mg and B powders to synthesize MgB<sub>2</sub>, in order to maximise grain boundary density [245, 246]. Such samples trapped maximum fields of 5.4 T (12 K) and 3.72 T (5 K) respectively. Similarly, Naito *et al* found that Ti addition (nominal composition Mg<sub>1-y</sub>Ti<sub>y</sub>B<sub>2</sub>) formed a thin layer of TiB<sub>2</sub> on MgB<sub>2</sub> crystal which pinned the grain boundaries of MgB<sub>2</sub> and avoided grain growth [248]. This TiB<sub>2</sub> was also thought to be a vortex pinning site. On the contrary, an increase in trapped field of Mg(B,C)<sub>2</sub> bulks in the present study is originated from the atomic level intra-band scattering, associated with C doping. Moreover, the increase has been achieved by simple addition and mixing of B<sub>4</sub>C with B powder, without the use of expensive techniques such as high energy ball milling. This

demonstrates that C doping via B<sub>4</sub>C is very effective way of fabricating high performance MgB<sub>2</sub> bulks that can generate high fields.

Finally, a five sample stack arrangement was made in order to examine the effect of thickness on the trapped field, as shown in figure 7.11(d). Two hall sensors were placed, one on top of the 5 bulk stack (H2) and another sandwiched between the bulks (H1). A maximum trapped flux density of 4.15 T and 2.2 T was obtained on H1 and H2 at 7.5 K. During the slow removal of field, a global flux jump occurred at 7.5 K, which resulted in a sudden loss of flux. This value of 4.15 T is the highest obtained in MgB<sub>2</sub> samples, fabricated under ambient pressure, to date. The trapped field of 2.32 T (H2 extrapolated to 5 K) represented a 10% increase in the magnetic field as compared to the single bulk. Interestingly, 4.3 T (H1 extrapolated to 5 K) was nearly 15% increase with respect to trapped field at the centre of 10% B<sub>4</sub>C (MPIG) at 5 K. This suggests that such a stack arrangement could be used to generate high trapped fields in MgB<sub>2</sub>, although a flux distribution within such a stack needs more careful consideration.

### 7.8.2 Flux creep

The stability of trapped magnetic flux in the MgB<sub>2</sub> bulk samples was investigated by measuring magnetic moment at 10 K and 20 K, after field removal. Figure 7.12(a-b), (c-d) and figure 7.13 (a-b) show the variation of the trapped field with time for a 5% B<sub>4</sub>C (MPIG), 10% B<sub>4</sub>C (MPIG) and stack-5 respectively at 10 and 20 K.

All the curves showed a typical logarithmic decay with time ( $t > 100$  s), although flux creep variation was non-logarithmic for  $t < 100$  s. The time dependence of normalised trapped field at 10 and 20 K for un-doped, 5% B<sub>4</sub>C (MPIG), 10% B<sub>4</sub>C (MPIG) and stack-5 is shown in figure 7.14 and the relationship is summed up in table 7.1. The drop in the normalised trapped field after one day at 20 K was observed to be more than 10 K. For example, 5% B<sub>4</sub>C (MPIG) showed 2.3% and 3.8% ‘leak’ in flux at 10 and 20 K respectively after 1 day. This can be explained by following equation from Anderson-Kim model [285].

$$J(t) = J_0 \left[ 1 - \frac{k_B T}{U_0} \ln \frac{t}{t_0} \right] \quad (7.3)$$

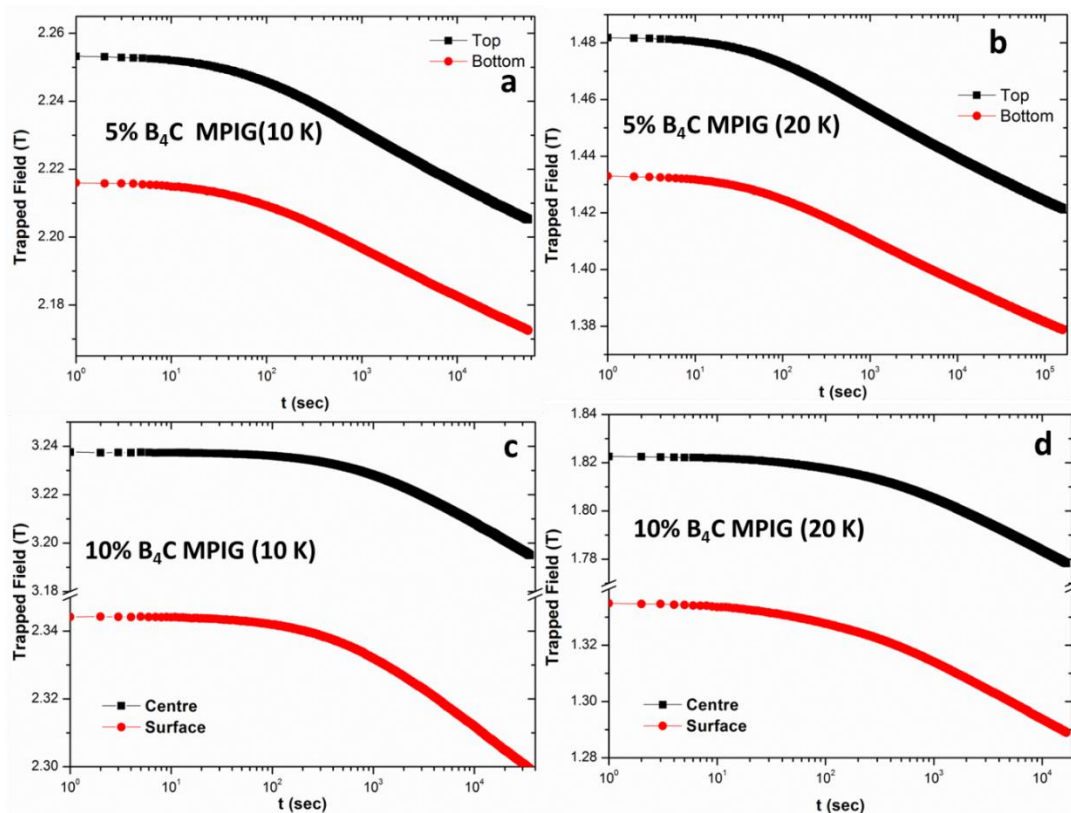


Figure 7.12 Time dependence of trapped magnetic flux density in 5% B<sub>4</sub>C (MPIG) on top and bottom at (a) 10 K and (b) 20 K. (c) and (d) shows field decay in centre and surface of two sample stack of 10% B<sub>4</sub>C (MPIG) bulks at 10 K and 20 K respectively.

Where  $U_o$  is activation energy for de-pinning of flux line and  $k_B$  is Boltzmann constant. Since current density decreases with temperature, the trapped field is also expected to decay.

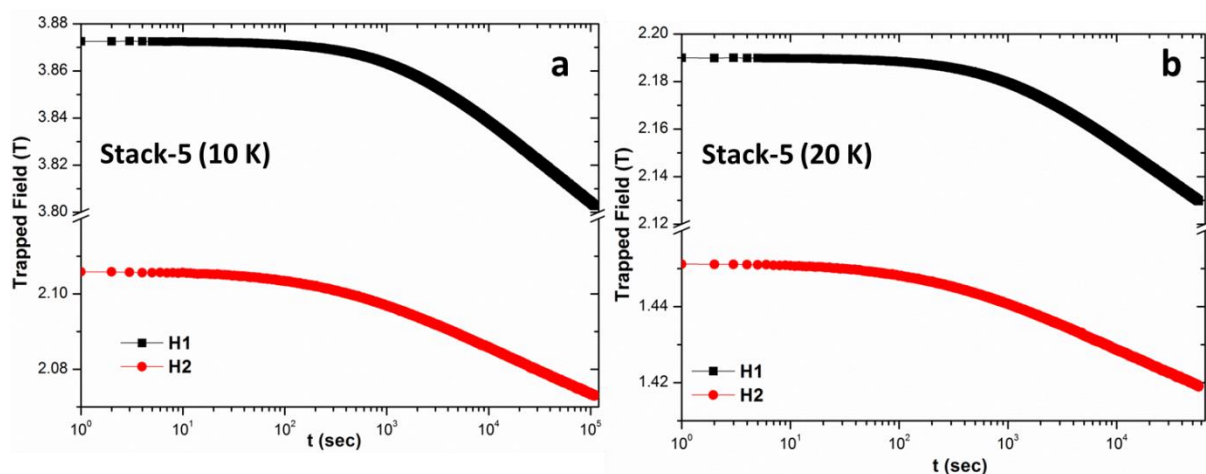


Figure 7.13 (a) and 7.13(b) showing the variation of trapped field in stack-5 obtained at hall sensors positioned at H1 and H2 at 10 K and 20 K respectively.



Interestingly, the creep rate was also found to increase from undoped → 5% B<sub>4</sub>C (MPIG) → 10% B<sub>4</sub>C (MPIG), since the activation energy  $U$  for de-pinning reduces with  $T/T_c$  according to following equation [285].

$$U = U_0 \left(1 - \frac{T}{T_c}\right)^{\alpha_c} \quad (7.4)$$

Where  $\alpha_c$  is a material parameter. Therefore flux lines//bundles can overcome pinning barrier and migrate relatively easily in samples with lower normalised  $T_c$ .

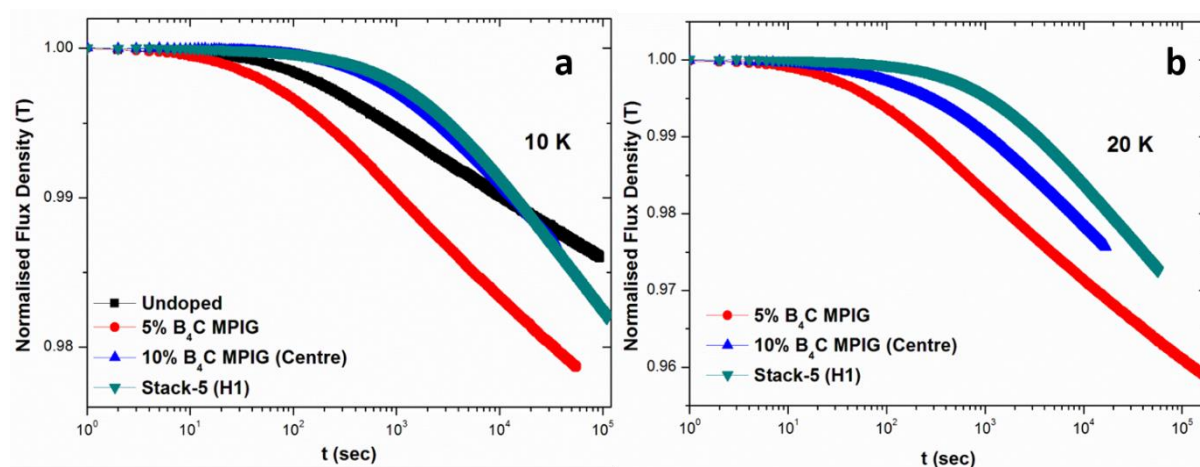


Figure 7.14(a) and (b) showing time dependence of normalised field decay in un-doped, 5% B<sub>4</sub>C (MPIG) (top of single bulk), 10% B<sub>4</sub>C (MPIG) (centre of stack), Stack-5 (H1), at 10 K and 20 K respectively.

	$B_{Normalised}$ (10 K)	$B_{Normalised}$ (20 K)
<b>Un-doped MPIG</b>	$-0.0042\log(t) + 1$	---
<b>5% B<sub>4</sub>C MPIG</b>	$-0.00653\log(t)+1$	$-0.0108\log(t)+1$
<b>10% B<sub>4</sub>C MPIG</b>	$-0.0072\log(t)+1$	$-0.012\log(t)+1$
<b>Stack-5 (H1)</b>	$-0.0087\log(t)+1$	$-0.0143\log(t)+1$

Table 7.1 Summarising flux creep, with linear dependence of  $\log t$ , for various bulks at 10 and 20 K

## 7.9 Summary

C-doped MgB<sub>2</sub> samples have been prepared by using B<sub>4</sub>C and SiC as sources of C. B<sub>4</sub>C addition showed a more homogeneous C distribution compared to SiC, which was attributed to its higher reactivity with Mg and atomically uniformly distributed C. Various phases in

B<sub>4</sub>C added samples were analysed using XRD and new lattice parameters of Mg(B,C)<sub>2</sub> were calculated. These samples showed significant enhancement in  $J_c$ , particularly at lower temperature and higher fields. This was explained by the generation of lattice strains and loss of crystallinity in MgB<sub>2</sub> accompanied by C-doping. The pinning force analysis also suggested the possibility of the contribution from point pinning, which probably contributed towards enhanced  $J_c$ . Significant increase in trapped fields was observed in C-doped MgB<sub>2</sub> bulks. The trapped field obtained (4.13 T) in five stacked of bulks is the highest obtained in MgB<sub>2</sub> bulks synthesized under ambient pressure conditions. Finally, it is believed that finer particle size of B<sub>4</sub>C is likely to yield more efficient and uniform C-doping, without the formation of MgB<sub>2</sub>C<sub>2</sub> and residual B<sub>4</sub>C. This together with nano-sized boron powder is likely to yield optimum combination of grain boundary pinning and increased  $H_{c2}$ , which could be the way forward towards pushing the boundaries of performance of the MgB<sub>2</sub>.

## Chapter 8. Conclusion

- A suitable source of B (HCC) was identified after analysing  $\text{MgB}_2$  samples prepared using various boron sources. The crystallinity and particle size were found to be important factors that determined reactivity with Mg and defects in the reacted product respectively.
- The IG process enabled fabrication of dense bulk  $\text{MgB}_2$  with high connectivity. The densification mechanism in IG differs significantly from conventional solid state sintering of  $\text{MgB}_2$ , in which the porosity is typically retained during processing resulting in poorly connected grains. This relatively simple technique is performed at ambient pressure and is therefore scalable to the fabrication of larger bulk  $\text{MgB}_2$  samples of more complex geometries. This is remarkable considering that thick sections and complex shapes can be fabricated with this method while the process does not requiring expensive high pressure apparatus.
- Continuous Mg channels were major defects in  $\text{MgB}_2$ -IG samples. These were eliminated by incorporating  $\text{Mg/AlB}_2/\text{MgB}_2$  powder in the precursor as a wetting enhancer to facilitate the in-flux of Mg, leading to a more uniform infiltration process, thereby enabling the fabrication of near-net shaped  $\text{MgB}_2$  bulk superconductors. An almost identical value of trapped magnetic flux was measured at the top and bottom surfaces of a single bulk sample suggest that the  $\text{MgB}_2$  bulk samples fabricated by such method are homogeneous.
- Microstructural analysis of  $\text{MgB}_2$ -IG samples revealed that  $\text{MgB}_2$  phase formation is a three stage process. With the formation of intermediate phase  $\text{Mg}_2\text{B}_{25}$  and associated volume expansion, as cracks were initiated in all boron particles. These cracks propagated radially inwards, originating from crack tip stresses, resulting in the fracture and disintegration in a number of particles and thereby offering better kinetics by exposing a large surface area for reaction. Mg infiltration in the precursor was rapid, aided probably by vapour phase transport. This was followed by  $\text{MgB}_2$  layer growth and simultaneous sintering together to form grain boundaries.
- C-doped  $\text{MgB}_2$  has been investigated by using  $\text{B}_4\text{C}$  and  $\text{SiC}$  as sources of C.  $\text{B}_4\text{C}$  addition showed a more homogeneous C distribution compared to  $\text{SiC}$ , which was attributed to its

higher reactivity with Mg and atomically uniformly distributed C. These samples showed significant enhancement in  $J_c$ , particularly at lower temperature and higher fields. This was explained by the generation of lattice strains and loss of crystallinity in  $\text{MgB}_2$  accompanied by C-doping. The pinning force analysis also suggested the possibility of contribution from point pinning, which probably contributed towards enhanced  $J_c$ .

- A significant increase (up to 23%) in trapped fields was observed in C-doped  $\text{MgB}_2$  bulks over undoped sample. The trapped field obtained (4.13 T) in five stack bulks is the highest obtained in  $\text{MgB}_2$  bulks synthesized under ambient pressure conditions. Moreover, the increase has been achieved by the simple addition and mixing of  $\text{B}_4\text{C}$  with B powder, without the use of expensive techniques such as high energy ball milling. This demonstrates that C doping via  $\text{B}_4\text{C}$  is very effective way of fabricating high performance  $\text{MgB}_2$  bulks that can generate high fields.

## Chapter 9. Suggestions for Future Work

This work was an exploration of Infiltration-Growth technique as a potential solution in view of the synthesis of dense bulk  $\text{MgB}_2$  that can be fabricated into larger and complex shapes. The samples showed a relatively high self-field  $J_c$  of  $400 \text{ kA/cm}^2$  (5 K), which was further enhanced up to 50% through C doping. This indicated that superconducting  $\text{MgB}_2$  was well-connected despite residual Mg content. The homogeneous cylindrical bulk samples, which were obtained with improved wetting, were not only extremely homogeneous but also trapped high magnetic fields. Clearly, the technique holds great promise, however certain areas need to be addressed to further the understanding and realise its true potential.

- **Unreacted Impurities:** The  $\text{MgB}_2$ -IG samples under the optimum reaction temperature showed unreacted Mg and  $\text{Mg}_2\text{B}_{25}$  impurities of ~10%. The formation of  $\text{MgB}_2$  layer on  $\text{Mg}_2\text{B}_{25}$  is diffusion controlled. Therefore longer heating at high temperature needs to be employed (~14 h at  $900 \text{ }^\circ\text{C}$ ) in order to ensure the complete transformation into  $\text{MgB}_2$ .
- **Optimum Particle Size:** The particle size determines size of capillaries in the pressed precursor, through which Mg infiltration may occur. This work provides sufficient evidence to suggest that a minimum particle size may be needed in order to ensure efficient Mg infiltration, especially when thicker samples are required. On the other hand, a finer B particle size is always desired in  $\text{MgB}_2$ . This reduced the required diffusion distance of Mg atoms and increases grain boundary density, which enhances pinning. Therefore the selection of an optimum B particle size is crucial.
- **Homogeneous C doping:**  $\text{B}_4\text{C}$  of particle size  $1 \text{ }\mu\text{m}$ , source of the C used in this study, resulted in relatively inhomogeneous C doping in  $\text{MgB}_2$  for higher  $\text{B}_4\text{C}$  additions and introduced impurities such as  $\text{MgB}_2\text{C}_2$  and unreacted  $\text{B}_4\text{C}$  in the final reacted product. Therefore use of finer  $\text{B}_4\text{C}$  is likely to result in uniform C doping and eliminate  $\text{MgB}_2\text{C}_2/\text{B}_4\text{C}$ .
- **TEM Observation of Defect Structures in  $\text{Mg}(\text{B}_{1-x}\text{C}_x)_2$ :** XRD analysis suggests the presence of considerable disorder in the carbon doped  $\text{MgB}_2$  lattice. Careful TEM analysis could reveal the nature and size of these defects e.g. linear, planar or point

defects. A representative image of C doped  $\text{MgB}_2$  ( $x=10$ ) is shown in figure 9.1. Such analysis would be helpful for better understanding of pinning sites in  $\text{MgB}_2$ .

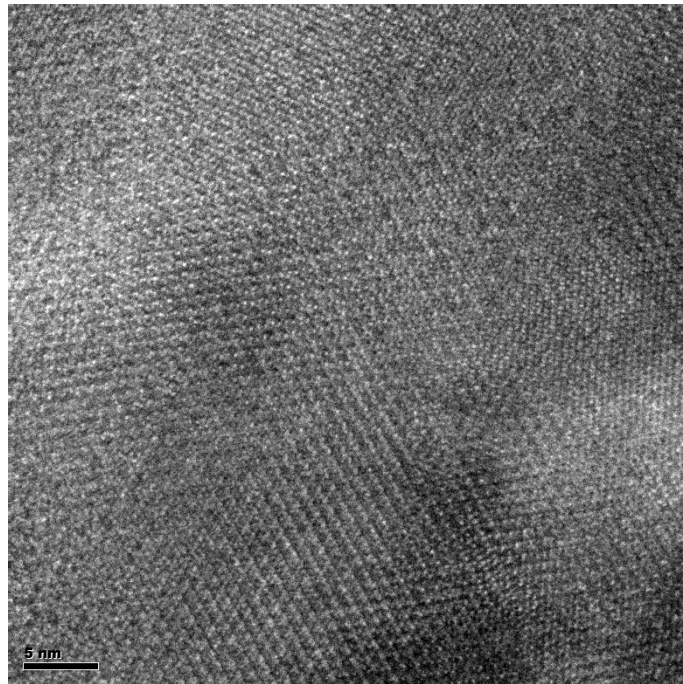


Figure 9.1 High resolution TEM micrograph of carbon doped  $\text{MgB}_2$

- **Effect of stacking/Field distribution in stacks:** Although the stacked arrangement of bulks raised the trapped flux density by 10% to the reference value, an unusual ratio between flux density at the centre to surface was observed, which can't easily be explained by the demagnetization factor alone. Therefore flux distribution within such an arrangement needs careful consideration.

## References

- [1] H K Onnes “The Resistance of Pure Mercury at Helium Temperature” 1911 *Commun. Phys. Lab. Univ. Leiden* **12** 120.
- [2] W Meissner and R Ochsenfeld “Ein neuer Effekt bei Eintritt der Supraleitfähigkeit” 1933 *Naturwissenschaften* **21** 787.
- [3] M Faraday “Experimental Researches in Electricity, Vol I, II and III” 1837, 1844 and 1855.
- [4] F. B. Silsbee “Electrical Conduction in Metals at Low Temperatures” 1916 *Journal of the Washington Academy of Sciences* **6** 597.
- [5] J Bardeen, L N Cooper and J R Schrieffer “Theory of Superconductivity” 1957 *Phys. Rev.* **108** 1175.
- [6] M Tinkham 1996 “Introduction to Superconductivity”, New York, NY: *McGraw-Hill*.
- [7][http://qudev.ethz.ch/content/courses/phys4/studentspresentations/supercond/Ford\\_The\\_rise\\_of\\_SC\\_6\\_7.pdf](http://qudev.ethz.ch/content/courses/phys4/studentspresentations/supercond/Ford_The_rise_of_SC_6_7.pdf)
- [8] V L Ginzburg and L D Landau “On the Theory of superconductivity” 1950 *Zh. Eksp. Teor. Fiz.* **20** 1064.
- [9] A A Abrikosov “On the Magnetic Properties of Superconductors of the Second Group” 1957 *J. Exptl. Theoret. Phys.* **32** 1442.
- [10] D Dew-Hughes “Flux Pinning Mechanisms in Type II Superconductors” 1974 *Philos. Mag.* **30** 293.
- [11] D Dew-Hughes “The Role of Grain Boundaries in Determining  $J_c$  in High-field High-current Superconductors” 1987 *Philos. Mag.* **55** 459.
- [12] H Hosono *et al* “Exploration of new superconductors and functional materials, and fabrication of superconducting tapes and wires of iron pnictides” 2015 *Sci. Technol. Adv. Mater.* **16** 033503.
- [13] B W Roberts “Survey of superconductive materials and critical evaluation of selected properties” 1976 *J. Phys. Chem. Ref. Data* **5** 581.
- [14] D Dew-Hughes “Superconducting A-15 compounds: A review” 1975 *Cryogenics* **15** 435.
- [15] M K Wu, J R Ashburn, C J Torng, P H Hor, R L Meng, L Gao, Z J Huang, Y Q Wang and C W Chu “Superconductivity at 93 K in a new mixed-phase Y-Ba-Cu-O compound system at ambient pressure” 1987 *Phys. Rev. Lett.* **58** 908.
- [16] H Maeda, Y Tanaka, M Fukutumi and T Asano "A New High- $T_c$  Oxide Superconductor without a Rare Earth Element" 1988 *Jpn. J. Appl. Phys.* **27** L209.
- [17] D Dimos, P Chaudhari, J Mannhart, and F K LeGoues “Orientation Dependence of Grain-Boundary Critical Currents in  $YBa_2Cu_3O_{7-\delta}$  Bicrystals” 1988 *Phys. Rev. Lett.* **61** 219.
- [18] J Nagamatsu, N Nakagawa, T Muranaka, Y Zenitani and J Akimitsu “Superconductivity at 39 K in magnesium diboride” *Nature* **410** 63.
- [19] Y Kamihara *et al* “Iron-Based Layered Superconductor:  $LaOFeP$ ” 2006 *J. Am. Chem. Soc.* **128** 10012.

- [20] G Z Li “Connectivity, Doping, and Anisotropy in Highly Dense Magnesium Diboride” 2015 PhD Thesis, Ohio State University.
- [21] V Russel, R Hirst, F Kanda and A. King “An X-ray study of the magnesium borides.” 1953 *Acta. Cryst.* **6** 870.
- [22] M E Jones and R E Marsh "The preparation and structure of magnesium boride" 1954 *J. Am. Chem. Soc.* **76** 1434.
- [23] K Vinod, R G Abhilash Kumar and U Syamaprasad “Prospects for MgB<sub>2</sub> superconductors for magnet application” 2007 *Supercond. Sci. Technol.* **20** R1.
- [24] R M Swift, D. White “Low Temperature Heat Capacities of Magnesium Diboride (MgB<sub>2</sub>) and Magnesium Tetraboride (MgB<sub>4</sub>)” 1957 *J. Am. Chem. Soc.* **79** 3641.
- [25] G Karapetrov, M Iavarone and W K Kwok, G W Crabtree and D G Hinks “Scanning Tunneling Spectroscopy in MgB<sub>2</sub>” *Phys. Rev. Lett.* **86** 4374.
- [26] F Bouquet, Y Wang, R A Fisher, D G Hinks, J D Jorgensen, A Junod and N E Phillips “Phenomenological two-gap model for the specific heat of MgB<sub>2</sub>” 2001 *Europhys. Lett.* **56** 856.
- [27] H Schmidt, J F Zasadzinski, K E Gray and D G Hinks “Energy gap from tunneling and metallic contacts onto MgB<sub>2</sub>: Possible evidence for a weakened surface layer” 2001 *Phys. Rev. B* **63** 220504.
- [28] A Sharoni, I Felner and O Millo “Tunneling spectroscopy and magnetization measurements of the superconducting properties of MgB<sub>2</sub>” 2001 *Phys. Rev. B* **63** 220508
- [29] H Kotegawa, K Ishida, Y Kitaoka, T Muranaka and J Akimitsu “Evidence for Strong-Coupling *s*-Wave Superconductivity in MgB<sub>2</sub>: B11 NMR Study” 2001 *Phys. Rev. Lett.* **87** 127001
- [30] S L Bud'ko, G Lapertot, C Petrovic, C E Cunningham, N Anderson and P C Canfield “Boron Isotope Effect in Superconducting MgB<sub>2</sub>” 2001 *Phys. Rev. Lett.* **86** 1877.
- [31] D G Hinks, H Claus and J D Jorgensen “The complex nature of superconductivity in MgB<sub>2</sub> as revealed by the reduced total isotope effect” 2001 *Nature* **411** 457.
- [32] H J Choi, D Roundy, H Sun, M L Cohen and S G Louie “The origin of the anomalous superconducting properties of MgB<sub>2</sub>” *Nature* **418** 758.
- [33] X K Chen, M J Konstantinovic, J C Irwin, D D Lawrie J P Frank "Evidence for two superconducting gaps in MgB<sub>2</sub>" 2001 *Phys. Rev. Lett.* **87** 157002.
- [34] P. Szabo *et al* "Evidence for two superconducting energy gaps in MgB<sub>2</sub> by point contact spectroscopy," 2001 *Phys. Rev. Lett.* **87** 137005.
- [35] Z K Liu, D G Schlom, Q L and X X Xi “Thermodynamics of the Mg–B system: Implications for the deposition of MgB<sub>2</sub> thin films” 2001 *Appl. Phys. Lett.* **78** 3678.
- [36] J D DeFouw, J P Quintana and D C Dunand "In situ X-ray synchrotron diffraction study of MgB<sub>2</sub> synthesis from elemental powders," 2008 *Acta. Mater.* **56** 1680.
- [37] Z Ma, Y Liu “The varied kinetics mechanisms in the synthesis of MgB<sub>2</sub> from elemental powders by low-temperature sintering” 2011 *Mater. Chem. Phys.* **126** 114.



- [38] H M Kim, S S Yim, K B Kim, S H Moon, Y W Kim and D H Kang “Growth kinetics of MgB<sub>2</sub> layer and interfacial MgO layer during ex situ annealing of amorphous boron film” 2004 *J Mater Res* **19** 3081.
- [39] G Z Li, M D Sumption and E W Collings “Kinetic Analysis of MgB<sub>2</sub> Layer Formation in Advanced Internal Magnesium Infiltration Processed MgB<sub>2</sub> Wires” 2015 *Acta Materialia*, **96** 66.
- [40] L Lyard *et al* “Anisotropy of the upper critical field and critical current in single crystal MgB<sub>2</sub>” 2002 *Phys. Rev. B* **66** 180502.
- [41] L. Lyard *et al* “Anisotropies of the lower and upper critical fields in MgB<sub>2</sub> single crystals” 2002 *Phys. Rev. Lett.* **92** 057001.
- [42] M Eisterer, M Zehetmayer and H W Weber “Current Percolation and Anisotropy in Polycrystalline MgB<sub>2</sub>” 2003 *Phys. Rev. Lett.* **90** 247002.
- [43] M Eisterer, C Krutzler and H W Weber “Influence of the upper critical field anisotropy on the transport properties of polycrystalline MgB<sub>2</sub>” 2005 *J. Appl. Phys.* **98** 033906.
- [44] D R Tilley “The Ginsburg-Landau equations for anisotropic alloys” 1965 *Proc. Phys. Soc. London* **86** 289.
- [45] M Zehetmayer, M Eisterer, J Jun, S M Kazakov, J Karpinski and H W Weber “Magnetic field dependence of the reversible mixed-state properties of superconducting MgB<sub>2</sub> single crystals and the influence of artificial defects” 2004 *Phys. Rev. B* **70** 214516.
- [46] D C Larbalestier *et al* “Strongly linked current flow in polycrystalline forms of the superconductor MgB<sub>2</sub>” 2001 *Nature* **410** 186.
- [47] M Kambara, N HariBabu , E S Sadki, J R Cooper, H Minami, D A Cardwell, A M Campbell and I Inoue “High intergranular critical currents in metallic MgB<sub>2</sub> superconductor” 2001 *Supercond. Sci. Technol.* **14** L5.
- [48] Y. Bugoslavsky, G K Perkins, X Qi, L F Cohen and A D Caplin “Vortex dynamics in superconducting MgB<sub>2</sub> and prospects for applications” 2001 *Nature* **410** 563.
- [49] M Martinez, P Mikheenko, M Martinez-Lopez, A Millan, A Bevan and J S Abell “Flux pinning force in bulk MgB<sub>2</sub> with variable grain size” 2007 *Phys. Rev. B* **75** 134515.
- [50] P Mikheenko, E Martínez, A Bevan, J S Abell and J L MacManus-Driscoll “Grain boundaries and pinning in bulk MgB<sub>2</sub>” *Supercond. Sci. Technol.* **20** 264.
- [51] N R Werthamer, E Helfand and P C Hohenberg “Temperature and Purity Dependence of the Superconducting Critical Field,  $H_{c2}$ . III. Electron Spin and Spin -Orbit Effects” 1966 *Phys. Rev.* **147** 295.
- [52] V Braccini *et al* “High-field superconductivity in alloyed MgB<sub>2</sub> thin films” 2005 *Phys. Rev. B* **71** 012504.
- [53] A Gurevich “Enhancement of the upper critical field by nonmagnetic impurities in dirty two-gap superconductors” 2003 *Phys. Rev. B* **67** 184515.
- [54] A Gurevich *et al* “Very high upper critical fields in MgB<sub>2</sub> produced by selective tuning of impurity scattering” 2003 *Supercond. Sci. Technol.* **17** 278.
- [55] M Putti, R Vaglio and J M Rowell “Radiation effects on MgB<sub>2</sub>: a review and a comparison with A15 superconductors” 2008 *Supercond. Sci. Technol.* **21** 043001.

- [56] Y Bugoslavsky, L F Cohen, G K Perkins, M Polichetti, T J Tate, R Gwilliam and A D Caplin “Enhancement of the high-magnetic-field critical current density of superconducting  $\text{MgB}_2$  by proton irradiation 2001 *Nature* **411** 561.
- [57] M Eisterer, M Zehetmayer, S Toenies, H W Weber, M Kambara, N Hari Babu, D A Cardwell and L R Greenwood “Neutron irradiation of  $\text{MgB}_2$  bulk superconductors” 2002 *Supercond. Sci. Technol.* **15** L9.
- [58] T C Shields “Microstructure and superconducting properties of hot isostatically pressed  $\text{MgB}_2$ ” 2002 *Supercond. Sci. Technol.* **15** 202.
- [59] D K Finnemore, J E Ostenson, S L Bud'ko, G Lapertot and P C Canfield “Thermodynamic and Transport Properties of Superconducting  $\text{Mg}_{10}\text{B}_2$ ” *Phys. Rev. Lett.* **86** 2420.
- [60] K Kawano, J S Abell, M Kambara, N Hari Babu and D A Cardwell “Evidence for high intergranular current flow in a single-phase polycrystalline  $\text{MgB}_2$  superconductor” 2001 *Appl. Phys. Lett.* **79** 2216.
- [61] N Hari Babu, Y Shi, K Iida and D A Cardwell “A practical route for the fabrication of large single-crystal (RE)–Ba–Cu–O superconductors” 2005 *Nature Materials* **4** 476.
- [62] J M Rowell “The widely variable resistivity of  $\text{MgB}_2$  samples” 2003 *Supercond. Sci. Technol.* **16** R17.
- [63] R F Klie, J C Idrobo, N D Browning, K A Regan, N Rodado and R J Cava “Direct observation of nanometer scale Mg and B oxide phases at grain boundaries in  $\text{MgB}_2$ ” 2001 *Appl. Phys. Lett.* **79** 1837.
- [64] J. M. Rowell *et al* “Critical current density and resistivity of  $\text{MgB}_2$  films” 2003 *Appl. Phys. Lett.* **83** 102.
- [65] V A Drozd, A M Gabovich, P Gierłowski, M Pękała and H Szymczak “Transport properties of bulk and thin-film  $\text{MgB}_2$  superconductors: effects of preparation conditions” 2004 *Physica C* **402** 325.
- [66] C Fischer *et al* “Critical current densities of superconducting  $\text{MgB}_2$  tapes prepared on the base of mechanically alloyed precursors” 2004 *Physica C* **406** 121.
- [67] W Hassler *et al* “ $\text{MgB}_2$  bulk and tapes prepared by mechanical alloying: influence of the boron precursor powder” 2006 *Supercond. Sci. Technol.* **19** 512.
- [68] A Serquis *et al* “Microstructure and high critical current of powder-in-tube  $\text{MgB}_2$ ” 2003 *Appl. Phys. Lett.* **82** 1754.
- [69] A Yamamoto, J Shimoyama, S Ueda, Y Katsura, S Horii and K Kishio “Synthesis of high  $J_c$   $\text{MgB}_2$  bulks with high reproducibility by a modified powder-in-tube method” 2004 *Supercond. Sci. Technol.* **17** 921.
- [70] A Yamamoto, J Shimoyama, S Ueda, Y Katsura, S Horii and K Kishio “Improved critical current properties observed in  $\text{MgB}_2$  bulks synthesized by low-temperature *solid-state* reaction” 2005 *Supercond. Sci. Technol.* **18** 116.
- [71] A Yamamoto, H Tanaka, J Shimoyama, H Ogino, K Kishio and T Matsushita “Improved critical current properties observed in  $\text{MgB}_2$  bulks synthesized by low-temperature *solid-state* reaction” 2012 *Japanese J. of Appl. Phys.* **51** 010105.

- [72] P Lezza, R Gladyshevskii, H L Suo and R Flükiger “Quantitative study of the inhomogeneous distribution of phases in Fe-sheathed *ex situ* MgB<sub>2</sub> tapes” 2005 *Supercond. Sci. Technol.* **18** 753.
- [73] B Birajdar, V Braccini, A Tumino, T Wenzel, O Eibl and G Grasso “MgB<sub>2</sub> multifilamentary tapes: microstructure, chemical composition and superconducting properties” 2006 *Supercond. Sci. Technol.* **19** 916.
- [74] A Serquis “Influence of microstructures and crystalline defects on the superconductivity of MgB<sub>2</sub>” 2002 *J. Appl. Phys.* **92** 351.
- [75] Y Eltsev, S Lee, K Nakao, N Chikumoto, S Tajima, N Koshizuka and M Murakami “Anisotropic superconducting properties of MgB<sub>2</sub> single crystals probed by in-plane electrical transport measurements” 2002 *Phys. Rev. B* **65** 140501
- [76] A V Sologubenko, J Jun, S M Kazakov, J Karpinski and H R Ott “Thermal conductivity of single-crystalline MgB<sub>2</sub>” 2002 *Phys. Rev. B* **66** 014504.
- [77] M. Eisterer “Magnetic properties and critical currents of MgB<sub>2</sub>” 2007 *Supercond. Sci. Technol.* **20** R47.
- [80] R J Cava, H W Zandbergen, K Inumaru “the substitutional chemistry of MgB<sub>2</sub>” 2003 *Physica C* **385** 8.
- [86] D G Hinks, J D Jorgensen, H Zheng, S Short “Synthesis and stoichiometry of MgB<sub>2</sub>” *Physica C* **382** 166.
- [87] I Pallecchi “Investigation of Li doped MgB<sub>2</sub>” 2009 *Supercond. Sci. Technol.* **22** 095014.
- [88] M R Cimberle, M Novak, P Manfrinetti and A Palenzona “Magnetic characterization of sintered MgB<sub>2</sub> samples: effect of substitution or 'doping' with Li, Al and Si” 2002 *Supercond. Sci. Technol.* **15** 43.
- [89] S M Kazakov, M Angst, J Karpinski, I M Fita, R Puzniak “Substitution effect of Zn and Cu in MgB<sub>2</sub> on  $T_c$  and structure” *Solid State Communications* **119** 1.
- [90] A Tampieri, G Celotti, S Sprio, D Rinaldi, G Barucca and R Caciuffo “ Effects of copper doping in MgB<sub>2</sub> superconductor” 2002 *Solid State Communications* **121** 497.
- [91] H Zhang, J Zhao, L Shi “The charge transfer induced by Cr doping in MgB<sub>2</sub>” 2005 *Physica C* **424** 79
- [92] E Kuzmann, Z Homonnay, Z Klencsar, M Kuhberger, A Vertes and G Gritzner “Local environments of iron and cobalt in doped MgB<sub>2</sub> superconductors” 2002 *Supercond. Sci. Technol.* **15** 1479.
- [93] N Novosel *et al* “Enhancement of the critical current density in MgB<sub>2</sub> wires doped with Ni nanoparticles” 2012 *Supercond. Sci. Technol.* **25** 095018
- [94] J D Guo , X L Xu, Y Z Wang, L Shi, D Y Liu “Preparation of Ag-doped Mg<sub>1-x</sub>Ag<sub>x</sub>B<sub>2</sub> superconductors” 2004 *Materials Letters* **58** 3707.
- [95] S Agrestini *et al* “Substitution of Sc for Mg in MgB<sub>2</sub>: Effects on transition temperature and Kohn anomaly” 2004 *Phys. Rev. B* **70** 134514.
- [96] M M A Sekkina, KM Elsabay “Narrow range of iridium-substitution on Mg<sub>1-x</sub>Ir<sub>x</sub>B<sub>2</sub> superconductor” 2003 *Physica C* **391** 217.

- [97] Yaxin Sun “Structural and superconducting properties of Ca-doped  $\text{MgB}_2$  superconductors” 2007 *Supercond. Sci. Technol.* **20** 261.
- [98] X L Xu, J D Guo, Y Z Wang and X Wang “Au-doping effects in the  $\text{Mg}_{1-x}\text{Au}_x\text{B}_2$  series” 2004 *Materials Letters* **58** 142.
- [99] S Xu, Y Moritomo, K Kato and A Nakamura “Mn-Substitution Effects on  $\text{MgB}_2$  Superconductor” 2001 *J. Phys. Soc. Jpn.* **70** 1889.
- [100] M A Susner, M D Sumption, A Takase and E W Collings “Evidence for Zr site-substitution for Mg in PLD-deposited  $\text{MgB}_2$  thin films” 2014 *Supercond. Sci. Technol.* **27** 075009.
- [101] J S Slusky *et al* “Loss of superconductivity with the addition of Al to  $\text{MgB}_2$  and a structural transition in  $\text{Mg}_{1-x}\text{Al}_x\text{B}_2$ ” 2001 *Nature* **410** 343.
- [102] J Karpinski *et al* “Al substitution in  $\text{MgB}_2$  crystals: Influence on superconducting and structural properties” 2005 *Phys. Rev. B* **71** 174506.
- [103] M. Putti *et al* “Critical field of Al-doped  $\text{MgB}_2$  samples: Correlation with the suppression of the  $\sigma$ -band gap” 2005 *Phys. Rev. B* **71** 144505.
- [104] M Putti, M Affronte, P Manfrinetti and A Palenzona “Effects of Al doping on the normal and superconducting properties of  $\text{MgB}_2$ : A specific heat study” 2003 *Phys. Rev. B* **68** 094514.
- [105] T Klein *et al* “Influence of Al doping on the critical fields and gap values in magnesium diboride single crystals” 2006 *Phys. Rev. B* **73** 224528.
- [106] P Postorino *et al* “Effect of the Al content on the optical phonon spectrum in  $\text{Mg}_{1-x}\text{Al}_x\text{B}_2$ ” 2001 *Phys. Rev. B* **65** 020507(R).
- [107] G. Profeta, A. Continenza, and S. Massidda “Phonon and electron-phonon renormalization in Al-doped  $\text{MgB}_2$ ” 2003 *Phys. Rev. B* **68** 144508.
- [108] H W Zandbergen, M Y Wu, H Jiang, M A Hayward, M K Haas, R J Cava “The complex superstructure in  $\text{Mg}_{1-x}\text{Al}_x\text{B}_2$  at  $x \approx 0.5$ ” 2002 *Physica C* **366** 221.
- [109] O de la Peña, A Aguayo and R de Coss “Effects of Al doping on the structural and electronic properties of  $\text{Mg}_{1-x}\text{Al}_x\text{B}_2$ ” 2002 *Phys. Rev. B* **66** 012511.
- [110] J Q Li, L Li, F M Liu, C Dong, J Y Xiang and Z X Zhao “Superconductivity, superstructure, and structure anomalies in  $\text{Mg}_{1-x}\text{Al}_x\text{B}_2$ ” 2002 *Phys. Rev. B* **65** 132505.
- [111] R H T Wilke, S L Bud’ko, P C Canfield, D K Finnemore, R J Suplinskas and S T Hannahs “Systematic Effects of Carbon Doping on the Superconducting Properties of  $\text{Mg}(\text{B}_{1-x}\text{C}_x)_2$ ” 2004 *Phys. Rev. Lett.* **92** 217003.
- [112] T Masui, S Lee, and S Tajima “Carbon-substitution effect on the electronic properties of  $\text{MgB}_2$  single crystals” 2004 *Phys. Rev. B* **70** 024504.
- [113] S X Dou *et al* “Enhancement of the critical current density and flux pinning of  $\text{MgB}_2$  superconductor by nanoparticle SiC doping” 2002 *Appl. Phys. Lett.* **81** 3419.
- [114] S X Dou *et al* “Mechanism of Enhancement in Electromagnetic Properties of  $\text{MgB}_2$  by Nano SiC Doping” 2007 *Phys. Rev. Lett.* **98** 097002.
- [115] R A Ribeiro, S L Bud’ko, C Petrovic and P C Canfield “Carbon doping of superconducting magnesium diboride” 2003 *Physica C* **384** 227.

- [116] J S Ahn, Y J Kim, M S Kim, S I Lee and E J Choi “Structural and superconducting properties of  $\text{MgB}_{2-x}\text{Be}_x$ ” 2002 *Phys. Rev. B* **65** 172503.
- [117] M M A Sekkina, K M Elsabay “Fluoride doping and Boron particle size effect on  $\text{MgB}_{2-x}\text{F}_x$  superconductor” 2002 *Solid State Communications* **123** 1.
- [118] B Birajdar, T Wenzel, P Manfrinetti, A Palenzona, M Putti and O Eibl “Al-alloyed  $\text{MgB}_2$ : correlation of superconducting properties, microstructure, and chemical composition” 2005 *Supercond. Sci. Technol.* **18** 572.
- [119] A Berenov, A Serquis, X Z Liao, Y T Zhu, D E Peterson, Y Bugoslavsky, K A Yates, M G Blamire, L F Cohen and J L MacManus-Driscoll “Enhancement of critical current density in low level Al-doped  $\text{MgB}_2$ ” 2004 *Supercond. Sci. Technol.* **17** 1093.
- [120] A Yamamoto, J Shimoyama, S Ueda, I Iwayama, S Horii and K Kishio “Effects of  $\text{B}_4\text{C}$  doping on critical current properties of  $\text{MgB}_2$  superconductor” 2005 *Supercond. Sci. Technol.* **18** 1323.
- [121] P Lezza, C Senatore and R Flükiger “Improved critical current densities in  $\text{B}_4\text{C}$  doped  $\text{MgB}_2$  based wires” 2006 *Supercond. Sci. Technol.* **19** 1030.
- [122] S.M. Kazakov, J Karpinski, J Jun, P Geiser, N D Zhigadlo, R Puzniak, A V Mironov “Single crystal growth and properties of  $\text{MgB}_2$  and  $\text{Mg}(\text{B}_{1-x}\text{C}_x)_2$ ” 2004 *Physica C* **408** 123.
- [123] A G Bhagurkar, A Yamamoto, N Hari Babu, J H Durrell, A R Dennis and D A Cardwell “Synthesis of dense bulk  $\text{MgB}_2$  by an infiltration and growth process” 2015 *Supercond. Sci. Technol.* **28** 015012.
- [124] T Takenobu, T Ito, D H Chi, K Prassides and Y Iwasa “Intralayer carbon substitution in the  $\text{MgB}_2$  superconductor” 2001 *Phys. Rev. B* **64** 134513.
- [125] W Mickelson, J Cumings, W Q Han and A Zettl “Effects of carbon doping on superconductivity in magnesium diboride” 2002 *Phys. Rev. B* **65** 052505.
- [126] I. Pallecchi *et al* “Magnetoresistivity as a probe of disorder in the  $\pi$  and  $\sigma$  bands of  $\text{MgB}_2$ ” 2005 *Phys. Rev. B* **72** 184512.
- [127] A Wisniewski, A Wisniewski, R Puzniak, J Judek, C Krutzler, M Eisterer, H W Weber, J Jun, S M Kazakov and J Karpinski “Comparison of the influence of carbon substitution and neutron-induced defects on the upper critical field and flux pinning in  $\text{MgB}_2$  single crystals” 2007 *Supercond. Sci. Technol.* **20** 256.
- [128] Jung Ho Kim *et al* “Microscopic role of carbon on  $\text{MgB}_2$  wire for critical current density comparable to NbTi” 2012 *NPG Asia Materials* **4** e3.
- [129] C B Eom *et al* “High critical current density and enhanced irreversibility field in superconducting  $\text{MgB}_2$  thin films” 2001 *Nature* **411** 558.
- [130] S K Chen, M Wei and J L MacManus-Driscoll “Strong pinning enhancement in  $\text{MgB}_2$  using very small  $\text{Dy}_2\text{O}_3$  additions” 2006 *Appl. Phys. Lett.* **88** 192512.
- [131] J Wang *et al* “High critical current density and improved irreversibility field in bulk  $\text{MgB}_2$  made by a scaleable, nanoparticle addition route” 2002 *Appl. Phys. Lett.* **81** 2026.
- [132] L B S Da Silva, E E Hellstrom and D Rodrigues Jr “ $\text{MgB}_2$  superconductors with addition of  $\text{ZrB}_2$  and different carbon sources” 2014 *Journal of Physics: Conference Series* **507** 012043.

- [133] T Nakane, H Takeya, H Fujii and H Kumakura “Effect of  $Nb_xB_2$  addition on the  $J_c$ - $B$  characteristics of  $MgB_2$  tapes” 2005 *Supercond. Sci. Technol.* **18** 521.
- [134] H L Xu, Y Feng, Z Xu, G Yan, C S Li, E Mossang, and A Sulpice “Effects of  $TiB_2$  doping on the critical current density of  $MgB_2$  wires” 2006 *Physica C* **443** 5.
- [135] M Burdusel *et al* “ $MgB_2$  with Addition of  $Bi_2O_3$  Obtained by Spark Plasma Sintering Technique” 2013 *J. Supercond. Nov. Magn.* **26** 1553.
- [136] L Saglietti “Doping by Rare-Earth Metals and Borides” 2012 *IEEE Trans. Appl. Superconduct.* **22** 6200504.
- [137] A Yamamoto, J Shimoyama, K Kishio and T Matsushita “Limiting factors of normal-state conductivity in superconducting  $MgB_2$ : an application of mean-field theory for a site percolation problem” 2007 *Supercond. Sci. Technol.* **20** 658.
- [138] C F Liu, G Yan, S J Du, W Xi, Y Feng, P X Zhang, X Z Wu and L Zhou “Effect of heat-treatment temperatures on density and porosity in  $MgB_2$  superconductor” 2003 *Physica C* **386** 603.
- [139] A Yamamoto, H Tanaka, J Shimoyama, H Ogino, K Kishio and T Matsushita “Towards the Realization of Higher Connectivity in  $MgB_2$  Conductors: *In-situ* or Sintered *Ex-situ*?” 2012 *Jpn. J. Appl. Phys.* **51** 010105.
- [140] T Matsushita, M Kiuchi, A Yamamoto, J Shimoyama and K Kishio “Essential factors for the critical current density in superconducting  $MgB_2$ : connectivity and flux pinning by grain boundaries” 2008 *Supercond. Sci. Technol.* **21** 015008.
- [141] A Matsumoto, H Kumakura, H Kitaguchi, B J Senkowicz, M C Jewell, E E Hellstrom, Y Zhu, P M Voyles and D C Larbalestier “Evaluation of connectivity, flux pinning, and upper critical field contributions to the critical current density of bulk pure and SiC-alloyed  $MgB_2$ ” 2006 *Appl. Phys. Lett.* **89** 132508.
- [142] M A Susner “Influences of Crystalline Anisotropy, Doping, Porosity, and Connectivity on the Critical Current Densities of Superconducting Magnesium Diboride Bulks, Wires, and Thin Films” PhD thesis 2012 *The Ohio State University*.
- [143] A V Pan, S Zhou, H Liu and S X Dou “Properties of superconducting  $MgB_2$  wires: *in situ* versus *ex situ* reaction technique” 2003 *Supercond. Sci. Technol.* **16** 639.
- [144] B A Glowacki, M Majoros, M Vickers, J E Evetts, Y Shi and I McDougall “Superconductivity of powder-in-tube  $MgB_2$  wires” 2001 *Supercond. Sci. Technol.* **14** (2001) 193.
- [145] H Kumakura, A Matsumoto, H Fujii and K Togano “High transport critical current density obtained for powder-in-tube-processed  $MgB_2$  tapes and wires using stainless steel and Cu-Ni tubes” 2001 *Appl. Phys. Lett.* **79** 2435.
- [146] S Jin, H Mavoori, C Bower and R B van Dover “High critical currents in iron-clad superconducting  $MgB_2$  wires” 2011 *Nature* **411** 563.
- [147] G Grasso, A Malagoli, C Ferdeghini, S Roncallo, V Braccini, A S Siri and M R Cimberle “Large transport critical currents in unsintered  $MgB_2$  superconducting tapes” 2001 *Appl. Phys. Lett.* **79** 230.
- [148] C E J Dancer, P Mikheenko, A Bevan, J S Abell, R I Todd and C R M Grovenor “A study of the sintering behaviour of magnesium diboride” 2009 *J. Europ. Cer. Soc.* **29** 1817.

- [149] A Gupta, A Kumar and A V Narlikar “Normal state connectivity and  $J_c$  of weakly coupled  $MgB_2$  particles” 2009 *Supercond. Sci. Technol.* **22** 105005.
- [150] S Mizutani, A Yamamoto, J Shimoyama, H Ogino and K Kishio “Understanding routes for high connectivity in *ex situ*  $MgB_2$  by self-sintering” 2014 *Supercond. Sci. Technol.* **27** 044012.
- [151] S Mizutani, A Yamamoto, J Shimoyama, H Ogino and K Kishio “Self-sintering-assisted high intergranular connectivity in ball-milled *ex situ*  $MgB_2$  bulks” 2014 *Supercond. Sci. Technol.* **27** 114001.
- [152] A Kario, R Nast, W Häßler, C Rodig, C Mickel, W Goldacker, B Holzapfel and L Schultz “Critical current density enhancement in strongly reactive *ex situ*  $MgB_2$  bulk and tapes prepared by high energy milling” 2011 *Supercond. Sci. Technol.* **24** 075011.
- [153] C Dancer “*Ceramic Processing of Magnesium Diboride*” PhD Thesis, University of Oxford, (2008).
- [154] C E J Dancer, D Prabhakaran, A Crossley, R I Todd and C R M Grovenor “The effects of attrition and ball milling on the properties of magnesium diboride” 2010 *Supercond. Sci. Technol.* **23** 065015.
- [155] H Tanaka, A Yamamoto, J Shimoyama, H Ogino and K Kishio “Strongly connected *ex situ*  $MgB_2$  polycrystalline bulks fabricated by solid-state self-sintering” 2012 *Supercond. Sci. Technol.* **25** 115022.
- [156] J H Durrell, C E J Dancer, A Dennis, Y Shi, Z Xu, A M Campbell, N Hari Babu, R I Todd, C R M Grovenor and D A Cardwell “A trapped field of  $>3$  T in bulk  $MgB_2$  fabricated by uniaxial hot pressing” 2012 *Supercond. Sci. Technol.* **25** 112002.
- [157] P Mikheenko, A I Bevan and J S Abell “Nucleation and growth of dense phase in compressed  $MgB_2$ ” 2006 *J. Phys.: Conf. Ser.* **43** 535.
- [158] P C Canfield, D K Finnemore, S L Bud’ko, J E Ostenson, G Lapertot, C E Cunningham and C Petrovic “Superconductivity in Dense  $MgB_2$  Wires” 2001 *Phys. Rev. Lett.* **86** 2423.
- [159] D C Dunand “Synthesis of superconducting Mg- $MgB_2$  composites” 2001 *Appl. Phys. Lett* **79** 4186.
- [160] J D DeFouw and D C Dunand “In situ synthesis of superconducting  $MgB_2$  fibers within a magnesium matrix” 2003 *Appl. Phys. Lett.* **83** 120.
- [161] G Giunchi “High density  $MgB_2$  obtained by reactive liquid Mg infiltration” 2003 *Inter. J. of Modern Phys. B* **17** 453.
- [162] G Giunchi, G Ripamonti, G T Cavallin and E Bassani “The reactive liquid Mg infiltration process to produce large superconducting bulk  $MgB_2$  manufactures” 2006 *Cryogenics* **46** 237.
- [163] J M Hur, K Togano, A Matsumoto, H Kumakura, H Wada and K Kimura “Fabrication of high-performance  $MgB_2$  wires by an internal Mg diffusion process” 2008 *Supercond. Sci. Technol.* **21** 032001.
- [164] K Togano, J Hur, A Matsumoto and H Kumakura “Microstructures and critical currents of single- and multi-filamentary  $MgB_2$  superconducting wires fabricated by an internal Mg diffusion process” 2010 *Supercond. Sci. Technol.* **23** 085002.

- [165] J Jiang, B J Senkowicz, D C Larbalestier and E E Hellstrom “Influence of boron powder purification on the connectivity of bulk  $\text{MgB}_2$ ” 2006 *Supercond. Sci. Technol.* **19** L33.
- [166] X Xu *et al* “Effect of boron powder purity on superconducting properties of  $\text{MgB}_2$ ” 2006 *Supercond. Sci. Technol.* **19** 466.
- [167] S K Chen, K A Yates, M G Blamire and J L MacManus-Driscoll “Strong influence of boron precursor powder on the critical current density of  $\text{MgB}_2$ ” 2005 *Supercond. Sci. Technol.* **18** 1473.
- [168] R A Ribeiro, S L Bud’ko, C Petrovic and P C Canfield “Effects of stoichiometry, purity, etching and distilling on resistance of  $\text{MgB}_2$  pellets and wire segments” 2002 *Physica C* **382** 194.
- [169] G Giunchi, G Ripamonti, S Raineri, D Botta, R Gerbaldo and R Quarantiello “Grain size effects on the superconducting properties of high density bulk  $\text{MgB}_2$ ” 2004 *Supercond. Sci. Technol.* **17** S583.
- [170] J H Kim, Y U Heo, A Matsumoto, H Kumakura, M Rindfleisch, M Tomsic and S X Dou “Comparative study of mono- and multi-filament  $\text{MgB}_2$  wires with different boron powders and malic acid addition” 2010 *Supercond. Sci. Technol.* **23** 075014.
- [171] F A L Dullien “Porous Media: Fluid Transport and Pore Structure” 1991 San Diego: Academic Press.
- [172] H Kumakura “Development of High Performance  $\text{MgB}_2$  Tapes and Wires” 2012 *J. Phys. Soc. Jpn.* **81** 011010.
- [172] M Maeda *et al* “Enhancing the Superconducting Properties of Magnesium Diboride Without Doping” 2013 *J. Am. Ceram. Soc.* **96** 2893.
- [173] D Wang, Y Ma, Z Yu, Z Gao, X Zhang, K Watanabe and E Mossang “Strong influence of precursor powder on the critical current density of Fe-sheathed  $\text{MgB}_2$  tapes” 2007 *Supercond. Sci. Technol.* **20** 574
- [174] W Hassler, H Hermann, M Herrmann, C Rodig, A Aubele, L Schmolinga, B Sailer and B Holzapfel “Influence of the milling energy transferred to the precursor powder on the microstructure and the superconducting properties of  $\text{MgB}_2$  wires” 2013 *Supercond. Sci. Technol.* **26** 025005.
- [175] C Wang *et al* “Effect of high-energy ball milling time on superconducting properties of  $\text{MgB}_2$  with low purity boron powder” 2012 *Supercond. Sci. Technol.* **25** 035018.
- [176] S Sugino, A Yamamoto, J Shimoyama and K Kishio “Enhanced trapped field in  $\text{MgB}_2$  bulk magnets by tuning grain boundary pinning through milling” 2015 *Supercond. Sci. Technol.* **28** 055016.
- [177] C Fischer *et al* “Preparation of  $\text{MgB}_2$  tapes using a nanocrystalline partially reacted precursor” 2003 *Appl. Phys. Lett.* **83** 1803.
- [178] O Perner *et al* “Microstructure and impurity dependence in mechanically alloyed nanocrystalline  $\text{MgB}_2$  superconductors” 2004 *Supercond. Sci. Technol.* **17** 1148.
- [179] Y Takano, H Takeya, H Fujii, H Kumakura and T Hatano “Superconducting properties of  $\text{MgB}_2$  bulk materials prepared by high-pressure sintering” 2001 *Appl. Phys. Lett.* **78** 2914.



- [180] C U Jung, M Park, W N Kang, M Kim, K H P Kim, S Y Lee and S Lee “Effect of Sintering Under High Pressure on the Superconductivity of  $\text{MgB}_2$ ” 2001 *Appl. Phys. Lett.* **78** 4157.
- [181] X Z Liao, A Serquis, Y T Zhu, L Civale, D L Hammon, D E Peterson, F M Mueller, V F Nesterenko and Y Gu “Defect structures in  $\text{MgB}_2$  wires introduced by hot isostatic pressing” 2003 *Supercond. Sci. Technol.* **16** 799.
- [182] S Brutti, G Balducci, G Gigli, A Ciccioi, P Manfrinetti and A Palenzona “Thermodynamic and kinetic aspects of decomposition of  $\text{MgB}_2$  in vacuum: Implications for optimization of synthesis conditions” 2006 *J. Cryst. Growth.* **289** 578.
- [183] Z Y Fan, D G Hinks, N Newman and J M Rowell “Experimental study of  $\text{MgB}_2$  decomposition” 2001 *Appl. Phys. Lett.* **79** 87.
- [184] A Yamamoto, J Shimoyama, S Ueda, Y Katsura, I Iwayama, S Horii and K Kishio “Universal relationship between crystallinity and irreversibility field of  $\text{MgB}_2$ ” 2005 *Appl. Phys. Lett.* **86** 212502.
- [185] J H Kim *et al* “The effects of sintering temperature on superconductivity in  $\text{MgB}_2/\text{Fe}$  wires” 2007 *Supercond. Sci. Technol.* **20** 448.
- [186] Z Q Ma and Y C Liu *et al* “Low-temperature synthesis of  $\text{MgB}_2$  superconductors” 2011 *Inter. Mat. Rev.* **56** 267.
- [187] N Rogado, M A Hayward, K A Regan, Y Wang, N P Ong, H W Zandbergen, J M Rowell and R J Cava “Low temperature synthesis of  $\text{MgB}_2$ ” 2002 *J. of Appl. Phys.* **91** 274.
- [188] R Zeng, L Lu, J L Wang, J Horvat, W X Li, D Q Shi, S X Dou, M Tomsic and M Rindfleisch “Significant improvement in the critical current density of *in situ*  $\text{MgB}_2$  by excess Mg addition” 2007 *Supercond. Sci. Technol.* **20** L43.
- [189] O Perner *et al* “Stoichiometry dependence of superconductivity and microstructure in mechanically alloyed  $\text{MgB}_2$ ” 2005 *J. Appl. Phys.* **97** 056105.
- [190] C H Jiang, T Nakane and H Kumakura “Superior high-field current density in slightly Mg-deficient  $\text{MgB}_2$  tapes” 2005 *Appl. Phys. Lett.* **87** 252505.
- [191] H Fujii, K Togano and H Kumakura “Enhancement of critical current densities of powder-in-tube processed  $\text{MgB}_2$  tapes by using  $\text{MgH}_2$  as a precursor powder” 2002 *Supercond. Sci. Technol.* **15** 1571.
- [192] H Kumakura, H Kitaguchi, A Matsumoto and H Yamada “Upper critical field, irreversibility field, and critical current density of powder-in-tube-processed  $\text{MgB}_2/\text{Fe}$  tapes” 2005 *Supercond. Sci. Technol.* **18** 1042.
- [193] S Hata *et al* “Microstructures of  $\text{MgB}_2/\text{Fe}$  tapes fabricated by an *in situ* powder-in-tube method using  $\text{MgH}_2$  as a precursor powder” 2006 *Supercond. Sci. Technol.* **19** 161.
- [194] A Ito, A Yamamoto, J Shimoyama, H Ogino and K Kishio “Synthesis of Denser In Situ  $\text{MgB}_2$  Bulks Using  $\text{MgB}_4$  Precursor” 2013 *IEEE Trans. Appl. Superconduct.* **23** 7101005.
- [195] D Nardelli *et al* “Large critical current density in  $\text{MgB}_2$  wire using  $\text{MgB}_4$  as precursor” 2013 *Supercond. Sci. Technol.* **26** 075010.
- [196] D Xu *et al* “Fabrication and superconducting properties of internal Mg diffusion processed  $\text{MgB}_2$  wires using  $\text{MgB}_4$  precursors” 2016 *Supercond. Sci. Technol.* **29** 105019.

- [197] K L Tan, K Y Tan, K P Lim, A H Shaari, S K Chen “Optimization of Phase Formation and Superconducting Properties in MgB<sub>2</sub> Prepared by Phase Transformation from MgB<sub>4</sub>” 2013 *J Elec. Mater.* **41** 673.
- [198] S K Chen, Z Lockman, M Wei, B A Glowacki and J L MacManus-Driscoll “Improved current densities in MgB<sub>2</sub> by liquid-assisted sintering” 2005 *Appl. Phys. Lett.* **86** 242501.
- [199] O V Shcherbakova, D I Santos, S X Dou “Effect of Mg–Ga powder addition on the superconducting properties of MgB<sub>2</sub> samples” 2007 *Physica C* **460** 583.
- [200] Q Zhao, Y Liu, N Zhao, S Penner and Z AMa “Novel Approach for Efficient Ni Nanoparticle Doping of MgB<sub>2</sub> by Liquid-Assisted Sintering” 2011 *IEEE Trans. Nanotechnol.* **10** 331.
- [201] D Kumar, S J Pennycook, J Narayan, H Wang and A Tiwari “Role of silver addition in the synthesis of high critical current density MgB<sub>2</sub> bulk superconductors” 2003 *Supercond. Sci. Technol.* **16** 455.
- [202] Y Zhao *et al* “High critical current density of MgB<sub>2</sub> bulk superconductor doped with Ti and sintered at ambient pressure” 2001 *Appl. Phys. Lett.* **79** 1154.
- [203] P Kovac, I Husek, T Melisek, C R M Grovenor, S Haigh and H Jones “Improvement of the current carrying capability of *ex situ* MgB<sub>2</sub> wires by normal particle additions” 2004 *Supercond. Sci. Technol.* **17** 1225.
- [204] W B Hillig “Melt infiltration approach to ceramic matrix composites” 1988 *J. Am. Ceram. Soc.* **71** C96.
- [205] Z Ahmad and J E Mark “Polyimide–Ceramic Hybrid Composites by the Sol–Gel Route” 2001 *Chem. Mater.* **13** 3320.
- [206] P Colombo, G Mera, R Riedel and G D Soraru “Polymer-Derived Ceramics: 40 Years of Research and Innovation in Advanced Ceramics” 2010 *J. Am. Ceram. Soc.* **93** 1805.
- [207] E Kroke, Y L Li, C Konetschny, E Lecomte, C Fasel and R Riedel “Silazane derived ceramics and related materials” 2000 *Mater. Sci. Eng.: R* **26** 97.
- [208] M S Newkirk, A W Urquhart, H R Zwicker and E Breval “Formation of Lanxide ceramic composite materials” 1986 *J. Mater. Res.* **1** 81.
- [209] R P Messner and Y M Chiang “Liquid-Phase Reaction-Bonding of Silicon Carbide Using Alloyed Silicon-Molybdenum Melts.” 1990 *J. Am. Ceram. Soc.* **73** 1193.
- [210] N Hari Babu, M Kambara, P J Smith, D A Cardwell and Y Shi “Fabrication of large single-grain Y–Ba–Cu–O through infiltration and seeded growth processing” 2000 *J. Mater. Res.* **15** 1235.
- [211] E Sudhakar Reddy, J G Noudem, M Tarka and G J Schmitz “Mono-domain YBa<sub>2</sub>Cu<sub>3</sub>O<sub>y</sub> superconductor fabrics prepared by an infiltration process” 2000 *Supercond. Sci. Technol.* **13** 716.
- [212] K. Aarstad PhD thesis, “Protective films on molten Mg”, Norwegian University of Science and Technology 2004.
- [213] <http://resource.npl.co.uk/mtdata/phdiagrams/femg.htm>. Accessed on 16<sup>th</sup> January 2017.
- [214] D X Chen and R B Goldfarb “Kim model for magnetization of type-II superconductors” 1989 *J. Appl. Phys.* **66** 2489.

- [215] C Marchal, J F Fagnard, Y H Shi, D A Cardwell, J Mucha, H Misiorek, R Cloots, B Vertruyen and P Vanderbemden “The influence of a grain boundary on the thermal transport properties of bulk, melt-processed Y-Ba-Cu-O” 2013 *Supercond. Sci. Technol.* **26** 015006.
- [216] P Laurent, J F Fagnard, N Hari Babu, D A Cardwell, B Vanderheyden and P Vanderbemden “Self-heating of bulk high temperature superconductors of finite height subjected to a large alternating magnetic field” 2010 *Supercond. Sci. Technol.* **23** 124004.
- [217] G Giunchi, C Orecchia, L Malpezzi and N Masciocchi “Analysis of Minority Crystalline Phases in Bulk Superconducting MgB<sub>2</sub> Obtained by Reactive Liquid Mg Infiltration” 2006 *Physica C* **433** 182.
- [218] G Giunchi, L Malpezzi and N Masciocchi “A New Crystalline Phase of the Boron-rich Metal-Boride Family: The Mg<sub>2</sub>B<sub>25</sub> Species” 2006 *Solid State Sciences* **8** 1202.
- [219] A F Albisetti, L Saglietti, E Perini, C Schiavone, G Ripamonti and G Giunchi, “The Mg<sub>2</sub>B<sub>25</sub> formation and its role in the preparation of bulk MgB<sub>2</sub> superconductors” 2012 *Solid State Sciences* **14** 1632.
- [220] E W Washburn “The Dynamics of Capillary Flow” 1921 *Phys. Rev. B.* **17** 273.
- [221] M Kulich, P Kovac, M Eisterer, I Husek, T Melisek, H W Weber and W Hassler “Effect of C and SiC additions into *in situ* or mechanically alloyed MgB<sub>2</sub> deformed in Ti sheath” 2009 *Physica C* **469** 827.
- [222] P Kovac P, M Kulich M, W Haessler, M Hermann, T Melisek and M Reissner “Properties of MgB<sub>2</sub> wires made of oxidized powders” 2012 *Physica C* **477** 20.
- [223] C U Jung, H J Kim, M S Park, M S Kim, J Y Kim, Z Du, S I Lee, K H Kim, J B Betts, M Jaime, A H Lacerda and G S Boebinger “Effects of unreacted Mg impurities on the transport properties of MgB<sub>2</sub>” 2002 *Physica C* **377** 21.
- [224] G Fuchs, K H Müller, A Handstein, K Nenkov, V N Narozhnyi, D Eckert, M Wolf and L Schultz “Upper critical field and irreversibility line in superconducting MgB<sub>2</sub>” 2001 *Solid State Communications* **118** 497.
- [225] M Zehetmayer, M Eisterer, J Jun, S M Kazakov, J Karpinski, A Wisniewski and H W Weber “Mixed-state properties of superconducting MgB<sub>2</sub> single crystals” 2002 *Phys. Rev. B* **66** 052505.
- [226] Giunchi G, Albsetti A F, Malpezzi L, Sagletti L and Perini E 2011 *Proceedings of 2011 IEEE International Conference on Applied Superconductivity and Electromagnetic Devices* 313.
- [227] M Maeda, Y Zhao, Y Nakayama, T Kawakami, H Kobayashi and Y Kubota “Fabrication of highly dense MgB<sub>2</sub> bulk at ambient pressure” 2008 *Supercond. Sci. Technol.* **21** 032004.
- [228] T A Prikhna, M Eisterer, H W Weber, W Hawalek, V V Kovylaev, M V Karpets, T V Basyuk and V E Moshchil “Nanostructural inhomogeneities acting as pinning centers in bulk MgB<sub>2</sub> with low and enhanced grain connectivity” 2014 *Supercond. Sci. Technol.* **27** 044013.
- [229] G Giunchi, T Cavallin, P Bassani and S Guicciardi “The mechanical properties of the MgB<sub>2</sub> bulk materials obtained by reactive liquid infiltration” 2008 *AIP Conf. Proc.* **986** 396.

- [230] J Horvat, S Soltanian, X L Wang and S X Dou “Effect of sample size on magnetic  $J_c$  for  $MgB_2$  superconductor” 2004 *Appl. Phys. Lett.* **84** 3109.
- [231] H Fujishiro, T Naito, D Furuta, T Arayashiki, Y Yanagi and Y Itoh “Direct  $J_c$  measurements and trapped field profiles using an identical superconducting bulk” 2011 *Supercond. Sci. Technol.* **24** 105003.
- [232] T Naito, A Ogino and H Fujishiro “Potential ability of 3 T class trapped field on  $MgB_2$  bulk surface synthesized by the infiltration capsule method” 2016 *Supercond. Sci. Technol.* **29** 115003.
- [233] R Zeng, L Lu, W X Li, J L Wang, D Q Shi, J Horvat, S X Dou, M Bhatia, M Sumption, E W Collings, J M Yoo, M Tomsic and M Rindfleisch “Excess Mg addition  $MgB_2/Fe$  wires with enhanced critical current density” 2008 *J. Appl. Phys.* **103** 083911.
- [234] T Wang, Z Chen, H Fu and T Li “Grain Refining Performance of Al-B Master Alloys with Different Microstructures on Al-7Si Alloy” 2013 *Met. Mater. Int.* **19** 367.
- [235] H E Calderona, R G I Hidalgo, Z H Melgarejoc and O M Suarezd “Effect of  $AlB_2$ -Mg interaction on the mechanical properties of Al-based composites” 2010 *Mater. Sci. Eng. A* **527** 2258.
- [236] J A Wilson, J W Steeds, H H Wills, D M J Wilkes, P S Goodwin, C M Ward-Close “Reaction of magnesium boride particles in mechanically alloyed Ti-4wt% $MgB_2$ ” 2001 *J. Mater. Sci.* **36** 67.
- [237] M Mudgel, V P S Awana, H Kishan, G L Bhalla “Aluminium substitution induced superstructures in  $Mg_{1-x}Al_xB_2$  ( $x = 0.0$  to  $0.50$ ): An X-ray diffraction study” 2007 *Physica C* **467** 31.
- [238] J Ma, A Sun, G Wei, L Zheng, G Yang and X Zhang “Al-Doping Effects on the Structural Change of  $MgB_2$ ” 2010 *J. Supercond. Nov. Magn.* **23** 187.
- [239] M S Park, C U Jung, J Y Kim, K H Kim, B W Kang and S I Lee “Effect of Al substitution on the Mg site in  $Mg^{11}B_2$  prepared under high-pressure conditions” 2003 *J. Low. Temp. Phys.* **131** 1165.
- [240] J Y Xiang, D N Zheng, J Q Li, L Li, P L Lang, H Chen, C Dong, G C Che, Z A Ren, H H Qi, H Y Tian, Y M Ni and Z X Zhao “Superconducting properties and  $c$ -axis superstructure of  $Mg_{1-x}Al_xB_2$ ” 2002 *Phys. Rev. B* **65** 214536.
- [241] J Karpinski, S M Kazakov, J Jun, N D Zhigadlo, M Angst, R Puzniak, A Wisniewski “ $MgB_2$  and  $Mg_{1-x}Al_xB_2$  single crystals: high-pressure growth and physical properties” 2004 *Physica C* **408** 81.
- [242] I Iwayama, S Ueda, A Yamamoto, Y Katsura, J Shimoyama, S Horii, K Kishio “ $J_c$  enhancement of high density  $MgB_2$  bulk made by Premix-PICT-Diffusion method” 2007 *Physica C* **460** 581.
- [243] A A Polyanskii, A Yamamoto, I Iwayama, J Shimoyama, K Kishio, D C Larbalestier “Magneto-Optical Studies on Polycrystalline  $MgB_2$  Bulks Manufactured by Different Processes” 2007 *IEEE Trans. Appl. Supercond.* **17** 2746.
- [244] H Fujishiro, T Naito and T Yoshida “Numerical simulation of the trapped field in  $MgB_2$  bulk disks magnetized by field cooling” 2014 *Supercond. Sci. Technol.* **27** 065019.
- [245] G Fuchs, W Haßler, K Nenkov, J Scheiter, O Perner, A Handstein, T Kanai, L Schultz and B Holzapfel “High trapped fields in bulk  $MgB_2$  prepared by hot-pressing of ball-milled

- precursor powder” 2013 *Supercond. Sci. Technol.* **26** 122002.
- [246] A Yamamoto *et al.* 2015 (*International Workshop on Processing and Applications of Superconducting (RE)BCO Large Grain Materials*).
- [247] A Yamamoto, A Ishihara, M Tomita and K Kishio “Permanent magnet with MgB<sub>2</sub> bulk superconductor” 2014 *Appl. Phys. Lett.* **105** 032601.
- [248] T Naito, T Yoshida and H Fujishiro “Ti-doping effects on magnetic properties of dense MgB<sub>2</sub> bulk superconductors” 2015 *Supercond. Sci. Technol.* **28** 095009.
- [249] J H Durrell, C E J Dancer, A Dennis, Y Shi, Z Xu, A M Campbell, N Hari Babu, R I Todd, C R M Grovenor and D A Cardwell “A trapped field of 3 T in bulk MgB<sub>2</sub> fabricated by uniaxial hot pressing” 2012 *Supercond. Sci. Technol.* **25** 112002.
- [250] R V Viznichenko, A A Kordyuk, G Fuchs, K Nenkov, K H Müller, T A Prikhna, and W. Gawalek “Temperature dependence of the trapped magnetic field in MgB<sub>2</sub> bulk superconductors” 2003 *Appl. Phys. Lett.* **83** 4360.
- [251] M Muralidhar, K Inoue, M R Koblischka, M Tomita and M Murakami “Optimization of processing conditions towards high trapped fields in MgB<sub>2</sub> bulks” 2014 *J. Alloys and Compounds* **608** 102.
- [252] N Naito, T Sasaki and H Fujishiro “Trapped magnetic field and vortex pinning properties of MgB<sub>2</sub> superconducting bulk fabricated by a capsule method” 2012 *Supercond. Sci. Technol.* **25** 095012.
- [253] E Perini, G Giunchi, L Saglietti, A F Albisetti, A Matrone and V Cavaliere “Magnetic Field Trapping in MgB<sub>2</sub> Bulks and Inserts” 2001 *IEEE Trans. Appl. Supercond.* **21** 2690.
- [254] G Giunchi, E Perini, T Cavallin, E Bassani, R Quarantiello, V Cavaliere and A Matrone “Superconducting Permanent Magnet Made by a Bulk MgB<sub>2</sub> Ring” 2008 *IEEE Trans. Appl. Supercond.* **18** 1216.
- [255] H Mochizuki, H Fujishiro, T Naito, A F Albisetti and G Giunchi “Trapped field properties of a concentric circled MgB<sub>2</sub> bulk composite magnetized by pulsed field and field cooling” 2015 *Supercond. Sci. Technol.* **28** 105004.
- [256] J Zou, M D Ainslie, H Fujishiro, A G Bhagurkar, T Naito, N Hari Babu, J-F Fagnard, P Vanderbemden and A Yamamoto “Numerical modelling and comparison of MgB<sub>2</sub> bulks fabricated by HIP and infiltration Growth” 2015 *Supercond. Sci. Technol.* **28** 075009.
- [257] A Yamamoto *et al.* 2011 “MgB<sub>2</sub> bulk superconducting magnet” *Abstracts of The 15th Japan-US Workshop on Advanced Superconductors* arXiv:1208.185.
- [258] T Johansen “Flux-pinning-induced stress and magnetostriction in bulk superconductors” 2000 *Supercond. Sci. Technol.* **13** R121.
- [259] M R Beasley, R Labusch and W W Webb “Flux creep in type-II superconductors” 1969 *Phys. Rev.* **181** 682.
- [260] E Bauer, C Paul, S Berger, S Majumdar, H Michor, M Giovannini, A Saccone and A Bianconi “Thermal Conductivity of superconducting MgB<sub>2</sub>” 2001 *J. Phys.: Condens. Matter* **13** L487.
- [261] T Ying, H Chi, M Zheng, Z Li and C Uher “Low-temperature electrical resistivity and thermal conductivity of binary magnesium alloys” 2014 *Acta Materialia* **80** 288.

- [262] M Tomita and Masato Murakami “High-temperature superconductor bulk magnets that can trap magnetic fields of over 17 tesla at 29 K” 2003 *Nature* **421** 517.
- [263] J D DeFouw and D C Dunand “Mechanism and Kinetics of  $MgB_2$  synthesis from Boron Fibers” 2008 *Acta Materialia*, **56** 5751.
- [264] K Zhao, M Pharr, Q Wan, W L Wang, E Kaxiras, J J Vlassak and Z Suo, “Concurrent Reaction and Plasticity During Initial Lithiation of Crystalline Silicon in Lithium Ion Batteries” 2012 *J. Electrochem. Soc.* **159** A238.
- [265] X H Liu, L Zhong, S Huang, S X Mao, T Zhu and J Y Huang “Size Dependent Fracture of Silicon Nanoparticles During Lithiation” 2012 *ACS Nano* **6** 1522.
- [266] M T McDowell, S W Lee, W D Nix and Y Cui “Understanding the Lithiation of Silicon and Other Alloying Anodes for Lithium Ion Batteries” 2013 *Adv. Mater.* **25** 4966.
- [267] M Ebner, F Marone, M Stampanoni and V Wood “Visualization and Quantification of Electrochemical and Mechanical Degradation in Li Ion Batteries” 2013 *Science* **342** 716.
- [268] S Huang, F Fan, J Li, S Zhang and T Zhu “Stress Generation During Lithiation of High Capacity Electrode Particles in Lithium Ion Batteries” 2013 *Acta Materialia* **61** 4354.
- [269] V F Nesterenko and Y Gu “Elastic Properties of Hot-Isostatically Pressed Magnesium Diboride” 2003 *Appl. Phys. Lett.* **82** 4104.
- [270] H Yanagida, K Koumoto, M Miyayama "The Chemistry of Ceramics", John Wiley & Sons (1996).
- [271] D L Portert and A H Heuer “Mechanism of Toughening Partially Stabilized Zirconia (PSZ)” 1977 *J. Am. Ceram. Soc.* **60** 183.
- [272] K Iida , N Hari Babu, Y Shi and D A Cardwell “Seeded Infiltration and Growth of Large, Single Domain Y-Ba-Cu-O Bulk Superconductors With Very High Critical Current Densities” 2005 *Supercond. Sci. Technol.* **18** 1421.
- [273] B E Deal and A S Grove “General Relationship for Thermal Oxidation of Silicon” 1965 *J. Appl. Phys.* **36** 3770.
- [274] H M Kim, S S Yim, K B Kim, S H Moon Y W Kim and D H Kang “Growth Kinetics of  $MgB_2$  Layer and Interfacial MgO Layer During *ex situ* Annealing of Amorphous Boron Film” 2004 *J. Mater. Res.* **19** 3081.
- [275] A K Mukhopadhyay, S K Datta and D Chakraborty “Hardness of silicon nitride and sialon” 1991 *Ceramics International* **17**121.
- [276] S Y Lee, S I Yoo, Y W Kim, N M Hwang, D Y Kim “Preparation of dense  $MgB_2$  bulk superconductors by spark plasma sintering” 2003 *J. Am. Ceram. Soc.* **86** 1800.
- [277] <http://fs.magnet.fsu.edu/~lee/plot/plotarchive.htm> (Accessed on 19th January 2017)
- [278] R H T Wilke, S L Budko, P C Canfield, D K Finnemore, S T Hannahs “Synthesis of  $Mg(B_{1-x}C_x)_2$  powders” 2005 *Physica C* **432**193.
- [279] S Lee, T Masui, A Yamamoto, H Uchiyama and S Tajima “Carbon substituted  $MgB_2$  single crystals” 2003 *Physica C* **397** 7.
- [280] B D Cullity *Elements of X-ray Diffraction* Addison-Wesley Publishing Company Inc., California, 1956.

- [281] X L Wang, S Soltanian, M James, M J Qin, J Horvat, Q W Yao, H K Liu, S X Dou “Significant enhancement of critical current density and flux pinning in MgB<sub>2</sub> with nano-SiC, Si, and C doping” 2004 *Physica C* **408** 63.
- [282] E J Kramer “Scaling Laws for Flux Pinning in Hard Superconductors” 1973 *J. Appl. Phys.* **44** 1360.
- [283] Matsushita, T. *Flux Pinning in Superconductors* 2nd edn, Ch. 9.2, 384–386 (Springer, 2014).
- [284] Y Yang, M D Sumption and E W Collings “Influence of Metal Diboride and Dy<sub>2</sub>O<sub>3</sub> Additions on Microstructure and Properties of MgB<sub>2</sub> Fabricated at High Temperatures and under Pressure” 2016 *Sci. Rep.* **6** 29306.
- [285] P W Anderson "Theory of flux creep in hard superconductors." 1962 *Phys. Rev. Lett.* **9** 309.